BULLETIN OF THE EARTHQUAKE RESEARCH INSTITUTE,
UNIVERSITY OF TOKYO. Vol. 37, Part 1. March, 1959.

東京大學
地震研究所彙報

第 37 號　第 1 册

昭和 34 年 3 月

目　次

論文及報告

			頁
1.	日本に於ける地磁気短周期変化の異常と地下構造（第8報）（英文）	力武常次・上田誠也・行武毅・棚岡巌子・中川英子	1
2.	地球中間層による地磁気永年変化の減衰（英文）	行武毅	13
3.	東京と三崎間の水準点の変動について．特に油壺験潮場内の基準石の変動について（英文）	山口生知	33
4.	地震断層の性状について (2)（dip が 90° でない場合の断層模型）（英文）	笠原慶一	39
5.	地下における地震動の研究（重複反射の問題）（英文）	金井清・田中貞二・吉沢静代	53
6.	釜石鉱山附近4回の爆破地震動の観測について（英文）	爆破地震動研究グループ	89
7.	爆破地震動による東北地方の地殻の構造（英文）	松沢武雄	123
8.	大理石の変形及び破壊についての実験的研究（第1報）特に圧縮強度のバラツキ及び強度と荷重速度との関係について（英文）	茂木清夫	155
9.	土地の脈動と台風（英文）	岸上冬彦・小高美江子	171
10.	山形市における土地脈動の三点観測（英文）	岸上冬彦・志田勇	177
11.	酒田における土地の脈動の三点観測（第2報）（英文）	岸上冬彦・志田勇	183
12.	庄内平野における土地脈動三点観測（英文）	岸上冬彦・志田勇	189
13.	超短波多重遠隔記録地震計（第2報）（邦文）	辻浦賢三・宮村摂	193

(The titles in occidental languages are given on the back cover.)

地震研究所彙報は，年4回定期に（ただし，第1号より第6号までは不定期に，第7号は3冊として刊行されだ），彙報別冊は不定期に刊行される．

この彙報に載せちれた論文及び報告についての責任は，すべてその著者のみにある．

この彙報についての照会通信は，すべて東京大学地震研究所長にあてられたい．

The Bulletin is published quarterly. (Vols. 1-6 were published at irregular intervals and Vol. 7 consisted of three parts.)
Supplementary Volume is published at irregular interval.

The authors of the papers alone are responsible for the statements and opinions contained in their respective papers.

All communications relating to this Bulletin should be addressed to the Director of the Earthquake Research Institute, University of Tokyo, Japan.

Earthquake Research Institute, University of Tokyo
Address:
No. 1, Motofuji-cho, Bunkyo-ku,
Tokyo Metropolis, Japan.
Telephone: 92-3161-Extension 6506
Cable address: ZISINKEN, TOKYO.

東京大学地震研究所
所在地
東京都文京区本富士町一番地
電話 小石川 92—3161 (代) 構内 6506
電略 ブンケウ トウダイ ヂシン

BULLETIN OF THE EARTHQUAKE
RESEARCH INSTITUTE
Vol. 37 (1959), pp. 1-11

1. The Anomalous Behaviour of Geomagnetic Variations of Short Period in Japan and Its Relation to the Subterranean Structure. The 8th report.

By Tsuneji RIKITAKE, Seiya UYEDA, Takesi YUKUTAKE, Iwao TANAOKA and Eiko NAKAGAWA,

Earthquake Research Institute.

(Read Oct. 29, 1958.—Received Oct. 29, 1958.)

Summary

As a result of the magnetic observations that were carried out on two islands in the south sea, roughly 270 and 340 *km* south of Tokyo respectively, it is concluded that the area in which we observe an anomalously large vertical component of short-period geomagnetic variations is not so wide as to cover these islands. The area seems to be very narrow covering only the southern part of Central Japan.

1. Introduction

The writers have thoroughly investigated[1),2),3),4),5)] the anomalous behaviour of geomagnetic variations of short period in Japan. Although it has been established that the anomalously large amplitudes of vertical component are observed only at stations situated in the central part of Japan and that this anomaly is caused by some agency within the earth, some further observations have been required in order to clarify the boundary of the anomalous area.

It has long been hoped, especially, to conduct observations on some of the islands which run towards the south along a line passing Central Japan, because nothing was known about the southern extent of the area in question. During the observation period of a solar eclipse that

1) T. RIKITAKE, I. YOKOYAMA and Y. HISHIYAMA, *Bull. Earthq. Res. Inst.*, **30** (1952), 207, **31** (1953), 19, 89, 101 and 119.

2) T. RIKITAKE and I. YOKOYAMA, *Bull. Earthq. Res. Inst.*, **33** (1955), 297.

3) T. RIKITAKE and I. YOKOYAMA, *Journ. Geomagn. Geoelectr.*, **5** (1953), 59.

4) T. RIKITAKE and I. YOKOYAMA, *Naturwissenschaften*, **41** (1954), 420.

5) T. RIKITAKE, I. YOKOYAMA, S. UYEDA, T. YUKUTAKE and E. NAKAGAWA, *Bull. Earthq. Res. Inst.*, **36** (1958), 1.

occurred on April 19, 1958 along the south coast of Japan Islands, we were able to have temporary stations on Hachijo-shima Island and Aogasima Island, 270 and 340 *km* south of Tokyo, together with a number of permanent and temporary stations widely distributed all over Japan. Accordingly, the observation net-work could provide the necessary magnetic data for investigating the southern limit of the anomalous area.

In the following, the outline of the magnetic observation carried out by the writers on Hachijo-shima Island will be briefly given. The anomalous distribution of the geomagnetic field that is associated with the geomagnetic bay at 12 *h* GMT on Apr. 18 will also be examined in detail with the aid of copies of magnetograms kindly sent from the other observatories. The changes that are likely to be correlated with the solar eclipse are illustrated for each station, too.

2. Magnetic observation on Hachijo-shima Island

At the time of the solar annular eclipse that occurred on Apr. 19, 1958, a net-work of stations for magnetic observation were organized by the National Committee for Solar Eclipse, Science Council of Japan. According to the observation plan proposed, the Earthquake Research Institute set up a magnetic station on Hachijo-shima Island, one of the Seven Izu Islands. Since no magnetic observations have been so far carried out on islands in the south sea, except on Ooshima Island, only 100 *km* south of Tokyo, the observation was expected to be useful not only for the detection of magnetic changes associated with the solar eclipse, but also for investigating the southern limit of the area in which we observe anomalously large amplitudes of geomagnetic variations of shord period.

A RMM magnetograph, of which the details were reported in the previous paper[5], was installed in a cave adjacent to the Hachijo Weather Station (33.°1 *N*, 139.°8 *E*). The environment around the station is shown in Fig. 1.

The observation covered a period from March to June though it was sometimes interrupted by unexpected troubles. It turns out that, on occasions of geomagnetic bays and polar magnetic storms, the changes in the vertical component (ΔZ) are not as large as those observed at the stations, *e.g.* Simosato, Aburatsubo and Kakioka, situated at the central part of the anomalous area. In contrast to those anomalous stations, we also found that shapes of ΔZ curves are different from those of ΔH (changes in the horizontal intensity). The maxima of both ΔH and ΔZ

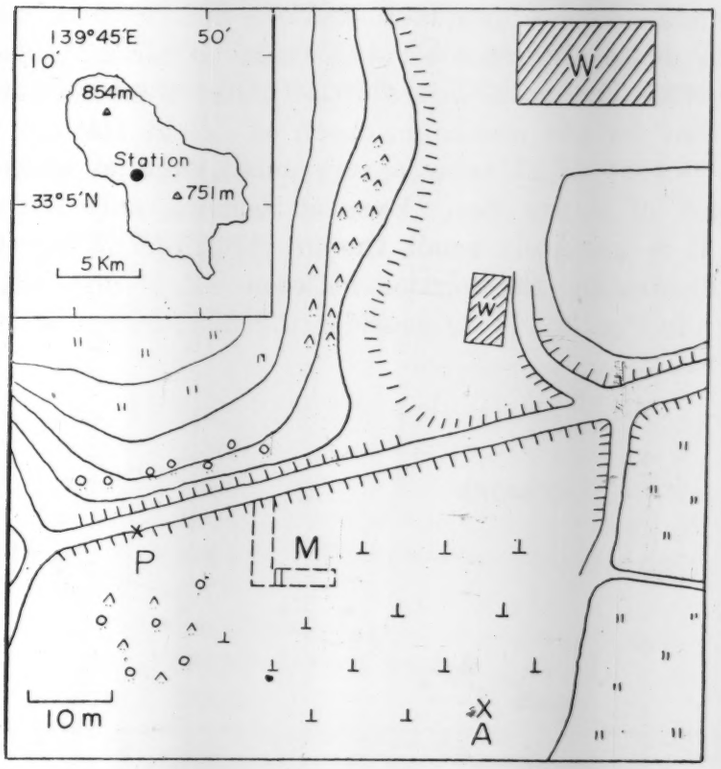

Fig. 1. Location and environment of the magnetic station on Hachijo-shima Island, W: Buildings of the Hachijo Weather Station, A: Absolute measurement point, M: Underground variometer room, P: Proton magnetometer.

do not occur at the same time at Hachijo station, while it has been confirmed that ΔH curves are parallel to ΔZ ones at Simosato, Aburatsubo and Kakioka. It seems likely that the maximum of ΔZ is delayed considerably compared to that of ΔH as can be seen, for example, in Fig. 5.

The relationship between $\Delta Z_{\max.}$ and $\Delta H_{\max.}$ are examined in regard to many bays and polar magnetic storms during the observation period. It is found that $\Delta Z_{\max.}$ is approximately proportional to $\Delta H_{\max.}$ as shown in Fig. 2, the mean value of $\Delta Z_{\max.}/\Delta H_{\max.}$ being estimated at 0.46. Since there is phase difference between ΔZ and ΔH, the ratio $\Delta Z/\Delta H$ at the maximum epoch of ΔH is substantially smaller than $\Delta Z_{\max.}/\Delta H_{\max.}$.

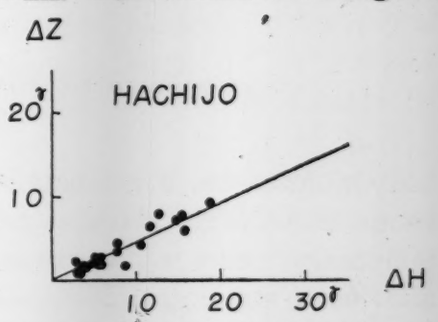

Fig. 2. The relationship between $\Delta Z_{\max.}$ and $\Delta H_{\max.}$ at Hachijo.

Similar relations between ΔZ and ΔH

have been examined for Aburatsubo, Kakioka and Ooshima Island, where we observe no phase difference between them, as already reported in the previous reports. The mean values of $\Delta Z/\Delta H$ at these stations are much larger than that for the maximum epoch of ΔH at Hachijo Station. It has been known that $\Delta Z/\Delta H$ takes a very small value at stations situated near the coast of Japan Sea. Even at Komoro, only 170 *km* north of Aburatsubo, it is generally small though $\Delta Z_{\max.}/\Delta H_{\max.}$ amounts to 0.30 there. For illustration the relation between $\Delta Z_{\max.}$ and $\Delta H_{\max.}$ for Komoro is shown in Fig. 3. If we consider the distribution of $\Delta Z/\Delta H$ along

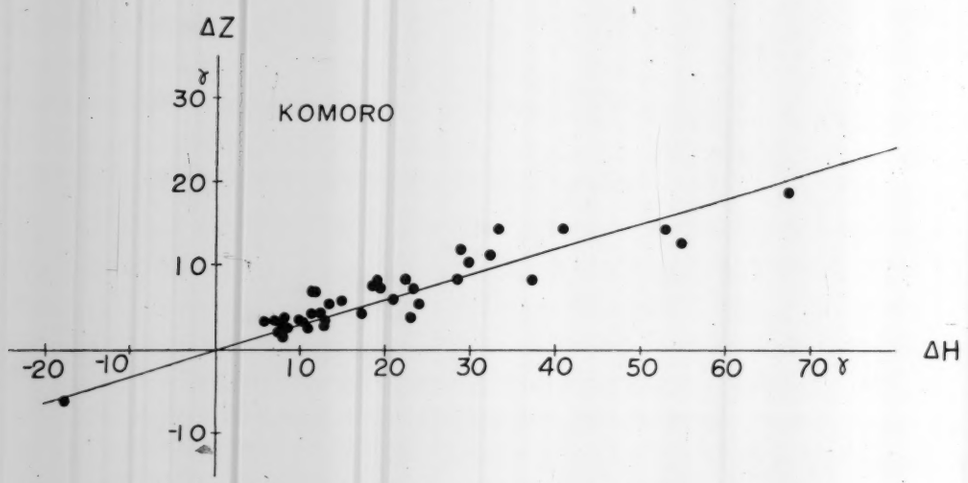

Fig. 3. The relationship between $\Delta Z_{\max.}$ and $\Delta H_{\max.}$ at Komoro.

a roughly north-west line passing Tokyo, we thus see that, for usual bays and polar magnetic storms, $\Delta Z/\Delta H$ at the maximum epoch of ΔH takes high values, 0.6 or so say, around the Tokyo area, though it falls off very steeply to small values on both sides of this area. The width in which $\Delta Z/\Delta H$ exceeds 0.5 would be approximately less than 200 *km*.

3. Geomagnetic bay that occurred at 12 *h* GMT on April 18, 1958

On April 18, a geomagnetic bay of moderate amplitude occurred at about 12 *h* GMT. On that occasion, 12 magnetic stations, permanent and temporary, were at work in Japan. They are Memambetsu, Kakioka and Kanoya (Central Meteorological Agency), Onagawa (Tohoku University), Kanosan (Geographical Survey Institute), Komoro, Aburatsubo and Hachijo (Earthquake Research Institute, Tokyo University), Aogasima

and Simosato (Hydrographic Office, Maritime Safety Agency), and Aso and Kikaigashima (Kyoto University). The geographic latitude and longitude of the stations are summarized in Table 1 and their localities are shown on the map in Fig. 4. The following study is made on the basis of copies of magnetogram kindly sent from these observatories.

Table 1. Magnetic station

Station	Geographic latitude	Geographic longitude
Memambetsu	43.°9*N*	144.°2*E*
Onagawa	38.4	141.5
Komoro	36.3	138.4
Kakioka	36.2	140.2
Kanosan	35.3	140.0
Aburatsubo	35.2	139.6
Simosato	33.6	135.9
Hachijo	33.1	139.8
Aso	32.9	131.0
Aogasima	32.5	139.8
Kanoya	31.4	130.9
Kikaigasima	28.6	129.9

Fig. 4. The locations of magnetic stations.

Changes in the three geomagnetic components during the three *hours* including the bay are illustrated in Fig. 5 for each station with the same scale throughout. In spite of the fairly regular distribution of changes in horizontal intensity and declination, we observe anomalously large ΔZ at stations in the central part of Japan. It is striking that ΔZ slightly exceeds ΔH at Simosato.

The observations on the two islands in the south sea clarify that the anomalous area does not extend that far south. The tendency of ΔZ observed there seems to be nearly the same as that observed at Komoro. The maximum of ΔZ takes place about half an *hour* later than that of ΔH, while in the anomalous area both the maxima of ΔH and ΔZ are observed at the same time.

Fig. 5. The changes in the three geomagnetic components at the time of the bay on April 18, 1958 the locations of the magnetic stations being also shown.

On asssuming that the normal variation, that should have been observed if the bay did not occur, is given by the straight line connecting the beginning of the bay with its end, we define ΔH and ΔZ as the departures from the normal curves. ΔH and ΔZ at 12 *h* 10 *m* GMT, when ΔH seems likely to reach its maximum, are given in Table 2. With these values, the distribution of ΔZ may be illustrated as shown in Fig. 6. In order to make up the equal-variation lines of ΔZ, results of many previous observations at various places are also taken into consideration though we have no observation this time. The previous observations made at the southern part of Izu Peninsula and Ooshima Island are of special importance.

Table 2. ΔH and ΔZ at 12 *h* 10 *m* on April 18.

Station	ΔH	ΔZ
Memambetsu	30.5$^{\gamma}$	7.2$^{\gamma}$
Onagawa	22.8	12.8
Komoro	24.2	3.2
Kakioka	23.2	17.5
Aburatsubo	25.5	25.4
Simosato	20.9	29.8
Hachijo	19.7	4.0
Aso	26.5	3.5
Aogasima	25.6	4.8
Kanoya	22.8	8.8
Kikaigasima	21.8	4.2

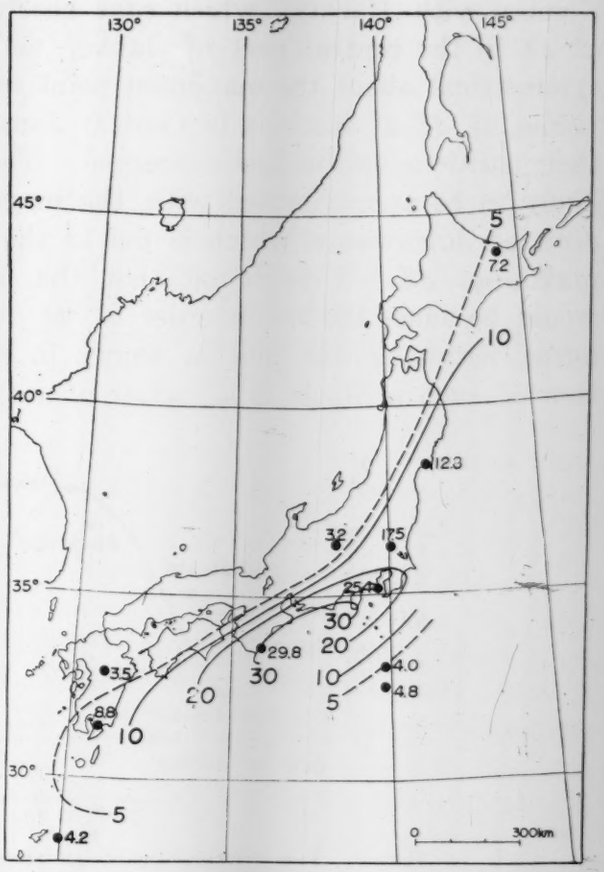

Fig. 6. The distribution of ΔZ for the maximum stage of the bay. (Unit: *gamma*)

At a glance, the general tendency of the distribution of ΔZ as demonstrated in Fig. 6 seems to be the same as that reported frequently in the writers' previous papers. It is important, however, that the southern extent of the anomaly can be brought out. Although practically nothing is known about the cause of such an anomaly, the present observation enables us to confirm that the anomalous area is a very con-

centrated one. From a close examination of ΔH, we see that its distribution is not utterly regular, for example, ΔH at Hachijo seems to be a little smaller than that expected from the general distribution. However, nothing definite can be said on this point until some more observations can be utilized from much denser net-work of observatories.

If we make up the distribution curve of ΔZ along a line connecting Komoro with Hachijo, which runs nearly perpendicular to the contours of ΔZ in the central part of Japan, we find that it is approximately symmetrical about the maximum point as can be seen in Fig. 7 in which values of ΔZ at stations in Central Japan are also shown by projecting their positions on the line concerned. The ΔZ curve thus obtained seems likely to be approximated with the magnetic field of a magnetic dipole, directed downwards, which is put in the earth right below the point for maximum ΔZ. It is found that the depth of the hypothetical dipole would be some 150 *km* in order to let its field on the earth's surface agree with the distribution shown in Fig. 7. Although the consideration of such a dipole is a matter of mathematical convenience, we may

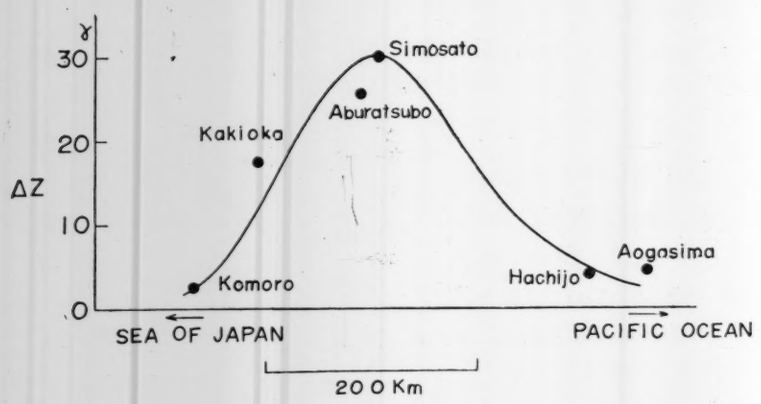

Fig. 7. The distribution of ΔZ along the line connecting Komoro with Hachijo. ΔZ's observed at stations around the anomalous area are also projected on the line.

take it that the origin of the anomalous distribution of ΔZ would lie somewhere at a depth not greatly different from that of the hypothetical dipole.

4. Geomagnetic changes that are likely to be associated with the solar eclipse on April 19, 1958

The influence of the solar eclipse on the earth's magnetic field ob-

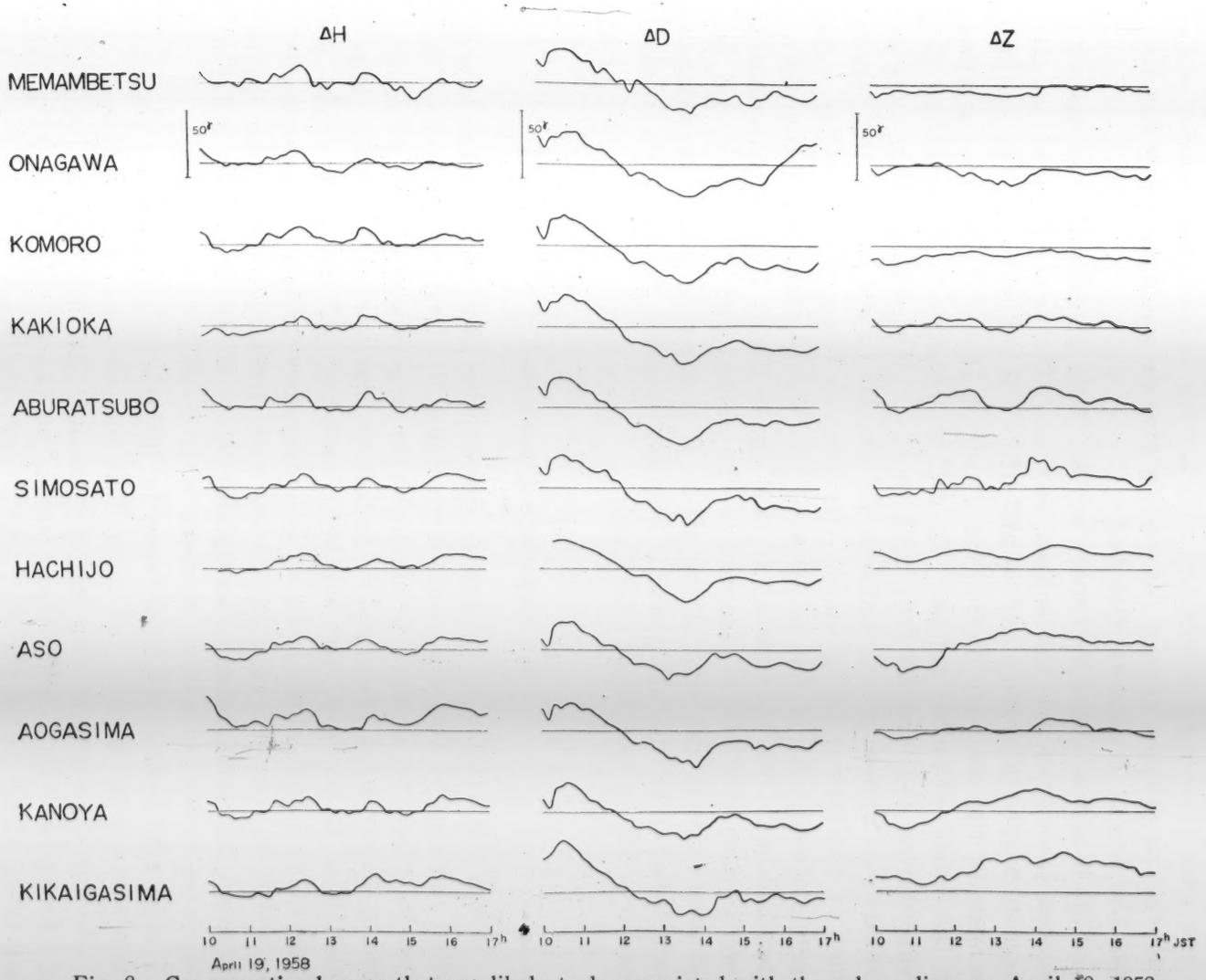

Fig. 8. Geomagnetic changes that are likely to be associated with the solar eclipse on April 19, 1958.

served during the present observation period will be reported in detail elsewhere[6]. However, it is of some interest to see how ΔZ will behave in the case of changes associated with a solar eclipse, because the overhead electric current system for such a change would be quite different from the one of a geomagnetic bay.

Fig. 8 shows the differences for the three geomagnetic components between the curves on the eclipse day and the ones obtained as the mean of a few calm days before and after the eclipse day. The marked decrease in the westerly declination at about 13 h JST may be regarded as the effect of solar eclipse. In ΔH, we observe a corresponding decrease during the interval from 12 h to 14 h. Meanwhile, ΔZ curves at Aburatsubo, Simosato and Kakioka are similar to ΔH curves, the amplitudes of the former being almost the same as those of the latter. At other stations, ΔZ is not so large as the values observed at the above three stations. We may thus say that the tendency that an anomalously large amplitude of ΔZ is observed in the central part of Japan can be also seen even in the case of the effect of a solar eclipse. The detailed characteristics of the geomagnetic changes relevant to the solar eclipse, however, will be published elsewhere.

5. Concluding remarks

From the results of magnetic observation during the observation period relevant to the solar eclipse on April 19, 1958, the extent of the area, in which we observe an anomalously large amplitude of ΔZ at the time of short-period geomagnetic variations, can be well located. Especially, it is found that the southern boundary of the area would lie somewhere around Hachijo-shima and Aogasima Islands. Consequently, the width of the area is found to be very limited, only 200 km being suggested for remarkable large amplitude of ΔZ as far as the distribution along a line connecting Komoro with Hachijo is concerned.

It is also pointed out that, even in the case of geomagnetic changes related to a solar eclipse, the anomalous tendency can be observed.

As for the cause of the anomaly, no definite idea can be obtained yet, though a rough estimate in regard to the depth of the origin has been tried. The model for the origin that has been discussed in the previous papers would still be the best explanation of the anomalous

6) T. RIKITAKE, S. UYEDA, T. YUKUTAKE, I. TANAOKA and E. NAKAGAWA, *Rep. Ionos. Res. Japan*, **12** (1958), 174.

phenomenon.

In conclusion, the writers thank the members of the Hachijo Weather Station with whose aid large parts of the observation on Hachijo-shima Island were carried out. The writers are also grateful to all the members of the magnetic stations, Memambetsu, Onagawa, Kakioka, Kanosan, Aogasima, Simosato, Aso, Kanoya and Kikaigasima, for copies of magnetogram by which the present work could be performed.

---

1. 日本に於ける地磁気短周期変化の異常と地下構造 (第8報)

地震研究所 力武常次
上田誠也
行武毅
棚岡巖
中川英子

1958 年 4 月 19 日の日本南方洋上に於ける日食の際に，日本全国に 12 カ所の地磁気観測所が設置された．この期間の観測結果を利用して，日本中部の地磁気変化異常地域の範囲を調べたところ，その南端は八丈島，青ガ島附近であろうことが推定された．

BULLETIN OF THE EARTHQUAKE
RESEARCH INSTITUTE
Vol. 37 (1959), pp. 13-32

2. *Attenuation of Geomagnetic Secular Variation through the Conducting Mantle of the Earth.**

By Takesi YUKUTAKE,

Graduate School, University of Tokyo.

(Read Nov. 18, 1958.—Received Dec. 28, 1958.)

Summary

On the assumption that a time-dependent electric current sheet, at the core boundary, of which the magnetic potential is equivalent to that due to magnetic dipoles distributed at random, is the source of geomagnetic secular variations, the decrease in amplitudes of the secular variation through the mantle is discussed by taking the existence of the conducting core into account. The lower harmonic components damp out more conspicuously than the higher ones. The electrical conductivity of the mantle to cause an attenuation most compatible with that inferred from the observation ranges 4.5×10^{-10} *e.m.u.* $\leqq\sigma\leqq2.0\times10^{-9}$ *e.m.u.* at the depth of 2500 *km*.

1. Introduction

Despite the great efforts to clarify the distribution of the electrical conductivity in the earth we have not yet succeeded in obtaining accurate values of the conductivity in every part of the earth. The electrical conductivity of the earth's core has been investigated from various points of view, and recognized to have such a high conductivity as 10^{-6} *e.m.u.* On the other hand, the conductivity distribution in the upper part of the mantle has been made fairly clear by Lahiri, Price, Rikitake and others from the study of the electric current induced in the mantle by disturbances of the magnetic field arising from outside the earth. As for the lower part of the mantle, we have only a vague idea of the conductivity distribution because no observation that gives the clue of inferring the electrical state of such a depth has been available.

The only method by which we may possibly investigate the electrical property of the lower part of the mantle is to study the attenuation,

* Communicated by T. RIKITAKE.

through conducting mantle, of geomagnetic secular variation that originates from inside the core. Elsasser[1] noticed that it was not uncommon to discern Fourier components of 50-*year* period in the records of the secular variation obtained at individual stations. In order that these frequencies were not damped out by the mantle, he estimated, the conductivity of the mantle should be 5×10^{-10} *e.m.u.* On the other hand, Runcorn[2] has assumed the spectrum of the secular variation at the bottom of the mantle to be independent of frequency and estimated the upper limit of the conductivity of the mantle so as to make the calculated spectrum of the screened secular variation agree with the observed spectrum of changes in the declination. His result shows that, if only the lower 1000 *km* of the mantle is uniformly conducting, the conductivity becomes 1.1×10^{-7} *e.m.u.* In the same paper, from the existence of sudden changes in the rate of the secular variation called "secular change impulse", Runcorn obtained 10^{-9} *e.m.u.* as the conductivity of the lower 2000 *km* of the mantle. Recently McDonald[3] has applied the attenuation theory to the mantle in which the radial distribution of the conductivity is given analytically with a few parameters. On the assumption that magnetic dipoles distributed at random at the core boundary cause the secular variation, he obtained a conductivity distribution as shown in Fig. 6.

In the case of non-conducting mantle, Elsasser[4] concluded that an arbitrary number of dipoles thrown at random very near the boundary of the core or below it may be regarded as the sources of the non-dipole part of the geomagnetic field. It seems, however, more realistic to consider that such dipoles are produced by the electric current flowing near the boundary of the core. In this paper it is assumed that the secular variation is caused by the change in those currents which are confined to a very thin shell near the core-mantle boundary. As the variation of a magnetic field or an electric current is affected by the existence of conducting material near the sources of the variation, it seems unjustifiable to ignore the existence of the conducting core in the problem of attenuating geomagnetic field. Taking into account of the electrical conductivity of the core, the attenuation of the magnetic field has been studied for various values of the conductivity in the mantle. The analyses of the secular variation enable us to select the most adequate value

1) W. M. ELSASSER, *Rev. Mod. Phys.*, **22** (1950), 1–35.
2) S. K. RUNCORN, *Trans. Amer. Geophys. Union*, **36** (1955), 191–198.
3) K. L. MCDONALD, *Jour. Geophys. Res.*, **62** (1957), 117–141.
4) W. M. ELSASSER, *Phys. Rev.*, **60** (1941), 876–883.

of the conductivity of the mantle by applying the attenuation theory to the above mentioned model of the secular variation. As has already been studied by Rikitake[5] in some other cases, the conducting core appreciably affects the attenuation of the secular change, but the electrical conductivity of the mantle thus inferred does not appear to differ notably from those obtained by use of the model of dipoles in which the existence of the conducting core is not taken into account.

2. Fundamental Equations

According to Rikitake's study[6], the conductivity near the surface of the earth is very low, whereas it increases quite steeply at a depth of about 400 *km* (Fig. 6). The conductivity of the core is regarded to be so high, compared with the conductivity in the upper part of the mantle, that we shall adopt a model of the earth, as shown in Fig. 1 which has two boundaries of electrical discontinuity at $r=q_1a$ and q_2a. In regions 1, 2 and 3, the electrical conductivities are assumed to be expressed as σ', $\sigma_0\rho^{-l}$ and σ_c respectively, where ρ denotes the ratio of the radial distance r to the radius of the earth a. σ' will be ignored in this study, because of the small conductivity compared with those in region 2 or 3.

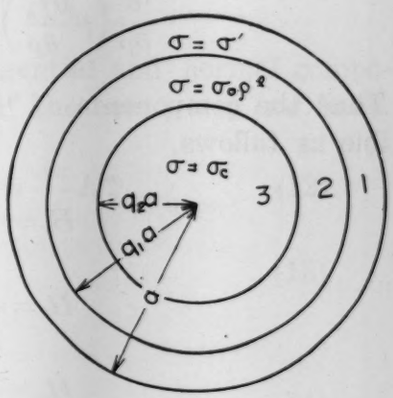

Fig. 1.

In the non-conducting material, the magnetic field can be derived from a scalar potential W. In order to compare the theory to the analyses of the secular variation observed we shall deal with the time-derivative of the magnetic field $\dot{\boldsymbol{H}}$ in place of $\boldsymbol{H}$ hereafter.

$$\dot{\boldsymbol{H}}=-\text{grad}\,\dot{W}\,, \tag{1}$$

where

$$\dot{W}=a\sum_n\sum_m \dot{i}_n^m\rho^{-n-1}S_n^m\,. \tag{2}$$

S_n^m denotes a spherical surface harmonic.

On the other hand, in the conducting region, we have,

5) T. RIKITAKE, *Bull. Earthq. Res. Inst.*, **29** (1951), 263–269; **30** (1952), 191–205.
6) T. RIKITAKE, *Bull. Earthq. Res. Inst.*, **28** (1950), 45 and 219.

$$\dot{\boldsymbol{H}}=\mathrm{rot}\,\dot{\boldsymbol{A}}\,,\qquad \dot{\boldsymbol{A}}=\sum_n\sum_m \dot{\boldsymbol{A}}_n^m\,,$$

in terms of vector potential $\boldsymbol{A}$ which satisfies the following equation for slowly varying phonomena,

$$\nabla^2\dot{\boldsymbol{A}}=4\pi\sigma(\rho)\frac{\partial\dot{\boldsymbol{A}}}{\partial t}\,. \tag{3}$$

The typical term of the solutions of (3) becomes

$$\dot{\boldsymbol{A}}_n^m=a\dot{f}_n(t,\ \rho)[\mathrm{r}\wedge\mathrm{grad}\,S_n^m]\,, \tag{4}$$

where $\dot{f}_n$ is a function satisfying the following equation,

$$\frac{\partial}{\partial\rho}\left(\rho^2\frac{\partial\dot{f}_n}{\partial\rho}\right)=\left\{n(n+1)+4\pi a^2\sigma(\rho)\rho^2\frac{\partial}{\partial t}\right\}\dot{f}_n\,. \tag{5}$$

Thus the components of the magnetic field in the conductor are expressible as follows,

$$\left.\begin{aligned}\dot{H}_r&=-n(n+1)\frac{1}{\rho}\dot{f}_nS_n^m\\ \dot{H}_\theta&=-\frac{1}{\rho}\frac{\partial}{\partial\rho}(\rho\dot{f}_n)\frac{\partial S_n^m}{\partial\theta}\\ \dot{H}_\varphi&=-\frac{1}{\rho}\frac{\partial}{\partial\rho}(\rho\dot{f}_n)\frac{\partial S_n^m}{\sin\theta\partial\phi}\,.\end{aligned}\right\} \tag{6}$$

When the conductivity distributions in region 1 and 2 are given as in Fig. 1, $\dot{f}_n$ becomes[7),8)]

$$\dot{f}_{n2}=\rho^{-1/2}\{\dot{C}_2K_\nu(z)+\dot{D}_2I_\nu(z)\}\,,\qquad \text{for region 2}\,, \tag{7}$$

where I_ν and K_ν denote the modified Bessel functions of the first and second kinds and of order ν, while

$$\rho^{1-(l/2)}=\frac{l-2}{2\zeta}z\,,\qquad \nu=\frac{2n+1}{l-2}\,,\qquad \zeta^2=4\pi a^2\sigma_0 p\,. \tag{8}$$

In the above expression, $\partial/\partial t$ is replaced by p.

$$\dot{f}_{n3}=\dot{C}_3\rho^nF_n(k^2\rho^2)\qquad \text{for region 3,} \tag{9}$$

7) B. N. LAHIRI and A. T. PRICE, *Phil. Trans. Roy. Soc. London A*, **227** (1939), 509.
8) S. CHAPMAN and J. BARTELS, *Geomagnetism*, (1940), 732–749.

where F_n represents the following function,

$$F_n(k^2\rho^2)=\frac{\Gamma(n+\frac{3}{2})}{(\frac{1}{2}ik\rho)^{n+\frac{1}{2}}}J_{n+\frac{1}{2}}(ik\rho)\ . \tag{10}$$

As has been pointed out by Elsasser[1], the current producing the time-dependent part of the magnetic field should originate in a thin layer just below the core-mantle boundary, because of the high conductivity of the core which prevents the currents from producing a field outside the core. In this case the secular variation is assumed to be caused by a change in the current at the boundary of the core which is represented by the following current function ψ,

$$\psi=\sum_n\sum_m K_n^m(t,\ r)S_n^m \qquad \text{at } \rho=q_2\ . \tag{11}$$

From the continuity condition of the tangential and normal components of the magnetic field at the boundary of the core $\rho=q_2$, we have,

$$\left[\frac{\partial}{\partial\rho}(\rho\dot{f}_{n,2})\right]_{\rho=q_2}-\left[\frac{\partial}{\partial\rho}(\rho\dot{f}_{n,3})\right]_{\rho=q_2}=\frac{4\pi}{a}\dot{K}_n^m \tag{12}$$

$$\{\dot{f}_{n,2}\}_{\rho=q_2}=\{\dot{f}_{n,3}\}_{\rho=q_2}\ . \tag{13}$$

We also have at $\rho=q_1$,

$$n\{\dot{f}_{n,2}\}_{\rho=q_1}=-\dot{i}_n q_1^{-n-1} \tag{14}$$

$$\left[\frac{\partial}{\partial\rho}(\rho\dot{f}_{n,2})\right]_{\rho=q_1}=\dot{i}_n q_1^{-n-1}\ . \tag{15}$$

On eliminating constants $\dot{C}_2$, $\dot{D}_2$ and $\dot{C}_3$ from the above simultaneous equations (12), (13), (14) and (15), we have a following relation between $\dot{K}_n^m$ and $\dot{i}_n$, already obtained by Rikitake[5], which contains the conductivity of the mantle as a parameter.

$$\frac{4\pi}{a}\dot{K}_n^m=q_1^{-n-1/2}q_2^{-1/2}\frac{2n+1}{n}z_1\left[\frac{z_2}{2\nu}\{K_{\nu+1}(z_1)I_{\nu+1}(z_2)-K_{\nu+1}(z_2)I_{\nu+1}(z_1)\}\right.$$

$$\left.+\frac{F_{n-1}(k^2q_2^2)}{F_n(k^2q_2^2)}\{K_\nu(z_2)I_{\nu+1}(z_1)+K_{\nu+1}(z_1)I_\nu(z_2)\}\right]\dot{i}_n \tag{16}$$

This equation is no other than a representation of an information transmission, that is to say, a process of a signal represented by $\dot{K}_n^m$ being

transmitted through the mantle to appear as the observed secular variation $\dot{i}_n^m$.

3. The Electric Current Sheet near the Boundary of the Core

It is generally assumed that the secular variation of the magnetic field is caused by the vicissitudes of magnetic dipoles located in the thin layer near the boundary of the core. Many attempts have been made to determine the distribution of these dipoles.[4),9),10),11),12)] These have been, however, performed by assuming the conductivity of the mantle negligible. In this problem in which the attenuation of the secular variation is treated in connexion with the conductivity of the mantle, there remains room for doubt whether or not the above obtained distributions are applicable as it is. Except for these investigations, however, we have no other clues to infer the state of the core boundary at present. Therefore the writer will refer to Elsasser's model of random distribution, since there is no reason now to presume any particular locations of dipoles.

Let a dipole be located at $(r_c, \vartheta, \varphi)$. The magnetic potential at (r, θ, ϕ) produced by this dipole becomes,

$$W(r, \theta, \phi)=M\sum_n n\frac{r_c^{n-1}}{r^{n+1}}\sum_m S_n^m(\vartheta, \varphi)S_n^m(\theta, \phi)\ , \tag{17}$$

where M denotes the dipole moment. On writing

$$A_n^m=\frac{M}{4\pi}\cdot n\cdot\frac{r_c^{n-1}}{r^{n+1}}S_n^m(\vartheta, \varphi)\ , \tag{18}$$

the equation (17) reduces to

$$W(r, \theta, \phi)=4\pi\sum_n\sum_m A_n^m S_n^m(\theta, \phi)\ . \tag{19}$$

Now let S designate the area of the shell and $[A_n^m]_2$ be defined as follows;

$$[A_n^m]_2=\frac{1}{S^{1/2}}\left[\iint(A_n^m)^2ds\right]^{1/2}. \tag{20}$$

9) A. G. MCNISH, *Trans. Amer. Geophys. Union*, **2** (1940), 287.
10) E. C. BULLARD, *M. N. R. A. S., Geophys. Suppl.*, **5** (1948), 248.
11) E. J. LOWES and S. K. RUNCORN, *Phil. Trans. Roy. Soc. London A*, **243** (1951), 525.
12) K. L. MCDONALD, *Jour. Geophys. Res.*, **60** (1955), 377.

With the aid of orthogonality of the spherical surface harmonic, the equation (20) can be written in a simple form as follows,

$$[A_n^m]_2=\frac{M}{\sqrt{4\pi}}\frac{n}{2n+1}\frac{r_c^{n-1}}{r^{n+1}}\,. \tag{21}$$

$[A_n^m]_2$ is the quadratic mean of the probability distribution, as has been pointed out by Elsasser[4], which is produced by a dipole thrown into the spherical shell at random. $\delta s/S$ means the probability of finding a coefficient of a (n, m)-th harmonic component between A and $A+dA$, where δs is the area in which the dipole must be located in order to give the (n, m)-th harmonic component a value between A and $A+dA$. Hence it may be said that $\iint (A_n^m)^2\frac{ds}{S}$ represents an expectation of $(A_n^m)^2$. We shall hereafter employ $[A_n^m]_2$ that is expressed in the form (21) instead of the (n, m)-th harmonic component of the magnetic potential itself.

On the other hand, the magnetic potential due to a current sheet on the spherical shell expressed in (11) is written as follows,

$$W(r, \theta, \phi)=4\pi\sum_n\sum_m\frac{n}{2n+1}K_n^m\frac{r_c^{n+1}}{r^{n+1}}S_n^m(\theta, \phi)\qquad \text{for } r>r_c\,. \tag{22}$$

From (19) and (22), we have

$$A_n^m=\frac{n}{2n+1}\frac{r_c^{n+1}}{r^{n+1}}K_n^m\,. \tag{23}$$

Calculating the root-mean-square of both the sides, we have

$$[K_n^m]_2=\frac{2n+1}{n}\frac{r^{n+1}}{r_c^{n+1}}[A_n^m]_2\,. \tag{24}$$

If it is assumed that the dipole varies only its magnetic moment and does not travel on the shell, we have the following equation about the time derivative of the coefficients K_n^m.

$$[\dot{K}_n^m]_2=\frac{\dot{M}}{\sqrt{4\pi}}\frac{1}{(q_2a)^2}\,. \tag{25}$$

It is noticeable that $[\dot{K}_n^m]_2$ does not depend on the degree and order of the harmonic compopnents.

As the law of superposition is also applicable to the theory of magnetic potential, we have the following relation when N-dipoles exist in the shell,

$$[K_n^m(1)+K_n^m(2)+\cdots+K_n^m(N)]_2=\frac{1}{\sqrt{4\pi}}\frac{1}{(q_2a)^2}\left[\sum_{k=1}^{N}M_k^2\right]^{1/2}. \qquad (26)$$

On writing

$$M=\left[\sum_{k=1}^{N}M_k^2\right]^{1/2},$$

(26) becomes quite the same as that of one dipole (25).

As the equation (17) and (22) are vaild in the non-conducting region alone, it may appear irrelevant to use these equations when the mantle is conducting. But this treatment may be allowed, when it is recollected that the assumption of the current sheet is nothing but to ignore the leakage of the current from the core boundary to the mantle, and that in the present case it is not aimed at employing these expressions in the very form of (17) and (22), but obtaining the form of a current function producing an equivalent potential to that of dipoles distributed at random in the shell.

4. The Attenuation of the Magnetic Field through the Mantle

If the mantle were non-conducting, the magnetic potential should be also expanded in the same form as the equation (2). If the potential could be expressed, even at the boundary of the core, in spherical surface harmonic series as follows,

$$W=a\sum_n\sum_m I_n^m S_n^m(\theta,\phi), \qquad (27)$$

then i_n^m/I_n^m would designate the attenuation of a harmonic component of the potential due to the conducting mantle. From the equation (19) we have

$$I_n^m=\frac{4\pi}{a}(A_n^m)_{\rho=q_2}. \qquad (28)$$

With the aid of (23), the above equation is written as

$$\frac{[\dot{i}_n^m]_2}{[\dot{I}_n^m]_2}=\frac{a}{4\pi}\frac{2n+1}{n}\frac{[\dot{i}_n^m]_2}{[\dot{K}_n^m]_2}. \qquad (29)$$

Let G_n be the function of σ_0 and l defined as

$$\frac{1}{G_n} = q_1^{-n-1/2} q_2^{-1/2} \frac{2n+1}{n} \left[z_1 \left\{ \frac{z_2}{2\nu} (K_{\nu+1}(z_1) I_{\nu+1}(z_2) - K_{\nu+1}(z_2) I_{\nu+1}(z_1)) + \frac{F_{n-1}(k^2 q_2^2)}{F_n(k^2 q_2^2)} (K_\nu(z_2) I_{\nu+1}(z_1) + K_{\nu+1}(z_1) I_\nu(z_2)) \right\} \right]_2 [\dot{i}_n]_2 , \tag{30}$$

then (29) is represented, using (16), as

$$\frac{[\dot{i}_n^m]_2}{[\dot{I}_n^m]_2} = \frac{2n+1}{n} G_n(\sigma_0, l; \sigma_c, T) . \tag{31}$$

This is the function that depends only on the conductivity of the mantle, namely σ_0 and l, as parameters, provided the conductivity of the core (σ_c) and the period of the secular variation (T) are given. In this study the period of the secular variation is assumed to be 50 *years*, because it is remarkable for the component $n=1$ as is shown in Fig. 4. Moreover by adopting the value 10^{-6} *e.m.u.* for the electrical conductivity of the core, $[\dot{i}_n^m]_2/[\dot{I}_n^m]_2$ can be calculated for various values of parameters σ_0 and l, the results of which are shown in Table 1. The attenuation curves for $l=4$ are drawn in Fig. 2a. These show that the attenuation does not depend on σ_0 while its value is small, but that it is very conspicuous above certain values of σ_0. Attention should be paid to the fact that, as far as the harmonics up to $n=3$ are concerned, the lower harmonic component damps out more conspicuously than the higher one.

If the mantle were non-conducting, the equation (16) is reduced to

$$\frac{4\pi}{a} \dot{K}_n^m = q_2^{-n-1} \frac{2n+1}{n} \frac{F_{n-1}(k^2 q_2^2)}{F_n(k^2 q_2^2)} \dot{i}_n^m , \tag{32}$$

therefore we have,

$$\frac{[\dot{i}_n^m]_2}{[\dot{I}_n^m]_2} = q_2^{n+1} \left[\frac{F_n(k^2 q_2^2)}{F_{n-1}(k^2 q_2^2)} \right]_2 . \tag{33}$$

Equation (33) is no other than the straight line part of the attenuation curves in Fig. 2.

Without regard to the conductivity of the core, we have

$$I_n^m = i_n^m q_2^{-n-1} , \tag{34}$$

and then

$$\frac{i_n^m}{I_n^m} = q_2^{n+1} , \tag{35}$$

Table 1. The attenuation of magnetic potential through the conducting core, $[\dot{i}_n]_2/[\dot{I}_n^m]_2$.

$2\pi\sigma_0/T$	l	n		
		1	2	3
10^{-16}	3	1.07×10^{-12}	1.53×10^{-12}	1.82×10^{-12}
	4	2.45×10^{-6}	3.63×10^{-6}	4.45×10^{-6}
	6	0.925×10^{-8}	1.38×10^{-8}	1.71×10^{-8}
	8	1.47×10^{-12}	—	—
	10	1.45×10^{-18}	—	—
	12	3.30×10^{-28}	5.00×10^{-28}	6.32×10^{-28}
	14	0.839×10^{-43}	1.27×10^{-43}	1.62×10^{-43}
	16	0.671×10^{-68}	1.03×10^{-68}	1.31×10^{-63}
10^{-18}	3	2.59×10^{-3}	2.99×10^{-3}	—
	4	1.34×10^{-2}	1.28×10^{-2}	1.03×10^{-2}
	6	—	—	—
	8	—	—	—
	10	1.54×10^{-3}	1.76×10^{-3}	1.78×10^{-3}
	12	1.69×10^{-4}	2.10×10^{-4}	2.12×10^{-4}
	14	—	—	—
	16	1.14×10^{-8}	1.55×10^{-8}	1.58×10^{-8}
10^{-20}	3	—	—	—
	4	1.60×10^{-2}	1.43×10^{-2}	1.08×10^{-2}
	6	1.60×10^{-2}	1.43×10^{-2}	1.08×10^{-2}
	8	1.59×10^{-2}	1.43×10^{-2}	1.08×10^{-2}
	10	1.58×10^{-2}	1.42×10^{-2}	1.07×10^{-2}
	12	—	—	—
	14	—	—	—
	16	8.38×10^{-3}	8.00×10^{-3}	6.36×10^{-3}
10^{-22}	3	1.60×10^{-2}	1.43×10^{-2}	1.08×10^{-2}
	4	1.60×10^{-2}	1.43×10^{-2}	1.08×10^{-2}
	6	1.60×10^{-2}	1.43×10^{-2}	1.08×10^{-2}
	8	1.60×10^{-2}	1.43×10^{-2}	1.08×10^{-2}
	10	1.60×10^{-2}	1.43×10^{-2}	1.08×10^{-2}
	12	1.60×10^{-2}	1.43×10^{-2}	1.08×10^{-2}
	14	1.60×10^{-2}	1.43×10^{-2}	1.08×10^{-2}
	16	1.59×10^{-2}	1.43×10^{-2}	1.08×10^{-2}
10^{-24}	3	1.60×10^{-2}	1.43×10^{-2}	1.08×10^{-2}
	4	1.60×10^{-2}	1.43×10^{-2}	1.08×10^{-2}
	6	1.60×10^{-2}	1.43×10^{-2}	1.08×10^{-2}
	8	1.60×10^{-2}	1.43×10^{-2}	1.08×10^{-2}
	10	1.60×10^{-2}	1.43×10^{-2}	1.08×10^{-2}
	12	1.60×10^{-2}	1.43×10^{-2}	1.08×10^{-2}
	14	1.60×10^{-2}	1.43×10^{-2}	1.08×10^{-2}
	16	1.60×10^{-2}	1.43×10^{-2}	1.08×10^{-2}

(T is assumed to be 50 *years*.)

which are also shown with broken lines in Fig. 2a. It results in that the conductivity of the core seriously affects the variation in the magnetic field originating at the core boundary compared with the case of the non-conducting core.

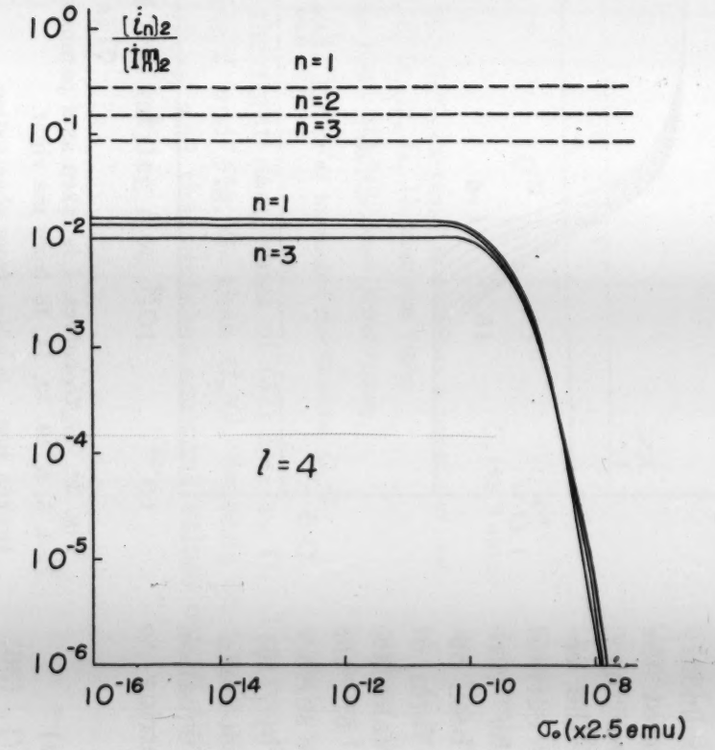

Fig. 2a. Attenuation for $l=4$, taking n as a parameter.
Full lines: The core and the mantle are both conducting.
Broken lines: The core and the mantle are both non-conducting.

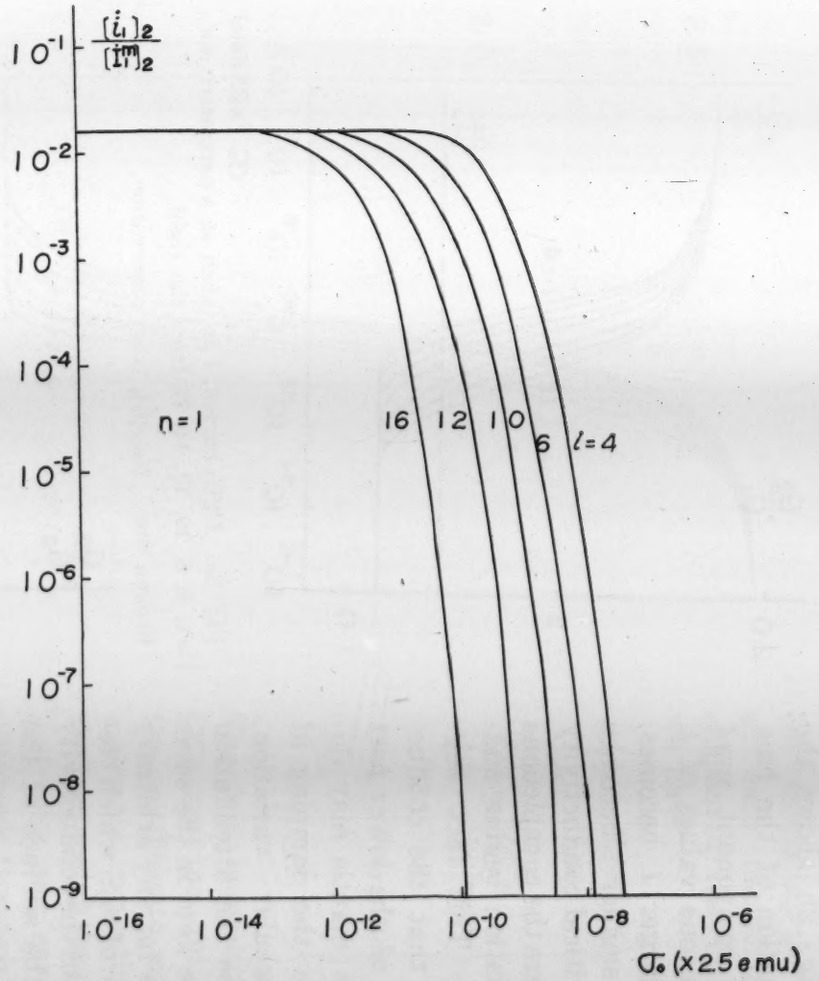

Fig. 2b. Attenuation for $n=1$, taking l as a parameter.

Fig. 2. Attenuation of the secular variation, in terms of $[\dot{i}_n]_2/[\dot{I}^m_n]_2$, against a variable σ_0.

Fig. 2b shows the attenuation of the harmonic component $n=1$ for various values of l. The larger l becomes, the smaller becomes the critical conductivity σ_0 where the conspicuous attenuation begins suddenly. This fact suggests that the conductivity of the lower part of the mantle may dominate the damping of the secular variation, because the attenuation will be kept in the same degree for any arbitrary values of σ_0, which designates the conductivity near the surface of the earth, if the conductivity near the core boundary is held at almost the same value by varying l.

Now that the coefficient of the current function at the core boundary has been obtained in the form of (25), we can calculate the coefficient of the potential on the surface of the earth by (16). Taking the root-mean-square of the equation (16), and referring to (30), we have

$$[\dot{i}_n]_2=4\pi\dot{M}(q_2a)^{-2} a^{-1}\cdot G_n(\sigma_0, l) \ . \quad (36)$$

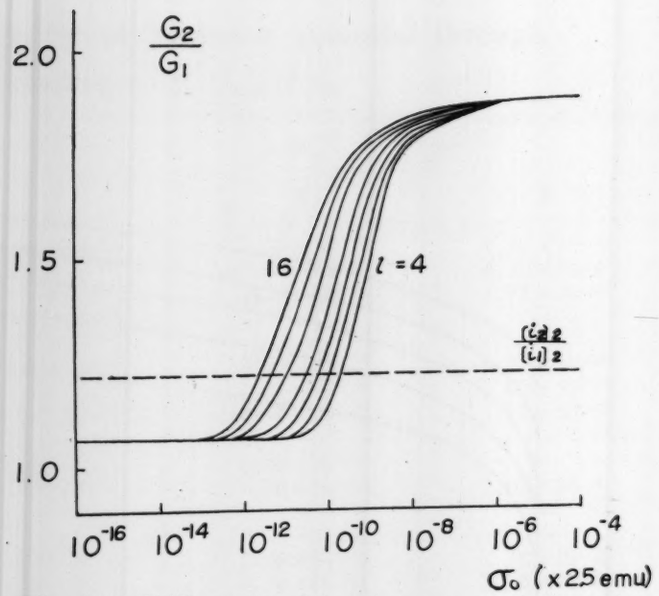

Fig. 3a. G_2/G_1-curves, l is taken as a parameter, *i.e.*, $l=4$, 6, 8, 10, 12, 14, 16 from the right.

Broken line: $[\dot{i}_2]_2/[\dot{i}_1]_2$ from observation.

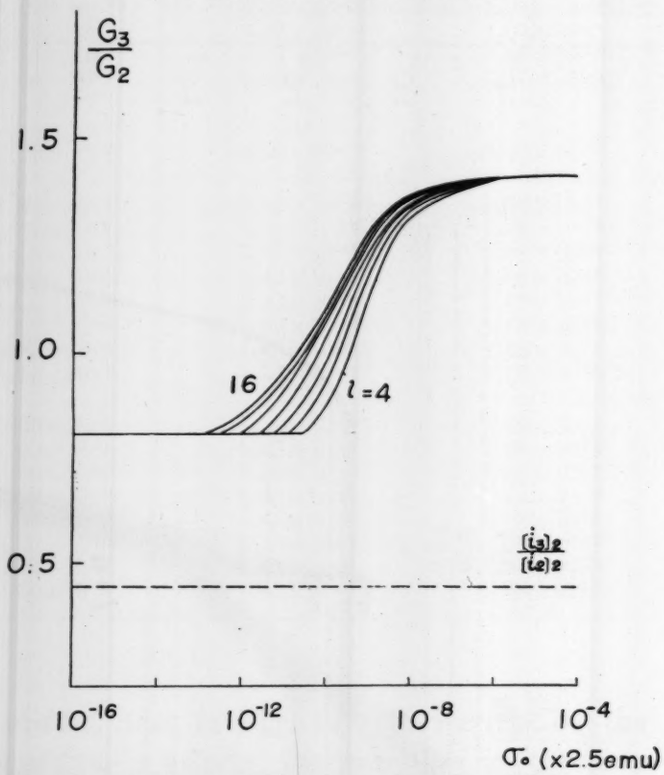

Fig. 3c. G_3/G_2-curves, l is taken as a parameter, *i.e.*, $l=4$, 6, 8, 10, 12, 14, 16 from the right.

Broken line: $[\dot{i}_3]_2/[\dot{i}_2]_2$ from observation.

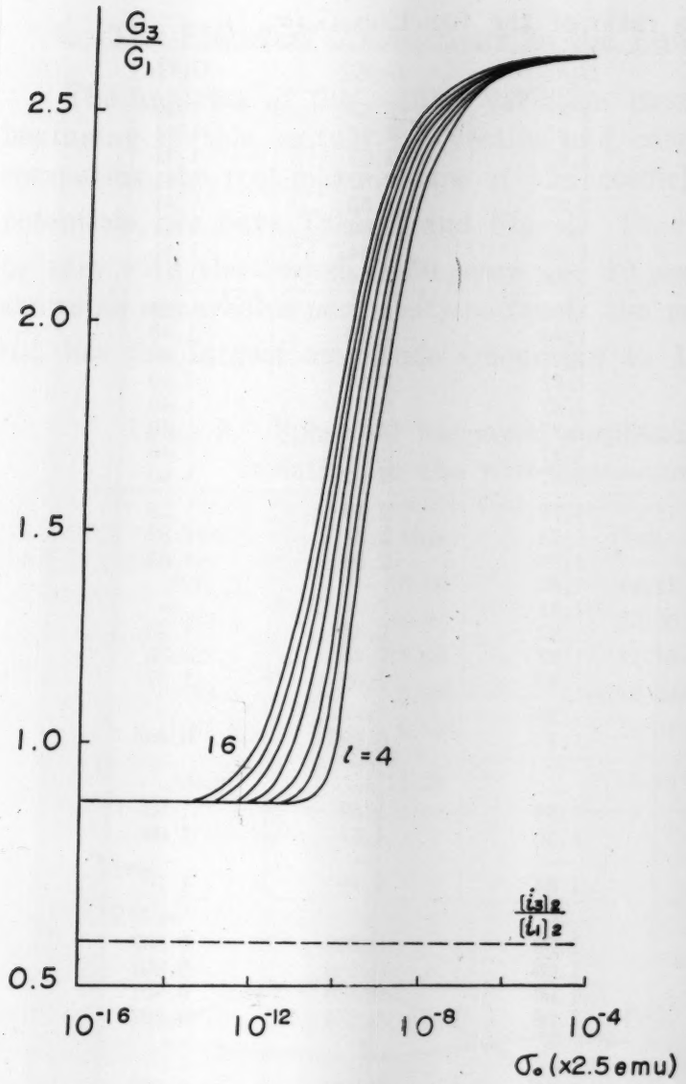

Fig. 3b. G_3/G_1-curves, l is taken as a parameter, *i.e.*, $l=4, 6, 8, 10, 12, 14, 16$ from the right.

Broken line: $[\dot{i}_3]_2/[\dot{i}_1]_2$ from observation.

Fig. 3. Ratios of harmonic coefficients, G_i/G_k.

On calculating the ratio of each harmonic coefficient to that of $n=1$, we have

$$\left.\begin{aligned} \frac{[\dot{i}_2]_2}{[\dot{i}_1]_2} &= \frac{G_2(\sigma_0, l)}{G_1(\sigma_0, l)} \\ \frac{[\dot{i}_3]_2}{[\dot{i}_1]_2} &= \frac{G_3(\sigma_0, l)}{G_1(\sigma_0, l)} \\ &\cdots\cdots\cdots \\ \frac{[\dot{i}_n]_2}{[\dot{i}_1]_2} &= \frac{G_n(\sigma_0, l)}{G_1(\sigma_0, l)} \\ &\cdots\cdots\cdots \end{aligned}\right\} . \quad (37)$$

The left hand sides of (37) are the ratios of the coefficients of the magnetic potential on the surface of the earth, and they can easily be obtained from observational data. If the equations of (37) are independent of each other, the conductivity of the mantle (σ_0, l) should be determined uniquely. As the complicate form of $G_n(\sigma_0, l)$, however, makes it quite difficult to solve the simultaneous equations, we shall calculate the right hand sides of (37) for (σ_0, l). The results are, as shown in Table 2 and Fig. 3, that G_n/G_1 depends on l only within a narrow range of σ_0, and that it takes constant values out of this range regardless of the varying l or σ_0.

Table 2. The ratio of the function $G_n(\sigma_0, l)$.

$2\pi\sigma_0/T$	l	G_2/G_1	G_3/G_1	G_3/G_2
10^{-12}	3	1.87	2.63	1.40
	4	1.87	2.63	1.41
	6	1.87	2.63	1.41
	8	1.87	2.63	1.41
	10	1.87	2.63	1.41
	12	1.87	2.64	1.41
	14	1.88	2.64	1.41
	16	1.88	2.64	1.41
10^{-14}	3	1.86	2.58	1.39
	4	1.86	2.60	1.40
	6	1.87	2.61	1.40
	8	1.87	2.61	1.40
	10	1.87	2.61	1.40
	12	1.87	2.62	1.40
	14	1.87	2.62	1.40
	16	1.87	2.62	1.40
10^{-16}	3	1.71	2.19	1.28
	4	1.78	2.34	1.32
	6	1.79	2.38	1.33
	8	1.80	—	—
	10	1.81	—	—
	12	1.82	2.47	1.36
	14	1.82	2.48	1.36
	16	1.83	2.50	1.37
10^{-18}	3	1.38	—	—
	4	1.15	0.993	0.865
	6	—	—	—
	8	—	—	—
	10	1.38	1.49	1.08
	12	1.50	1.61	1.08
	14	—	—	—
	16	1.64	1.79	1.10
10^{-20}	3	—	—	—
	4	1.08	0.869	0.807
	6	1.08	0.869	0.807
	8	1.08	0.869	0.807
	10	1.08	0.871	0.807
	12	—	—	—
	14	—	—	—
	16	1.15	0.976	0.852
10^{-22}	3	1.08	0.868	0.807
	4	1.08	0.868	0.807
	6	1.08	0.868	0.807
	8	1.08	0.868	0.807
	10	1.08	0.868	0.807
	12	1.08	0.869	0.807
	14	1.08	0.869	0.807
	16	1.08	0.869	0.807
10^{-24}	3	1.08	0.868	0.807
	4	1.08	0.868	0.807
	6	1.08	0.868	0.807
	8	1.08	0.868	0.807
	10	1.08	0.868	0.807
	12	1.08	0.868	0.807
	14	1.08	0.868	0.807
	16	1.08	0.868	0.807

(T is assumed to be 50 *years*.)

5. The Electrical Conductivity in the Lower Part of the Mantle

The analyses of the secular variation have been continued since the beginning of this century by Vestine and others[13),14)]. With these data, computing the root-mean-square of the coefficients of secular variation potentials, we have Table 3 and Fig. 4. From these $[\dot{i}_1]_2$ and $[\dot{i}_2]_2$ appear to vary with the period of 50 *years* and 20 *years* respectively, while $[\dot{i}_3]_2$ shows no remarkable periodicity so far as the present data are concerned. $[\dot{i}_1]_2$ has the largest amplitude amounting to $13\,\gamma/year$, whereas $[\dot{i}_2]_2$ has

Table 3. Spherical harmonic amplitudes of the secular variation in the root-mean-square terms.

Year	$[\dot{i}_1]_2$	$[\dot{i}_2]_2$	$[\dot{i}_3]_2$
1912.5	15.00	14.11	7.635
1922.5	16.82	13.26	6.611
1932.5	13.60	12.78	6.380
1942.5	5.354	13.59	5.057
1952.5	5.686	15.01	4.644
Mean	11.29	13.75	6.065

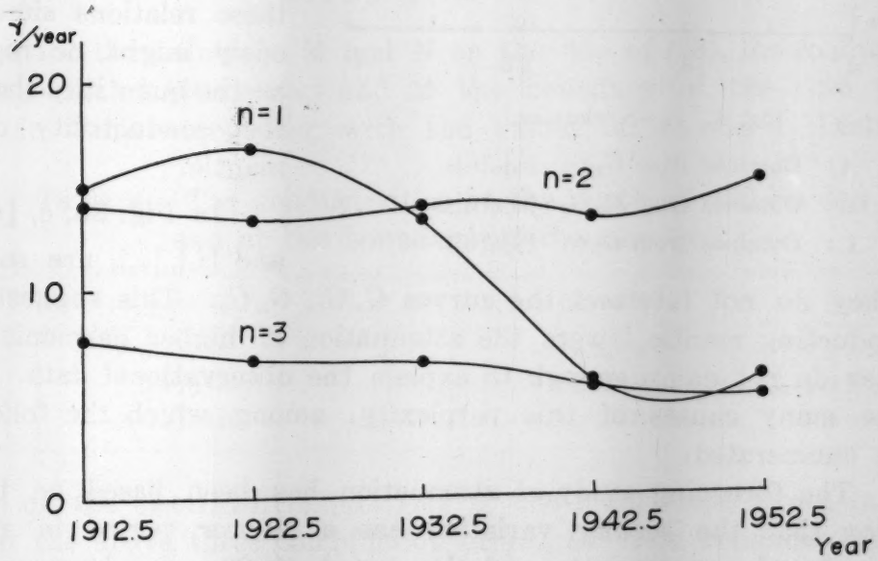

Fig. 4. Spherical harmonic amplitudes of the secular variation.

13) E. H. VESTINE, I. LANGE, L. LAPORTE and W. E. SCOTT, *Carnegie Inst. Pub.*, No. **580** (1947).

14) T. NAGATA and T. RIKITAKE, *Jour. Geomag. Geoele.*, **9** (1957), 42-50.

$2\gamma/year$ of the amplitude at most. On calculating the time average of these, the ratios of each harmonic component become

$$\frac{[\dot{i}_2]_2}{[\dot{i}_1]_2}=1.218\,,\qquad \frac{[\dot{i}_3]_2}{[\dot{i}_1]_2}=0.5372\,,\qquad \frac{[\dot{i}_3]_2}{[\dot{i}_2]_2}=0.4411\,.$$

These values are also shown with straight lines in Fig. 3, which are to correspond to those coefficient ratios of harmonic terms calculated in the preceding section. In Fig. 3a intersection points of a group of G_2/G_1-curves with this straight line indicate the combinations of σ_0 and l that are reasonable to illustrate the observed coefficient ratios of harmonic components. Fig. 5 shows relations between σ_0 and l which are obtained from G_2/G_1 and $[\dot{i}_2]_2/[\dot{i}_1]_2$ in Fig. 3. In the same way $[\dot{i}_3]_2/[\dot{i}_1]_2$ and $[\dot{i}_3]_2/[\dot{i}_2]_2$ should give σ_0-l relations, and σ_0 and l which satisfy these relations simultaneously might be regarded as the quantities that give the conductivity of the mantle.

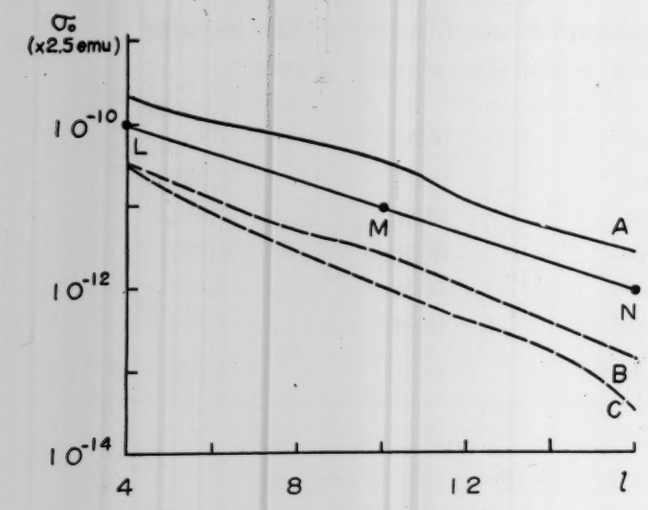

Fig. 5. σ_0-l relations.

A: Obtained from $G_2/G_1-[\dot{i}_2]_2/[\dot{i}_1]_2$,
B: Obtained from $G_3/G_2-[\dot{i}_3]_2/[\dot{i}_2]_2$,
C: Obtained from $G_2/G_1-[\dot{i}_3]_2/[\dot{i}_1]_2$.

In Fig. 3b, c, $[\dot{i}_3]_2/[\dot{i}_1]_2$ and $[\dot{i}_3]_2/[\dot{i}_2]_2$ are so small that they do not intersect the curves G_3/G_1, G_3/G_2. This suggests that the conducting mantle lowers the attenuation of higher harmonic terms and they do not damp enough to explain the observational data. There may be many causes of this perplexity, among which the followings will be enumerated.

1) The foregoing study of attenuation has been based on the assumption that the secular variation has a 50-*year* period in general, while as for the component $n=2$ the period of 20 *years* is remarkable. As the attenuation differs by the period, there may arise a question against the assumption of a uniform period regardless the degree of a harmonic component.

2) When the mantle is regarded as conducting, it might be irrelevant to ascribe the secular variation to the growth and decay of magnetic dipoles distributed *at random*.

3) The uncertainty of analyses of the secular variation for $n=3$ might affect the above calculation seriously.

For a while let the second reason be overlooked. Then the fact that short period phenomena damp out notably might be advantageous for higher harmonic terms to be reduced to smaller values than before, that is, to approach the observed ones. Taking into account the uncertainty of the analyses, σ_0-l relations would be obtained from the lower limits to G_3/G_1 and G_3/G_2 in Fig. 3b, c, which are shown with broken lines in Fig. 5. If it went well, an intersection point of these three curves would determine σ_0 and l. Here σ_0-l will be approximated by the straight line L–M in Fig. 5, which is expressible as follows,

$$6 \log \sigma_0+53.6=-l\ . \tag{38}$$

On regarding the linear approximation of $[\dot{i}_2]_2/[\dot{i}_1]_2$ and $[\dot{i}_3]_2/[\dot{i}_1]_2$ in Fig. 5 as the upper and lower limits to σ_0—l relations respectively, we have

$$6.67 \log \sigma_0+58.0=-l\ , \tag{39}$$

$$4.44 \log \sigma_0+41.5=-l\ , \tag{40}$$

As for the points L, M and N on the line of (38), the conductivities at the depth of 400 *km* (σ_1) and at the boundary of the core (σ_2) are given in Table 4 together with the values of σ_0 and l. Distribution

Table 4. The conductivities at the depth of 400 *km* (σ_1) and at the boundary of the core (σ_c).

	σ_0 (*e.m.u.*)	l	σ_1 (*e.m.u.*)	σ_c (*e.m.u.*)
L	2.5×10^{-10}	4	3.2×10^{-10}	2.9×10^{-9}
M	2.5×10^{-11}	10	4.7×10^{-11}	1.1×10^{-8}
N	2.5×10^{-12}	16	6.7×10^{-12}	4.8×10^{-8}

curves of the electrical conductivity in the mantle are shown in Fig. 6 against the above three combination of (σ_0, l). The conductivity distribution in the mantle is unable to be determined uniquely, because of the innumerable possibilities of combining (σ_0, l) that may fall on the straight line of (38). If the relation between σ_0 and l is given, however, as follows;

$$a \log \sigma_0 + b = -l \,, \tag{41}$$

it is easily proved that σ is equal to $10^{-b/a}$ at $\rho = 10^{-1/a}$ whatever values σ_0 or l may take. Let these specified σ and ρ be designated σ_s and ρ_s, then from (38), (39) and (40) we have

$$\left.\begin{aligned} &(38): \rho_s = 0.681 \quad \sigma_s = 1.16 \times 10^{-9} e.m.u., \\ &(39): \rho_s = 0.708 \quad \sigma_s = 1.99 \times 10^{-9} e.m.u., \\ &(40): \rho_s = 0.596 \quad \sigma_s = 4.53 \times 10^{-10} e.m.u.. \end{aligned}\right\} \tag{42}$$

Namely, it will be inferred that the conductivity is about $1.16 \times 10^{-9} e.m.u.$ at $\rho = 0.681$ and in its neighbourhood the above results restrict the probable range of σ as

$$\begin{aligned} 4.53 \times 10^{-10}\, e.m.u.(\rho = 0.596) &\leqq \sigma \\ &\leqq 1.99 \times 10^{-9}\, e.m.u.(\rho = 0.708) \end{aligned} \tag{43}$$

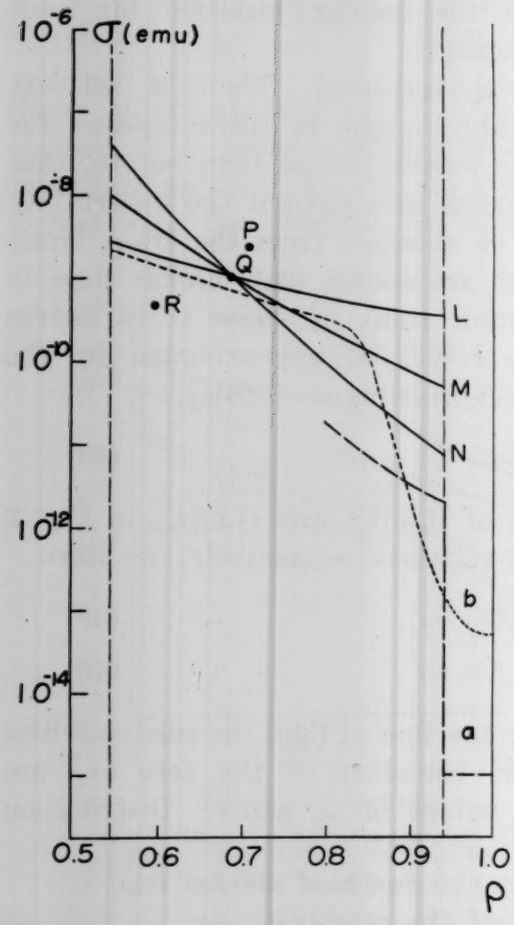

Fig. 6. Distribution of the electrical conductivity in the mantle.
L: $\sigma = 2.5\,\rho^{-4} \times 10^{-10}\, e.m.u.$
M: $\sigma = 2.5\,\rho^{-10} \times 10^{-11}\, e.m.u.$
N: $\sigma = 2.5\,\rho^{-16} \times 10^{-12}\, e.m.u.$
Q: $\sigma_s = 1.16 \times 10^{-9}\, e.m.u.$ at $\rho_s = 0.681$.
P: The upper limit of the conductivity, $\sigma_s = 1.99 \times 10^{-9}\, e.m.u.$ at $\rho_s = 0.708$.
R: The lower limit of the conductivity, $\sigma_s = 4.53 \times 10^{-10}\, e.m.u.$ at $\rho_s = 0.596$.
a: After Rikitake.
b: After McDonald.

6. The Magnetic Field on the Surface of the Earth

Variation in the magnetic field on the earth may be written in the following form,

$$\dot{W} = a[\dot{i}_1]_2 \sum_n \frac{[\dot{i}_n]_2}{[\dot{i}_1]_2} P_n(\cos\theta) \tag{44}$$

with the expression of root-mean-square, where θ denotes the co-latitude. As $[\dot{i}_n]_2/[\dot{i}_1]_2$ has been calculated in section 4, the typical figure of $\dot{W}$ that is normalized at the pole can be drawn for various σ_0 and l. In Table 5 the coefficients of (44) obtained from observation are compared with those of particular combi-

Table 5. Relative coefficients of the magnetic potential.

σ_0 (*e.m.u.*)	l	$2\pi\sigma_0/T$	$[\dot{i}_1]_2/[\dot{i}_1]_2$	$[\dot{i}_2]_2/[\dot{i}_1]_2$	$[\dot{i}_3]_2/[\dot{i}_1]_2$
2.5×10^{-10}	4	10^{-18}	1	1.15	0.993
2.5×10^{-11}	10	10^{-19}	1	1.15	0.995
2.5×10^{-12}	16	10^{-20}	1	1.15	0.976
Observation			1	1.22	0.537

nations of σ_0 and l, that is, L, M and N in the preceding section. The forms of the potential $\dot{W}$ are not so sensitive to the quantities of σ_0 and l that they accord with one another for different values of these, for example L, M and N, as Fig. 7 shows in which the observed potential is also drawn for the comparison.

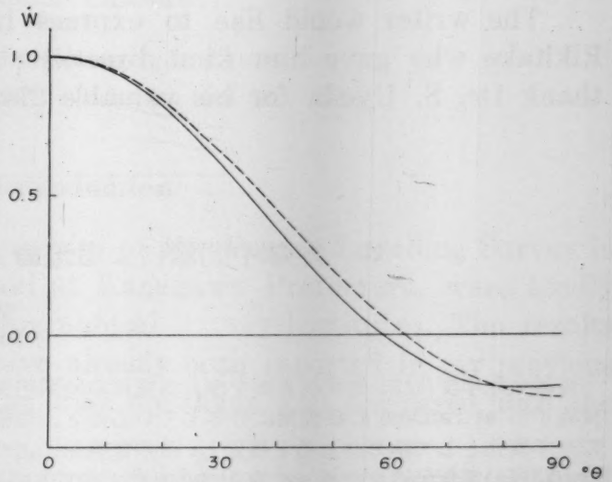

Fig. 7. Comparison of the calculated potential (broken line), which is normalized at the pole, with that of the observation (full line): where θ denotes co-latitude.

7. Concluding Remarks

It has been assumed that the secular variation observed on the surface of the earth is caused by a time-dependent current sheet at the core boundary that may produce the same field as that of dipoles distributed at random. The magnetic potentials on the earth have been calculated by taking the conductivity of the mantle as a parameter in regard to the above mentioned model. It turns out that the coefficients of higher harmonic terms attenuate more slowly with the increase in the conductivity than those of lower ones, and that the calculated amplitudes of the higher harmonic components do not diminish to such small values as would explain the observed ones. One of the causes considerable from which this disagreement of the calculation with the observation originates may lie in disregard of change in the period with the harmonic components of the potential. It has been committed to future study to investigate the relation between a spacial extension of the secular change and its variation with time.

The electrical conductivity in the mantle which is determined to fit the observation best with daring approximation has the range

$$4.5\times10^{-10}\ e.m.u.\leqq\sigma\leqq2.0\times10^{-9}\ e.m.u.\ ,$$

at about $\rho=0.6\sim0.7$.

8. Acknowledgments

The writer would like to express his sincere gratitude to Dr. T. Rikitake who gave him kind directions and advice. He also wishes to thank Dr. S. Uyeda for his valuable discussion.

---

2. 地球中間層による地磁気永年変化の減衰

東京大学大学院
地球物理学課程　行　武　　毅

地磁気永年変化は，地球核表面を流れる電流の時間的変化によつて生ずると考えられている．磁気双極子が at random に核表面に分布しているのと，等価な電流系を考え，その時間的変化が地表面で永年変化として観測されると仮定し，その電流系によつて地表面にできる磁気ポテンシャルが，地球中間層の電気伝導度を種々に変えることによつてどのように変化するかを求めた．中間層の電気伝導度を大きくしてゆくと，$n=3$ 迄では，低い harmonic の係数ほど，減衰度が大となり，実測より得られているような，ポテンシャルの係数比を得ることが困難になる．今，計算の結果が，実測より得られたポテンシャルの形にもつとも近いように，中間層の電気伝導度をきめると，2500 *km* 位の深さで

$$4.5\times10^{-10}\ e.m.u.\leqq\sigma\leqq2.0\times10^{-9}\ e.m.u.$$

という値が得られた．

BULLETIN OF THE EARTHQUAKE
RESEARCH INSTITUTE
Vol. 37 (1959), pp. 33-37

3. *On the Change in the Heights of Bench Marks between Tokyo and Misaki at Kanagawa Prefecture. Change in the Height of Fixed Plane inside the Mareographic Station at Aburatubo.*

By Seiti YAMAGUTI,

Earthquake Research Institute.

(Read Sept. 16, 1958.—Received Dec. 20, 1958.)

Introduction

The data from the recent results of the Precise Levelling Survey in 1957 between Tokyo and Misaki at Kanagawa Prefecture, were kindly placed at my disposal by the Geographical Survey Institute. The results for the years 1952 and 1955 have already been reported in my previous paper[1]. This time, the data for 1957 are taken and compared with the preceding data.

Next, two values of the amount of change in the height of fixed plane inside the Mareographic Station at Aburatubo, were obtained, first, from the Precise Levelling Survey, the height of Standard Origin of Bench Mark at Miyakesaka, Tiyoda Ward, Tokyo, being assumed unchanged or constant, and second, from monthly mean sea-level, taking the mean for those months of executing Levelling Survey, and comparing them with each other.

Method of Investigation, and Results

1. After taking the differences, Δh, of the heights of Bench Marks obtained by the Levelling Survey executed in 1955 and in 1952, in 1957 and in 1955, and also those in 1957 and in 1952, diagrams were plotted with these values from Tokyo to Misaki, as ordinates against the positions of Bench Marks taken as abscissa, and three curves were obtained as shown in Fig. 1, (a), (b) and (c).

The mode of change in the height of Bench Mark during the period of about two years, from Aug.~Dec., 1952 to Jan.~March, 1955, seems different from that, during the period of about two years, from Jan.~

1) S. YAMAGUTI, *Journ. Geodetic Society of Japan*, **3** (1957), [iii, iv].

March, 1955 to June~July, 1957, or rather they seem contrary to each other as shown in Fig. 1, (a) and (b). This fact may be considered to show the existence of block motions of the earth's crust in this district, separated into about six in number, whose boundaries are near Tukizi, Higasi-rokugô, Kanagawa, Huzisawa and Misaki, respectively, as shown by dotted lines in Fig. 1.

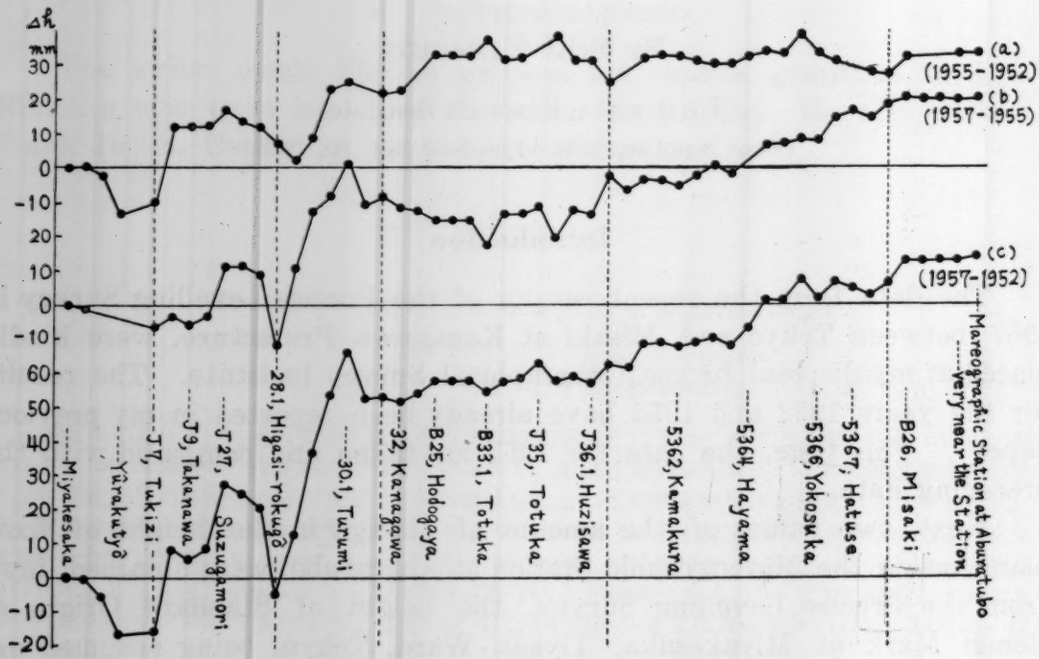

Fig. 1. Change in the height of Bench Mark.

2. The relation between the value of the change in the height of fixed plane inside the Mareographic Station at Aburatubo, resulting from the Levelling Survey from the Standard Origin in Tokyo, to Aburatubo at Misaki carried out in the years, 1923, 1925, 1930, 1934, 1937, 1939, 1944 and 1947, and the negative value of the change in the height of monthly mean sea-level at Aburatubo during the whole period has already been reported in my previous paper[2].

This time, I have tried to compare the above cited two values, changed from the year 1947 to 1957. As to the value of the change in the height of monthly mean sea-level, I will explain here once more in detail as it is necessary for the following discussion on the comparison of two values, one of which is results from the Levelling Survey, and the other is derived from mean sea-level.

2) S. YAMAGUTI, *Bulletin Geographical Survey Institute*, **2** (1950), [i], 15.

Monthly deviations of sea-levels from 40 years' mean for each month are denoted by $\Delta L'$, which are considered to be devoid of astronomical, oceanographical, and meteorological tides with the first approximation.

Similarly, monthly deviations of barometric pressure, and those of sea-water temperature from 40 years' mean for each months are denoted by $\Delta b'$ and $\Delta T'$, respectively. Residual values of $\Delta L'$, corrected with $\Delta b'$ and $\Delta T'$, represented by $\Delta L''=\Delta L'-p\Delta b'-q\Delta T'$, were calculated. In this equation, as the value of p, theoretical value, 13.2 was taken, and as the value of q, 13.3 was taken by the method of least squares, $\Delta L'$ being measured in millimetre, $\Delta b'$ in mmHg, and $\Delta T'$ in degree centigrade. So-called probable error for the last residual value of $\Delta L''$ was calculated and we obtained the value ± 25 in millimetres.

Moreover, the duration of a Levelling Survey is usually longer than two or three months, and the mean of $\Delta L''$ for those corresponding months was taken, so that the mean error of $\Delta L''$ will become smaller value, that is ± 15 in millimetres. In particular cases, even if the Levelling Survey was carried out in one month, the mean of $\Delta L''$ was taken for three months, involving the months of the before and the after as well as the surveying month.

On the other hand, the Levelling Survey was executed from Standard Origin to the Mareographic Station at Aburatubo along many Bench Marks, about 50 in number, each interval of successive two marks being 2 kilometres. So that the value of the change in the height of fixed plane inside the Mareographic Station $\Delta h'$, derived from the Levelling Survey may have a probable error of the amount of about ± 15 millimetres, admissible error of the Levelling Survey being ± 1.5 mm/1 kilometre and the distance from Tokyo to Aburatubo, being 100 kilometres along Bench Marks.

Taking the values of $(-\Delta L'')$, $\Delta h'$ and $(-\Delta L''-\Delta h')$ as ordinates against the year, we have obtained three diagrams, mean height of fixed plane above the mean sea-level during the period of 40 years (1900～1939), 3336 mm, being taken as zero as shown in Fig. 2.

At first glance, the value of the difference of $-\Delta L''$ and $\Delta h'$ seems to decrease from the year 1947 to 1957, nearly proportional to time (year), so that we have tried to extend the diagram to former year, 1923. Then, we have obtained an unexpected result that, the value of the difference of the two, $(-\Delta L''-\Delta h')$, increases in some year and next, decreases and becomes zero and again increases and decreases to

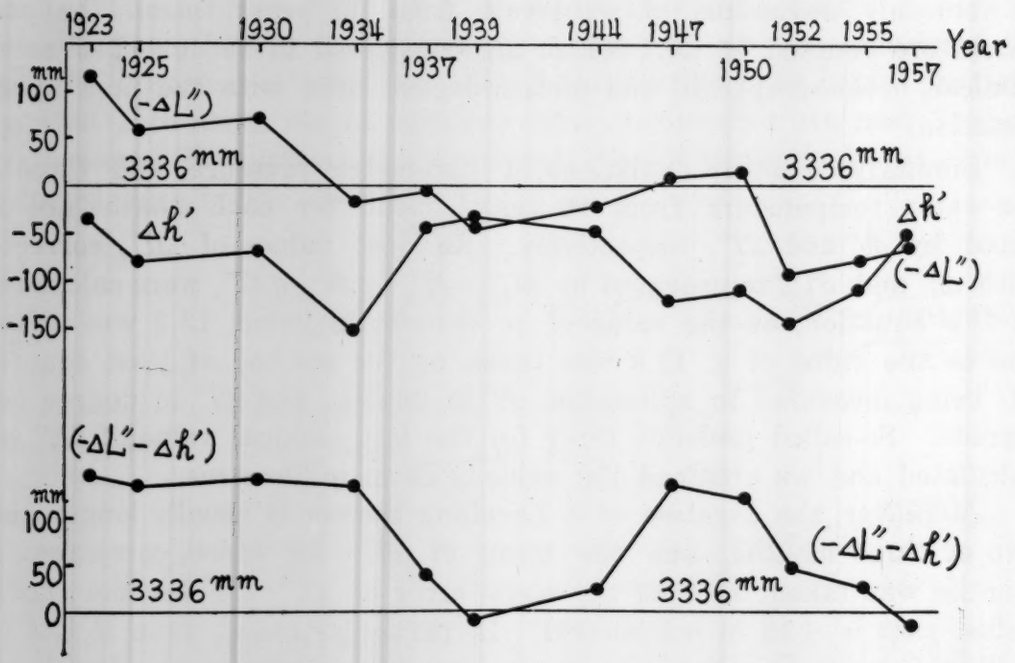

Fig. 2. Change in the height of Fixed Plane inside the Mareographic Station at Aburatubo.

$-\Delta L''$: derived from mean sea-level
$\Delta h'$: derived from the Levelling Survey

zero, with the period of about 18 years. We could not discover the physical meaning of this systematic change of the value of the difference of $-\Delta L''$ and $\Delta h'$.

This change with the period of about 18 years may be caused by the earth's tide due to the motion of moon's ascending node, or by the change of the mode of rotation of the earth.

We have also obtained a second result that the amount of the change of mean sea-level is comparable to that of the earth's crust, derived from the Levelling Survey or these amounts of changes stand in the same order to each other.

In order to ascertain this relation, the ratios of the amounts of successive change along years of executing the Levelling Survey, $\delta(-\Delta L'')/\delta\Delta h'$, were calculated and tabulated in Table 1. The amount of the ratios, shown in this Table, remains in the limit from 0.15 to 3.46, following our expectation.

A study of the physical meaning of the systematic change of the value of $(-\Delta L''-\Delta h')$, may be worth following up in future.

Table 1. Change in the height of the Fixed Plane inside the Mareographic Station at Aburatubo.

Year	1923	1925	1930	1934	1937	1939	1944	1947	1950	1952	1955	1957
	mm											
$-\Delta L''$	116	56	72	−16	− 5	−43	−23	9	15	−96	−82	−62
$\Delta h'$	−31	−79	−71	−151	−46	−35	−49	−121	−107	−146	−112	−51
$-\Delta L''-\Delta h'$	147	135	143	135	41	− 8	26	130	122	50	30	−11

	mm										
$\delta(-\Delta L'')$	−60	16	−88	11	−38	20	32	6	−111	14	20
$\delta\Delta h'$	−48	8	−80	105	11	−14	−72	14	−39	34	61
$\delta(-\Delta L'')/\delta\Delta h'$	1.25	2.00	1.10	0.15	−3.46	−1.43	−0.44	0.43	2.85	0.41	0.33

$-\Delta L''$: derived from the mean sea-level.
$\Delta h'$: derived from the Levelling Survey.

In conclusion, I wish to express my hearty thanks to the Geographical Survey Institute for the kindness of giving me many valuable data obtained there.

---

3. 東京と三崎間の水準点の変動について．特に油壺験潮場内の基準石の変動について

地震研究所　山　口　生　和

1. 東京三宅坂の原点から三崎の油壺までの水準点の変動を 1952 年，1955 年及び 1957 年に行われた水準測量の資料より調べてみた．その結果，1952 年から 1955 年までの間の水準点の変動の模様と，1955 年から 1957年までの間の水準点の変動の模様とは，違つていることがうかがわれる．即ち東京と三崎との間の地盤は，少なくとも 6 個の地塊に分れて運動しているように見える．

2. 油壺験潮場内の基準石の変動量を，水準測量によつて求めた値と，気象潮や海洋潮等の出来るだけの修正を施した月平均海水面から求めた値との 2 つを出して，この 2 つの値を比較研究してみた．その結果，これ等の 2 つは或時は一致し，或時は大きくはなれ，再た或時は一致するというように，組織的な変化をしていることが分つた．そしてその週期は約 18 年で天体の運動による地殻の変動に基因するかも知れないがその物理的意義については未だ詳でない．而してこれ等 2 つの値の年月に対する変動量は同程度のものであることが確かめられた．

BULLETIN OF THE EARTHQUAKE
RESEARCH INSTITUTE
Vol. 37 (1959), pp. 39-51

4. *Physical Conditions of Earthquake Faults II.*

(*A Model of Strike-slip Faults with Various Dip Angles.*)

By Keichi KASAHARA,

Earthquake Research Institute.

(Read December 23, 1958.—Received December 27, 1958.)

Summary

The writer deals with a model of strike-slip faults for the purpose of studying the characteristics of crustal deformation when the dip of the fracture plane is not given as 90°. The model is presented on the assumptions which are similar to those in the previous paper, but no assumption on the dip angle is made in the present one. An orthodox analysis of such a model being very difficult even in the simplest case, the writer reduces the problem to the Laplace equation and solves it by the relaxation method as well as by model experiments based on the electric-elastic analogy.

It is proved that the pattern of deformation is no more symmetric with respect to the fault but the deformation on the side of the fault, to which it dips, appears systematically larger than that of the other side. The more the dip angle differs from 90°, the more remarkable the asymmetry becomes.

We are able to point out some examples, the deformation in which is likely to be explained more suitably by the present model rather than by the primary one. However, definite conclusions on that point will be postponed until we accomplish more detailed examination.

1. Introduction

It is widely accepted that the crustal deformation around an earthquake fault is closely related to the characteristics of the earthquake origin. Notwithstanding a great store of geodetic data, however, few papers have been written until L. Knopoff[1], P. Byerly and J. DeNoyer[2],

1) L. KNOPOFF, *Geophys. Journ., R.A.S.*, **1** (1958), 44–52.

2) P. BYERLY and J. DENOYER, *Contributions in Geophysics in Honor of B. Gutenberg* (1958), 17–35.

and the present writer[3] worked out studies, in which physical conditions of several faults were discussed on the basis of these observational data. Since it was hardly possible to deal with such complicated features of actual faulting in detail, the above-mentioned writers took very simplified models representing only the most predominant conditions of strike-slip faults.

The present writer's model assumed, for instance, the fracture plane in the earth's crust to be of infinite length and of finite (constant) depth, in which the initial shear stress is liberated. For the sake of simplicity in mathematical analysis, it was also assumed that the fault appears with a dip of 90°. The foregoing analyses have proved that the above-mentioned model can provide satisfactory explanation for the most outstanding features of some actual faultings, so that it may be accepted as a reasonable model in the step of first approximation.

It is needless to say that such a conclusion has been stated by disregarding some sorts of discrepancy from the observational facts, which should be taken into account when we undertake further improvement of the model. One of the discrepancies is noticed in the diminution curve of v_0. The primary model concludes that the curves for both sides of a fault are to be perfectly antisymmetric with each other, in the absence of the distortion due to the elastic drift in the earth's crust. The distribution of v_0 on the east and west sides of the Imperial Valley fault (or of the Fairview Peak fault) is likely to be represented more suitably by the two curves of different diminution rather than by curves of the same diminution (see Figs. 4 and 6 in the previous paper). Such a tendency can not be explained so long as we take the primary model which assumes the dip to be 90°. One of the way to overcome this difficulty might be to do away with the assumption on the dip angle, so that we are going to deal with the model improved in the following way.

2. Fundamental considerations

The model cited here is on the same assumptions as the primary one except that on the dip angle (φ) of the fracture plane (Fig. 1). Let us take the symbols for coordinates, displacements, and elastic constants as same with those in the former papers, then the condition of elastic equilibrium is given by the following equations,

3) K. KASAHARA, *Bull. Earthq. Res. Inst.*, **35** (1957), 473-532; *ibid.*, **36** (1958), 21-53; *ibid.*, **36** (1958), 455-464.

$$\left.\begin{aligned}(\lambda+\mu)\frac{\partial}{\partial x}\Delta+\mu\left(\frac{\partial^2}{\partial x^2}+\frac{\partial^2}{\partial y^2}+\frac{\partial^2}{\partial z^2}\right)u=0\ ,\\ (\lambda+\mu)\frac{\partial}{\partial y}\Delta+\mu\left(\frac{\partial^2}{\partial x^2}+\frac{\partial^2}{\partial y^2}+\frac{\partial^2}{\partial z^2}\right)v=0\ ,\\ (\lambda+\mu)\frac{\partial}{\partial z}\Delta+\mu\left(\frac{\partial^2}{\partial x^2}+\frac{\partial^2}{\partial y^2}+\frac{\partial^2}{\partial z^2}\right)w=0\ .\end{aligned}\right\} \qquad (1)$$

It is evident, from the physical considerations, that the deformation is uniform in the direction of y, that is,

$$\frac{\partial}{\partial y}\equiv 0\ . \qquad (2)$$

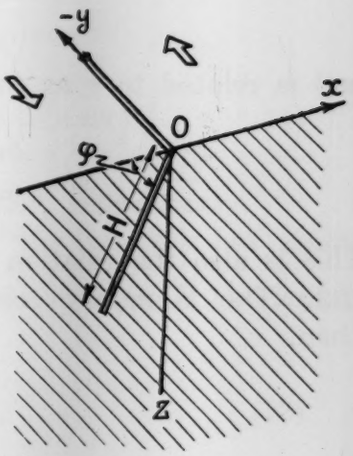

Fig. 1. Model of a strike-slip fault.

Eq. (1) can be rewritten, then, as follows,

$$\mu\left(\frac{\partial^2}{\partial x^2}+\frac{\partial^2}{\partial z^2}\right)v=0\ , \qquad (3)$$

and,

$$\left.\begin{aligned}(\lambda+2\mu)\frac{\partial^2 u}{\partial x^2}+(\lambda+\mu)\frac{\partial^2 w}{\partial x\partial z}+\mu\frac{\partial^2 u}{\partial z^2}=0\ ,\\ (\lambda+2\mu)\frac{\partial^2 w}{\partial z^2}+(\lambda+\mu)\frac{\partial^2 u}{\partial x\partial z}+\mu\frac{\partial^2 w}{\partial x^2}=0\ .\end{aligned}\right\} \qquad (4)$$

We know, therefore, that the fundamental equations are given for u and w separately from that for v. Since the model assumes no initial stress except a uniform shear, Y_x, it is only the stress component relating to v that is liberated in the fracture plane, whereas no change occurs in the other components relating to u and w, there. Taking these conditions into account, we may take as,

$$u=w=0\ , \qquad (5)$$

which does not contradict (4) as well as the initial and the boundary conditions stated above. That is to say, the deformation in the present model is represented by a pure shear field.

Let us introduce the potential of the field, ϕ, which satisfies the Laplace equation,

$$\nabla^2\phi=0\ , \tag{6}$$

and is related to v as follows.

$$\frac{\partial v}{\partial x}=-\frac{\partial \phi}{\partial z}\ , \qquad \frac{\partial v}{\partial z}=\frac{\partial \phi}{\partial x}\ . \tag{7}$$

This is also the relation between the stream function ψ and the potential. The boundary condition for v or ϕ at the free surface is given, then,

$$\frac{\partial v}{\partial n}=0 \quad \text{or} \quad \phi=\text{const.}, \tag{8}$$

where, n is the direction normal to the surface.

3. Solution by relaxation method

The fundamental considerations have shown that the problem with which we are concerned is reducible to that of a potential field. The solution for the problem should satisfy the Laplace equation within the medium, and, at the same time, the conditions for a free surface in the fracture as well as at the earth's surface. With the aid of (8), it is evident that ϕ is constant (we suppose it as 0) in these planes. From the physical point of view, we also know that the value of ϕ approaches Cz (C is a constant) at a great distance from the fault.

The relaxation method is useful for solving such a problem. In case of $\varphi=60°$, for instance, it is convenient to deal with the numerical calculation with respect to the triangular network (Fig. 2). The operator ∇^2 is expressed in polar coordinates as follows.

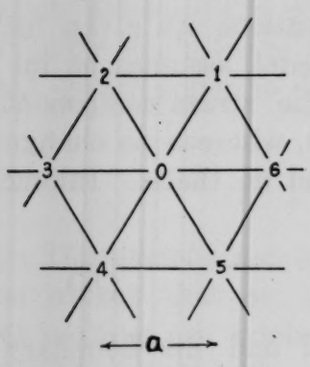

Fig. 2. Relaxation net ($N=6$).

$$\nabla^2\equiv\frac{\partial^2}{\partial r^2}+\frac{1}{r}\frac{\partial}{\partial r}+\frac{1}{r^2}\frac{\partial^2}{\partial \theta^2}\ . \tag{9}$$

Let us also take the expression for ϕ in the expanded forms, that is,

$$\phi(r,\ \theta)=A_0(r)+\sum_n \{A_n(r)\cos n\theta+B_n(r)\sin n\theta\}\ . \tag{10}$$

Hence we get,

$$\nabla^2\phi = A_0'' + \frac{1}{r}A_0' + \sum_n \left\{ \left(A_n'' + \frac{1}{r}A_n' - \frac{n^2}{r^2}A_n \right) \cos n\theta + \left(B_n'' + \frac{1}{r}B_n' - \frac{n^2}{r^2}B_n \right) \sin n\theta \right\}, \tag{11}$$

where, the symbols $'$ and $''$ denote $\partial/\partial r$ and $\partial^2/\partial r^2$, respectively.

Let $\sum_{a,N}(\phi)$ denote the summation of ϕ at the nearest net points which are at equal distances from the point 0, $r=a$ (a is the length of the mesh-side and $a \ll 1$), then, we get[4],

$$\frac{1}{N}\sum_{a,N}(\phi) = A_0(a) + O(a^N) + \cdots, \tag{12}$$

and

$$A_0(r) = \phi_0 + \frac{r^2}{4}(\nabla^2\phi)_0 + \frac{r^4}{64}(\nabla^4\phi)_0 + \cdots, \tag{13}$$

where, the suffix 0 corresponds to the point 0 and N is the number of the nearest network points ($N=6$ in the present case). Therefore, by neglecting the terms of higher powers of a we arrive at the following relation,

$$\frac{1}{N}\sum_{a,N}(\phi) - \phi_0 \fallingdotseq \frac{a^2}{16}\left[\left(3\nabla^2\phi + \frac{1}{N}\sum_{a,N}(\nabla^2\phi) \right) \right]. \tag{14}$$

That is to say, when the Laplace equation is satisfied by ϕ, (6) is reduced to the following relation of finite-difference form, *viz.*,

$$\frac{1}{N}\sum_{a,N}(\phi) - \phi_0 = 0\,. \tag{15}$$

In the relaxation method, we first assume the first approximation values of ϕ for all the net points, and calculate the residual of the left-hand side of (15) for each point. The residual is fed back, then, to the assumed values at all the surrounding points in order to take the second approximation values. Such a procedure is repeated until we look for the most suitable values which satisfy (15) at all points.

In the present study we take the depth of the fault, H, as the unit distance and the length of the mesh-side, a, as 1/8 of the unit. Fig. 3 illustrates the relaxation net and the equal-value lines of ϕ in relative values thus calculated. Since it is not ϕ but ψ that corresponds

4) R. V. SOUTHWELL, *Relaxation Methods in Theoretical Physics I* (1946), p. 20.

to v, we have to deduce the distribution of ψ from the result shown in Fig. 3. This procedure is easily accomplished with the aid of the relation between ϕ and ψ (cf. (7)), so that we finally obtain the pattern for ψ as shown in Fig. 4.

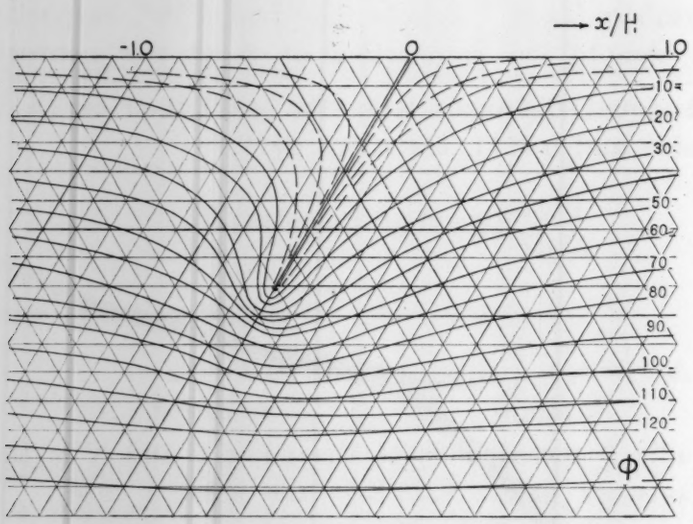

Fig. 3. Relaxation net and distribution of ϕ.

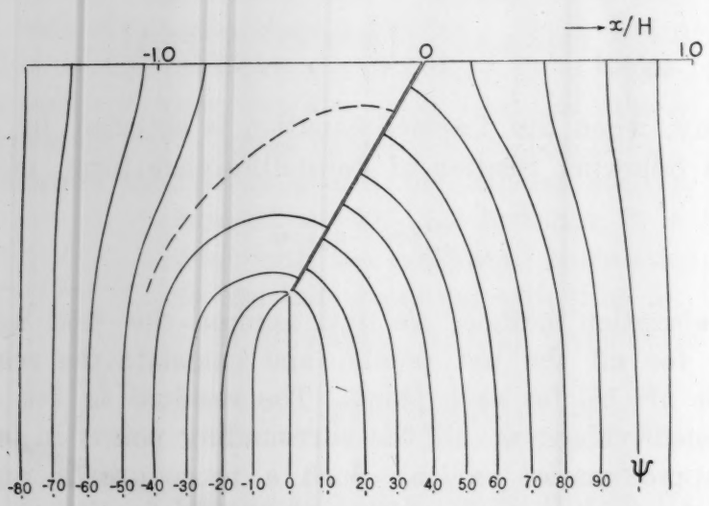

Fig. 4. Distribution of ϕ.

The distribution which is directly related to the faulting is known as the difference of the pattern in Fig. 4 from the one before faulting. We know, therefore, that it is only the part nearby the fault that is subject to remarkable deformation, whereas the part away from there

is unaffected as the distribution of parallel lines indicates. The lines approaching the earth's surface or the fracture plane are normal to the respective boundaries, which means that the condition for the free surface (8) is satisfied. The most notable effect is the asymmetric distribution around the fault. It is evident that the deformation in the left half part of the space is larger than that in the other half. This tendency being in good agreement with the result of the following model experiment, we shall discuss it in more detail in the next section.

4. Model experiment based on electric-elastic analogy

The relaxation method is applicable, in principle, not only to the case of $\varphi=60°$ but also to the other cases. Numerical computation would be, however, more complicated in such case, so that we shall take another way in order to study the present problem easily.

L. Knopoff has shown that the analogy of an electrostatic field is applicable to the problem of a pure shear field (see Table 1)[5]. Taking

Table 1. Two-dimensional analogies (after L. Knopoff).

Electric quantity	Elastic quantity
Electric field	Rotation vector
Dielectric constant	Shear modulus
Potential	Potential
Stream function	Displacement
Perfect conductor	Perfectly weak crack

this analogy into consideration, we are able to find out, experimentally, the solution for various values of φ by inserting a conductor of proper shape into a uniform electric field and by tracing equi-value lines of ϕ around it. The technique using a thin layer of electrolyte has frequently been applied to studies of electrostatic field around a conductor. It is a necessary condition for the technique that the resistivity of the electrolyte is far higher than that of the electrode which forms the conductor under the test. Let us call such a type a conductor model of the electrostatic field.

The technique applied in the following study is the one using an insulator model, in which the objective is not given by a conductive electrode but is represented by an insulator of the same shape. As is

5) L. KNOPOFF, *loc cit.*, 1).

well-known, the equipotentials of an electrostatic field (or of a field of stationary current) are normal to the stream lines, and the former is normal to the boundary of an insulator as the latter is, to a conductor. Therefore, the pattern of the stream lines in a conductor model must be identical with that of the equi-potential lines in an insulator model, when the above-mentioned correspondence holds between them.

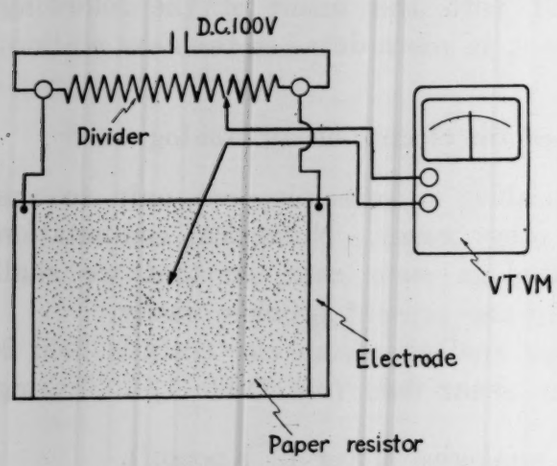

Fig. 5. Laboratory set of model experiment.

Fig. 5 illustrates the laboratory set using an insulator model. A sheet of paper resistor (26 cm × 37 cm) is in contact with the electrodes at its ends, to which D.C. voltage (100 V) is supplied. Then the potential is of a constant gradient from one electrode to the other, and the equi-potential lines appear normally to the upper rim of the paper resistor, which corresponds to the surface of the earth. This represents the initial state of the earth's crust being subject to uniform shear stress, $Y_x = S$.

Production of a fracture is represented by applying a narrow cut from the upper rim of the resistor to a certain depth. This cutting causes distortion of the equi-potential lines, which are traced with a VTVM connected to a potential divider as shown in the same figure. Since the input resistance of this apparatus is extremely high, we can trace distribution of the potential ϕ without disturbing the condition of the field. Uniformity of resistivity in the test paper has much influence upon the accuracy of the experimental result. Facsimile paper is used in the present experiment, as it shows uniform and suitable resistivity. This method of experiment being very simple in its treatment, it could be conveniently applied to the other sorts of problems which relates to the Laplace equation.

5. Result and discussions

We worked out the model experiment for the cases of $\varphi = 90°$, 80°, 70° and 60°, where the depth of cutting was kept unchanged ($H = 10$ cm). The results are shown in Figs. 6~9. The lower part of each figure il-

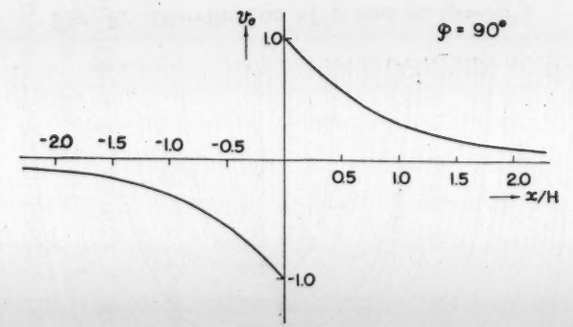

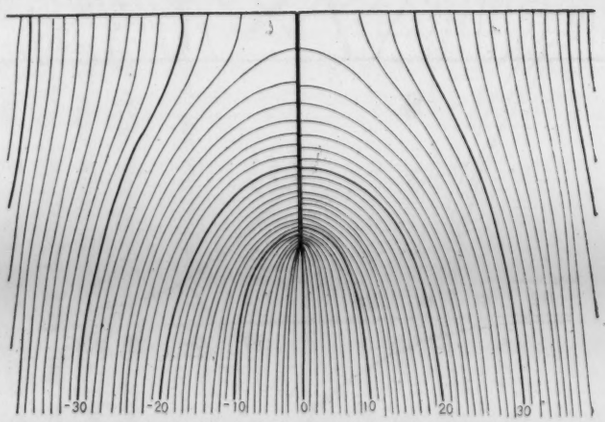

Fig. 6. Distribution of v and v_0 ($\varphi=90°$).

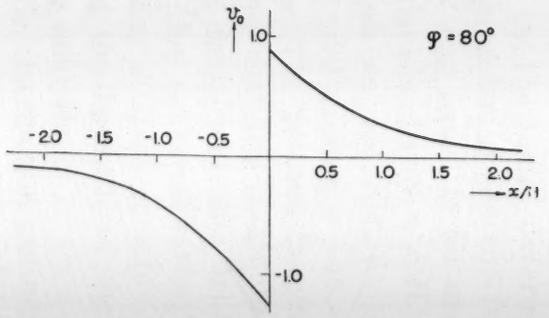

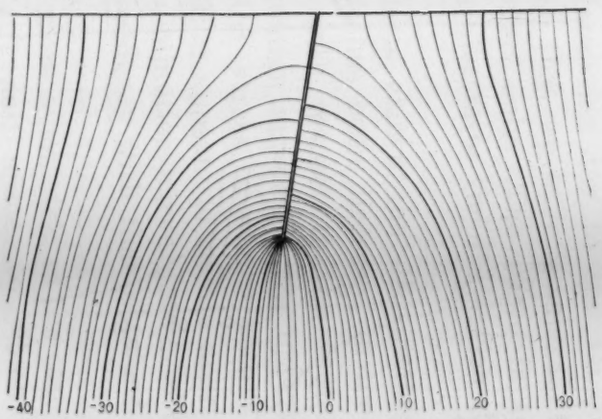

Fig. 7. Distribution of v and v_0 ($\varphi=80°$).

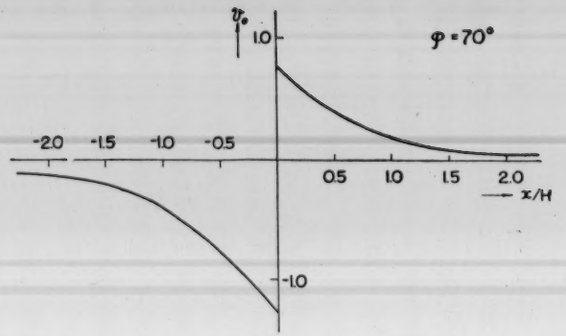

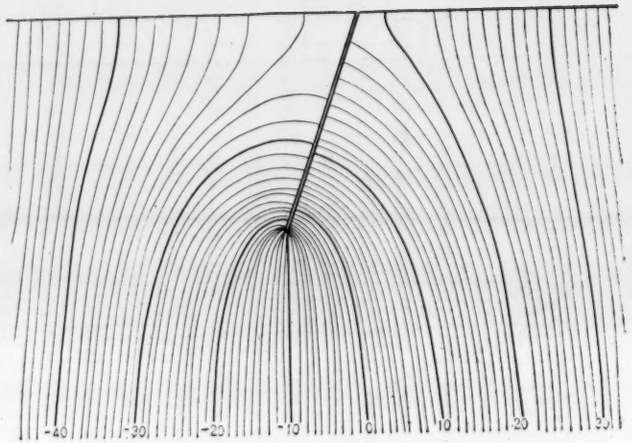

Fig. 8. Distribution of v and v_0 ($\varphi=70°$).

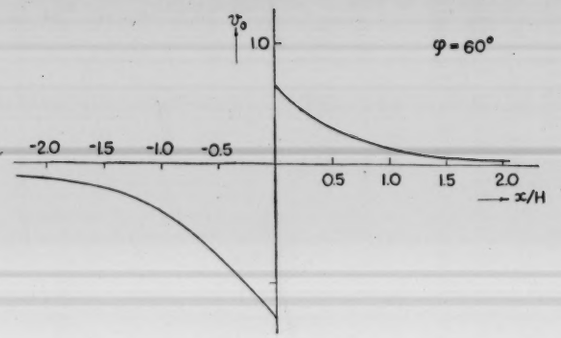

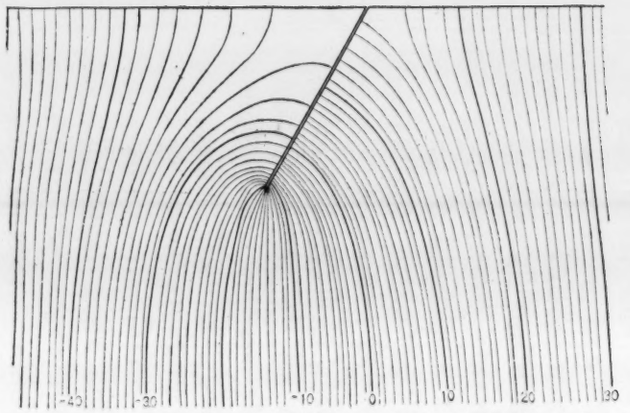

Fig. 9. Distribution of v and v_0 ($\varphi=60°$).

lustrates the distribution of electric potential in the insulator model, so that it should be understood as the distribution of v in the elastic model. The pattern itself indicates the deformation due to the faulting overlapped by the initial deformation, so that we have to subtract the latter effect in order to see the former effect only. The curve in the upper part of the figure is for one which illustrates the diminution of v_0 with dimensionless distance x/H.

First we see Fig. 6, in which is shown the distribution pattern when $\varphi=90°$. This is the case that has been discussed in the previous papers. The pattern is symmetric with respect to the fault. It also indicates that the maximum deformation appears in the uppermost part of the fault whereas the maximum stress is at the bottom. It also shows that no remarkable deformation appears at points apart from the fault, say $x/H=1$ or more. The diminution curve drawn in the upper part of the figure is of the same tendency with that obtained from the former analysis.

The distribution pattern is no more symmetric in the case of $\varphi=80°$ (Fig. 7). The deformation in the left half space, to which the fault dips, is more remarkable than that in the opposite side one. This tendency of asymmetry can be seen more concretely in the diminution curve,

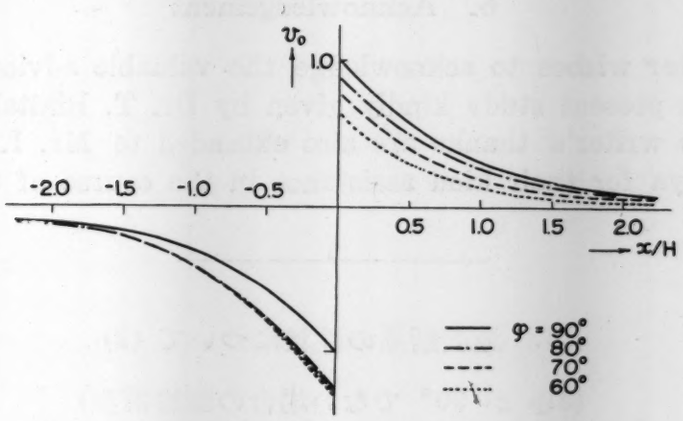

Fig. 10. Diminution curves for various values of φ.

the ordinate of which is scaled taking the value of v_0 at $x=0$ when $\varphi=90°$ as the unit. The more the dip deviates from 90°, the more remarkable the asymmetry becomes. Such a tendency can be seen clearly by drawing the curves for various values of φ in the same coordinates (Fig. 10).

We have mentioned, in the first section of this paper, a notable

characteristic of diminution curves in the cases of the Imperial Valley fault and the Fairview Peak fault. In each of these cases triangulation stations on the east side of the fault shifted more than those on the opposite side (see Figs. 4 and 6 in the previous paper). It is needless to say that this tendency can not be attributed to the elastic drift in the earth's crust, because the interval between the surveys before and after the faulting was very short in the said cases and v_0 approaches 0 with the increase of x. The asymmetric distribution of v_0 concluded from the present model is likely to provide a more reasonable explanation for the mentioned effect. Especially in the case of the Fairview Peak fault, a notable data has been reported by C. Romney, who investigated the fault-plane solution for the earthquake[6]. According to his result, the fault plane is likely to dip as much as 65° to east. This sense of dipping to east agrees well with the above-mentioned tendency of the diminution curve, although the larger angle (80° or so) is likely to be concluded from the present model. We would not like to develop further discussion here, as we have no more concrete data for comparison. Definite conclusions will be postponed until we accomplish detailed examination in future.

6. Acknowledgement

The writer wishes to acknowledge the valuable advice and suggestions for the present study kindly given by Dr. T. Rikitake of this Institute. The writer's thanks are also extended to Mr. I. Tanaoka and Miss R. Iwaya for their kind assistance in the course of the study.

---

4. 地震断層の性状について (2)

(dip が 90° でない場合の断層模型)

地震研究所 笠 原 慶 一

横辷り型であり，且つその dip が 90° であるような断層模型については，既に前報においてその基本的特性を考察し，いくつかの実例に対する比較をも試みて来た．今回はこの模型を拡張して dip が 90° でない場合にどういう特性の地殻変動（水平移動）が期待されるかを調べたものである．

このような力学模型に対する解析的な解を求めることは極めて困難であるから，dip が 60° の場合については relaxation method による数値解法を行い，更に一般の場合については (φ=90°～60°) 電場と辷り歪の場との類似性に基づく模型実験を行つた．

6) C. ROMNEY, *Bull. Seis. Soc. Amer.*, **47** (1957), 301-320.

$\varphi=90°$ の場合に対する実験結果は，当然のことながら，既報の計算結果とよく一致する．dip が 90° でなく，断層面がどちらかの側に傾いていると，その側の変動は他方の側のそれよりも顕著に現われる．従つてこの場合，$\varphi=90°$ の模型について見られたような変動の対称性（逆対称性）はもはや認められない．断層面の深さを一定に保ちながら，φ の変化による変動分布の特性を比較して見ると，φ が 90° を遠ざかる程非対称性が目立つて来る．

今回の模型では辷り歪力の役割のみを強調して，他の歪力成分（例えば地殻中に存在する静水圧的な歪力等）の影響を無視する立場をとつている．従つて今回の結果をそのまま現実の地殻に適用することには問題が残されているが，φ が 90° から余り離れていない範囲で dip 変化の影響を考察する限り充分参考になるであろう．

実際の地殻変動の分布（三角点の水平移動）を詳細に検討して見ると，その分布曲線が断層の両側で完全な逆対称でない場合が認められる（前報所載の Imperial Valley 断層や Fairview Peak 断層の場合等）．これらの地震断層の dip について明確な資料が得られない現状で断定的な議論をすることは差し控えたいが，例えば後者の場合，地震波の押し引き分布から推定される断層面は東側に傾いていたという報告もある．それが事実とすれば定性的には上記模型と適合することになる．より詳細な検討については今後の研究を進めたい．

尚，今回採用した電場模型の実験方法は，電解液と交流ブリッジとを組み合わせて行う従来のものと原理的に若干異なつており，実用上便利な点が多い．Laplace 方程式に関する各種の問題に広く適用することができると思う．

BULLETIN OF THE EARTHQUAKE
RESEARCH INSTITUTE
Vol. 37 (1959), pp. 53-87

5. *Comparative Studies of Earthquake Motions on the Ground and Underground. (Multiple Reflection Problem).*

By Kiyoshi KANAI, Teiji TANAKA and Shizuyo YOSHIZAWA,

Earthquake Research Institute.

(Read Dec. 17, 1957 and May 27, 1958.—Received Dec. 28, 1958.)

Summary

A spectral analysis of seismograms obtained both on the ground and underground has been carried out. The observation places were at Hitachi Mine and Tokai-mura, Ibaraki Prefecture.

It was clarified by comparing the observational results with the theoretical results, that the amplitude on the ground grows very large according to the multiple reflection of seismic waves in the superficial layer.

1. Introduction

It has been proved by many authors[1] that the amplitudes of earthquake motions underground are smaller than the one on the ground and the shorter the period of earthquake is, the smaller the ratio of the amplitudes underground to the one on the ground. Recently, the following points were clarified from the results of comparative observations made at Hitachi Mine, Ibaraki Prefecture, both on the ground and in the depth of the ground.

(i) The distribution of the horizontal component of seismic waves as to the depth in the earth is not so simple as considered formerly, and the component takes the maximum or the minimum amplitudes of waves at a certain depth like 150 meters underground in general[2].

(ii) In cases where the period of the seismic waves at a great

1) J. MILNE, *Trans. Seism. Soc.*, **10**.
S. SEKIYA and F. OMORI, *Trans. Seism. Soc.*, **16** (1892).
S. T. NAKAMURA, *Proc. Physico-Mathem. Soc. Japan*, **7** (1925), 127.
N. NASU, *Bull. Earthq. Res. Inst.*, **9** (1931), 454.
W. INOUE, *Bull. Earthq. Res. Inst.*, **12** (1934), 712.

2) K. KANAI and T. TANAKA, *Bull. Earthq. Res. Inst.*, **29** (1951), 107–113.

depth coincides with the peak period of the period-frequency curve on the surface which corresponds to the natural period of surface layer, the amplitude at the surface of the ground grows very large. But, when the successive waves of the same period are few, the surface layer has little influence upon the amplitude on the ground, even if the periods of primary waves may be approximate to the natural period of surface layer[3].

(iii) The peak period of the period-frequency curve of micro-tremor is coincident with the natural period of surface layer in case of *S*-waves[4].

(iv) The relation between the maximum displacement of the spectral response of the seismic waves at the great depth of 100 km epicentral distance, $A_{m.s}$, and the period corresponding to it, T_m, may be written as follows:

$$A_{m.s}=0.053T_m^{2.56}\ ^{5)}$$

The amplitude-period relation of seismic waves at the great depth, excepting those of considerably short and long periods, can be assumed as follows:

$$\frac{2\pi A}{T}(\equiv\text{velocity})=\text{constant}.$$

In the present investigations, firstly, we are going to carry out the spectral analysis[6] of seismograms obtained both on the ground and underground at Hitachi Mine and Tokai-mura, Ibaraki Prefecture. Secondly, mathematical examinations based on the theory of the multiple reflection of seismic waves in the visco-elastic layer will be made of the results of this spectral analysis.

2. The case of Hitachi Mine, Ibaraki Prefecture

The places of comparative observations were on the ground surface 370 meters above sea-level and at a depth of 300 meters from the ground surface.

---

3) K. KANAI, K. OSADA and S. YOSHIZAWA, *Bull. Earthq. Res. Inst.*, **31** (1953), 227–234.

4) K. KANAI, K. OSADA and S. YOSHIZAWA, *Bull. Earthq. Res. Inst.*, **32** (1954), 361–370.

5) K. KANAI and S. YOSHIZAWA, *Bull. Earthq. Res. Inst.*, **36** (1958), 275–293.

6) R. TAKAHASI, *Proc. 3rd Japan National Congr., Applied Mech.* (1953), 373.

The positions of seismograph stations together with the geological formations of the area and the velocity distribution of *P*-waves in the depth of the same area are shown in Figs. 1 and 2. In Table 1 the

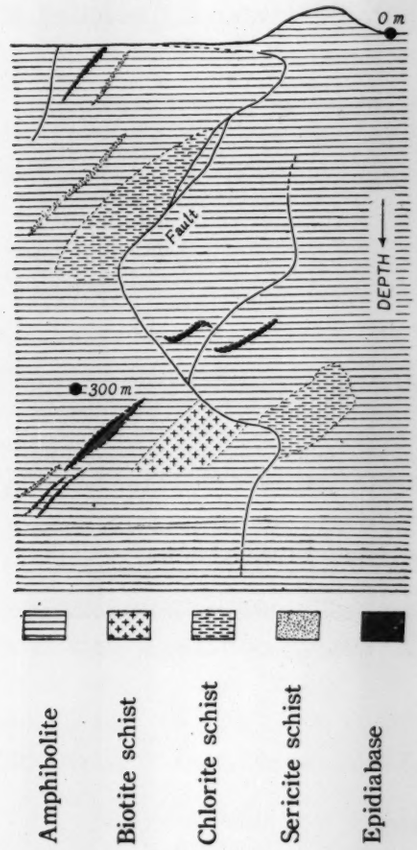

Fig. 1. Geological formations of the neighbouring part of observing stations at Hitachi Mine.

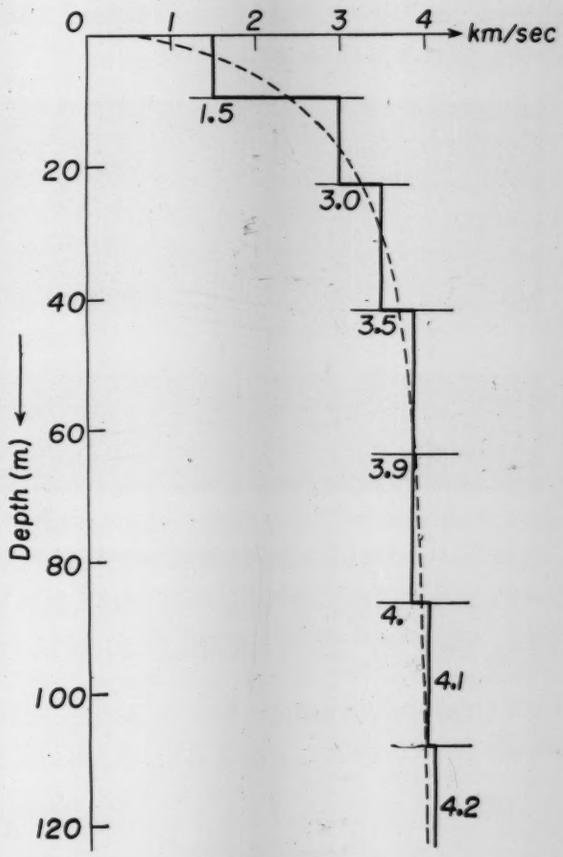

Fig. 2. Velocity of *P*-waves versus depth from the earth's surface at Hitachi Mine.

Table 1. Constants of seismographs used at Hitachi Mine.

Position	Observing direction	Natural period in sec	Damping ratio	Magnification
0 m (surface)	EW	1.0	13:1	220, 440
	NS	0.9	13:1	180, 380, 400
−300 m	EW	0.9	13:1	200, 430
	NS	1.0	13:1	465, 430

constants of the seismographs used in the present case are shown. The representative records obtained both on the earth's surface and 300 meters underground are illustrated in Fig. 3.

The observing places and the epicenters treated in this case are shown in Fig. 4. And in Table 2 the number, data and hypocenter of these earthquakes are listed.

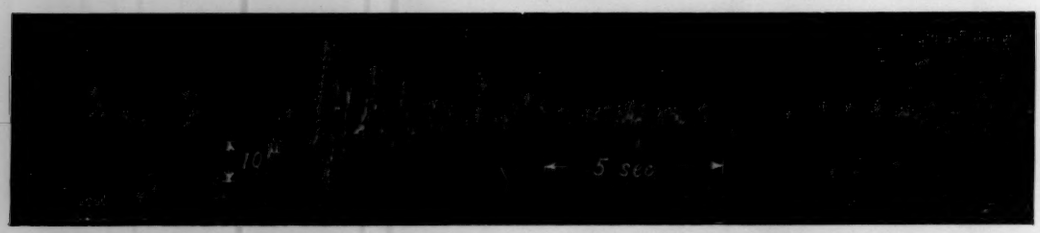

0 m.

−300 m.

Fig. 3. Representative seismograms obtained at Hitachi Mine.

In the cases of Nos. 797, 828 and 837, newbuilt electric self-starters[7] were used in the recording system and the recording speed was 1 cm

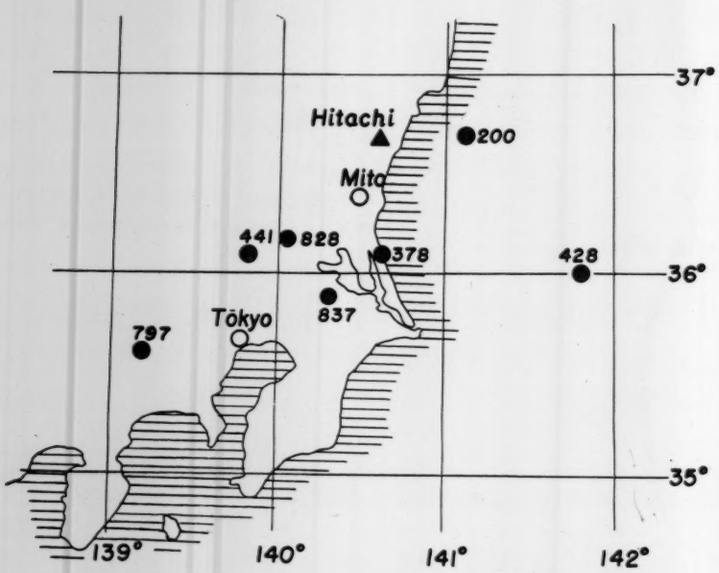

Fig. 4. Epicenters of the earthquakes observed at Hitachi Mine.

7) T. TANAKA, *Bull. Earthq. Res. Inst.*, **36** (1958), 445.

Table 2. Earthquakes observed at Hitachi Mine.

Earthquake No.	Date	Origin			Duration preliminary tremer in sec	Observing direction
		N	E	Depth in km		
200	1952 III 10	36.7	141.1	40	8.0	EW
378	〃 XI 18	36.1	140.6	60	9.9	NS
428	1953 I 14	36.0	141.8	60	14.3	EW
441	〃 〃 26	36.1	139.9	40	9.8	〃
797	1956 XII 19	35.6	139.2	120	—	NS
828	1958 II 8	36.2	140.1	80	—	〃
837	〃 III 17	35.6	140.3	70	—	〃

per sec. In other cases, that is, Nos. 200, 378, 428 and 441, no starter was used and then recording speed was 0.21 cm per sec.

The displacement spectra of the earthquake motions obtained by means of the response computer are shown in Figs. 12～18. The velocity and acceleration spectra have been calculated from the displacement spectra on the assumption of simple harmonic motion. The velocity and acceleration spectra are presented in Figs. 19～25 and 26～32, respectively. Generally speaking, it will be seen from Figs. 12～18 that there is a peak in every displacement-period curve and the larger the maximum displacement is, the longer the period corresponding to it will be. Figs. 19～25 tell us that the velocity-period curve at 300 meters underground, excepting a few cases, takes a considerably flat form. And then, as it

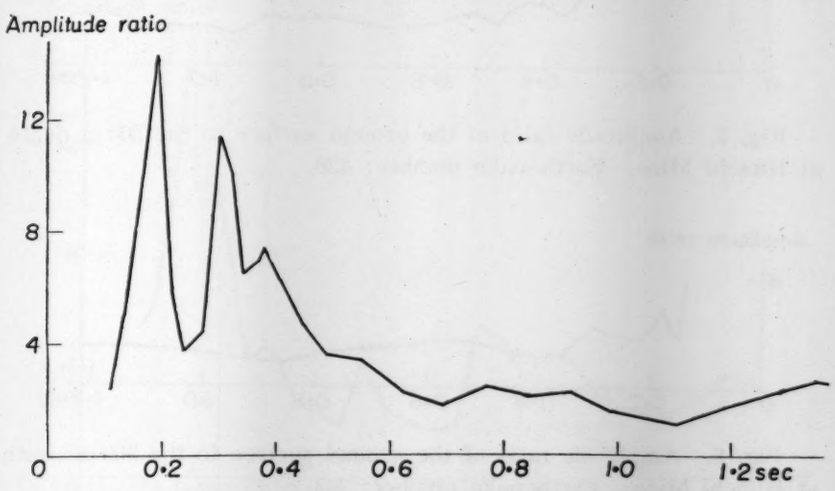

Fig. 5. Amplitude ratio of the ground surface to the 300 m depth at Hitachi Mine. Earthquake number: 200.

can be seen from Figs. 26~32, excepting considerably short periods the shorter the period of earthquake motions at 300 meters depth is, the larger the acceleration will be.

These displacement-, velocity- and acceleration-period relations of earthquake motion have already been examined closely in the previous paper[8].

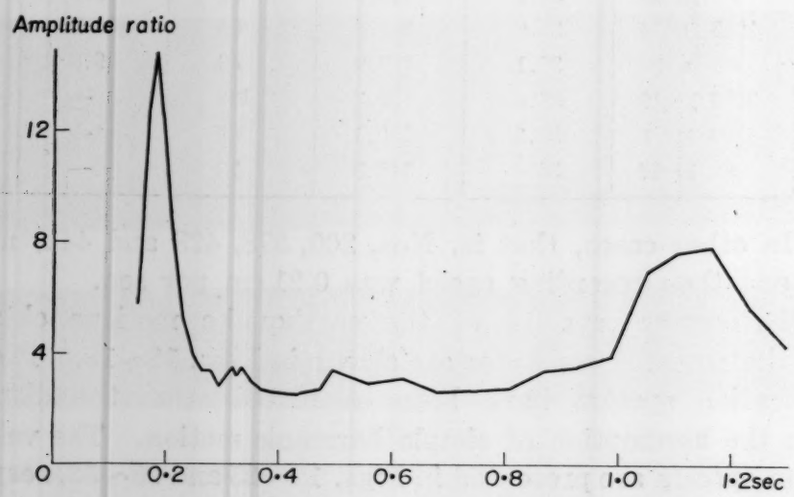

Fig. 6. Amplitude ratio of the ground surface to the 300 m depth at Hitachi Mine. Earthquake number: 378.

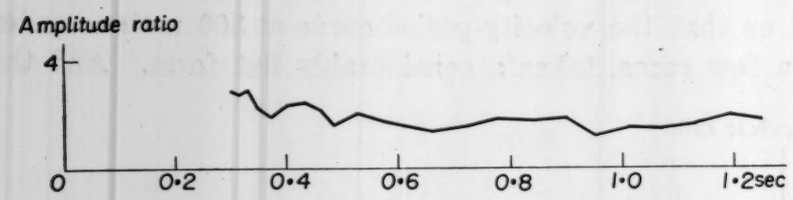

Fig. 7. Amplitude ratio of the ground surface to the 300 m depth at Hitachi Mine. Earthquake number: 428.

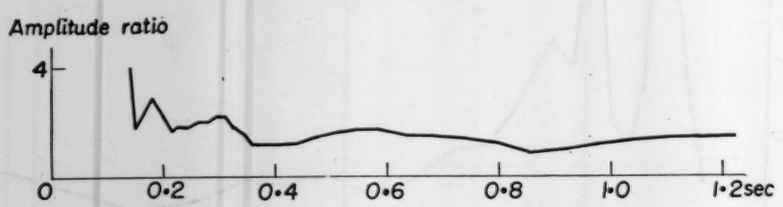

Fig. 8. Amplitude ratio of the ground surface to the 300 m depth at Hitachi Mine. Earthquake number: 441.

8) *loc. cit.*, 5).

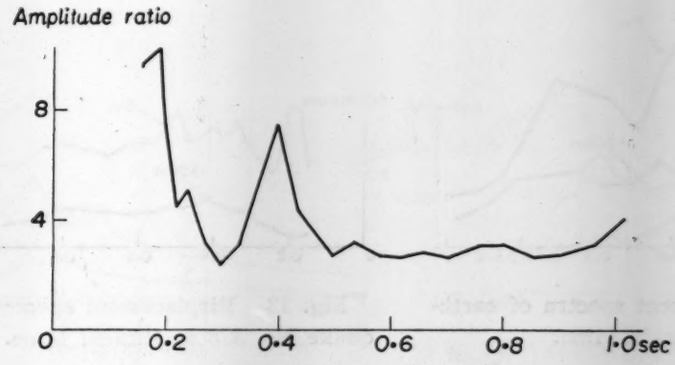

Fig. 9. Amplitude ratio of the ground surface to the 300 m depth at Hitachi Mine. Earthquake number: 797.

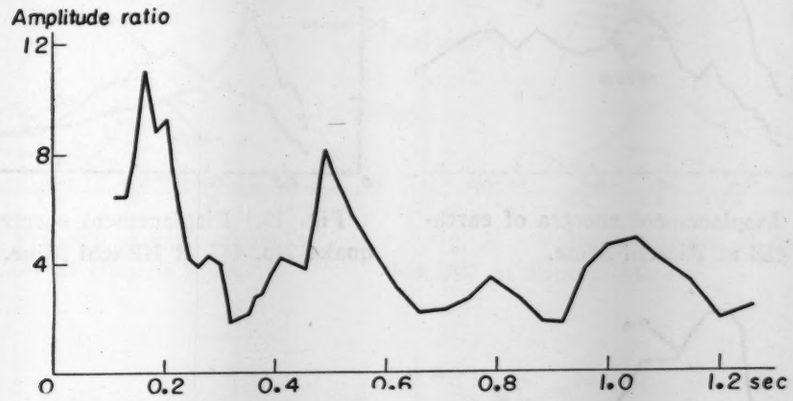

Fig. 10. Amplitude ratio of the ground surface to the 300 m depth at Hitachi Mine. Earthquake number: 828.

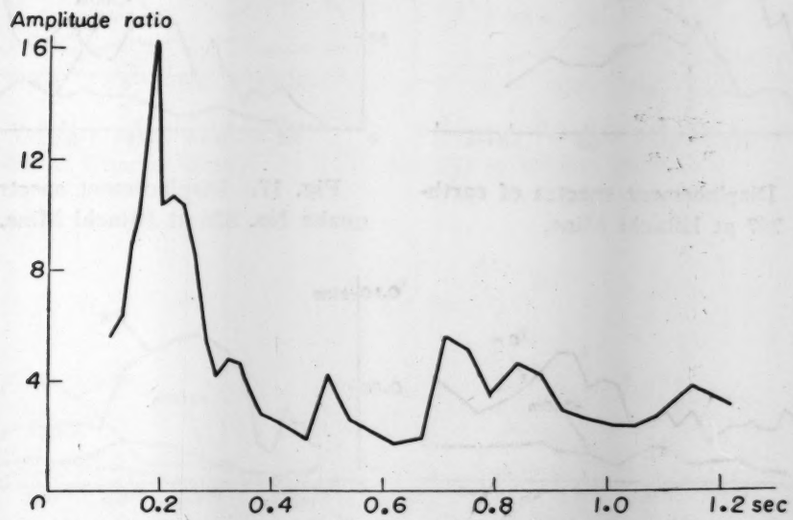

Fig. 11. Amplitude ratio of the ground surface to the 300 m depth at Hitachi Mine. Earthquake number: 837.

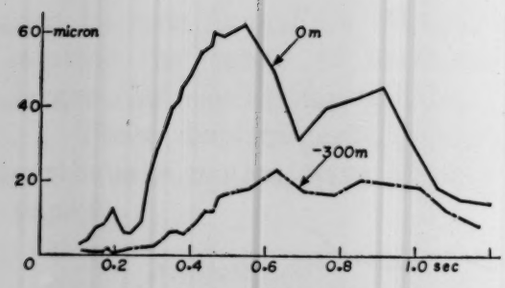

Fig. 12. Displacement spectra of earthquake No. 200 at Hitachi Mine.

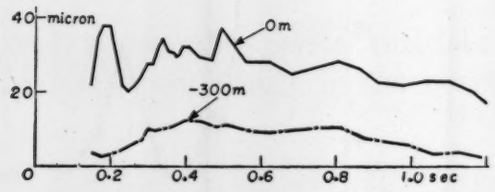

Fig. 13. Displacement spectra of earth quake No. 378 at Hitachi Mine.

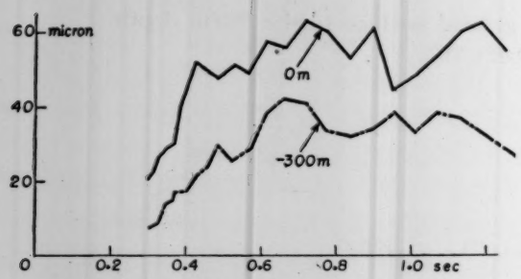

Fig. 14. Displacement spectra of earthquake No. 428 at Hitachi Mine.

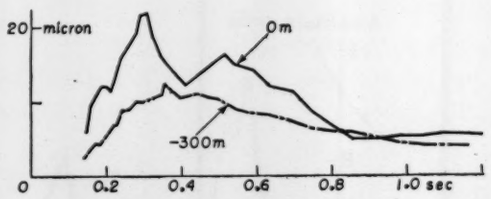

Fig. 15. Displacement spectra of earthquake No. 441 at Hitachi Mine.

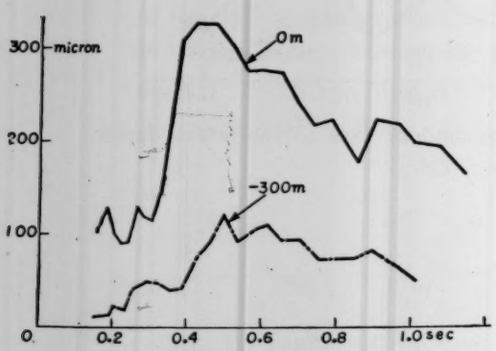

Fig. 16. Displacement spectra of earthquake No. 797 at Hitachi Mine.

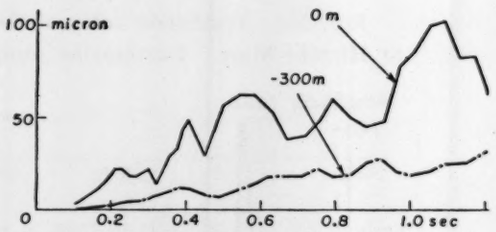

Fig. 17. Displacement spectra of earthquake No. 828 at Hitachi Mine.

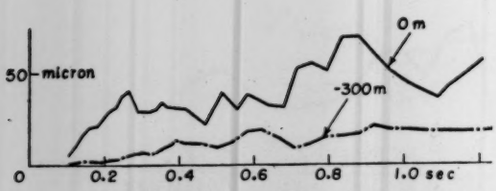

Fig. 18. Displacement spectra of earthquake No. 837 at Hitachi Mine.

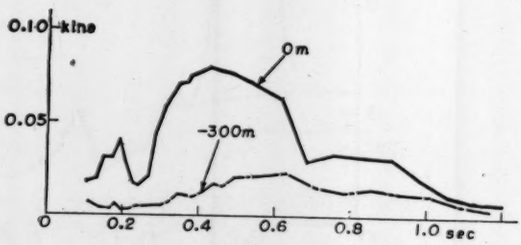

Fig. 19. Velocity spectra of earthquake No. 200 at Hitachi Mine.

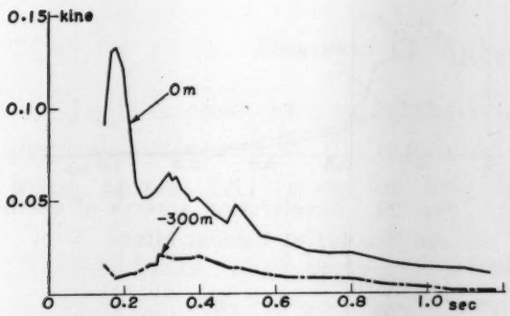

Fig. 20. Velocity spectra of earthquake No. 378 at Hitachi Mine.

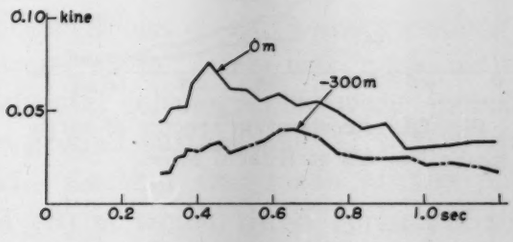

Fig. 21. Velocity spectra of earthquake No. 428 at Hitachi Mine.

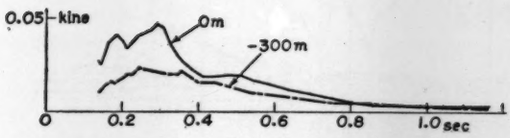

Fig. 22. Velocity spectra of earthquake No. 441 at Hitachi Mine.

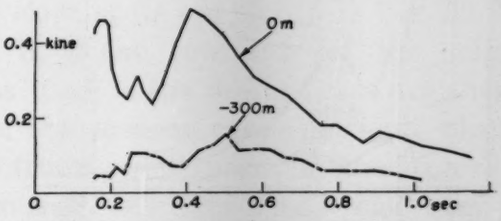

Fig. 23. Velocity spectra of earthquake No. 797 at Hitachi Mine.

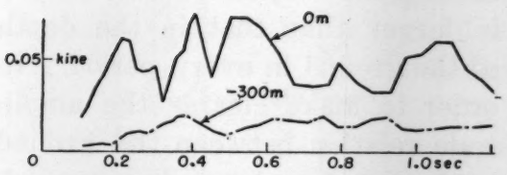

Fig. 24. Velocity spectra of earthquake No. 828 at Hitachi Mine.

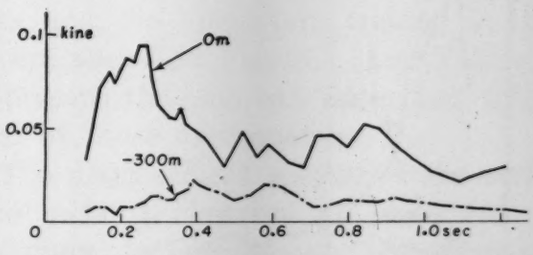

Fig. 25. Velocity spectra of earthquake No. 837 at Hitachi Mine.

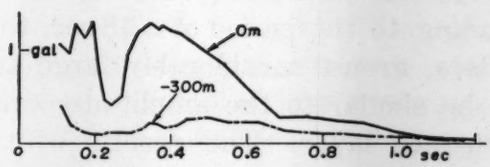

Fig. 26. Acceleration spectra of earthquake No. 200 at Hitachi Mine.

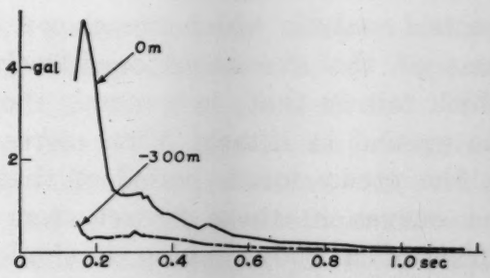

Fig. 27. Acceleration spectra of earthquake No. 378 at Hitachi Mine.

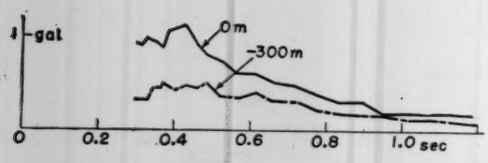

Fig. 28. Acceleration spectra of earthquake No. 428 at Hitachi Mine.

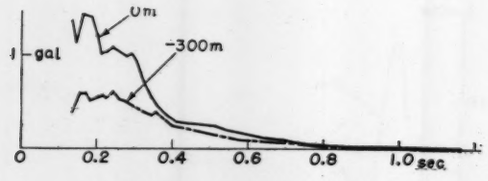

Fig. 29. Acceleration spectra of earthquake No. 441 at Hitachi Mine.

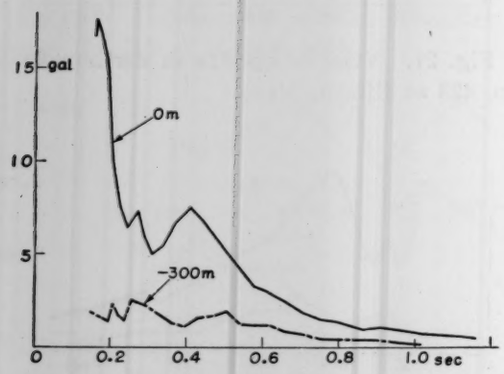

Fig. 30. Acceleration spectra of earthquake No. 797 at Hitachi Mine.

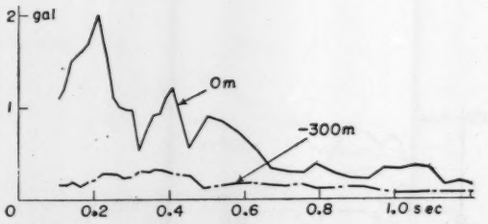

Fig. 31. Acceleration spectra of earthquake No. 828 at Hitachi Mine.

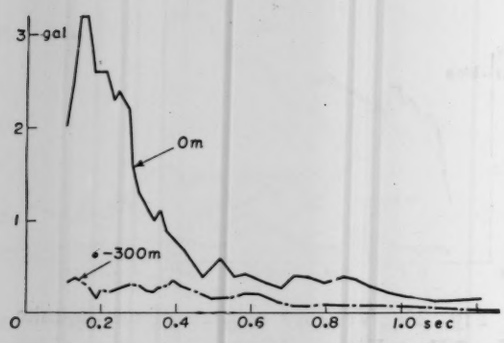

Fig. 32. Acceleration spectra of earthquake No. 837 at Hitachi Mine.

Also, it may be found from Figs. 12～18 that the amplitude of earthquake motion on the ground is larger than that in the depth of the ground in every period. In order to make clearer the amplitude relation between the ground surface and underground, we calculated the amplitude ratio of the ground surface to the underground in each period from the results of spectral analysis which are shown in Figs. 12～18. And then, the relations of the abovementioned ratio to period are shown in Figs. 5～11, which tell us that, in general, the amplitude of earthquake motions on the ground in Hitachi Mine corresponding to the period of 0.18 sec, that is, the predominant period of that place, grews considerably large and the curves in these figures seem to be similar to the amplitude-period curve of a body having a single surface layer. The results of the mathematical studies concerning these features will be described in the next section but one.

3. The case of Tokai-mura, Ibaraki Prefecture

In this case, two comparative observations of earthquake motions at ground surface and underground were made. One was made at the place named (A) in which two horizontal seismographs were installed at the ground surface and 21.1 m underground. Another was made at the place named (B) in which three horizontal seismographs were installed at the ground surface, 7 m and 21.3 m underground. Subsoil conditions detected by boring and observation spots are shown in Fig. 33. In Table 3, 4 the constants of the seismographs used in the present case are shown.

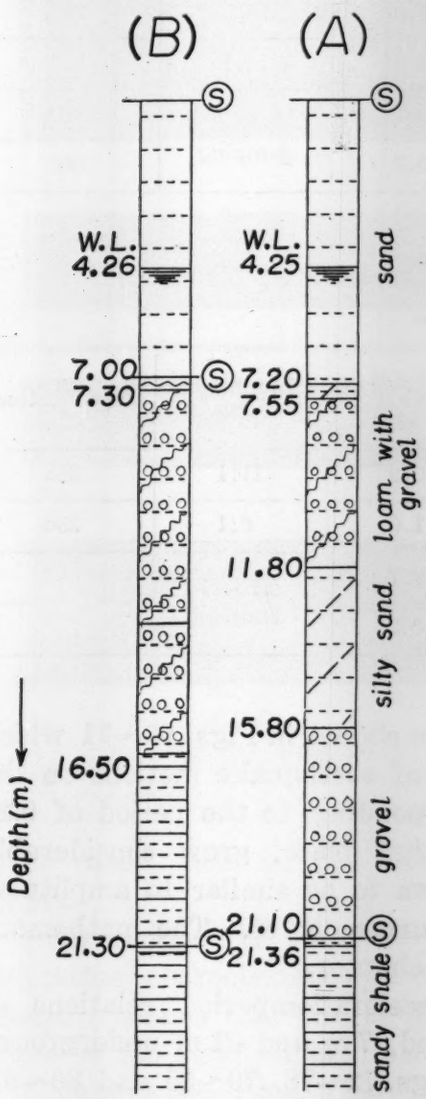

Fig. 33. Subsoil conditions of places (A) and (B) in Tokai-mura as detected by boring.

In the present case, newbuilt electric self-starters were used in the recording system and recording speed was 1 cm per sec. The representative records obtained both on the earth's surface and underground are illustrated in Fig. 34. The observing places and the epicenters treated in this case are shown in Fig. 35. And Tables 5, 6 represent the number, date and hypocenter of these earthquakes.

The displacement spectra of the earthquake motions observed at place (A) in Tokai-mura by means of the response computer are shown in Figs. 36～44. The velocity and acceleration spectra have been calculated from the displacement spectra on the assumption of simple harmonic motion. They are presented in Figs. 45～53 and Figs. 54～62, respectively. It will be seen from Figs. 36～62 that, in general, the displacement-, velocity- and acceleration-period relations of earthquake motions are the same as the results mentioned in the previous paper and also in the preceding chapter.

The ratio of the amplitude on the ground to that underground in

Table 3. Constants of seismographs used at place (A) in Tokai-mura.

Type	Position	Observing direction	Natural period in sec	Damping ratio	Magnification
mechanical	0 m	EW	0.9	13:1	276
		NS	1.0	13:1	278
electro-magnetic	0 m	NS	0.7	critical damping	400
self-levelling	−21.1 m	NS	0.7		600

Table 4. Constants of seismographs used at place (B) in Tokai-mura.

Type	Position	Observing direction	Natural period in sec	Damping ratio	Magnification
mechanical	0 m	EW	0.9	11:1	265
		NS	1.0	8:1	250
self-levelling	− 7.0 m	NS	0.7	critical damping	400
	−21.3 m	NS	0.7		1200 950

each period obtained from Figs. 36∼44 are shown in Figs. 63∼71 which tell us that, in general, the amplitude of earthquake motions on the ground at place (A) in Tokai-mura corresponding to the period of 0.27 sec, that is, the predominant period of that place, grew considerably large and the curves in these figures seem to be similar to amplitude-period curve of a body having a single surface layer. The mathematical studies will be presented in the next chapter.

The displacement-, velocity- and acceleration-period relations of earthquake motions observed on the ground, 7 m and 21 m underground of place (B) in Tokai-mura are shown in Figs. 72∼78, 79∼85 and 86∼92, respectively. And then, the relation between the ratios of the amplitude on the ground and 7 m underground to the one 21 m underground and period are shown in Figs. 93∼99. In the present case, as seen in Figs. 93∼99, the relation between the amplitude ratio mentioned above and period seems to be somewhat complex in comparison with the for-

0 m at place (A).

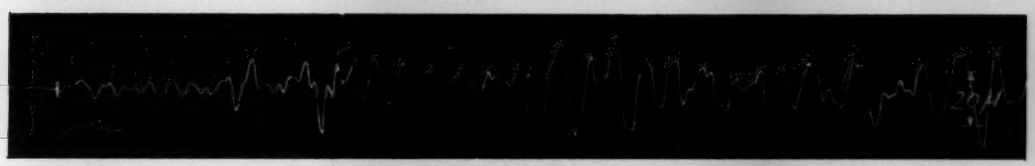

−21 m at place (A).

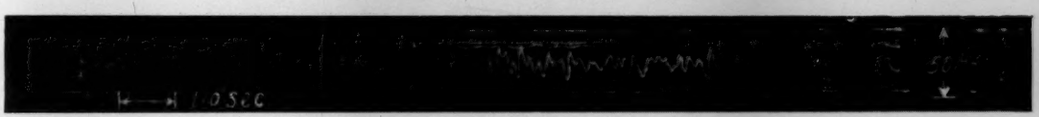

0 m at place (B).

−7 m at place (B).

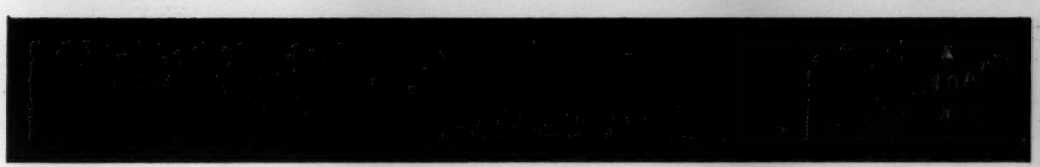

−21 m at place (B).

Fig. 34. Representative seismograms observed at Tokai-mura.

mer cases, that is, the cases at Hitachi Mine and place (A) in Tokai-mura.

In general, in cases when the earthquake origin is in the sea, the vibration characteristics of short period of ground scarcely appear because it seems that the amplitude of short period of earthquake motions is too small in the case of the sea earthquake.

Otherwise, Figs. 72∼92, especially velocity-period relation of Figs. 80∼83, tell us that the amplitude of earthquake motions on the ground at place (B) in Tokai-mura corresponding to the period of 0.24 sec, that is, the predominant period of that place, grew considerably large. The mathematical treatment of this problem will be dealt with in the next chapter.

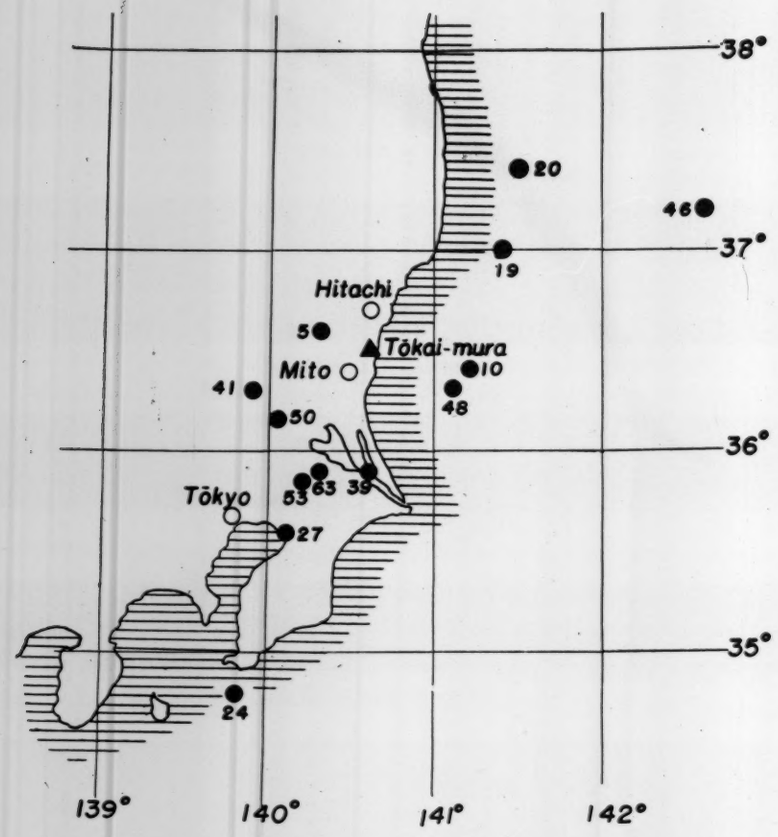

Fig. 35. Epicenters of earthquakes observed at Tokai-mura.

Table 5. Earthquakes observed at place (A) in Tokai-mura.

Earthquake No.	Date	Origin		
		N	E	Depth in km
39	1957 XII 27	35.9	140.6	about 40
41	1958 I 22	36.3	139.9	80
46	〃 〃 29	37.1	142.6	60
48	〃 II 5	36.3	141.1	40
50	〃 〃 8	36.2	140.1	80
53	〃 〃 18	35.9	140.2	60
63	〃 III 17	35.9	140.3	70

Table 6. Earthquakes observed at place (B) in Tokai-mura.

Earthquake No.	Date	Origin		
		N	E	Depth in km
3	1957 VII 26	Off E coast of Ibaraki Prefecture		
5	〃 VIII 2	36.6	140.3	110
10	〃 〃 7	36.4	141.2	shallow
19	〃 〃 18	37.0	141.4	about 60
20	〃 〃 31	37.4	141.5	about 30
24	〃 IX 7	34.8	139.8	about 90
27	〃 X 4	35.6	140.1	about 60

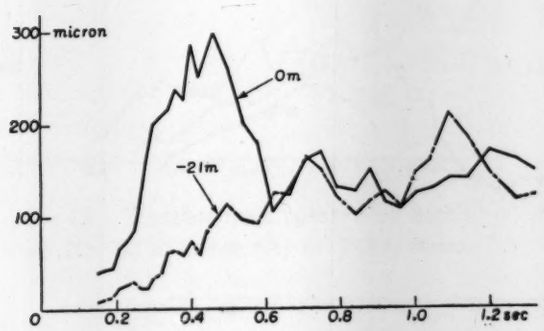

Fig. 36. Displacement spectra of earthquake No. 39 at place (A) in Tokai-mura.

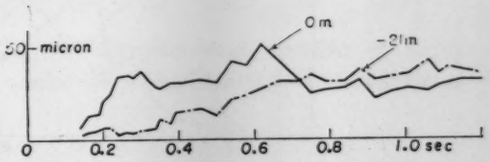

Fig. 37. Displacement spectra of earthquake No. 41 at place (A) in Tokai-mura

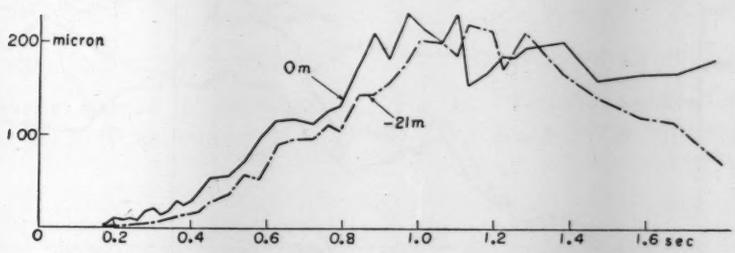

Fig. 38. Displacement spectra of earthquake No. 46 at place (A) in Tokai-mura.

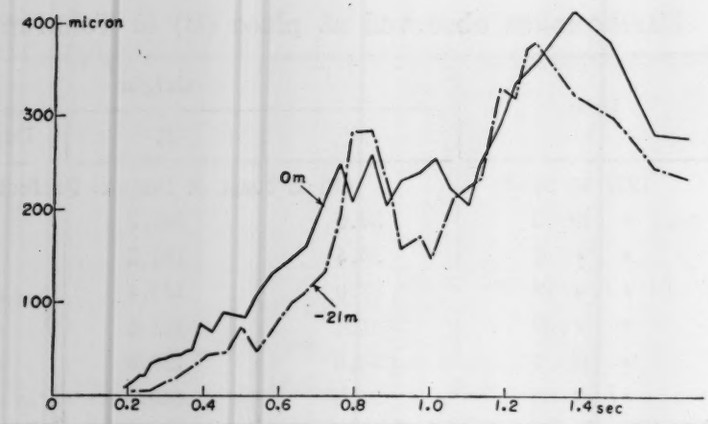

Fig. 39. Displacement spectra of earthquake No. 50 at place (A) in Tokai-mura.

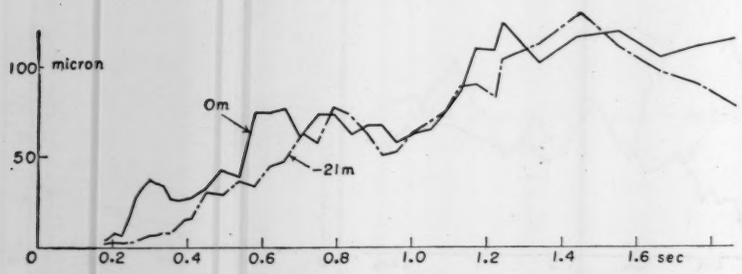

Fig. 40. Displacement spectra of earthquake No. 53 at place (A) in Tokai-mura.

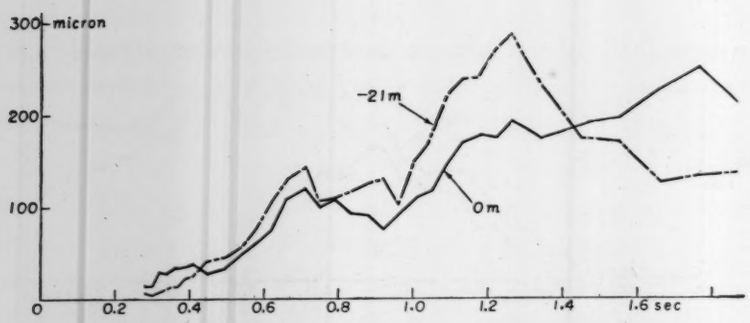

Fig. 41. Displacement spectra of earthquake No. 55 at place (A) in Tokai-mura.

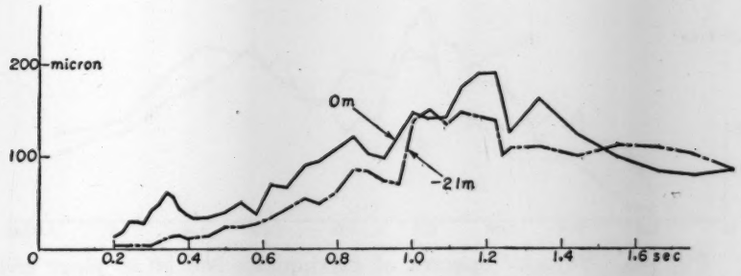

Fig. 42. Displacement spectra of earthquake No. 56 at place (A) in Tokai-mura.

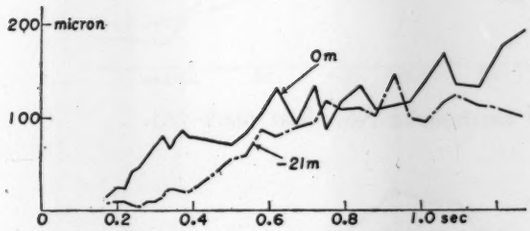

Fig. 43. Displacement spectra of earthquake No. 63 at place (A) in Tokai-mura.

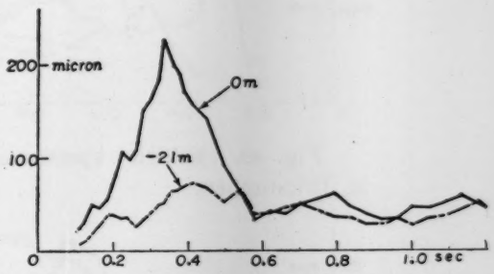

Fig. 44. Displacement spectra of earthquake No. 48 at place (A) in Tokai-mura.

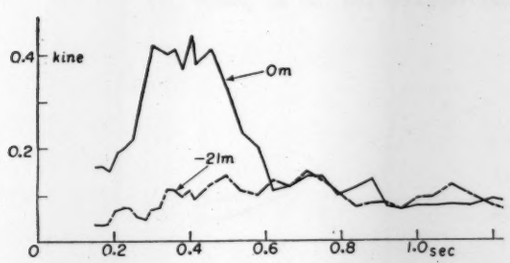

Fig. 45. Velocity spectra of earthquake No. 39 at place (A) in Tokai-mura.

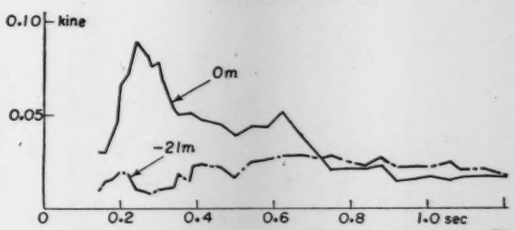

Fig. 46. Velocity spectra of earthquake No. 41 at place (A) in Tokai-mura.

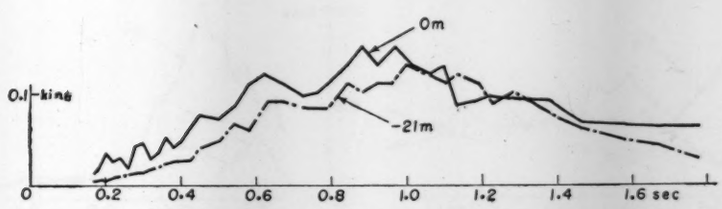

Fig. 47. Velocity spectra of earthquake No. 46 at place (A) in Tokai-mura.

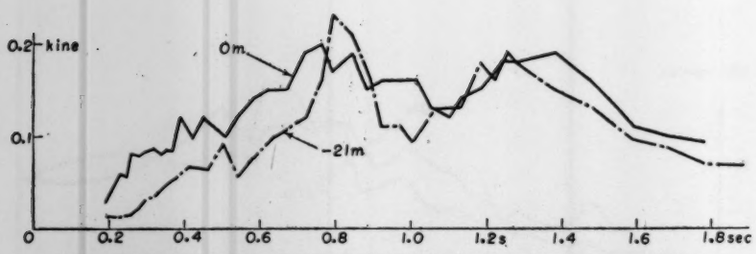

Fig. 48. Velocity spectra of earthquake No. 50 at place (A) in Tokai-mura.

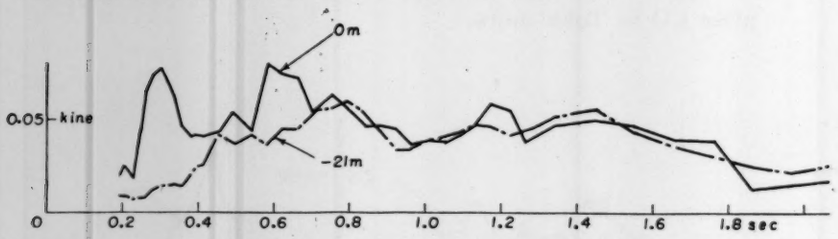

Fig. 49. Velocity spectra of earthquake No. 53 at place (A) in Tokai-mura.

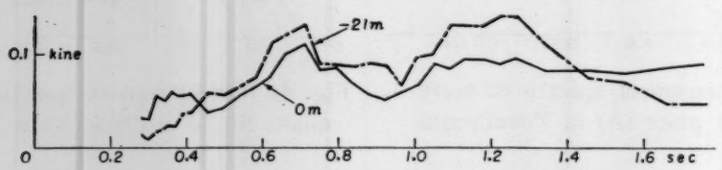

Fig. 50. Velocity spectra of earthquake No. 55 at place (A) in Tokai-mura.

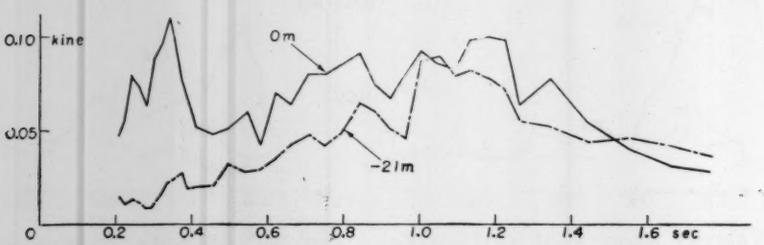

Fig. 51. Velocity spectra of earthquake No. 56 at place (A) in Tokai-mura.

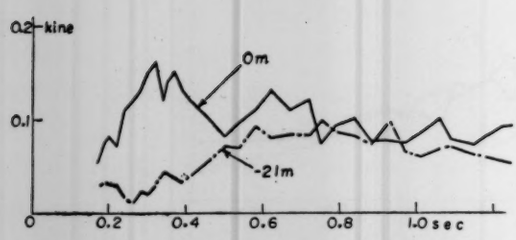

Fig. 52. Velocity spectra of earthquake No. 63 at place (A) in Tokai-mura.

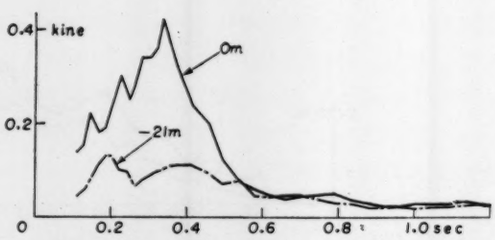

Fig. 53. Velocity spectra of earthquake No. 48 at place (A) in Tokai-mura.

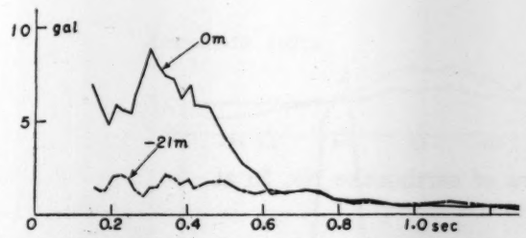

Fig. 54. Acceleration spectra of No. 39 earthquake at place (A) in Tokai-mura.

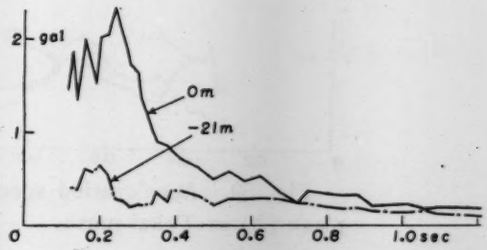

Fig. 55. Acceleration spectra of No. 41 earthquake at place (A) in Tokai-mura.

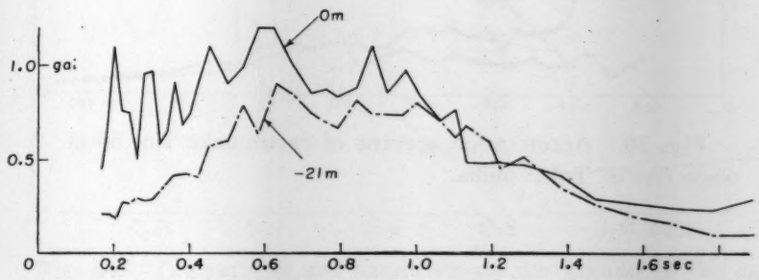

Fig. 56. Acceleration spectra of No. 46 earthquake at place (A) in Tokai-mura.

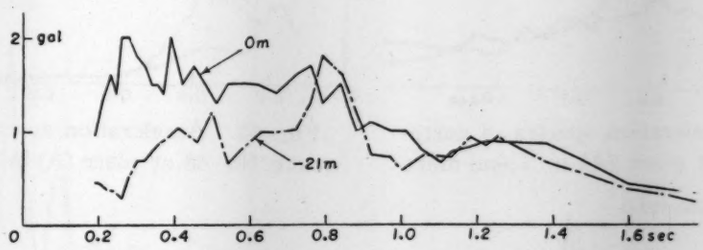

Fig. 57. Acceleration spectra of No. 50 earthquake at place (A) in Tokai-mura.

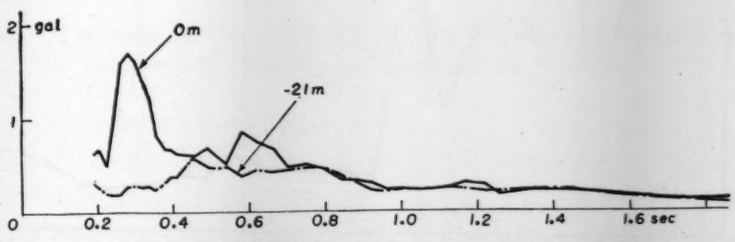

Fig. 58. Acceleration spectra of No. 53 earthquake at place (A) in Tokai-mura.

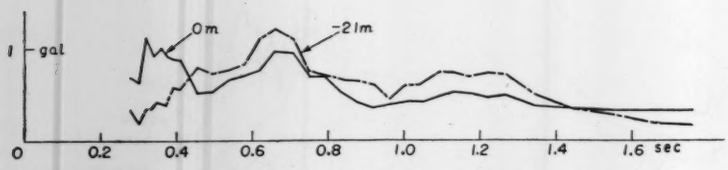

Fig. 59. Acceleration spectra of earthquake No. 55 at place (A) in Tokai-mura.

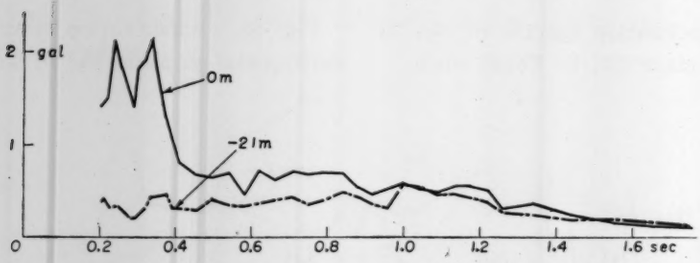

Fig. 60. Acceleration spectra of earthquake No. 56 at place (A) in Tokai-mura.

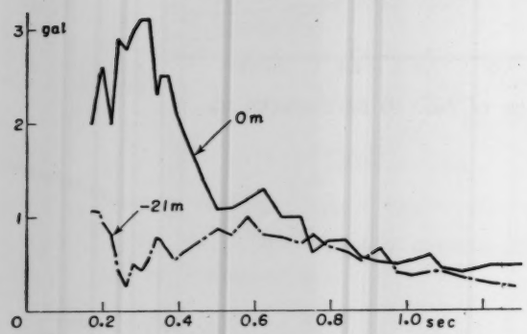

Fig. 61. Acceleration spectra of earthquake No. 63 at place (A) in Tokai-mura

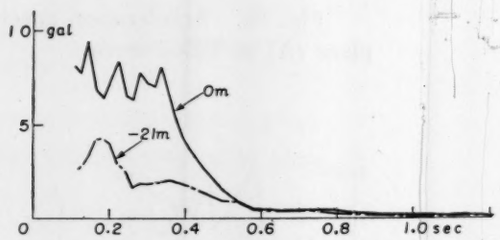

Fig. 62. Acceleration spectra of earthquake No. 48 at place (A) in Tokai-mura.

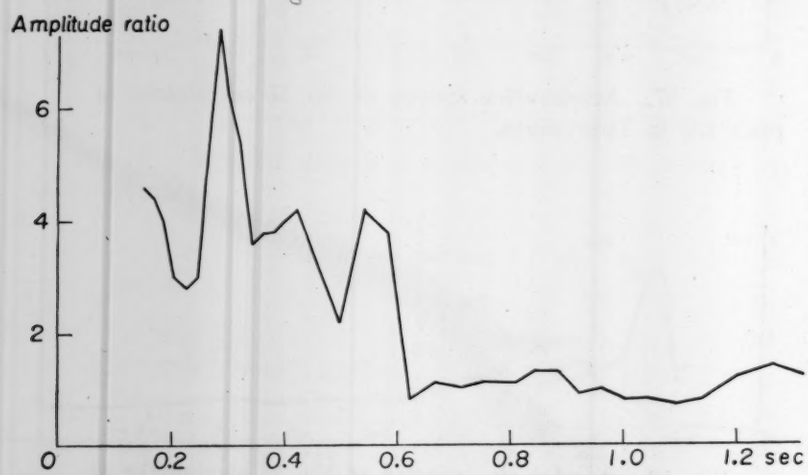

Fig. 63. The ratio of the amplitude on the ground to the one 21 m depth at place (A) in Tokai-mura. Earthquake number: 39.

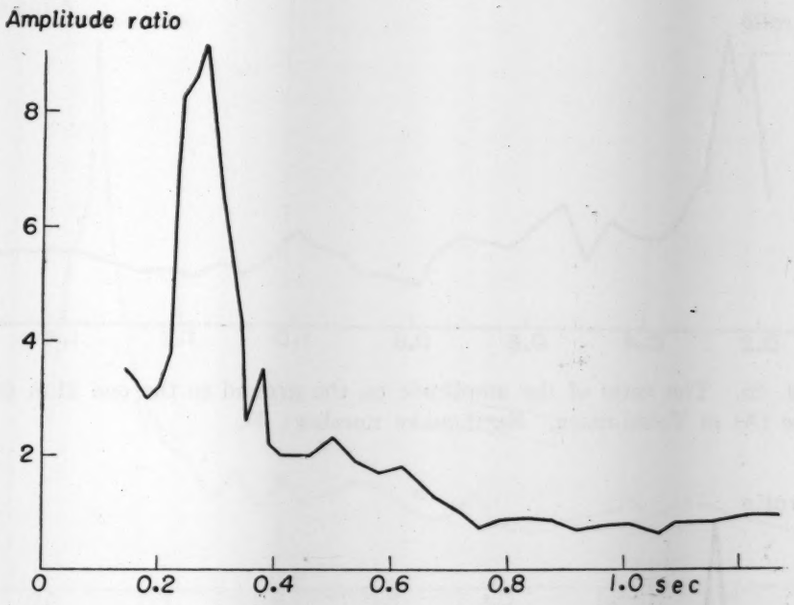

Fig. 64. The ratio of the amplitude on the ground to the one 21 m depth at place (A) in Tokai-mura. Earthquake number: 41.

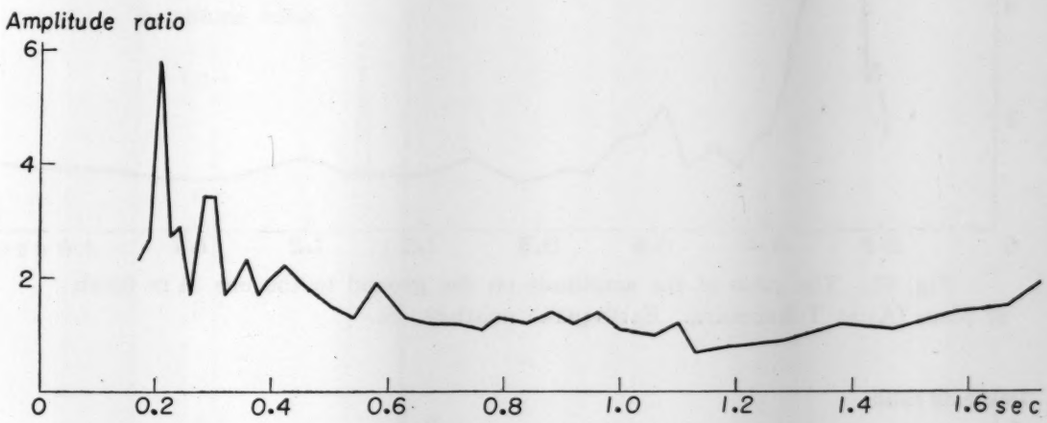

Fig. 65. The ratio of the amplitude on the ground to the one 21 m depth at place (A) in Tokai-mura. Earthquake number: 46.

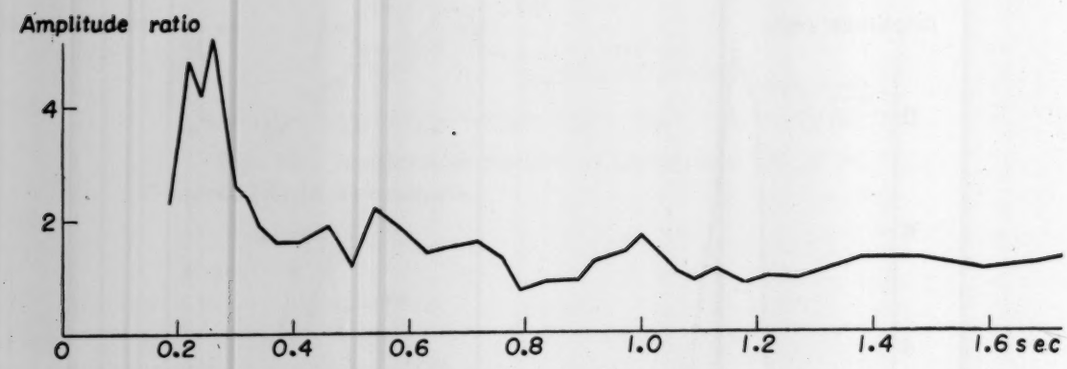

Fig. 66. The ratio of the amplitude on the ground to the one 21 m depth at place (A) in Tokai-mura. Earthquake number: 50.

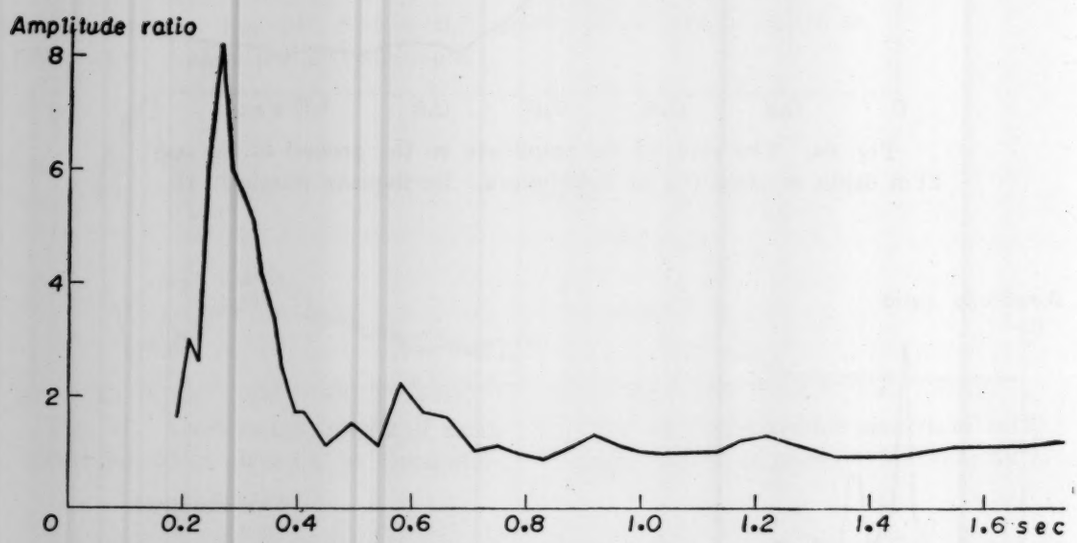

Fig. 67. The ratio of the amplitude on the ground to the one 21 m depth at place (A) in Tokai-mura. Earthquake number: 53.

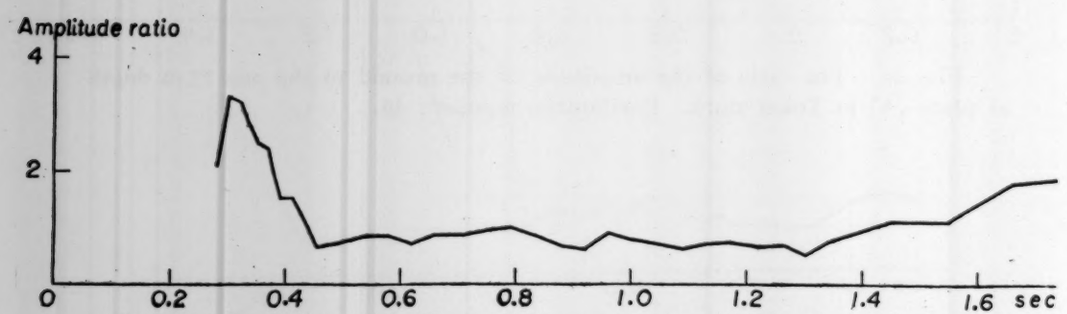

Fig. 68. The ratio of the amplitude on the ground to the one 21 m depth at place (A) in Tokai-mura. Earthquake number: 55.

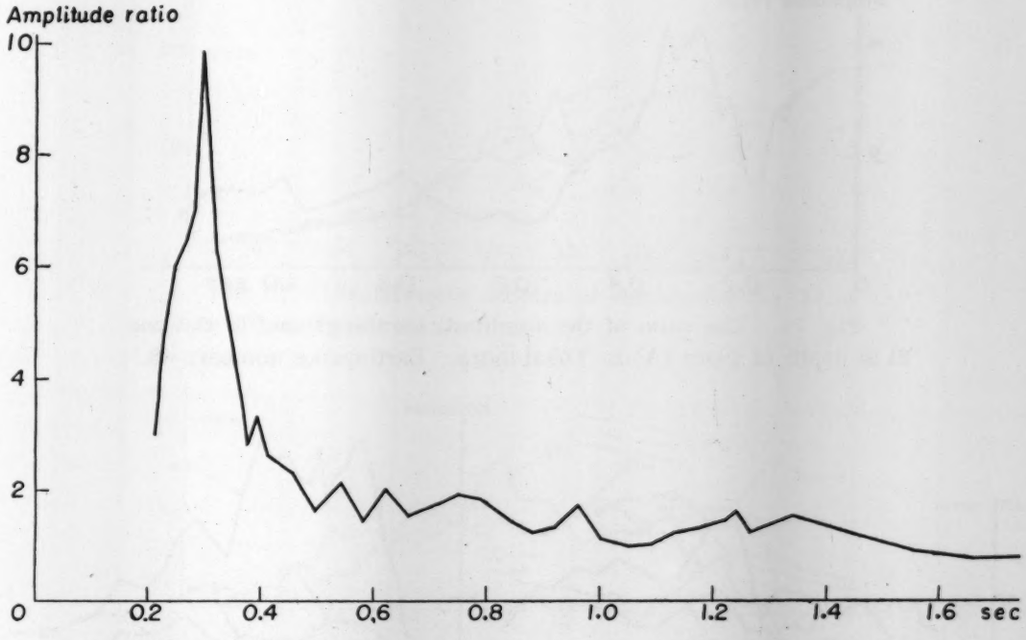

Fig. 69. The ratio of the amplitude on the ground to the one 21 m depth at place (A) in Tokai-mura. Earthquake number: 56.

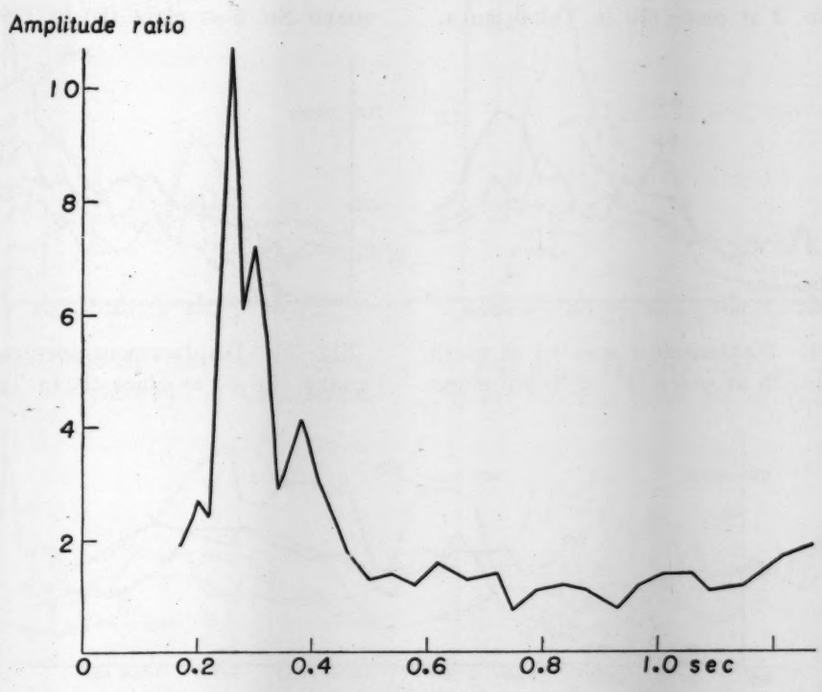

Fig. 70. The ratio of the amplitude on the ground to the one 21 m depth at place (A) in Tokai-mura. Earthquake number: 63.

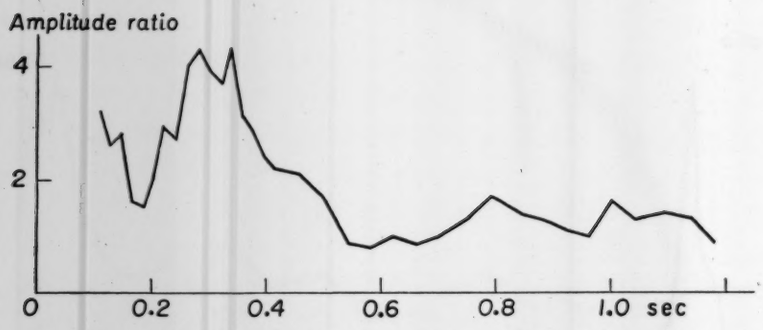

Fig. 71. The ratio of the amplitude on the ground to the one 21 m depth at place (A) in Tokai-mura. Earthquake number: 48.

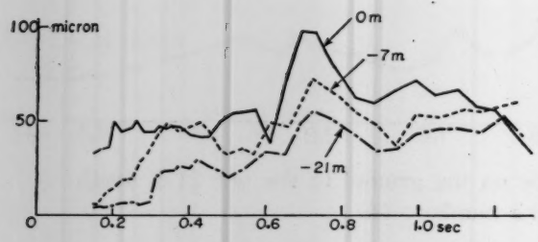

Fig. 72. Displacement spectra of earthquake No. 3 at place (B) in Tokai-mura.

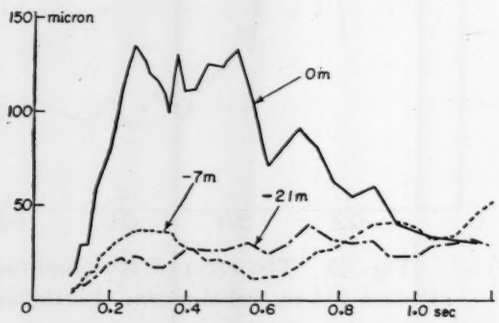

Fig. 73. Displacement spectra of earthquake No. 5 at place (B) in Tokai-mura.

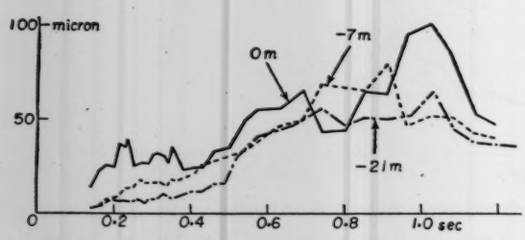

Fig. 74. Displacement spectra of earthquake No. 10 at place (B) in Tokai-mura.

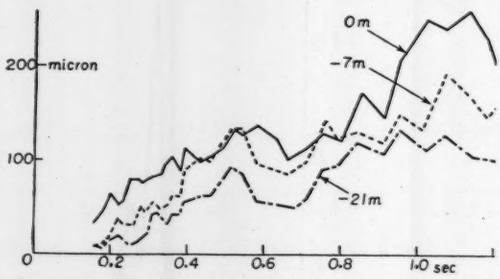

Fig. 75. Displacement spectra of earthquake No. 20 at place (B) in Tokai-mura.

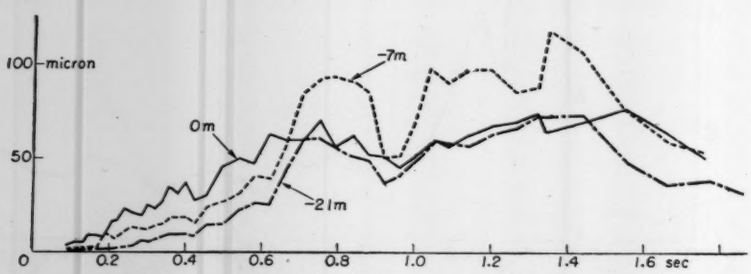

Fig. 76. Displacement spectra of earthquake No. 19 at place (B) in Tokai-mura.

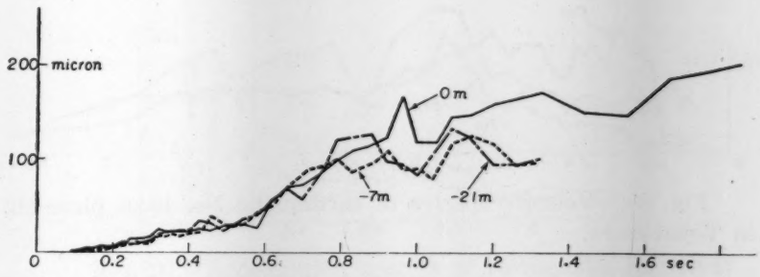

Fig. 77. Displacement spectra of earthquake No. 24 at place (B) in Tokai-mura.

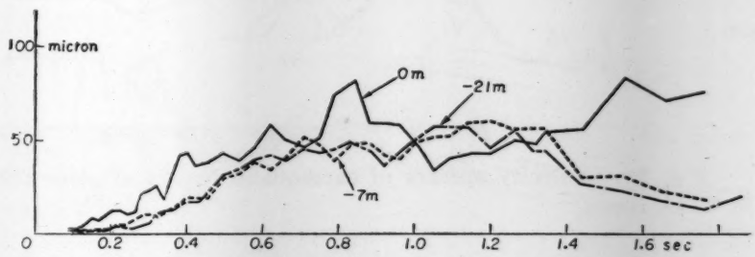

Fig. 78. Displacement spectra of earthquake No. 27 at place (B) in Tokai-mura.

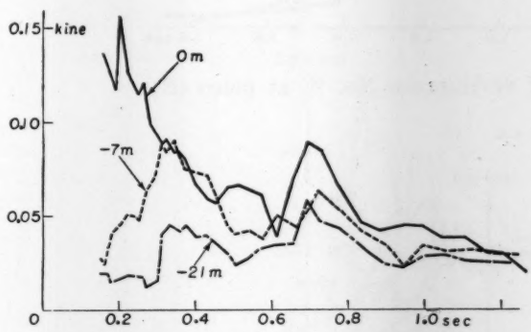

Fig. 79. Velocity spectra of earthquake No. 3 at place (B) in Tokai-mura.

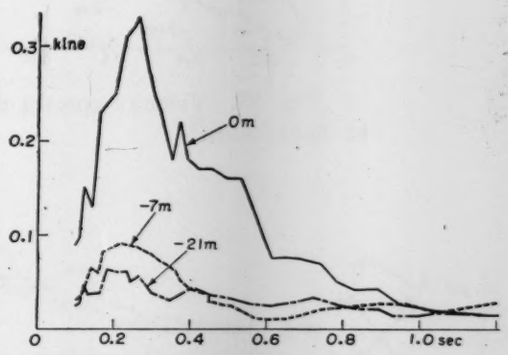

Fig. 80. Velocity spectra of earthquake No. 5 at place (B) in Tokai-mura.

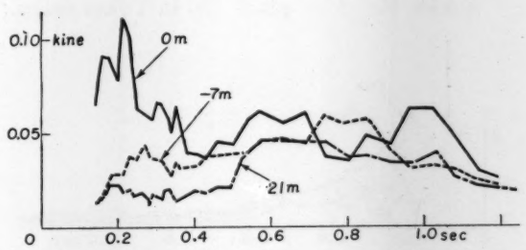

Fig. 81. Velocity spectra of earthquake No. 10 at place (B) in Tokai-mura.

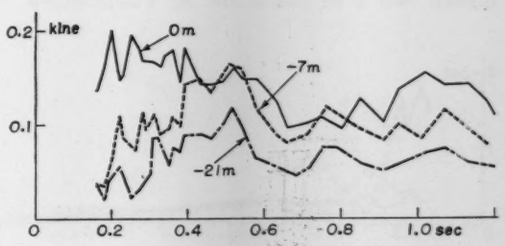

Fig. 82. Velocity spectra of earthquake No. 20 at place (B) in Tokai-mura.

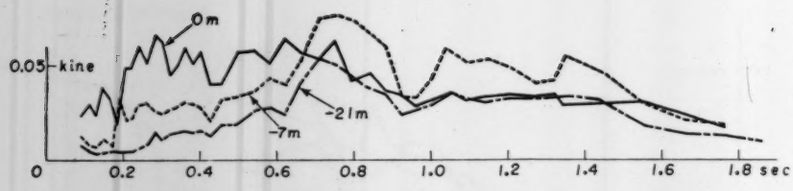

Fig. 83. Velocity spectra of earthquake No. 19 at place (B) in Tokai-mura.

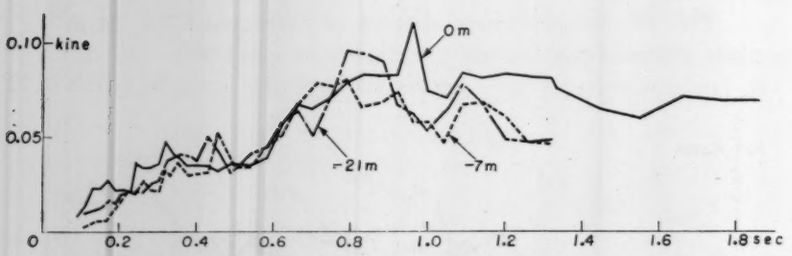

Fig. 84. Velocity spectra of earthquake No. 24 at place (B) in Tokai-mura.

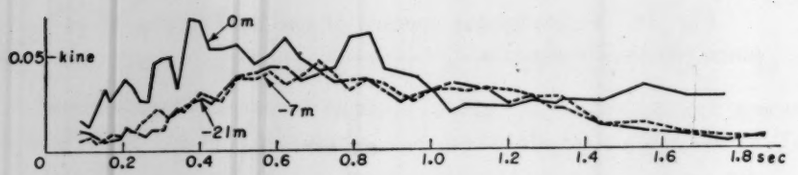

Fig. 85. Velocity spectra of earthquake No. 27 at place (B) in Tokai-mura.

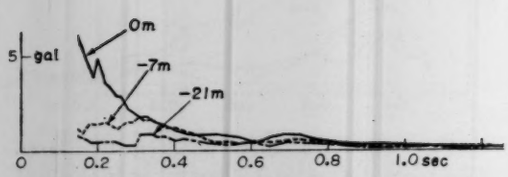

Fig. 86. Acceleration spectra of earthquake No. 3 at place (B) in Tokai-mura.

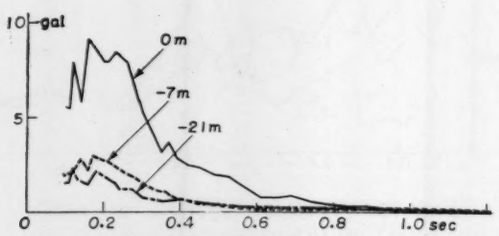

Fig. 87. Acceleration spectra of earthquake No. 5 at place (B) in Tokai-mura.

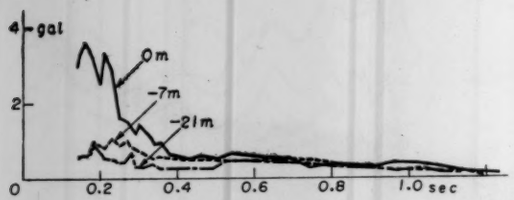

Fig. 88. Acceleration spectra of earthquake No. 10 at place (B) in Tokai-mura.

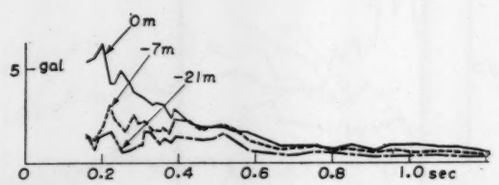

Fig. 89. Acceleration spectra of earthquake No. 20 at place (B) in Tokai-mura.

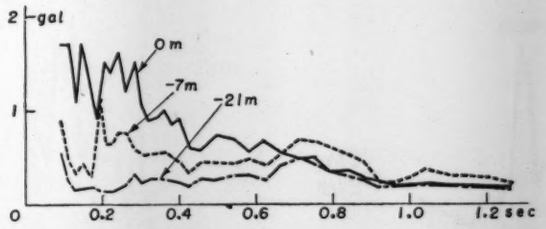

Fig. 90. Acceleration spectra of earthquake No. 19 at place (B) in Tokai-mura.

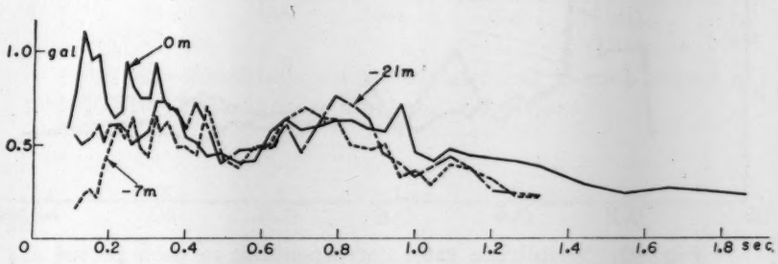

Fig. 91. Acceleration spectra of earthquake No. 24 at place (B) in Tokai-mura.

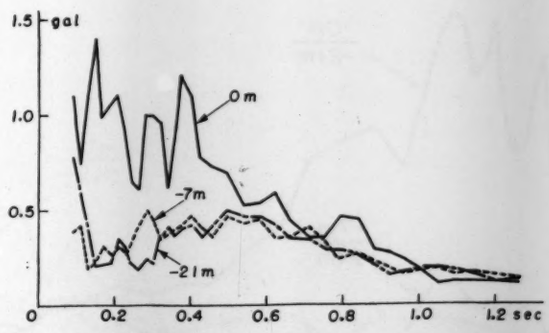

Fig. 92. Acceleration spectra of earthquake No. 27 at place (B) in Tokai-mura.

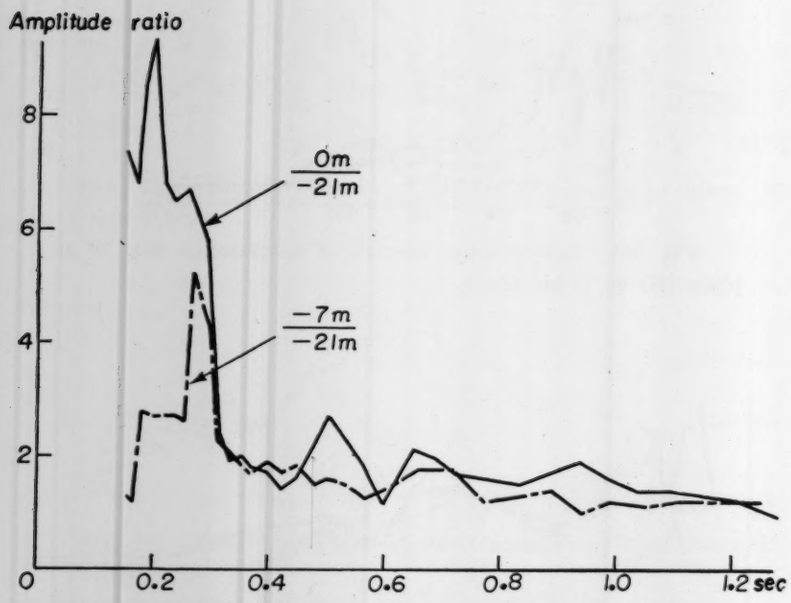

Fig. 93. Amplitude ratio corresponding to each period at place (B) in Tokai-mura. Earthquake number: 3.

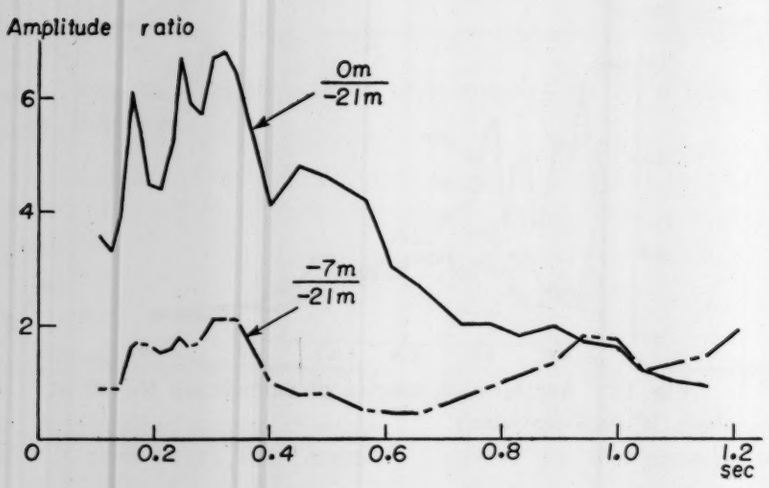

Fig. 94. Amplitude ratio corresponding to each period at place (B) in Tokai-mura. Earthquake number: 5.

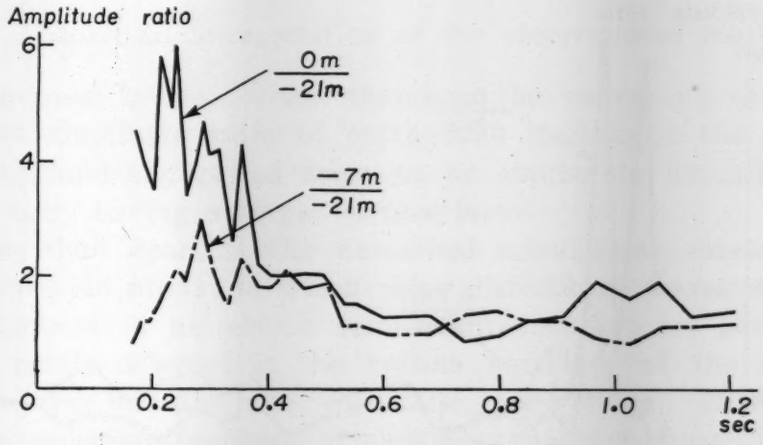

Fig. 95. Amplitude ratio corresponding to each period at place (B) in Tokai-mura. Earthquake number: 10.

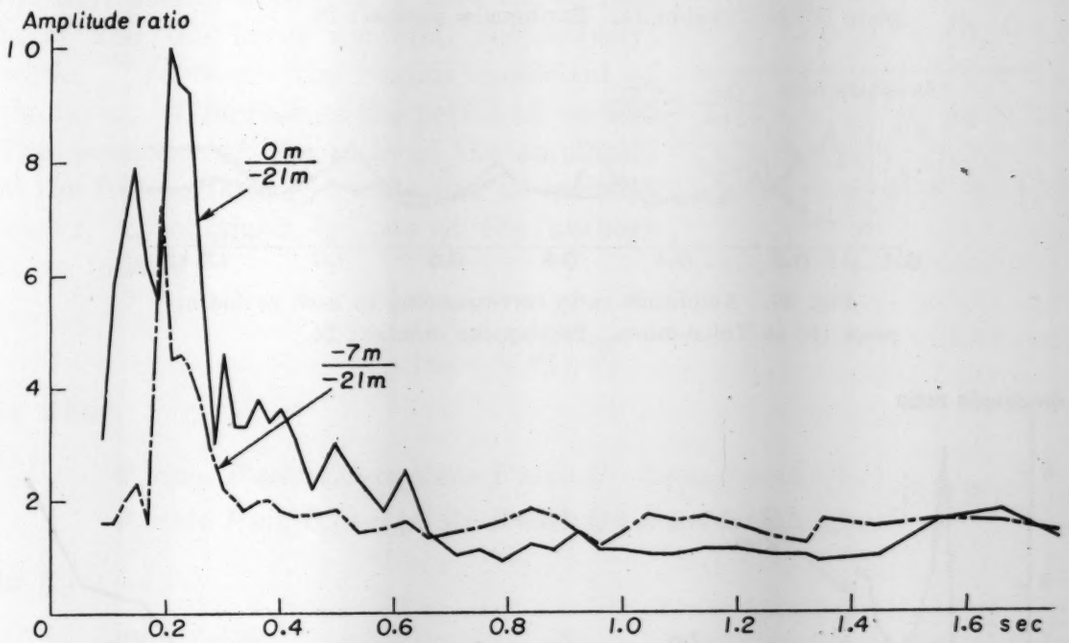

Fig. 96. Amplitude ratio corresponding to each period at place (B) in Tokai-mura. Earthquake number: 19.

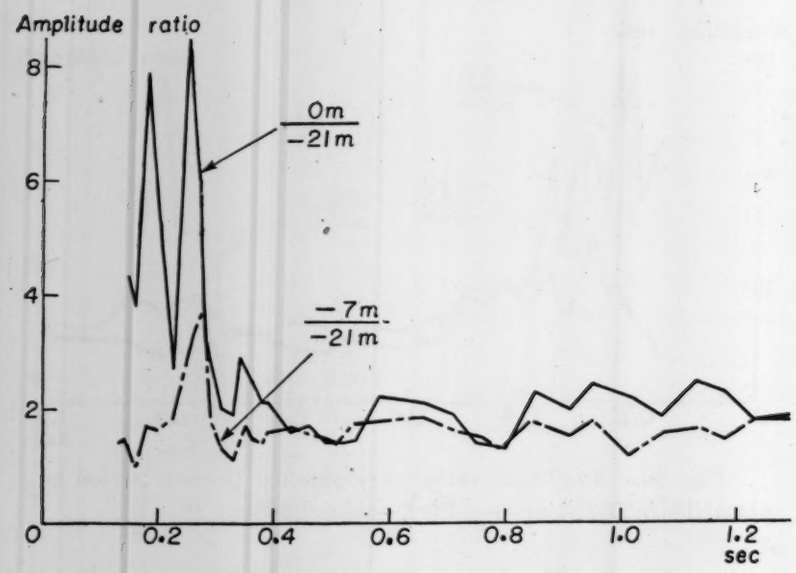

Fig. 97. Amplitude ratio corresponding to each period at place (B) in Tokai-mura. Earthquake number: 20.

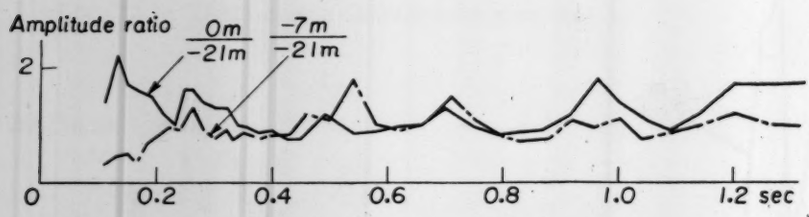

Fig. 98. Amplitude ratio corresponding to each period at place (B) in Tokai-mura. Earthquake number: 24.

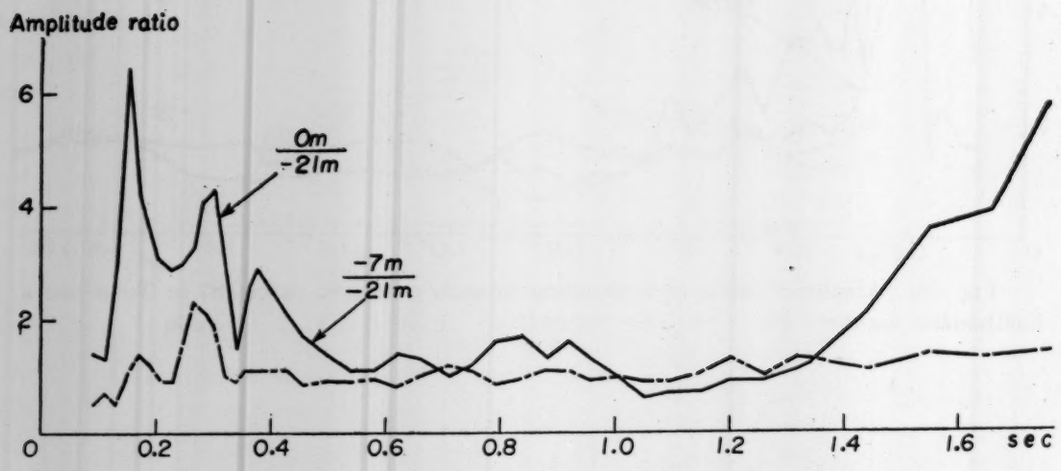

Fig. 99. Amplitude ratio corresponding to each period at place (B) in Tokai-mura. Earthquake number: 27.

4. Theoretical interpretation of the observational results

As mentioned in the former chapters, the curves of the relation between the amplitude ratio of earthquake motions on the ground to those underground and period seem to be similar to amplitude-period curve of a body having a single surface layer.

Here we shall examine the numerical calculations concerning the problem mentioned above, in which plane distortional waves propagated vertically upward in an elastic semi-infinite medium are partly transmitted and partly reflected at the bottom boundary of the superficial visco-elastic layer and are reflected at the free surface. This is one of the multiple reflection problems of elastic waves in a superficial layer.

Let the axis of z be drawn vertically downwards from the free surface of the layer of thickness H, and ρ_1, μ_1; ρ_2, μ_2 be density, elastic constants of both the surface layer and the lower medium, respectively, while, ξ_1 represent the viscous coefficient of the layer. T represents the period of waves. The equation of the ratio of the amplitude at the free surface, U, to the one of incident waves, u_0, obtained by one of the authors is as follows:[9]

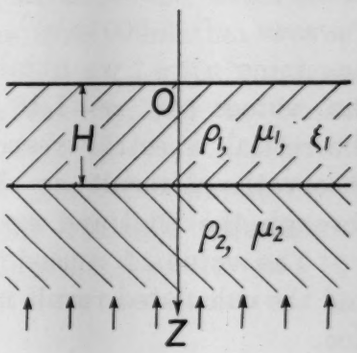

Fig. 100.

$$\frac{|U|}{|u_0|}=\frac{2}{\sqrt{\Phi_1^2+\Phi_2^2}} \tag{1}$$

in which

$$\left.\begin{aligned}\Phi_1&=\cos P\cosh Q+\alpha(R\cos P\sinh Q-S\sin P\cosh Q)\,,\\ \Phi_2&=\sin P\sinh Q+\alpha(R\sin P\cosh Q+S\cos P\sinh Q)\,,\end{aligned}\right\} \tag{2}$$

in (2)

$$\left.\begin{aligned}&P=\frac{\pi T_0}{2T}M\cos(N)\,, && Q=\frac{\pi T_0}{2T}M\sin(N)\,,\\ &R=M\left\{\cos(N)+\frac{\tau}{T}\sin(N)\right\}\,, && S=M\left\{\frac{\tau}{T}\cos(N)-\sin(N)\right\}\,,\\ &\alpha=\frac{v_1\rho_1}{v_2\rho_2}\,, && T_0=\frac{4H}{v_1}\end{aligned}\right\} \tag{3}$$

9) K. KANAI, *Bull. Earthq. Res. Inst.*, **28** (1950), 31–35.

in (3)

$$M=\left\{1+\left(\frac{\tau}{T}\right)^2\right\}^{-1/4}, \qquad N=\frac{1}{2}\tan^{-1}\left(\frac{\tau}{T}\right), \qquad \tau=\frac{2\pi\xi_1}{\mu_1} \qquad (4)$$

The average curves of the amplitude ratio of the ground surface to the underground at Hitachi Mine, and at places (A) and (B) in Tokai-mura are shown in Figs. 101, 102 and 103, respectively by full lines. Fig. 104 represents the amplitude ratio at two spots of different depth at place (B) in Tokai-mura.

(i) The case of Hitachi Mine.

Now, we adopt 132 m/s[10] as v_1 and the predominant period of the ground obtained from the frequency analysis of micro-tremor, 0.18 sec, as T_0. The value of $v_2=1730$ m/s is estimated from the velocity of P-waves of 3,000 m/s[11] and the assumption of Poisson's ratio=1/4. Assuming $\rho_1=\rho_2$, we obtain the value of $\alpha=1/13$ as ρ_1v_1/ρ_2v_2. Substituting the values of $\alpha=1/13$ and $T_0=0.18$ sec in equations (1)~(4), the theoretical spectral response curve, which coincides mostly with the observational result as shown in Fig. 101 by full line, can be obtained through the trial and error method by changing the value of τ.

The value of τ used finally is $\tau=0.034$, that is, $\xi_1/\mu_1=5.4\times10^{-3}\,\mathrm{sec}^{-1}$ and the calculated result mentioned above is shown in Fig. 101 by broken line.

(ii) The case of place (A) in Tokai-mura.

The predominant period of the ground obtained from the frequency analysis of micro-tremor, 0.27 sec, is adopted as T_0.

The value of $v_1=112$ m/s is estimated from the relations of $v_1=4H/T_0$ and $H=7.55$ m, which is thickness of the sand layer (see Fig. 33).

The value of $v_2=920$ m/s is estimated from the velocity of P-waves of 1,600 m/s[12] and the assumption of Poisson's ratio=1/4. Assuming $\rho_1=\rho_2$, we obtain the value of $\alpha=1/8.2$ as ρ_1v_1/ρ_2v_2.

Substituting the values of $\alpha=1/8.2$ and $T_0=0.27$ sec in equations (1)~(4) and carrying out the trial and error method, we obtained the theoretical spectral sesponse curve, which coincides mostly with the observational result as shown in Fig. 102 by a full line. (In this case, the numerator of equation (1) takes 1 without 2, because, the observation value at -21 m is considered twice of the value of the incident waves.) The value of τ used finally is $\tau=0.020$, that is, $\xi_1/\mu_1=3.2\times10^{-3}\,\mathrm{sec}^{-1}$ and

10) K. KANAI, T. TANAKA and T. SUZUKI, *Bull. Earthq. Res. Inst.*, **36** (1958), 215.
11) K. KANAI, *Bull. Earthq. Res. Inst.*, **29** (1951), 506, Fig. 4.
12) S. OMOTE, *Monthly Meeting of the Earthquake Research Institute*, (Feb. 1957).

the calculated result mentioned above is shown in Fig. 102 by broken line.

(iii) The case of place (B) in Tokai-mura.

In this case, the predominant period of the ground obtained from the frequency analysis of micro-tremor, 0.24 sec, is adopted as T_0. The value of $v_1=117$ m/s is estimated from the relations of $v_1=4H/T_0$ and $H=7$ m, which is thickness of the sand layer (see Fig. 33). The value of $v_2=920$ m/s is the same as the case of place (A). Assuming $\rho_1=\rho_2$, we obtain the value of $\alpha=1/7.9$ as $\rho_1 v_1/\rho_2 v_2$.

Substituting the values of $\alpha=1/7.9$ and $T_0=0.24$ sec in equations (1)~(4) and using the trial and error method, too, we obtained the theoretical spectral response curve, which is coincident mostly with the observational result as shown in Fig. 103 by full line. (In this case, the numerator of equation (1) takes 1 without 2, because the observation value at -21 m is considered twice of the value of the incident waves.) The value of τ used finally is $\tau=0.017$, that is, $\xi_1/\mu_1=2.7\times10^{-3}$ sec^{-1} and the calculated result mentioned above is shown in Fig. 103 by broken line.

Figs. 101~103 tell us a noteworthy result that the amplitude on the ground grows very large depending on the multiple reflection of seismic waves in the superficial layer, as the values of $\xi_1/\mu_1=(3\sim5)\times10^{-3}$

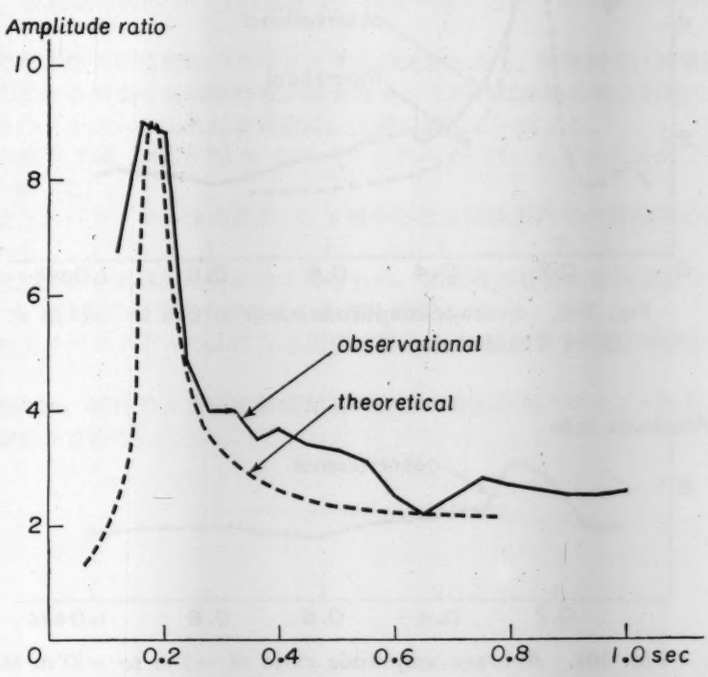

Fig. 101. Average amplitude ratio of 0 m to -300 m at Hitachi Mine.

sec^{-1} are plausible and the observational and calculated results coincide considerably well with each other.

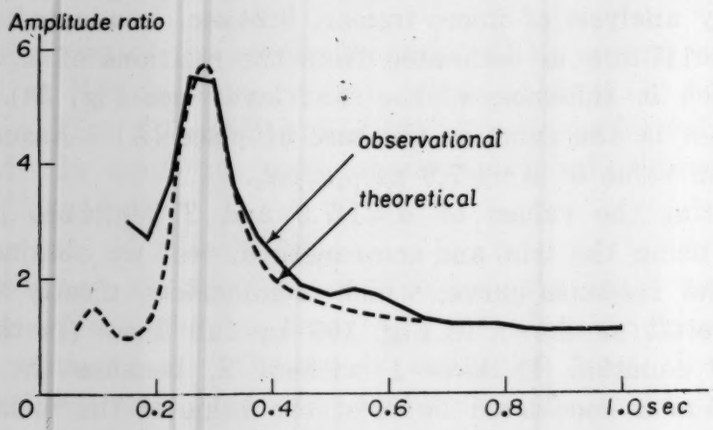

Fig. 102. Average amplitude ratio of 0 m to −21 m at place (A) in Tokai-mura.

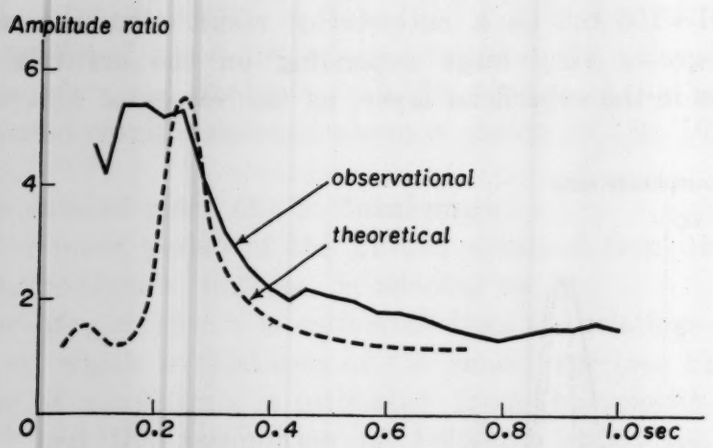

Fig. 103. Average amplitude ratio of 0 m to −21 m at place (B) in Tokai-mura.

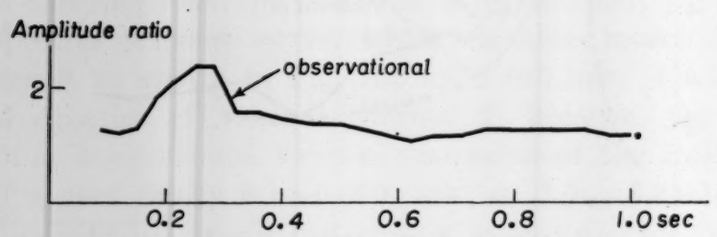

Fig. 104. Average amplitude ratio of −7 m to −21 m at place (B) in Tokai-mura.

5. Acknowledgement

In conclusion, we wish to express our thanks to Motoyama-office, Hitachi Mine and Japan Atomic Power Research Institute for their co-operation in the course of these investigations, and also to Messrs. T. Suzuki and K. Osada without whose help this work could not be done.

---

5. 地下における地震動の研究
(重複反射の問題)

地震研究所 { 金井 清 / 田中貞二 / 吉沢静代 }

この研究は，茨城県日立鉱山の地上と地下 300 m，茨城県東海村（日本原子力研究所構内）の地上と地下 21 m (場所 (A))，地上と地下 7 m，21 m (場所 (B)) の 3 組の地震動比較観測を行い，その記録をレスポンス，コンピューターによつて周期解析したものである．次に，この研究でわかつたことを列挙する．

（1） 地下深所における地震動の変位スペクトラムには山があり，その山になる周期は地震が大きいほど長くなる．

（2） 変位スペクトムラの極大になる周期よりも長い周期のものと，0.1 秒位よりも短い周期のものとをのぞくと，各周期の波についての速度は，ほぼ一定である．即ち勢力の等分配の法則が大体成り立つ．

（3） 地下に対する地上の地震動のスペクトラムの比をとると，或周期で，非常にはつきりした山ができる．その山になる周期は各場所特有の値となり，この値は地盤の固有周期に相当する．

（4） 加速度スペクトラムの山になる周期は，上述の周期と一致する．

（5） 東海村の地下 7 m と地下 21 m のスペクトラム比には，わずかな山ができ，この山の周期は前述の周期と一致する．

（6） 地下対地上スペクトラム比の曲線は，1 層からなる地表層内での弾性波の重複反射現象で，相当よく説明される．

（7） 上述の数理計算を実測値に合わせて得られた，表面層の物質の粘性係数 ξ と剛性率 μ の比は $\xi/\mu=0.02\ \mathrm{sec}^{-1}$ で，他の研究から求められた値と矛盾しない．

（8） 地下対地上スペクトラムの山になる周期は地上における常時微動の頻度の山になる周期とよく合う．

（9） この観測には，新作の，自動水準式地震計並びに地震計用スターターを使つたが，これらの計器は所期の成績をおさめた．

BULLETIN OF THE EARTHQUAKE
RESEARCH INSTITUTE
Vol. 37 (1959), pp. 89-121

6. *Observations of Seismic Waves from Four Explosions near the Kamaisi Mine.*

By The Research Group for Explosion Seismology.

(Read Dec. 23, 1958.—Received Dec. 27, 1958.)

1. Data of observations.

As stated in other papers,[1] the boundary between a layer with *P*-wave velocity 5.75～5.85 km/sec and one with 6.10～6.20 km/sec on the west side of the Kamaisi mine was calculated to have a probable dip 6°～11° rising eastward. In order to determine more precisely its position and the form near its shallowest point, we set off four explosions as in Table 1.

Table 1.

Shot Point	Latitude	Longitude	Height	Shot time	Amount of charge
A Dôsen	39°14′24.8″	141°46′ 0.6″	380m	1954, May 1, 1h35m00.28 s	0.1ton.
B Sin'yama	17 36.7	41 31.6	360	3 35 00.513	1.0
C Daidô	14 32.5	41 23.9	530	3, 1 35 00.170	0.1
D Takinosawa	15 54.1	54 55.2	2	3 35 00.513	1.0

All four explosions were observed at stations and by observers common to all of them. Positions of shot points and observation stations are as shown in Fig. 1, and tabulated in Table 2, with additional data of instruments.

Examples of seismograms are shown in Fig. 2～17.

The positions were determined by the method of aerial photography and the plane table survey. The maximum error of the horizontal distance is about 10 m and that of the height is 2 m. The accuracy of the relative time is within the limit of 1/100 sec.

Results of measurements are shown in Table 3.

Travel times for each shot are shown respectively in Fig. 18, Fig. 19, Fig. 20, and Fig. 21.

1) Research Group for Explosion Seismology, *Pub. Bureau Central Séismologique International. Série A. Travaux Scientifiques*, **19** (1954) 229-242; T. Matuzawa, *Bull. Earthq. Res. Inst.*, **37** (1959).

Table 2.

Observation point	Location			Electro-magnetic Seismometer	Observers
	Latitude	Longitude	Height		
1. SIN'YAMA a	39°17′32.9″	141°41′35.7″	350 m	3 c/s Vertical-4	Omote, Kobayashi, Saito
b	18.5	42 9.5	350		
c	3.7	41.6	350		
d	16 54.5	43 3.7	302		
2. ÔHASI a	16 28.0	43 24.0	230	3 c/s Vertical-1	Mikumo, Otsuka, Tanaka
b			255	2 c/s Hor.-2	
3. ÔMATU a	15 15.9	44 21.8	190	3 c/s Vertical-5	Mine, Ishigaki, Shima
b	8.4	44.9	180		
c	13.8	44.6	175		
4. DÔSEN a	14 49.0	46 10.8	102	3 c/s Vertical-3	Suzuki, Den, Haseba
b	42.5	6.5	120		
c	47.3	19.5	118		
d	47.7	37.1	122		
e			102		
5. MATUKURA	15 13.0	48 3.7	60	3 c/s Vertical-1	Shima, Shibano
6. NODA a	15 23.6	49 17.4	70	3 c/s Vertical-3	Asano, Yanagisawa
b	22.9	17.4	45		
7. KOSANO a	15 45.5	50 22.4	35	2 c/s Hor.-3	Okano, Morimoto
b	46.2	29.3	34		
8. NAKATUMA	16 16.7	51 33.4	26	3 c/s V-2, 3c/s H-1	Matumoto, Karakama
9. TAKINOSAWA a			2	3 c/s Vertical-3	Murauchi, Honda, Asanuma
b			2		
c	16 0.8	54 49.2	2		
d			2		
e			4		

(to be continued)

(continued)

10. KAMAISI-KÔ	a	15 55.2	53 34.2	−4	Morishita
	b			−4	
11. URESI		15 35.7	53 35.2	7	3 c/s V-1, 10 c/s H-1	Kasahara, Sato
12. TÔNI		12 23.9	53 36.4	5	3 c/s V-1, 3 c/s H-1	Noritomi, Takagi
13. OKIRAI		6 51.8	49 5.1	19	3 c/s Vertical-4	Tazime, Akamatu, Oguchi, Ueda
14. HIKOROITI	a	7 24.3	40 41.4	82	3 c/s Vertical-3	Utsu, Usami
	b	26.9	37.4	82		
	c	26.9	37.4	82		
15. DAIDÔ	a	14 35.1	41 42.6	520	3 c/s Vertical-1 30 c/s Vertical-3	Furuya Ogawa Suyehiro
	b	29.5	23.6	520		
	c	23.9	10.5	520		
	d	23.6	10.0	520		
16. ASIGASE	a	15 35.2	39 45.9	512	P-11	Yamazaki, Kobayashi, Daikubara
	b			508		
	c			505		
	d			504		
	e			503		
	f			501		
	g			500		
	h			500		
	i			501		
	j			501		
	k			502		
	l			502		
17. TÔNO		18 9.6	32 21.0	303	3 c/s V-1, 3 c/s H-1	Hori, Tsujiura

Different pick-up positions belonging to one observation point are made out by symbols a, b, c, ...

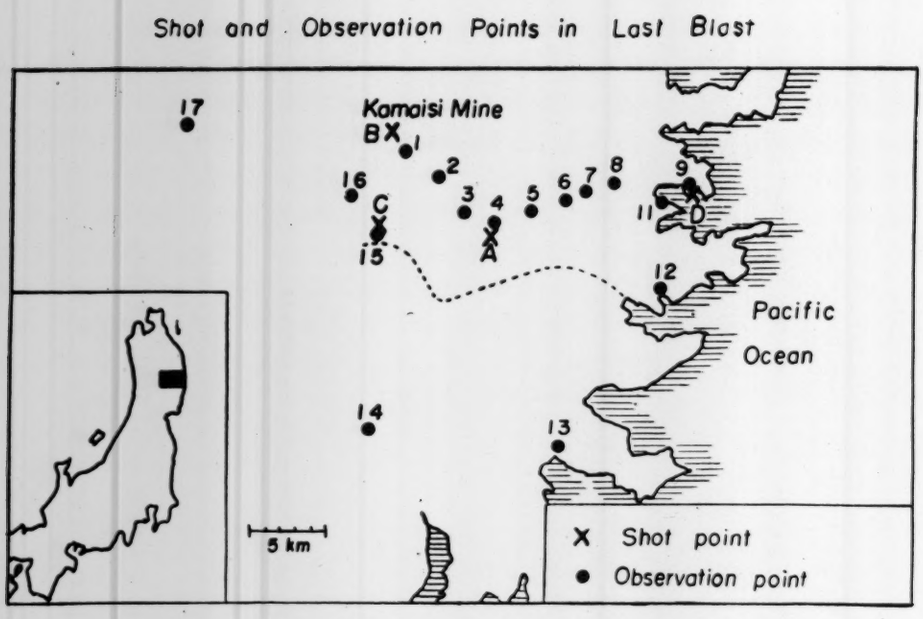

Fig. 1.

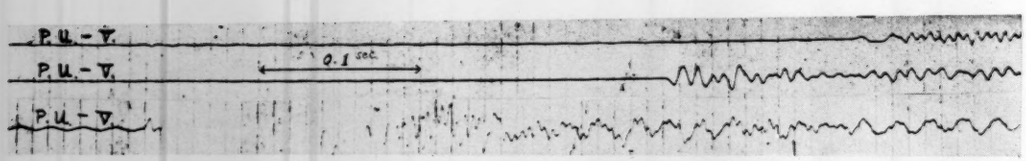

Fig. 2. Seismogram at Sin'yama for shot B.

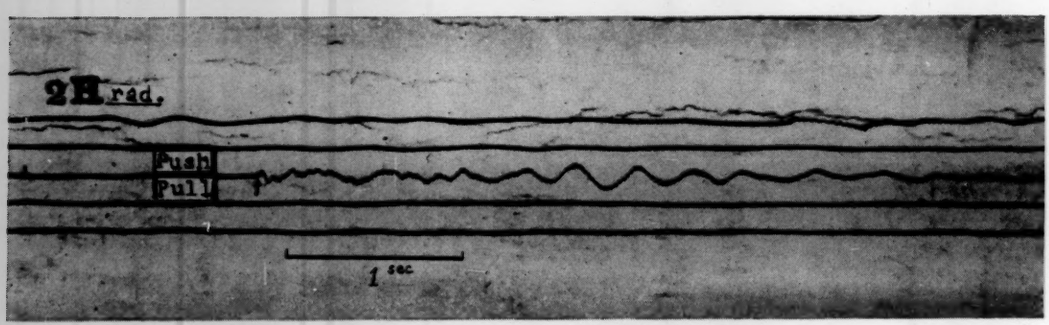

Fig. 3 (1). Seismogram at Ôhasi for shot A.

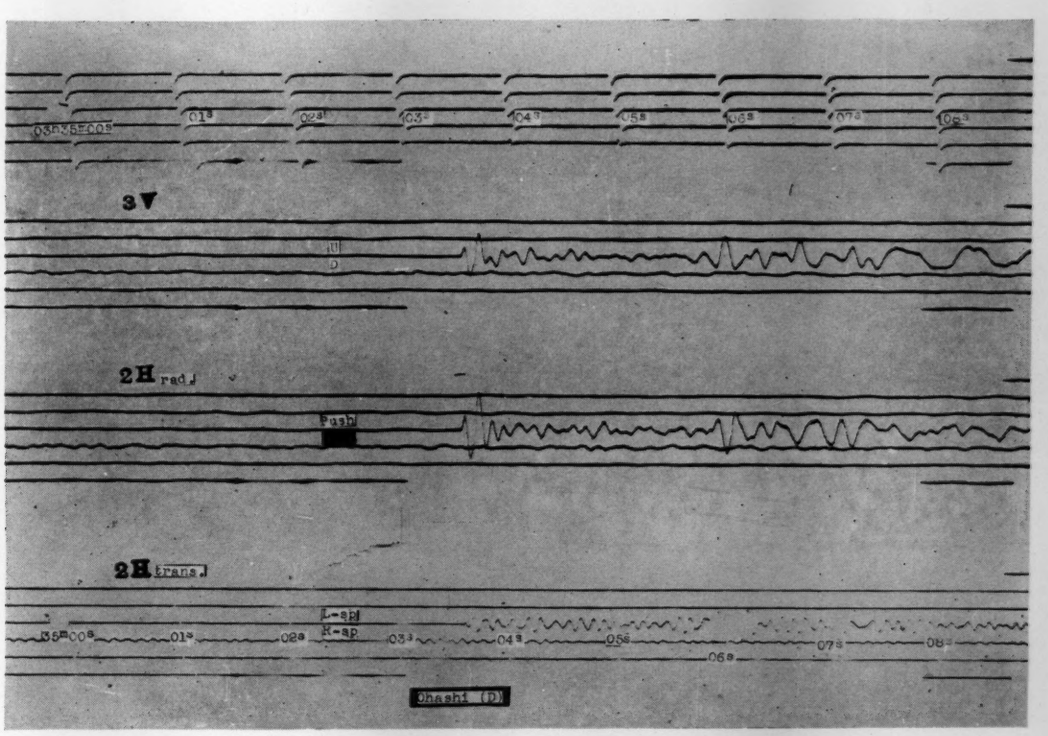

Fig. 3 (2). Seismogram at Ôhasi for shot D.

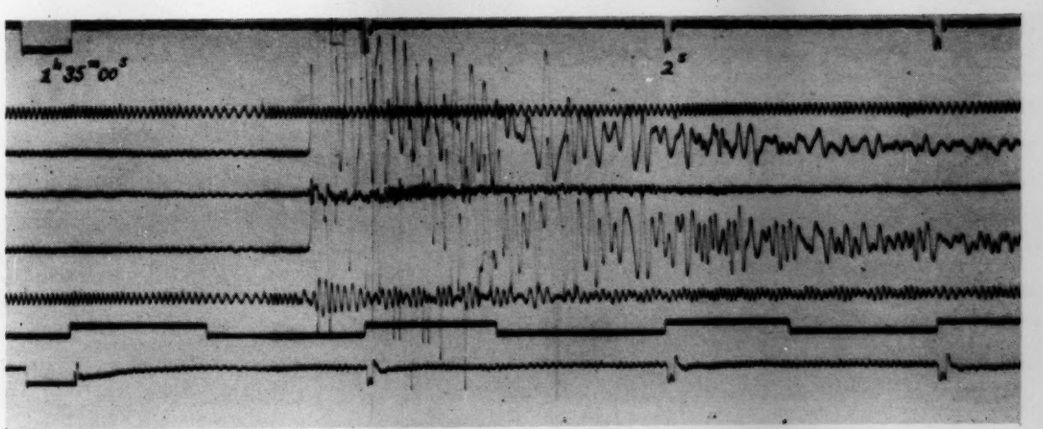

Fig. 4 (1). Seismogram at Ômatu for shot A.

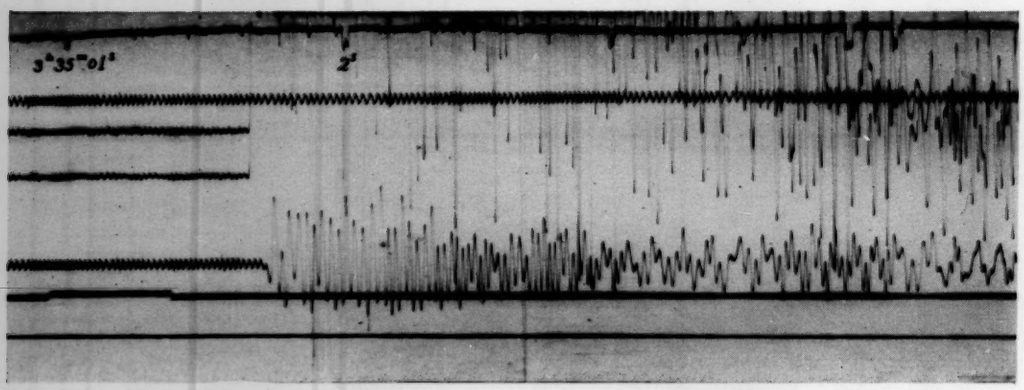

Fig. 4 (2). Seismogram at Ômatu for shot B.

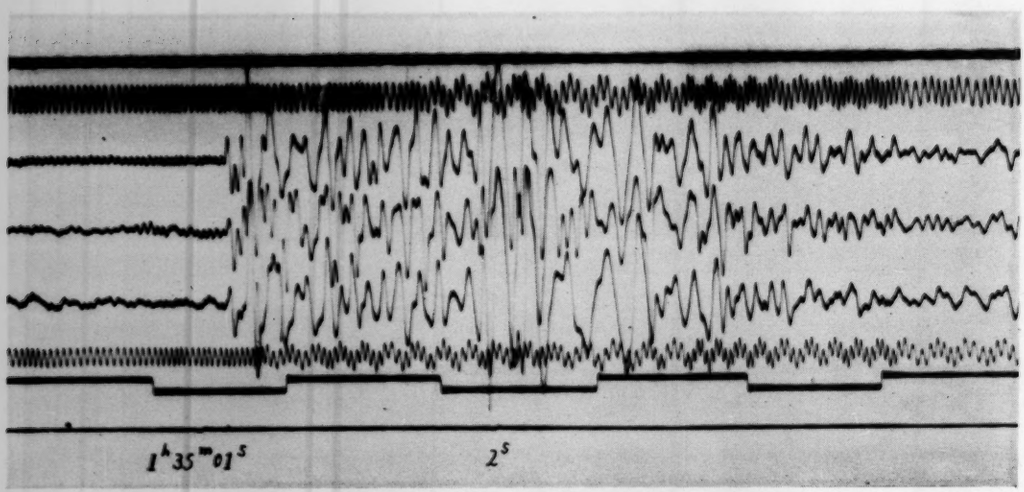

Fig. 4 (3). Seismogram at Ômatu for shot C.

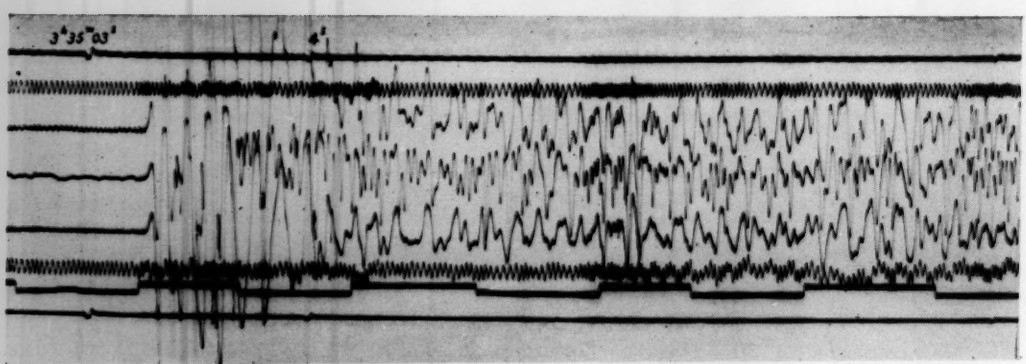

Fig. 4 (4). Seismogram at Ômatu for shot D.

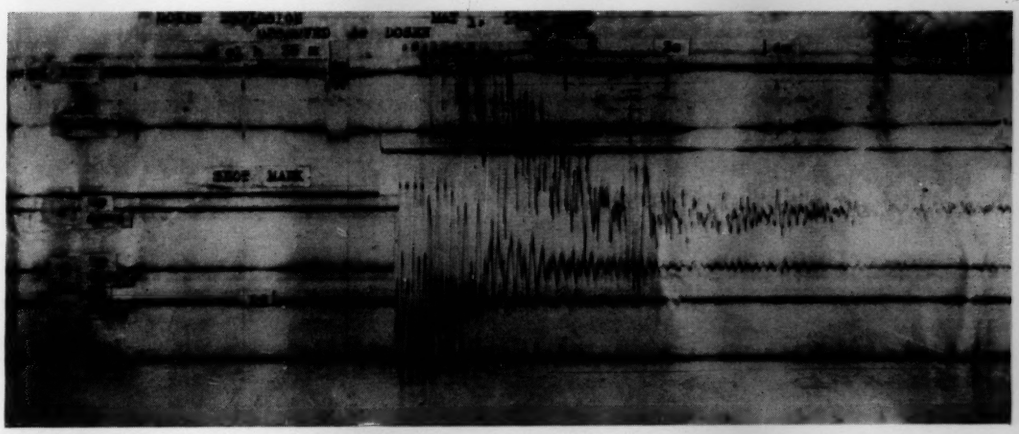

Fig. 5 (1). Seismogram at Dôsen for shot A.

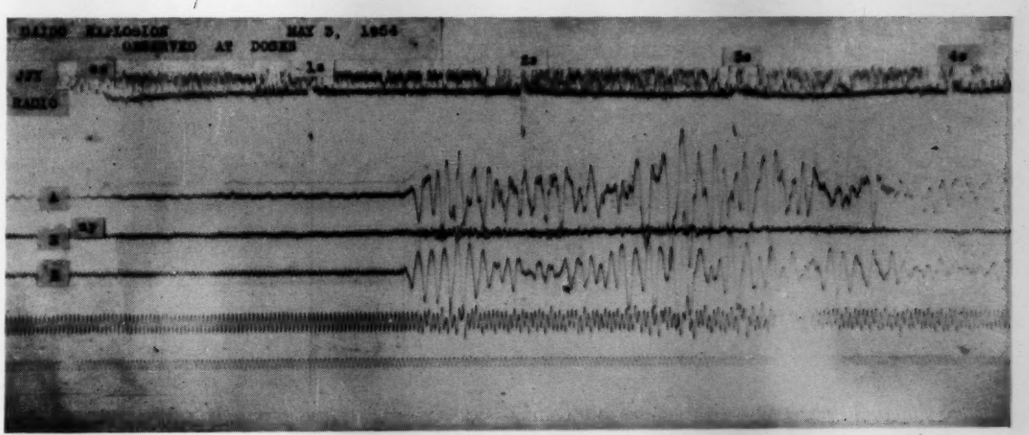

Fig. 5 (2). Seismogram at Dôsen for shot C.

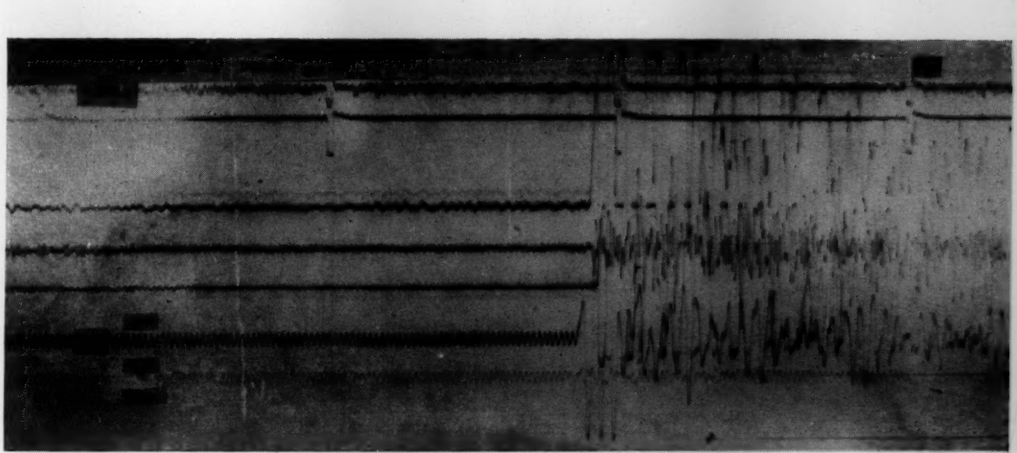

Fig. 5 (3). Seismogram at Dôsen for shot D.

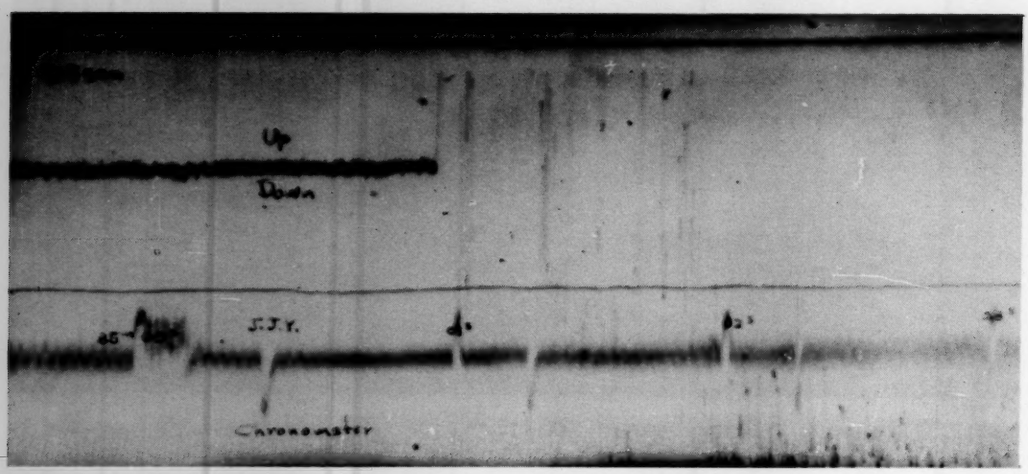

Fig. 6. Seismogram at Matukura for shot A.

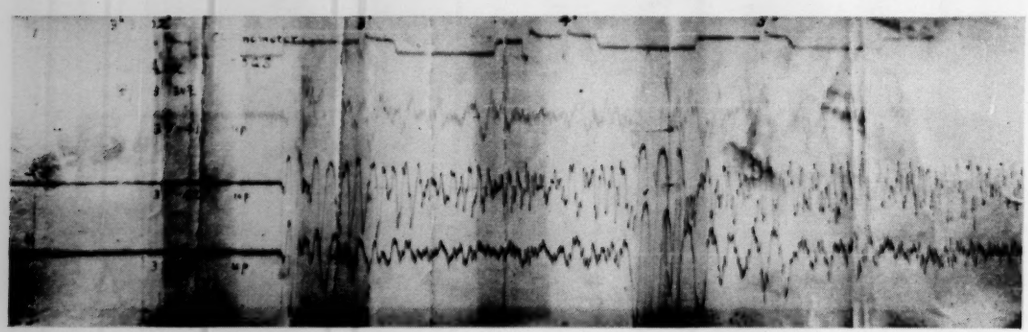

Fig. 7 (1). Seismogram at Noda for shot B.

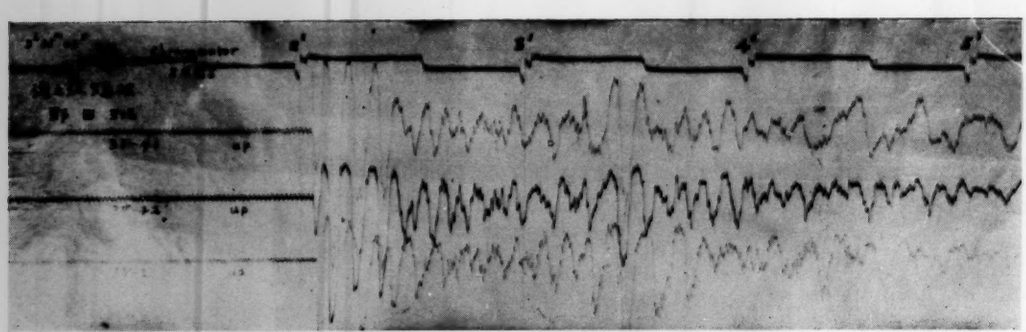

Fig. 7 (2). Seismogram at Noda for shot D.

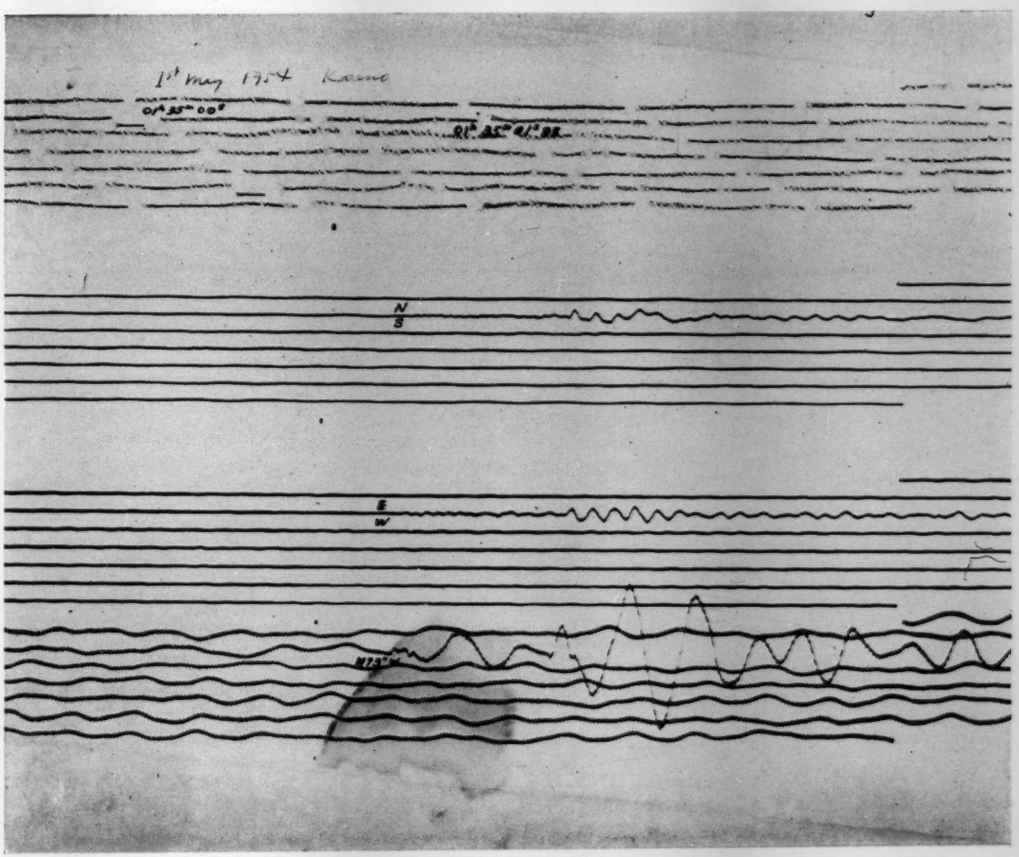

Fig. 8 (1). Seismogram at Kosano for shot A.

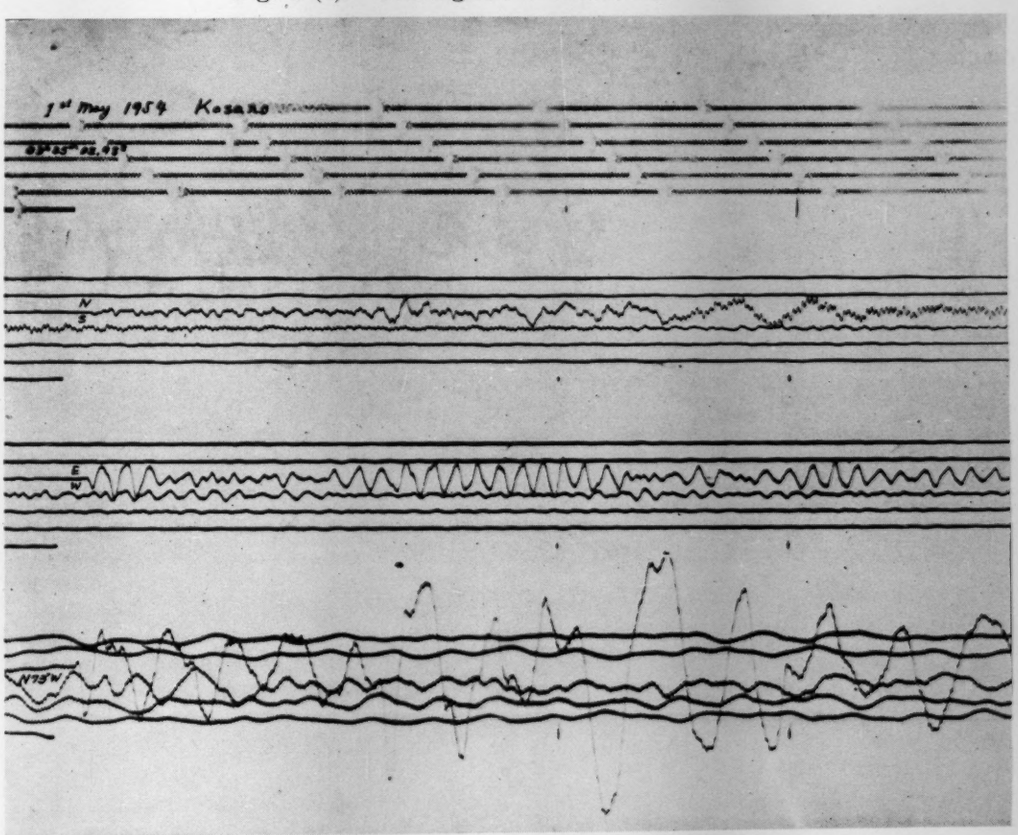

Fig. 8 (2). Seismogram at Kosano for shot B.

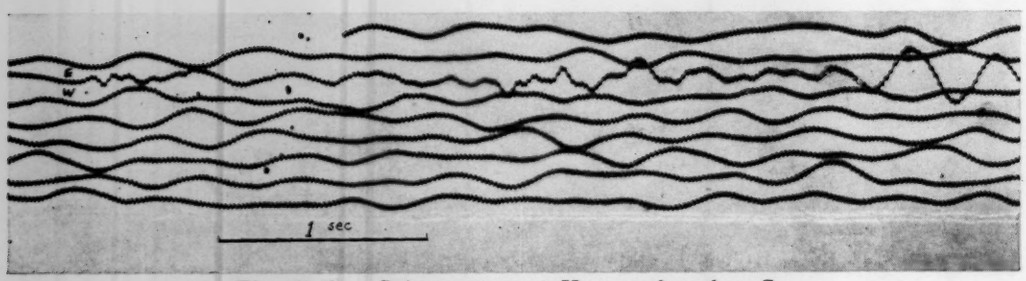

Fig. 8 (3). Seismogram at Kosano for shot C.

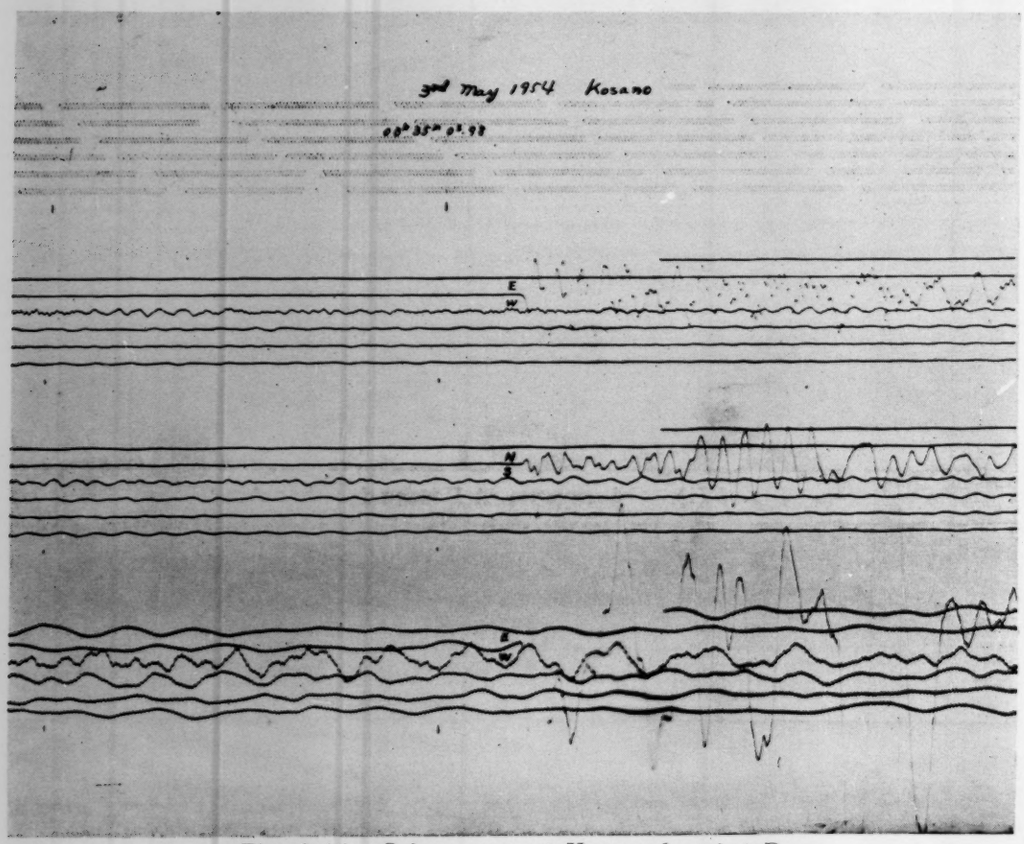

Fig. 8 (4). Seismogram at Kosano for shot D.

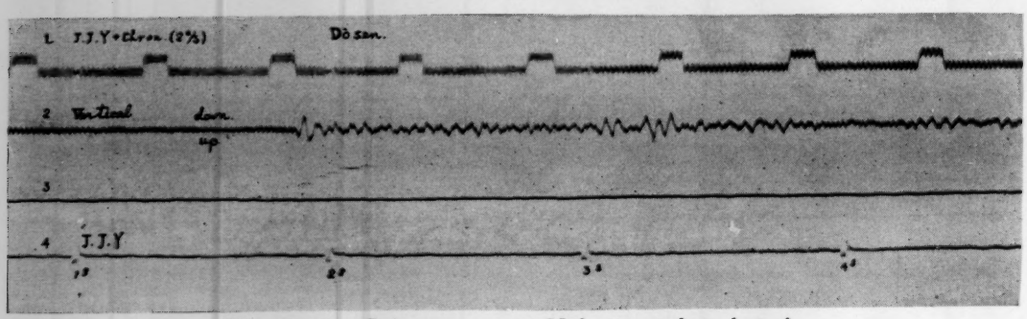

Fig. 9 (1). Seismogram at Nakatuma for shot A.

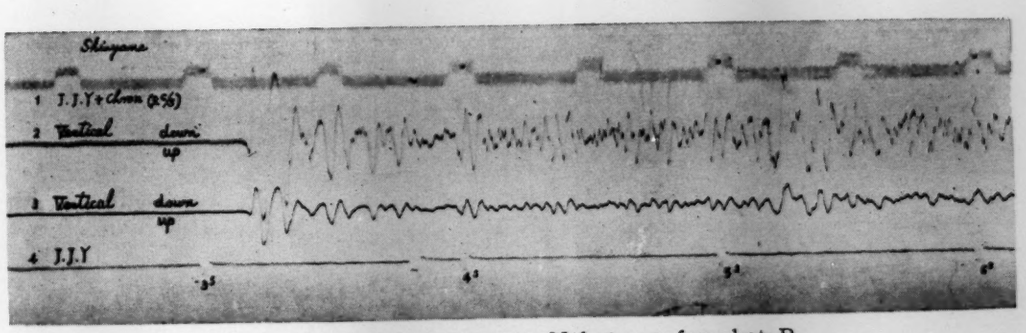

Fig. 9 (2). Seismogram at Nakatuma for shot B.

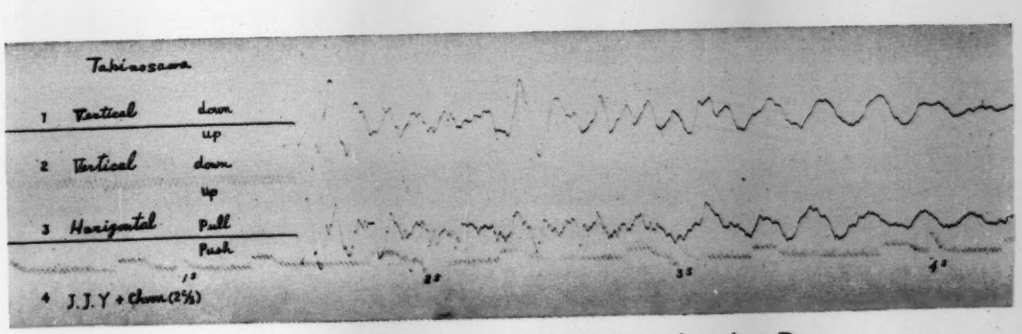

Fig. 9 (3). Seismogram at Nakatuma for shot D.

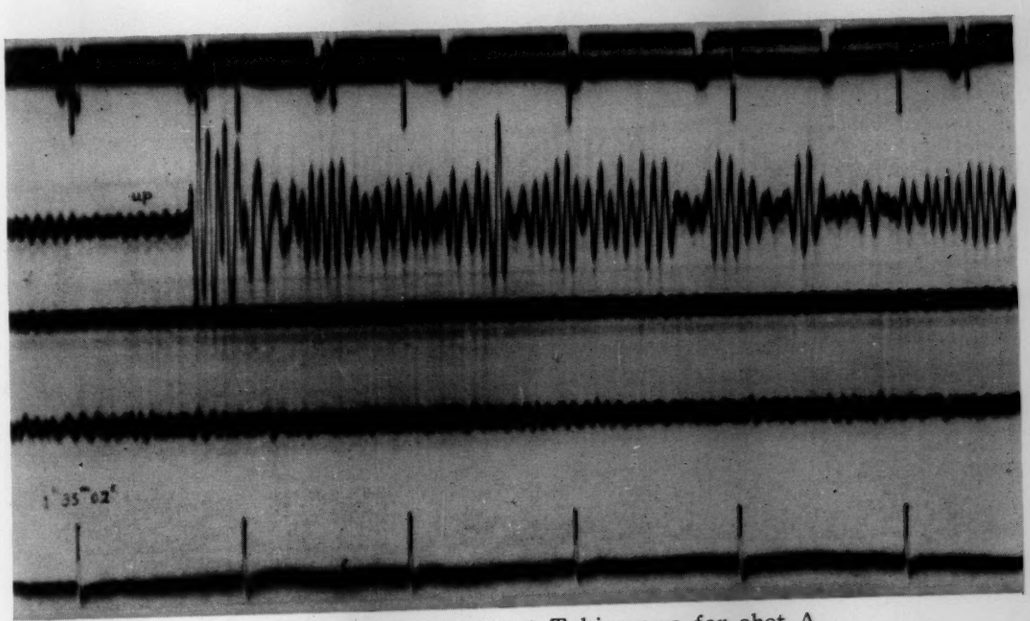

Fig. 10 (1). Seismogram at Takinosawa for shot A.

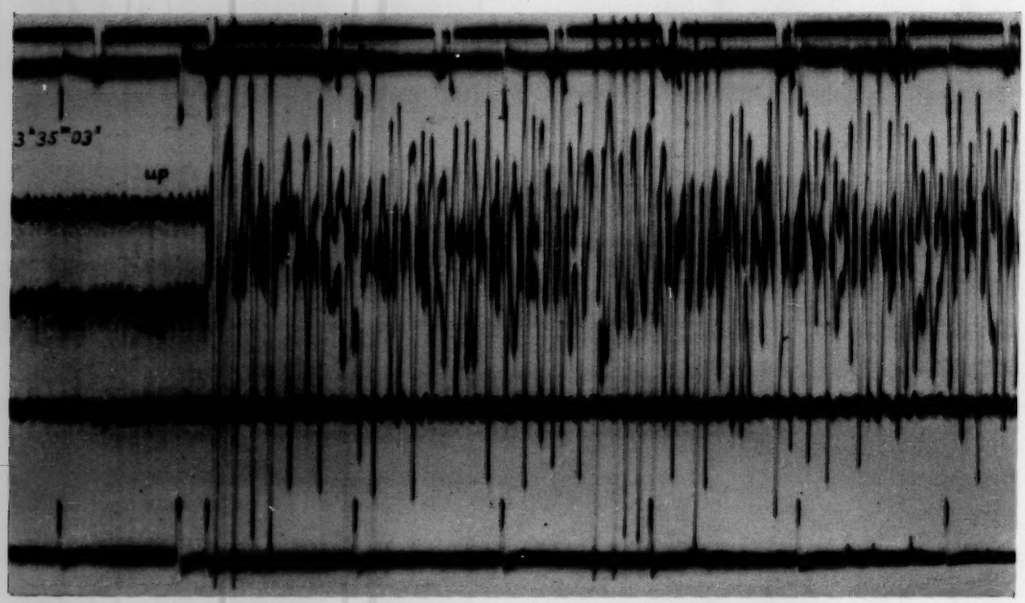

Fig. 10 (2). Seismogram at Takinosawa for shot B.

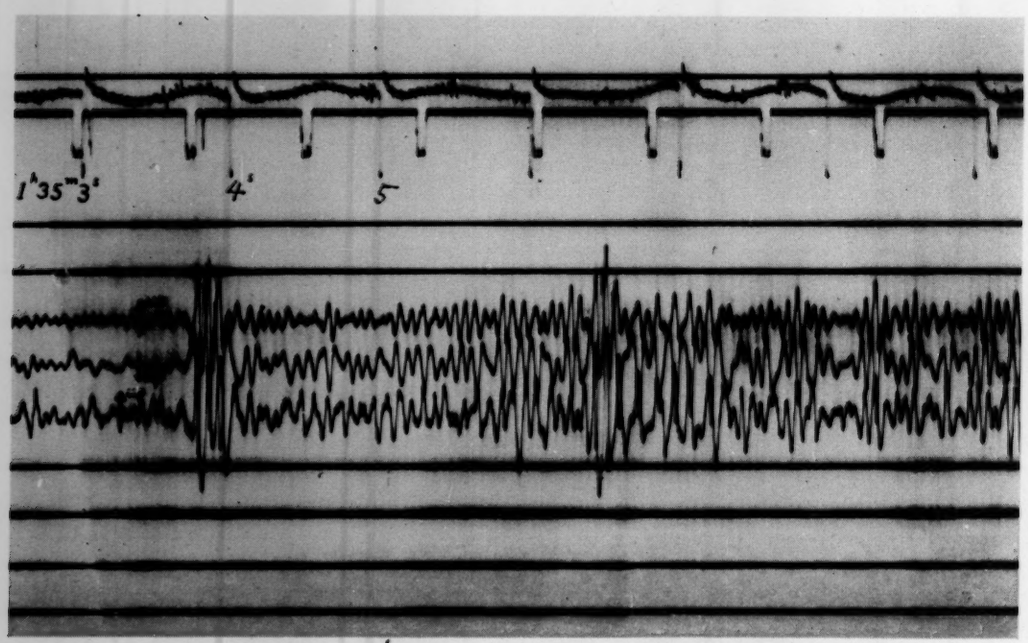

Fig. 10 (3). Seismogram at Takinosawa for shot C.

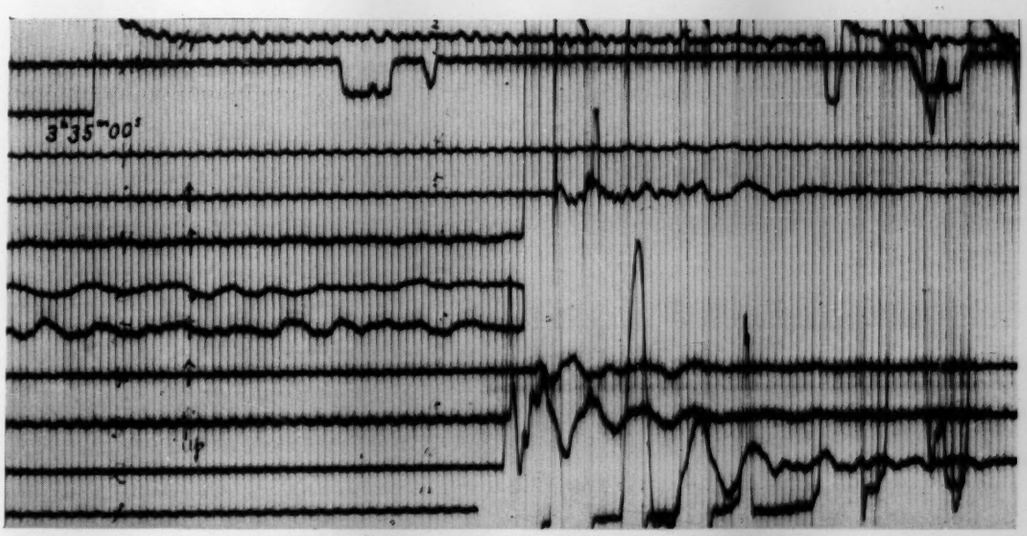

Fig. 10 (4). Seismogram at Takinosawa for shot D.

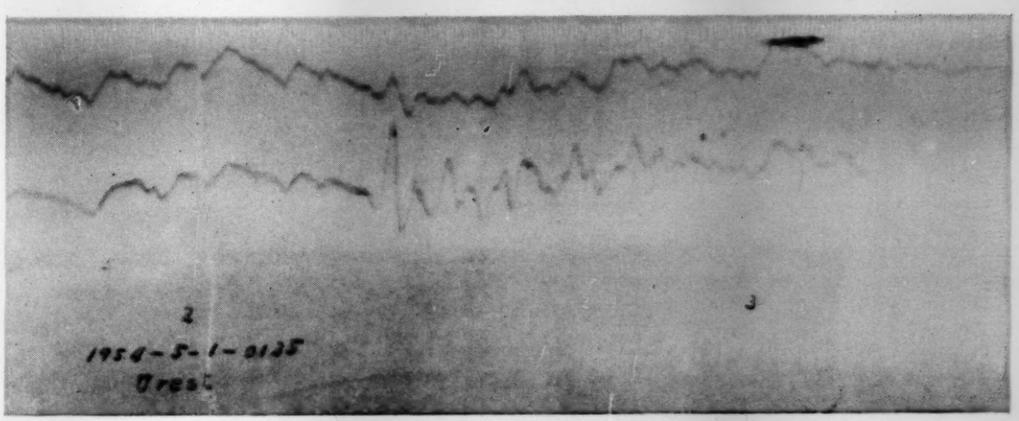

Fig. 11 (1). Seismogram at Uresi for shot A.

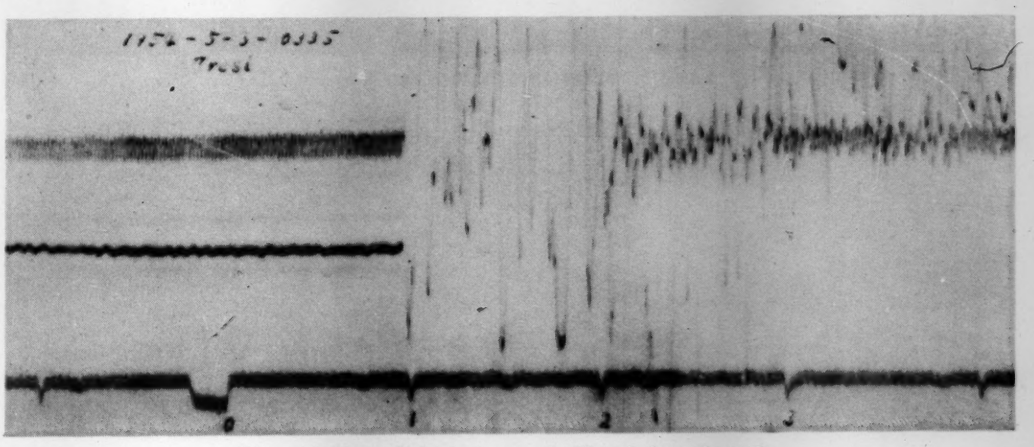

Fig. 11 (2). Seismogram at Uresi for shot D.

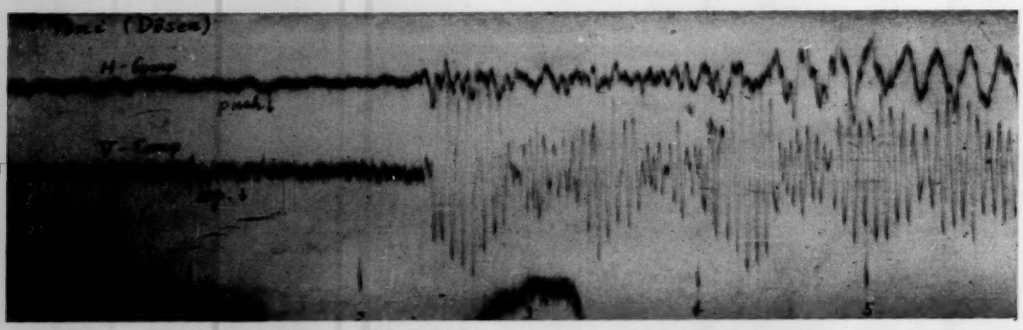

Fig. 12 (1). Seismogram at Tôni for shot A.

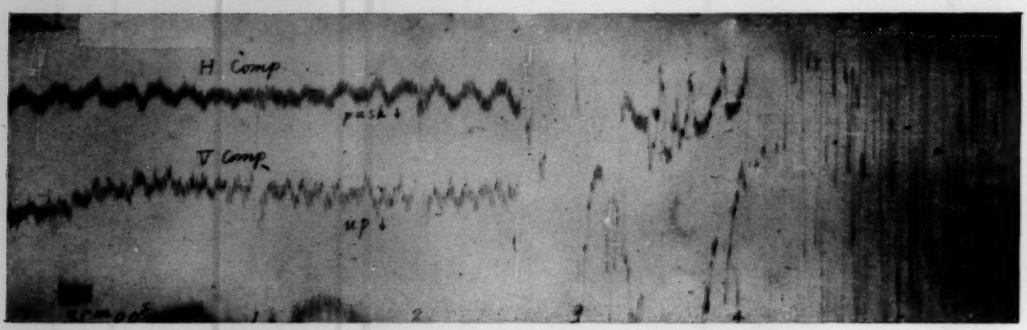

Fig. 12 (2). Seismogram at Tôni for shot B.

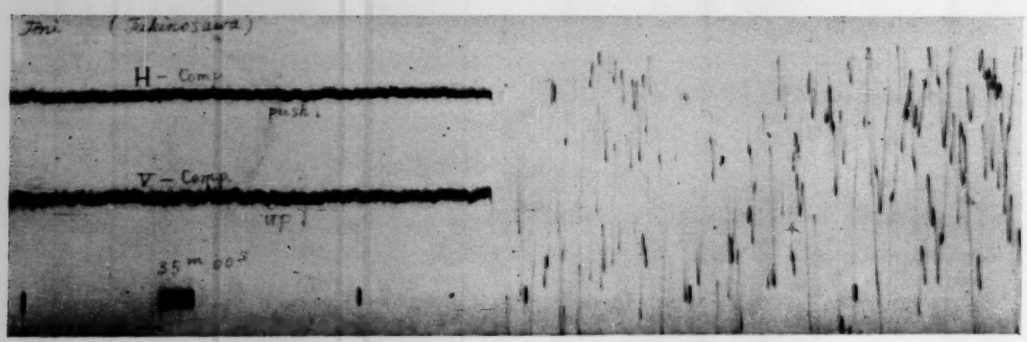

Fig. 12 (3). Seismogram at Tôni for shot D.

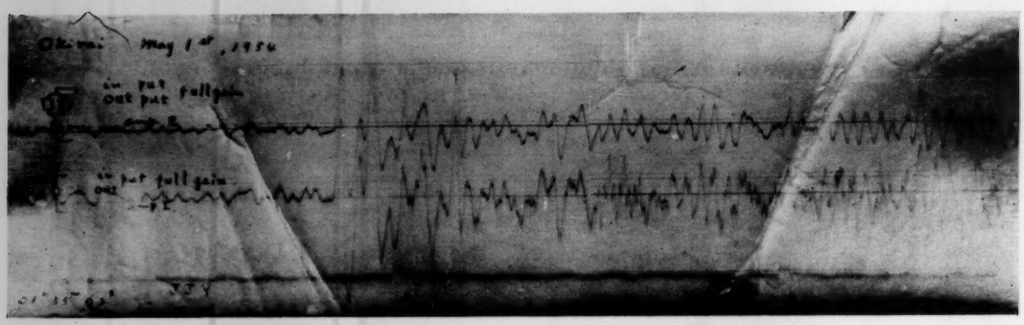

Fig. 13 (1). Seismogram at Okirai for shot A.

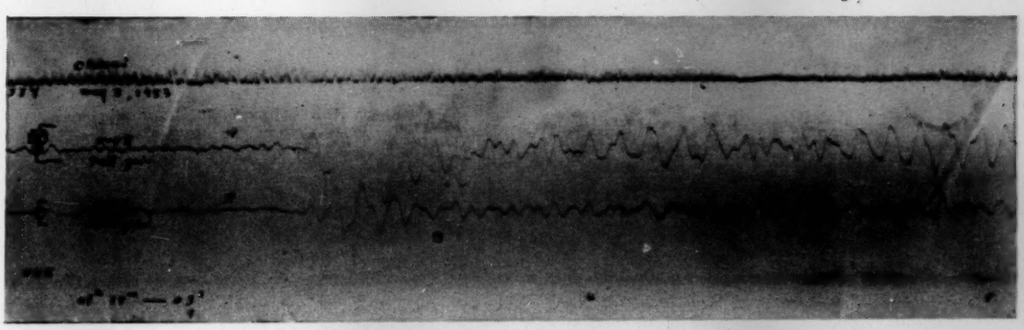

Fig. 13 (2). Seismogram at Okirai for shot C.

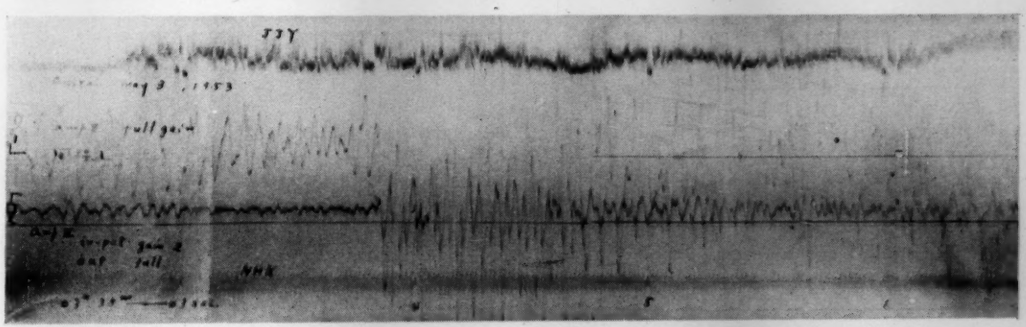

Fig. 13 (3). Seismogram at Okirai for shot D.

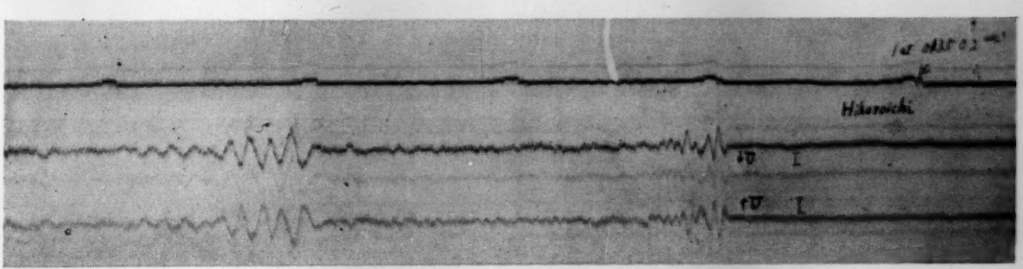

Fig. 14 (1). Seismogram at Hikoroiti for shot A.

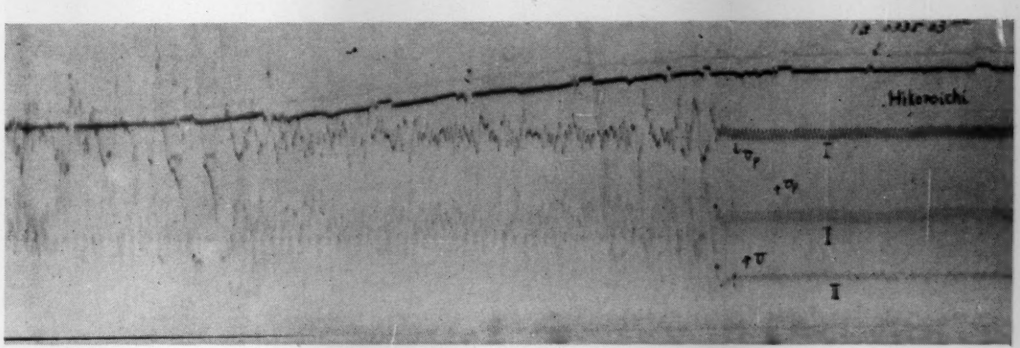

Fig. 14 (2). Seismogram at Hikoroiti for shot B.

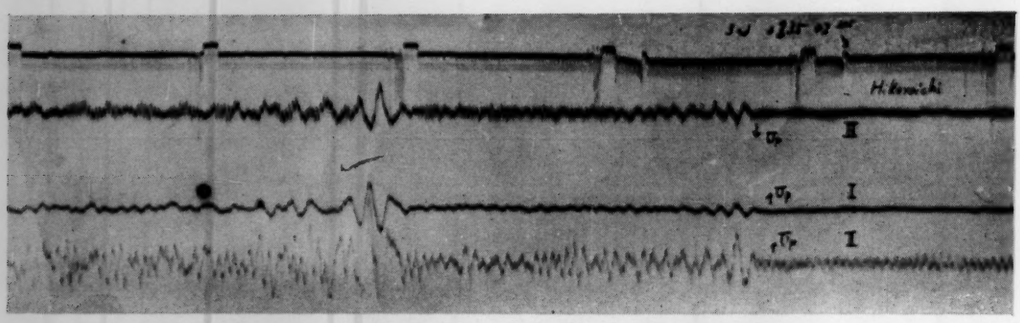

Fig. 14 (3). Seismogram at Hikoroiti for shot C.

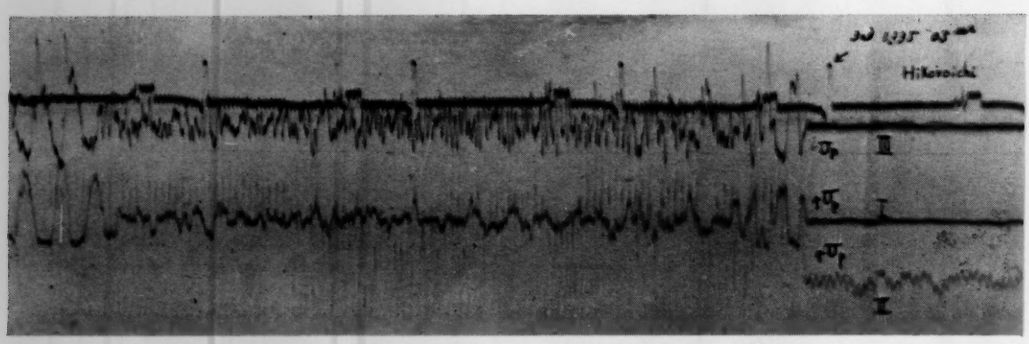

Fig. 14 (4). Seismogram at Hikoroiti for shot D.

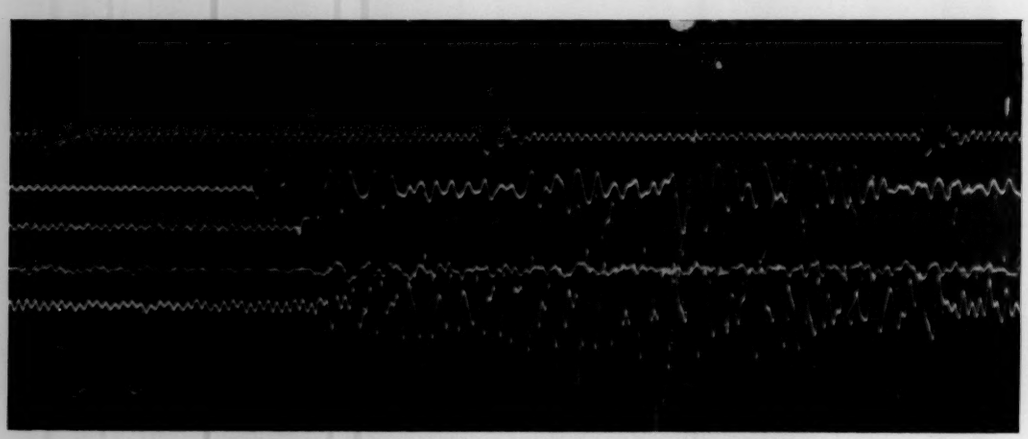

Fig. 15 (1). Seismogram at Daidô for shot A.

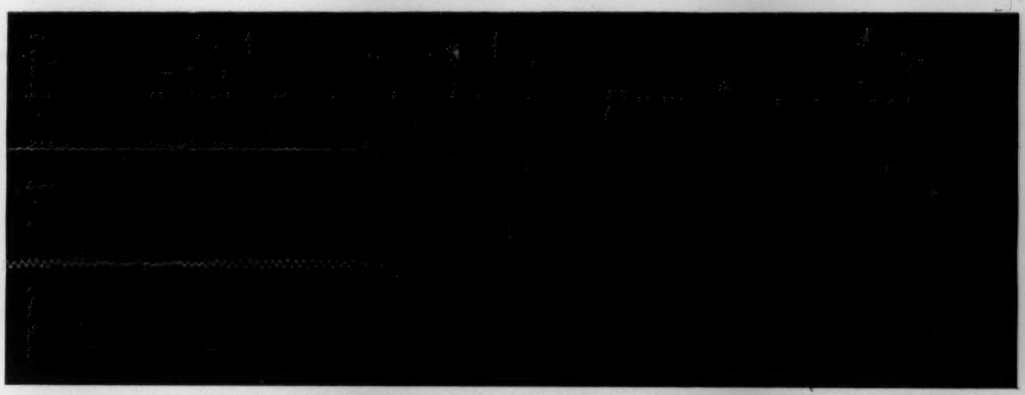

Fig. 15 (2). Seismogram at Daidô for shot B.

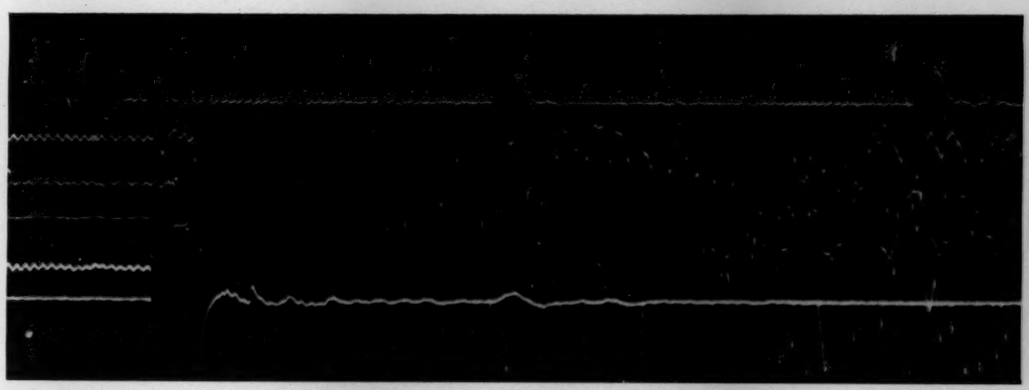

Fig. 15 (3). Seismogram at Daidô for shot C.

Fig. 15 (4). Seismogram at Daidô for shot D.

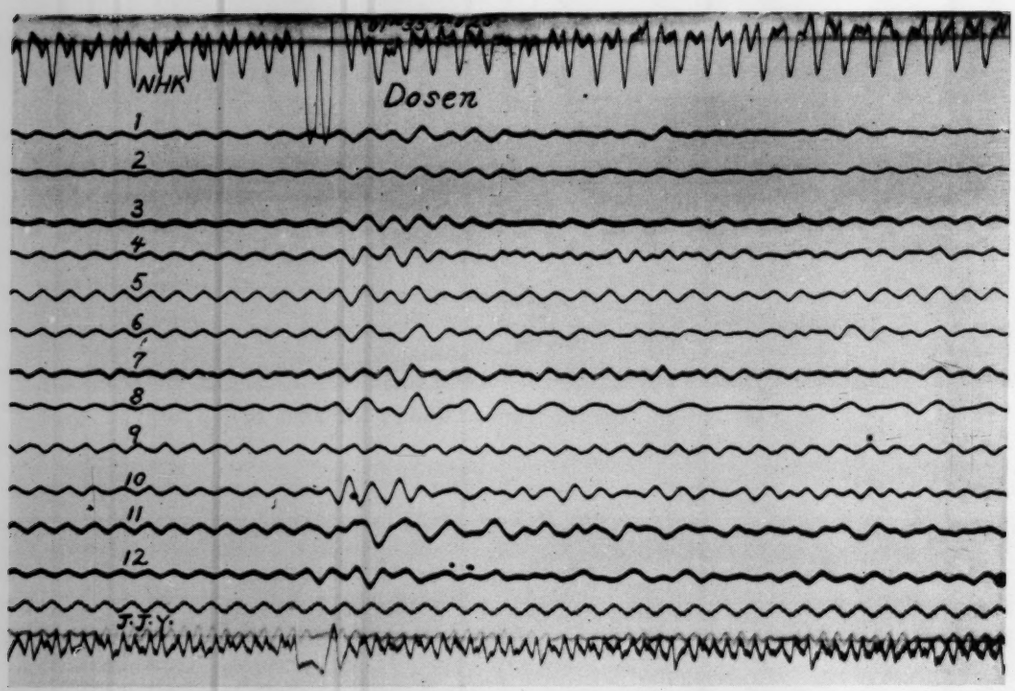

Fig. 16 (1). Seismogram at Asigase for shot A.

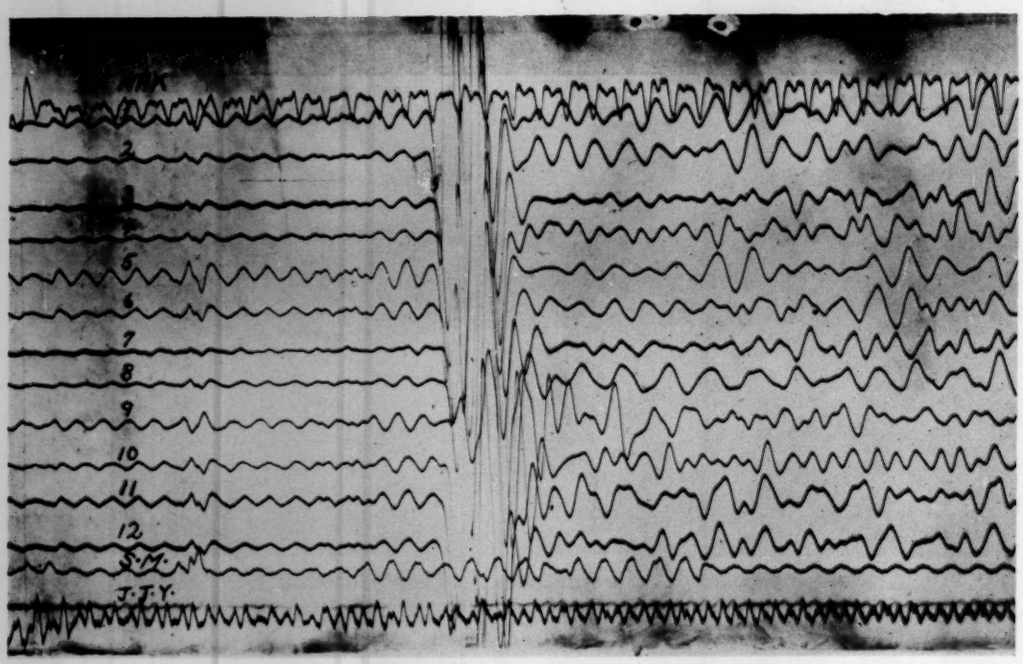

Fig. 16 (2). Seismogram at Asigase for shot B.

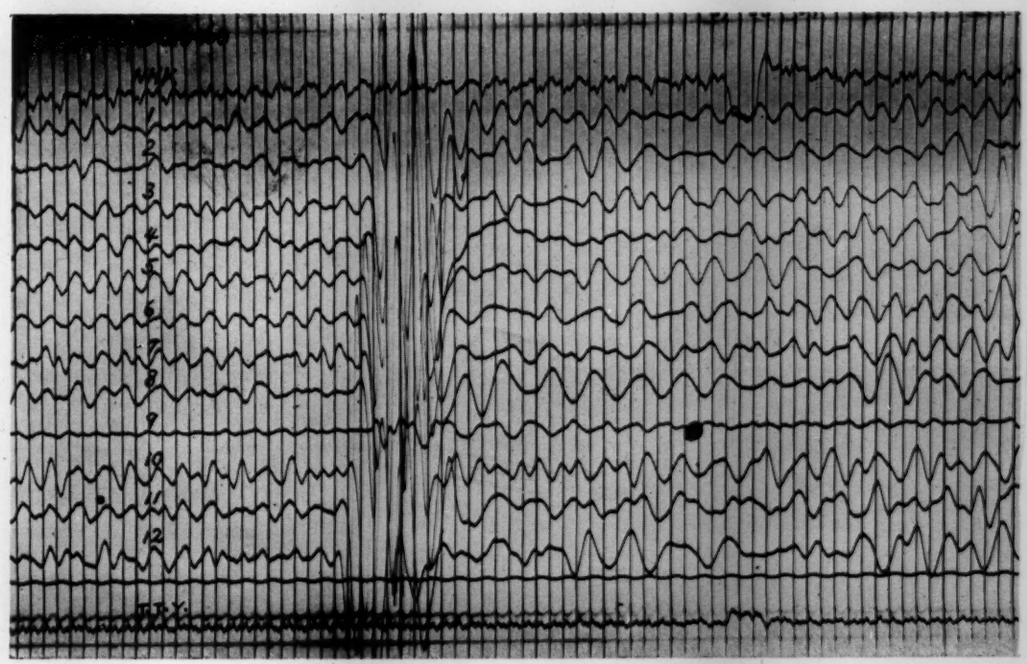

Fig. 16 (3). Seismogram at Asigase for shot C.

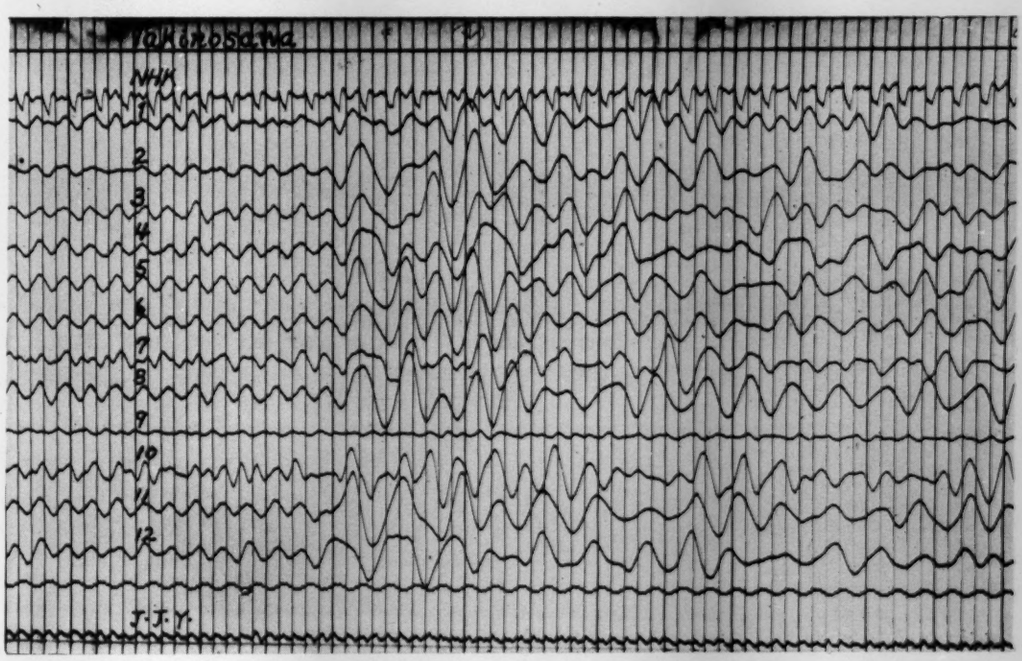

Fig. 16 (4). Seismogram at Asigase for shot D.

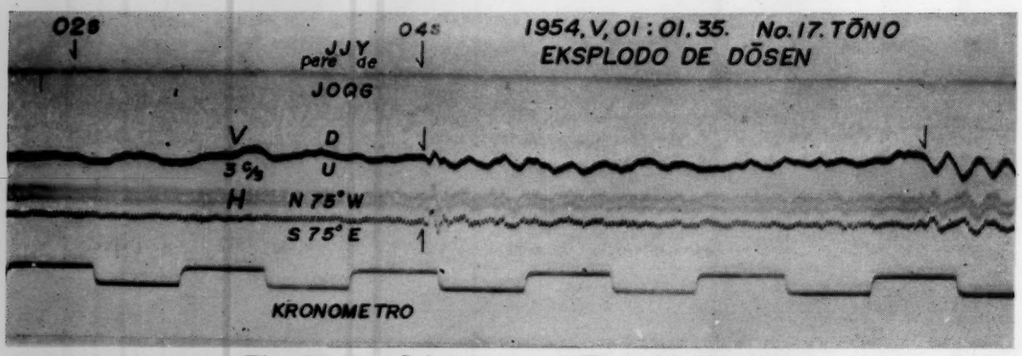

Fig. 17 (1). Seismogram at Tôno for shot A.

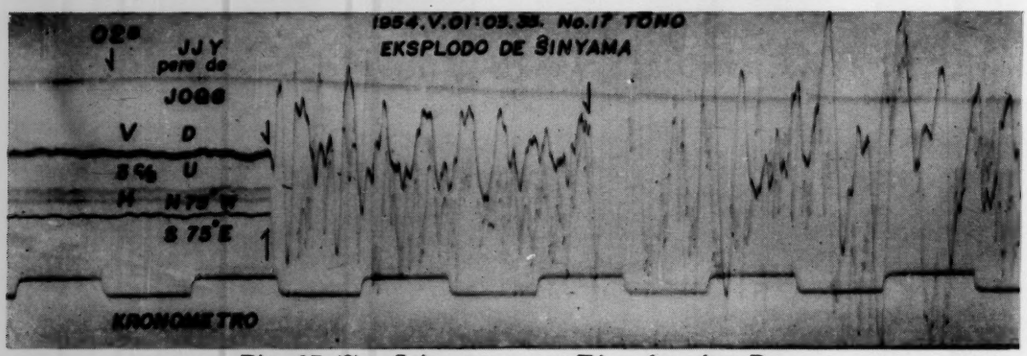

Fig. 17 (2). Seismogram at Tôno for shot B.

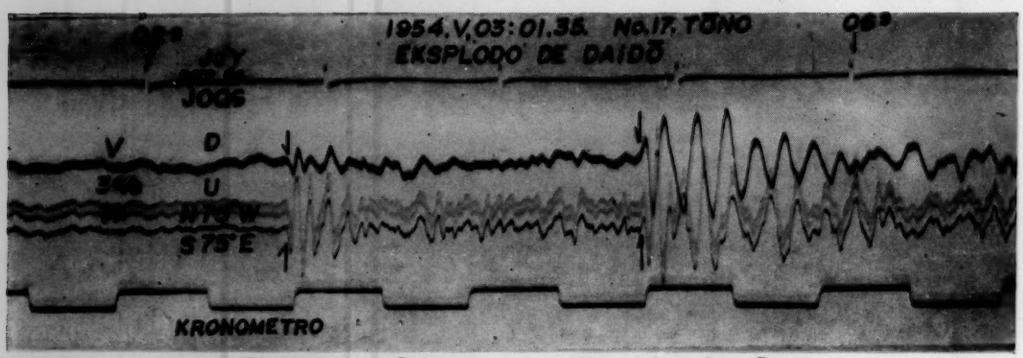

Fig. 17 (3). Seismogram at Tôno for shot C.

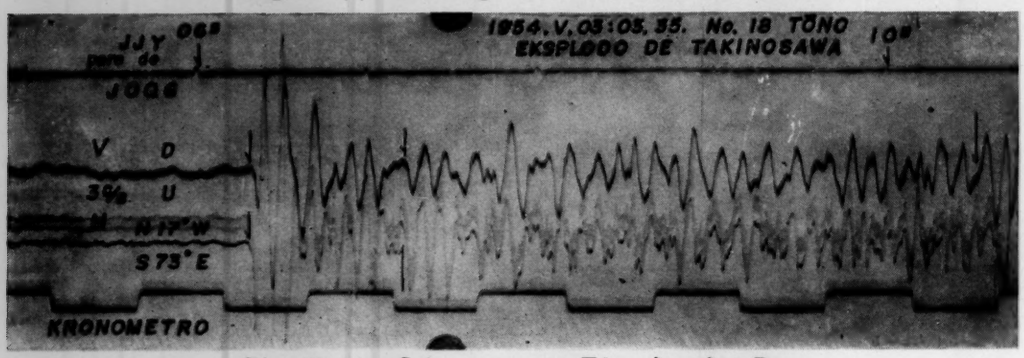

Fig. 17 (4). Seismogram at Tôno for shot D.

In Fig. 22 travel times for all shot points are plotted in such a way, that all shot points are on a common axis of abscissa, however, point B is put at the same position as point C. Travel times belonging to one and the same shot point are grouped into two branches, which correspond to the east side and west side relative to the shot point. The epicentral distance is taken as the abscissa, however, it is not the distance projected on the east-west section but the true distance.

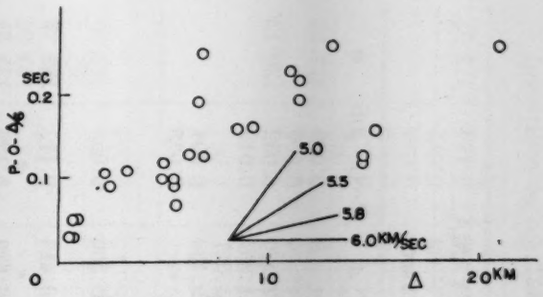

Fig. 18. Travel time for shot A.

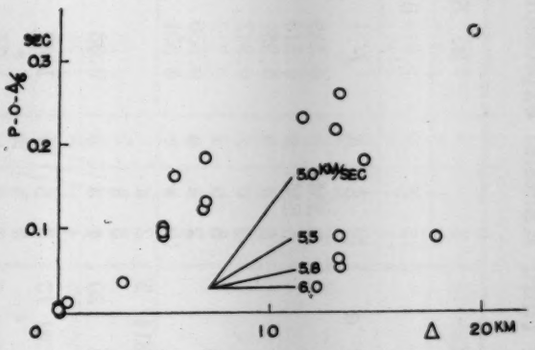

Fig. 19. Travel time for shot B.

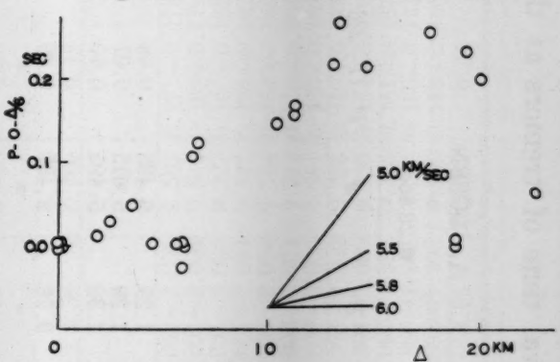

Fig. 20. Travel time for shot C.

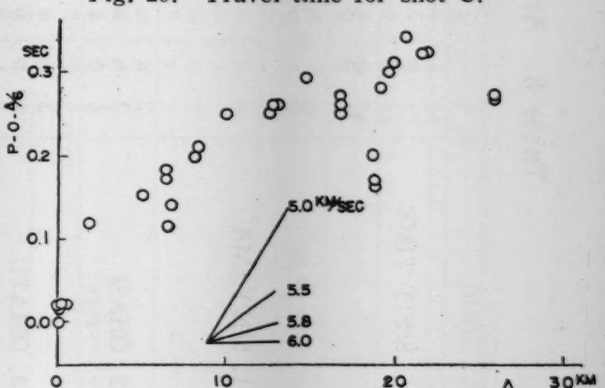

Fig. 21. Travel time for shot D.

2. Principles for deducing a structural model from the observed data.

In deducing a structural model the following guiding principles are adopted:

(a) To adopt as simple a model as possible, that means, a model which can explain well the observed data with the least number of probable assumptions.

(b) To make the difference between the observed travel time T_0 and the travel time T_c calculated from the assumed model, lie within the limit of ± 0.03 sec. For a few points under special circumstances this condition is neglected.

Table 3. Arrival time of tremors at the third Kamaisi explosion set.

SHOT TIME	A. DÔSEN 0.28 sec							B. SIN'YAMA 0.513 sec						
	L	S	A	P	Δ	$P-O-\Delta/6$	Θ	L	S	A	P	Δ	$P-O-\Delta/6$	Θ
1. SIN'YAMA								2	SM4		0.519	0	0.006	
								3	SM1	x	0.513	0	0.000	
								5	d	u	0.957	2.470	0.032	120°13′
								6	c	x	0.842	1.897	0.013	
								8	b	u	?	1.027		
								9	a	u	0.536	0.139	0.004	
								10	a	z	0.531	〃	−0.005	
2. ÔHASI	2	a	u	1.29	5.495	0.09	314° 2′	2	a					
	3	b	z	1.29	5.615	0.07		3	a					
	4	c	z	1.30	5.495	0.10	20	4	a	y	0.63	3.500	0.05	
3. ÔMATU	3	b	x	0.78	2.437	0.09	301 13	3	b	x	1.69	6.415	0.11	135 7
	4	b	y	〃	〃	〃	〃	4	b	x	〃	〃	〃	〃
	5	b	x	〃	〃	〃	〃	5	c	y	1.74	6.629	0.125	135 31
	6	c	y	0.74	2.171	0.109	310 40							128 7
4. DÔSEN	4	a	x	0.46	0.753	0.05	7 42							128 23
	5	b	x	0.41	0.592	0.03	357 40							127 32
	6	c	x	0.43∼0.44	0.760	〃	24 4							125 51
	7	d	xy	0.49	0.982	0.05	46 4							
5. MATUKURA	2		x	0.92	3.177	0.11	62 9	2		x	2.38	10.325	0.149	115 39
6. NODA	2	b	z	1.20	4.913	0.101		2	b	x	2.65	11.831	0.17	110 39
	3	a	y	1.22	4.921	0.120	68 25	3	a	x	2.64	11.822	0.16	110 33
	4	a	y	1.22	4.921	0.120		4	a	x	〃	〃	〃	〃
7. KOSANO	2	b	u	1.660	6.774	0.251	?	2	b	u	2.99	13.247	0.27	105 16
	3	b	u	1.626	〃	0.219		3	b	u	2.99	13.247	0.27	?
	4	a	yz	1.576	6.618	0.193		4	a	u	2.91	13.097	0.22	105 6
8. NAKATUMA	2		x	1.86	8.513	0.16	66 16	2		x	3.16	14.590	0.218	101 23
								3		x	〃	〃	〃	

(to be continued)

(continued)

9. TAKINOSAWA	3 c	*xy*	2.693	12.895	0.26	76 44	2 c 3 c	*z* *x*	3.97 〃	19.335 〃	0.237 〃	99 5
10. KAMAISI-KO												
11. URESI	1,2	*y*	2.33	10.943	0.23	76 45	2 3	*y* *y*	3.70 〃	17.565 〃	0.262 〃	100 49
12. TÔNI	1 2	*y* *y*	2.38 2.40	11.414 〃	0.196 0.22	109 1	1 2	*u* *u*	4.03 〃	19.909 〃	0.202 〃	119 12
13. OKIRAI	2 3	*x* *x*	2.83 2.82	14.509 〃	0.13 0.12	163 51	2 3	*y* *y*	4.34 〃	22.590 〃	0.065 〃	151 55
14. HIKOROITI							1 b	*u*	3.67	18.897	0.010	Down 183 56
	2 a 3 a	*y* *y*	2.96 〃	15.108 〃	0.16 〃	211 6	2 a 3 a	*u* *u*	〃 〃	18.971 〃	0.002 〃	183 38 183 56
15. DAIDÔ	3 a 4 b 5 b 6 b	*x* *x* *z* *y*	1.45 1.56 1.56 1.56	6.252 6.900 〃 〃	0.13 0.13 〃 〃	271 12 269 36	3 a 4 b 5 c 6 d	*u* *u* *y* *y*	1.46 1.47 1.52 1.52	5.681 5.980 6.023 6.043	0.003 −0.020 0.006 0.003	178 40 182 4 183 30 〃
16. ASIGASE	3 a 4 b 5 c 6 d 7 e 8 f 9 g 10 h 11 i 12 j 13 k 14 l	*u* *u* *u* *u* *u* *z* *z* *z* *z* *z* *y* *y*	2.002~2.004 2.001~2.004 2.002~2.004 2.001~2.004 2.001~2.004 2.000~2.003 1.999~2.002 1.998~2.002 1.994~2.000 1.992~1.998 1.986~1.991 1.983~1.998	9.303 9.315 9.327 9.341 9.354 9.372 9.381 9.356 9.330 9.305 9.280 9.255	0.171~0.173 0.168~0.171 0.167~0.169 0.164~0.167 0.162~0.165 0.158~0.161 0.155~0.158 0.159~0.163 0.164~0.170 0.161~0.167 0.159~0.164 0.160~0.165		2 a 3 b 4 c 5 d 6 e 7 f 8 g 9 h 10 i 11 j 12 k 13 l	*x* *x* *x* *x* *x* *x* *x* *x* *x* *x* *x* *x*	1.309 〃 1.314 1.317 1.314 1.318 1.321 〃 1.327 1.321 1.318 1.315	4.447 4.474 4.501 4.528 4.555 4.582 4.592 4.580 4.567 4.554 4.542 4.530	0.055 0.050 0.051 0.049 0.042 0.041 0.043 0.045 0.053 0.049 0.048 0.047	213 28
17. TÔNO	2 3	*x* *x*	4.03 〃	20.962 〃	0.26 〃	289 15	2 3	*x* *x*	2.91 〃	13.294 〃	0.184 〃	273 57

(to be continued)

Table 3. (Continued)

SHOT TIME	C. DAIDÔ 0.170 sec							D. TAKINOSAWA 0.513 sec						
	L	S	A	P	Δ	$P-O-\Delta/6$	Θ	L	S	A	P	Δ	$P-O-\Delta/6$	Θ
1. SIN'YAMA	7	c	u	1.772	5.145	0.745		7	b	z	3.76~3.77	18.546	0.16~0.17	
	8	c	u	〃	〃	〃								
2. ÔHASI								2	b	y	3.57	16.729	0.27	
								3	b	y	3.56	〃	0.26	
								4	b	x	3.55	〃	0.25	
3. ÔMATU	2			not identified										
	3	b	x	1.084	4.943	0.090	76 08	3	b	y	3.25	14.698	0.29	264 30
	4	b	x	1.089	〃	0.095	〃	4	b	y	〃	〃	〃	
	5	b	x	1.094	〃	0.100	〃	5	b	y	〃	〃	〃	
	6	c	u	1.240	5.454	0.161	disturbed							
4. DÔSEN	3	a	x	1.450	6.898	0.131	85 46	3	a	x	2.89	12.730	0.26	260 56
	4	e	y	1.502	6.885	0.185	86 26	5	b	x	2.92	12.865	0.26	260 08
	5	b	x	1.425	6.800	0.122	87 32	6	c	x	2.85	12.533	0.25	260 33
5. MATUKURA								2		x	2.42	9.945	0.25	262 41
6. NODA	2		u	not clear, disturbed				2	a	y	2.07	8.154	0.20	263 14
	3	a	u	2.31	11.458	0.23	obscure	3	a	x	〃	〃	〃	〃
							82 12	4	b	x	2.08	8.162	0.21	263 23
7. KOSANO	2	b	u	2.642	13.270	0.260	?	2	b	y	1.749	6.381	0.172	267 47
								3	b	y	1.762	〃	0.185	〃
	4	a	u	2.572	13.111	0.217		4	a	y	1.760	6.545	0.116	267 40
8. NAKATUMA								1		x	1.47	4.887	0.15	278 10
								2		x	〃	〃	〃	
								3		x	〃	〃	〃	

(to be continued)

(continued)

9. TAKINOSAWA	6 c	y	3.705	19.498	0.285	83 19	1 SM	x	0.513	0	0.000		
	7 c	x	3.702	〃	0.282		5 e	x	0.618	0.504	0.021		
	8 c	x	3.705	〃	0.285		6 c	x	0.575	0.251	0.020	326 01	
							7 c	x	0.576	〃	0.021		
							8 c	x	0.575	〃	0.020		
							9 d	x	0.591	0.344	0.021		
							10 b	x	0.555	0.153	0.016		
							11 a	x	0.548	0.088	0.020		
10. KAMAISI-KO													
11. URESI	1	u	3.362	17.729	0.237	82 03	1	y	0.96	1.999	0.12	253 33	
			−3.539		∼0.414		2	y	〃	〃	〃		
12. TÔNI	Disturbed, cannot be identified						1	x	1.77	6.737	0.14	Doubt on parallax	
							2	y	〃	〃	〃		
13. OKIRAI	2	x	3.254	17.857	0.108	142 38	2	y	3.82	18.679	0.20	206 43	
		y	Time mark, not clear				3	y	〃	〃	〃		
14. HIKOROITI	1 b	y	2.429	13.171	0.064	184 52	1 b	x	5.088	25.829	0.270	232 50	
	2 a	y	〃	13.244	0.052	184 25	2 a	x	5.080	25.801	0.267	232 33	
	3 c	u	2.455	13.171	0.090		3 c	y	5.096	25.855	0.274		
15. DAIDÔ	3 a	x	0.258	0.458	0.012	82 50	3 a	x	3.96	19.033	0.28	262 53	
	4 b	x	0.223	0.301	0.003	181 56	4 b	x	4.09	19.649	0.30	262 35	
	5 c	x	0.246	0.421	0.004	229 50	5 c	z	<4.14	19.930	<0.31	261 51	
	6 d			0.442	induction by shot		6 d	z	<4.19	20.065	<0.34		
	7 SM		0.170	0	0.000								
16. ASIGASE	3 a	x	0.723	3.088	0.038		4∼10	y	4.46	21.735	0.32	268 28	
	4 b	x	0.717	3.080	0.034					∼21.805	P obscure		
	5 c	x	0.719	3.072	0.037								
	6 d	x	0.719	3.064	0.038								
	7 e	x	0.712	3.056	0.033								
	8 f	x	0.713	3.048	0.035								
	9 g	x	0.715	3.043	0.038	309 23							
	10 h	x	0.711	3.026	0.035								
	11 i	x		3.009									
	12 j	x	0.704	2.992	0.035								
	13 k	x	0.699	2.995	0.030								
	14 l	x	0.693	2.958	0.030								
17. TÔNO	2	x	2.790	14.638	0.181	297 10	2	y	6.32	32.718	0.36	277 19	
	3	x	〃	〃	〃		3	y	〃	〃	〃		

L; line number reckoned from top to bottom on the original seismograms.
S; position of pick-up whose elements are given in Table 2.
A; accuracy of readings of the initial phase classified as follows:

x	y	z	u
<0.01 sec	<0.02 sec	<0.03 sec	>0.03 sec

At many places, late phases as well as the S phase were clearly observed, however, the travel time of the first P phase was exclusively used in this analysis.

3. The first approximation to the model in the east-west vertical section.

As apparent from Fig. 1, it may be safely assumed that shot points A, B, C, D, and observation points 1～11, 15, 16 and 17 approximately lie in a common east-west profile. Therefore, from travel times at these places, the first approximation of the model in this section is deduced.

First, if we compare the travel time at point 9 from shot A with that at point 4 from shot D (Table 3), the difference is very small i.e. 0.01 sec. This fact fulfils the condition that the ray path is common between both shots.

If travel times at points 4～11 from both shots A and D are plotted in a figure (Fig. 23), points belonging to shot A are arranged on a line clearly different from that through points belonging to shot D. The

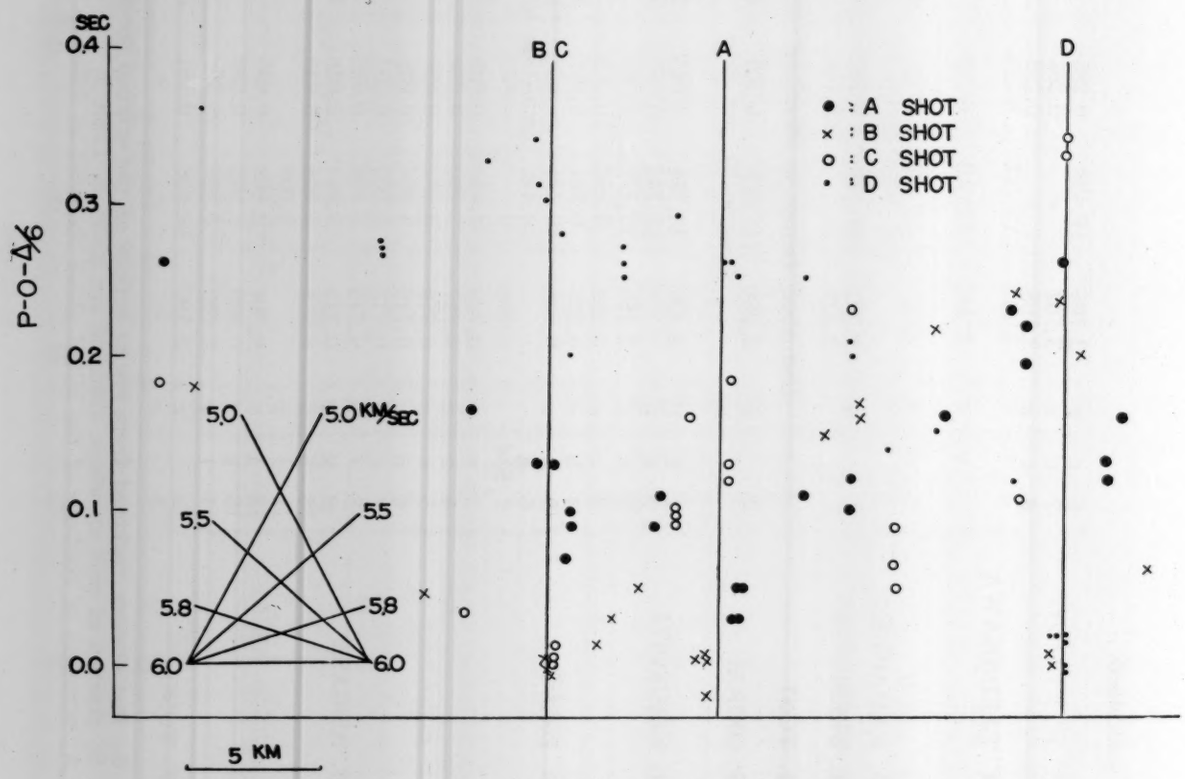

Fig. 22. Travel time for shot A, B, C, and D transferred to the section CAD.

apparent velocities are deduced respectively as 5.45 km/sec and 5.54 km/sec. Therefore, their mean value 5.50 km/sec is taken as the true velocity in the second layer.

In Fig. 23 another branch of travel time curves is observed at points near the shots. Its approximate velocity is given as 4.5 km/sec, and this value is adopted as the velocity in the first layer. The point of intersection is at a distance of 0.78 km for shot A and 2 km for shot D. Hence the depth of the first layer is 122 m at A and 314 m at D. Consequently the dip of the boundary between layer 1 and layer 2 is $\theta_{1.2}=50.3'$ to the east.

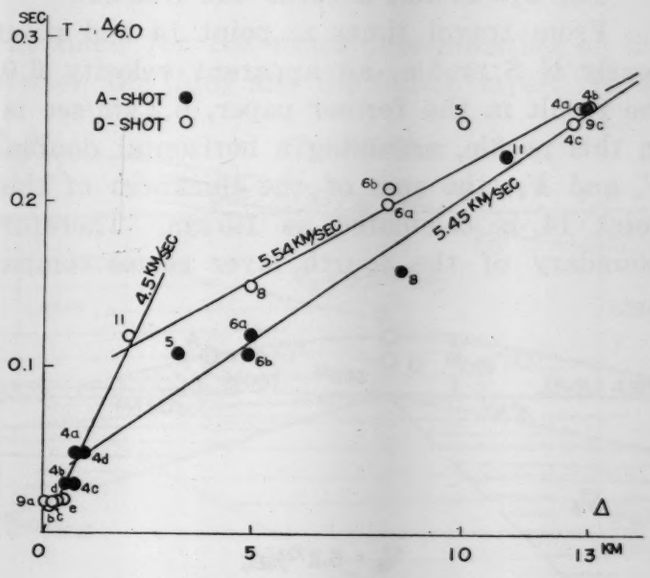

Fig. 23. Travel time for shots A and D.

Next, from the eastward branch of the travel times for shot B (Fig. 19) the apparent velocity V_s is found slightly larger than $V_2=5.5$ km/sec, with no intercept time. Therefore, it is inferred that there is a third layer with true velocity larger than V_s and the boundary between layer 2 and layer 3 dips toward the east and layer 3 is almost exposed at point B. Exact value of the true velocity of layer 3 is yet uncertain. In Fig. 21 point 16 and point 17 for shot D lie probably on the farthest branch, which shows the apparent velocity 5.86 km/sec and the break point at 14 km from the shot point. Adopting a triple layered model and using V_1, V_2, $\theta_{1,2}$ and apparent velocity 5.86 km/sec, a set of dip angles of the boundary between the second and the third layer, $\theta_{2.3}$ can be calculated, taking V_3, the velocity in the third layer as the parameter. (Table 4)

Table 4.

V_3	$\theta_{2.3}$
5.78 km/sec	1° 3′ 20″
5.80	30 20
5.82	−6 40

As obtained before, the boundary must dip eastward. Therefore, V_3 must be less than 5.81 km/sec. Thus we infer that $V_2=5.8$ km/sec

in the former paper[2] corresponds to V_3 in this case, and put $V_3=5.8$ km/sec. Assuming this value and $\theta_{2.3}=30'$, and taking travel times at point 16 and 17 into consideration, the following relation between the thickness of the second layer h km at D and the distance Δ_c km of the break point of the travel time curve is deduced. Namely,

$$h=0.0808\Delta_c-0.0659\,.$$

For $\Delta_c=14$ km, h turns out 1.05 km.

From travel times at point 14 and point 15 for shot B, i.e. in the nearly N–S profile, an apparent velocity 6.0 km/sec is got. Comparing the result in the former paper, 6.2 km/sec is adopted as V_4 in this case. In this profile, assuming a horizontal double layered model with layers V_3 and V_4, the sum of the thickness of the V_3 layer at shot B and at point 14 is calculated as 1.5 km. Therefore, the depth of the upper boundary of the fourth layer seems comparatively shallow in the B–C

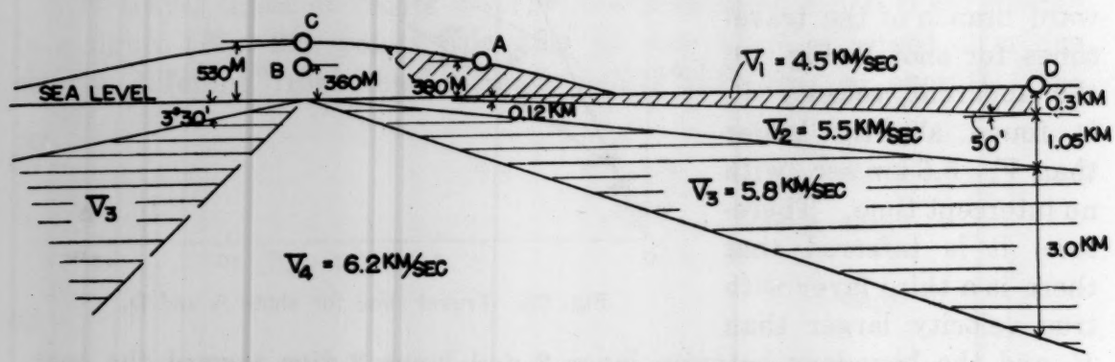

Fig. 24. First approximation to the crustal model in section CAD.

section. From the southward profile for the D-shot, the depth to the fourth layer at point D seems somewhat deep, however, its exact value cannot be given. Taking the westward travel times for shot D into account, we tentatively put the depth equal to 4.5 km. The travel times at point 17 for shot B and C seem to belong to the path through layer 3.

If we assume that the top edge of the third layer be at sea level, the dip of the upper surface toward the west is calculated $\theta'_{2.3}=4°20'$ from shot B and $\theta'_{2.3}=2°50'$ from shot C. The mean value 3°30′ is taken as the first approximation.

From above considerations, a section as shown in Fig. 24 is taken as the first approximation.

2) *loc. cit.*, 1).

4. Determination of the east-west profile.

For further approximation, heights of the observation points and shot points, which were neglected in the first approximation, are taken into account. Starting from the approximate structure in Fig. 24, by the trial and error method we get the final structure as shown in Fig. 25, which is so determined that the O–C residues as a whole remain within the limit 0.03 sec. The residues thus calculated are shown in Table 5.

No sufficient data are at hand for the exact determination of the position of the boundary between the third and the fourth layer. How-

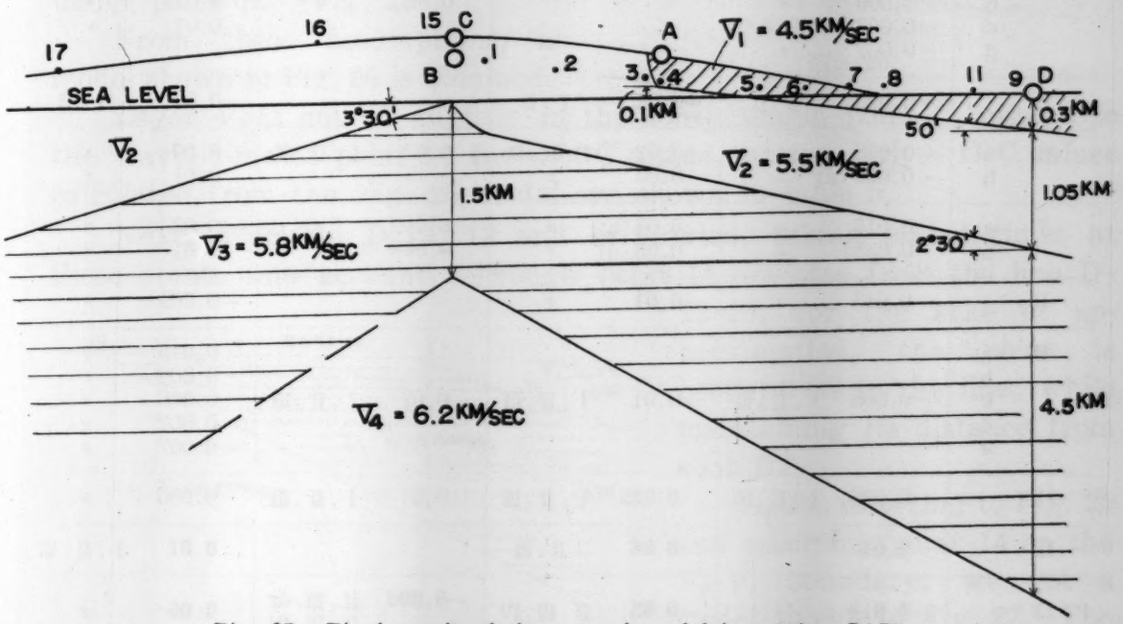

Fig. 25. Final result of the crustal model in section CAD.

ever, it is qualitatively doubtless that it dips down away from the B shot. The third and fourth layers in this report respectively correspond to the P_2 and P_3 layer in the former paper.[3)]

The presumption stated in the former paper, that the P_2, P_3 boundary should rise eastward and almost appear on the surface near the Kamaisi mine, is confirmed in this study.

5. Underground structure in the southern part.

We have 3 observation points, 12, 13, and 14 in the south. The unique determination of the underground structure from these scanty

3) *loc. cit.*, 1).

Table 5. T_0–T_c (unit in sec)

Station & P. U. Position \ Shot		A		B		C		D	
1	c			−0.024	II				
	d			−0.007	〃				
2	a	−0.035	I , II	−0.008	〃				
	b	−0.045	〃					0.04	I , II , III
3	b	0.006	〃	0.00	I , II	0.01	II	0.04	〃
	c	0.015	〃	0.013	〃				
4	a	0.007	I			−0.016	I , II	0.02	I , II , III
	b	0.000	〃			0.02	〃	0.03	〃
	c	−0.007	〃					0.01	〃
	d	−0.007	〃						
5		−0.025	I , II	−0.04	I , II			0.03	I , II
6	a	−0.035	〃	0.02	I , II , III	0.03	I , II , III	0.00	〃
	b	−0.055 (z)	〃	0.03	〃			0.01	〃
7	a	0.015	〃	0.04 (u)	〃	0.012	〃	−0.02	〃
	b	0.035	〃	0.08 (u)	〃	0.048	〃	0.01	〃
8		−0.015	〃	−0.01	〃			−0.009	〃
9	a							0.015	I
	b							0.008	〃
	c	−0.005	I , II , III	−0.01	I , II , III	−0.02	I , II , III	0.006	〃
	d							0.002	〃
	e							−0.007	〃
11		−0.026	I , II , III	0.025	I , II , III	−0.01	I , II , III	0.005	〃
12		**0.04**	〃	**0.06**	II , III			**0.01**	I , II , III
13		**−0.018**	〃	**−0.05**	II , III , IV	**−0.008**	II , III or II , III , IV	**0.00**	〃
14	a	**0.05**	I , II , III , IV	**0.015**	〃			**0.11**	I , II , III , IV
	b			**0.015**	〃	**−0.01**	III	**0.12**	〃
	c					**−0.03**	〃	**0.12**	〃
15	a	−0.015	I , II	**−0.05**	II , III	0.005	II	**0.03**	I , II , III
	b	−0.020	〃	**−0.08**	〃	0.00	〃	0.05	〃
	c			**−0.08**	〃	0.00	〃		
	d			**−0.08**	〃				
16	a			−0.008	II	−0.01	II	−0.06	I , II , III
	c			−0.018	〃	−0.008	〃		
	e	0.00	I . II	−0.03	〃	−0.015	〃		
	l					−0.018	〃	−0.04	I , II , III
17		−0.003	I , II , III	0.015	II , III	0.00	II , III	0.17	I , II , III , IV

I, II, ...denote layers through which the wave, that reached the observation point at first, passed. Values of O–C in Gothic type are obtained by the method of § 5.

data is almost impossible. Thus we must resort to search for such a model, which is compatible with the result in the east-west section and makes the O–C residues at these points as small as possible.

To begin with, a profile B-C-14-15 is tried, taking travel times at point 14 and 15 for shot B and at point 14 for shot C into consideration. Referring to the former results, we assume point 14 is on the boundary between the third and fourth layer, the boundary between the second and third layer under point B and C is at sea level, and the thickness of the V_3 layer is 1.5 km under point B. (Fig. 25)

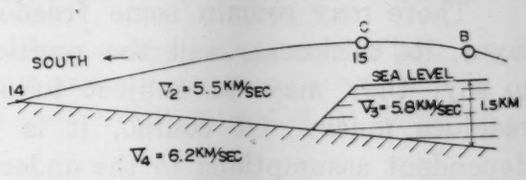

Fig. 26.

From these assumptions, a model shown in Fig. 26 is obtained.

Layer V_3 is cut off slightly in the south under point C, otherwise the travel time at point 14 for shot C comes out too early. O–C values calculated from the Fig. 26 model are shown in table 5.

Next, a profile D–12, 13 and 14 is tried, taking travel times at these points into account. Though point 14 deviates from the line D–12–13, for the sake of approximation, the point is brought on to the line, while maintaining its distance from shot D.

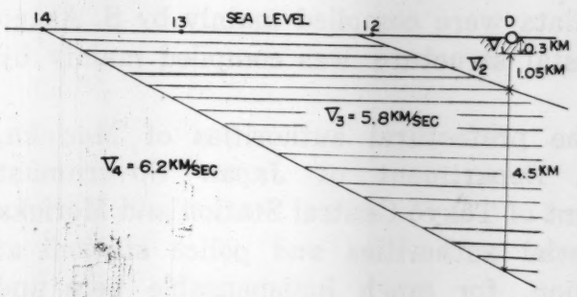

Fig. 27.

Again referring to Fig. 25 and assuming point 14 on the V_3–V_4 boundary, we get a model shown in Fig. 27. The V_2–V_3 boundary is determined in such a way that the residue O–C at point 12 be nearly zero. The wave path in this case should pass through the V_3 layer.

Referring to Fig. 25, 26, and 27, the depth of each boundary under each shot point and observation point is given. Thus, travel times for all combinations of shot points and observation points can be calculated. In this procedure, slight interpolations to the position of the boundary are taken for granted. For example, in the profile A–14, as the depth of each boundary is given at A and 14, connecting each corresponding boundary, we take the connecting line as the corresponding boundary under A–14 section.

As for the V_2–V_3 boundary in section A–14, the boundary in Fig.

27 is prolonged to the vertical line at point 14, and its intersection point is connected to the corresponding point under A. Thus we can calculate the travel time at point 14 from shot A.

O–C residues thus obtained are tabulated in Table 5.

6. Concluding remarks.

There may remain some freedom as to the true velocity in the V_1 layer, its thickness, and the position of the V_3–V_4 boundary. That is to say, they may be subject to some change without changing O–C residues much. Of course, it is possible to add some mutually independent assumptions to the underground structure, in order to ameliorate each O–C residue, for example, to insert a certain very local singularity in the path of waves. This means to add one assumption to one datum. Such a way of procedure is excluded from our guiding principle stated in 2.

Geologically speaking, the dotted line in Fig. 1 is a boundary between granite and palaeozoic strata, which is almost coincident with the boundary between the V_2 and V_3 layers.

In this report the observed data were compiled mainly by S. Asano and the part concerning the crustal structure was compiled mainly by T. Usami.

We are much obliged to the prefectural authorities of Morioka, Huzi-Seitetu Company, Morioka Department of Japan Government Railway, the Technical Department of Tôkyô Central Station and Morioka Branch Station of NHK., provincial authorities and police stations at each temporary observation station, for much indispensable help and facilities given by them.

6. 釜石鉱山附近4回の爆破地震動の観測について

爆破地震動研究グループ

すでに行われた石淵 3 回および釜石鉱山 2 回の大爆破の観測結果を綜合して，東北地方の地下構造が推算された．そのとき得られた地層のうち，P 波速度 5.8 km/sec および 6.1 km/sec の 2 層の境の面のありさまは，特に興味あるものであるが，その東辺の構造が充分よくわからなかつたので，おもに，それをきめるために，釜石鉱山および釜石港附近の 4 点の爆破のくわしい観測を行つたものである．

爆破点については表 1，観測点については表 2 に示され，その位置のあらましは，第 1 図にも示してある．走時その他は表 3 にくわしく示され，又走時図は図 18～22 に示すとおりである．

地下構造の東西断面については第 25 図，南北断面（ふたつの断面）については，第 26 図および第 27 図のようなものが推定される．

BULLETIN OF THE EARTHQUAKE
RESEARCH INSTITUTE
Vol. 37 (1959), pp. 123-154

7. *On the Crustal Structure in North-East Japan by Explosion Seismic Observations.*

By Takeo MATUZAWA,
Geophysical Institute, Faculty of Science, The University of Tôkyô.
(Read Dec. 23, 1958.—Received Dec. 27, 1958.)

1. Prefatory remarks

Several sets of seismic observations were made by our research group for explosion seismology on the occasions of large blasts in North-east Japan. A summarizing report[1] of the investigation of those observations was presented to the Rome Assembly of the I.U.G.G., 1954 under the title "Crustal structure in North-east Japan by explosion seismic observations". In that report broad aspects of our investigations were given but detailed discussions were omitted. In the present paper our precise discussions made in the course of our reductions will be given in order to furnish exact knowledge of the reliability of our results. We shall put forward our statements, referring to the Rome Assembly Report (later reference, R.A.R.). In R.A.R. the romanization of the name of places in Japan was sometimes confused, i.e. the Japanese system and the Hepburn system were mingled. In the present paper the Japanese system is adopted. The romanization of the personal name is of course left to the usage of each person.

The main differences between them are as follows;

Japanese system	Hepburn system	Japanese system	Hepburn system
Hu	Fu	Ti	Chi
Si	Shi	Tu	Tsu
Sya	Sha	Tya	Cha
Syu	Shu	Tyu	Chu
Syo	Sho	Tyo	Cho
Zi	Ji	An	Am (before b, p and m.)
Zya	Ja	In	Im (before b, p and m.)
Zyu	Ju	Un	Um (before b, p and m.)
Zyo	Jo	En	Em (before b, p and m.)
		On	Om (before b, p and m.)

1) Research group for explosion seismology (Japan), *Pub. Bureau Central Séism. Intern. Série A. Trav. Sci. Fasc.*, **19** (1954), 229-242.

In the Japanese system a circonflex is put on a vowel, which should be pronounced somewhat long, for example, Tôkyô in stead of Tokyo or Tokio in the Hepburn system.

Members of the group, who participated in this reduction and discussion, were, in the alphabetical order, T. Asada, S. Asano, N. Den, T. Kaneko, K. Kasahara, H. Kawasumi, N. Kobayashi, T. Matsumoto, T. Matuzawa, T. Mikumo, S. Miyamura, S. Murauti, A. Okada, S. Omote, E. Shima, S. Suyehiro, Z. Suzuki, A. Takagi, I. Tamaki and T. Usami. Voluminous and tedious reductions for the crustal structure were carried out for the most part by N. Den and Z. Suzuki.

Detailed descriptions of observation points, blasts, instruments, observers, etc. in English were reported in the following publications.

Blast	Publication		
I. 1	Bull. Earthq. Res. Inst.,	29	(1951), p. 97.
I. 2		30	(1952), p. 279.
I. 3		31	(1953), p. 281.
K.1		32	(1954), p. 79.
K.2		33	(1955), p. 693.

2. Determination of the shot times of both the Isibuti 1 and Isibuti 2 blasts

In order to construct synthetical travel time curves from several sets of observations of blasts, it was necessary to know the accurate time of each blast, because each set had very few, if any, common observation points, and the precise position of each shot was not the same. At the first two Isibuti blasts the shot times were not marked on the seismogram. We determined them as follows.

The Data of travel times for I.1, I.2 and I.3 blasts are given in Table 1.

These values are plotted in Fig. 1.

For I.3, putting $T=a\Delta$, we obtain by the method of least squares $1/a(\text{velocity})=2.51\pm0.052$ km/sec.

For I.2, putting $T=a\Delta+b$, we get the same value of a and the shot time $12^h05^m59.82^s$.

For I.1, assuming the same value of a, we get $12^h06^m07.64^s$ as the shot time, which is different by 0.33 sec from the value, deduced from remote observations. Of course this shot time should be adopted.

Table 1.

Blast	Station	Epicentral distance (km)	travel time (sec)	shot time
I.1[2)]	Isibuti	1.69	0.67	$12^h06^m07.97^s$ deduced from arrival times within 4 km.
I.2	Tunnel 1	0.24	0.088	$12^h05^m59.84^s$ deduced from arrival times within 5 km.
	Tunnel 2	0.33	0.127	
	Orose	1.08	0.43	
	Isibuti	1.69	0.68	
I.3	Tunnel 1	0.22	0.05	$12^h04^m59.42^s$. Shot time marked on the seismogram.
	Tunnel 2	0.31	0.09	
	A	1.50	0.60	
	B	1.73	0.69	

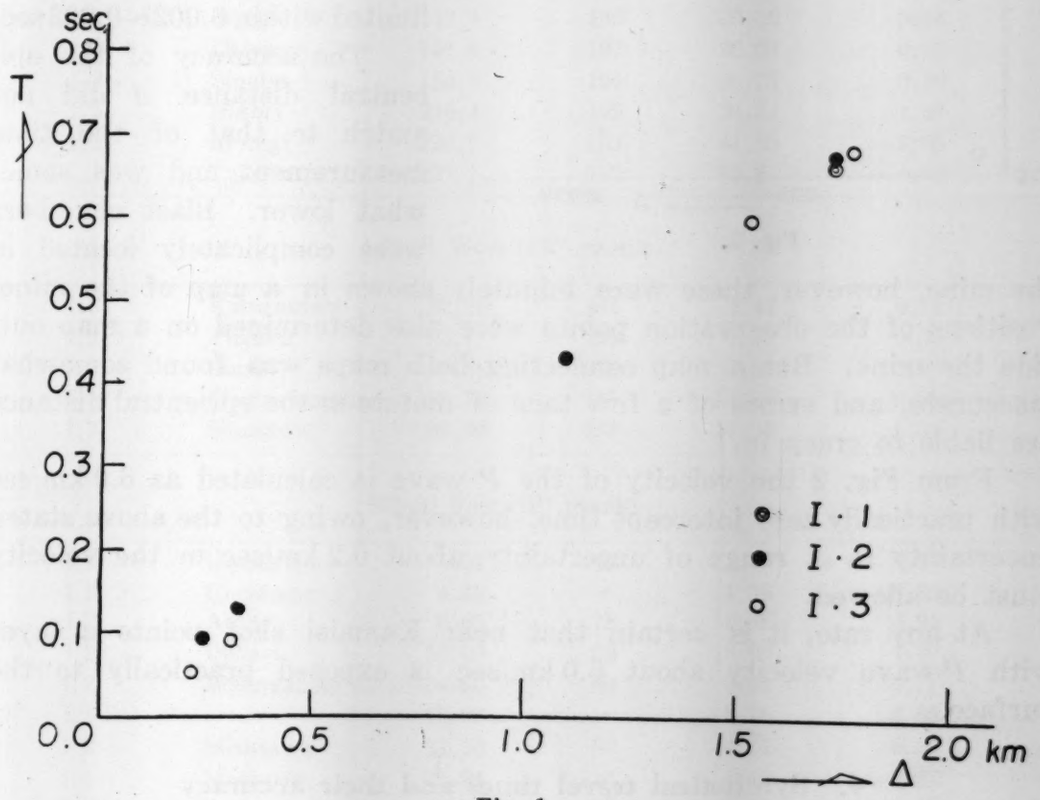

Fig. 1.

2) The longitude of the Isibuti shot point I.1 must be 140°53′37″E instead of 140°51′37″E printed in Table 1 in Report I.1.

3. The *P*-wave velocity in the uppermost layer near shot points

(i) Near Isibuti shot points.

As stated in 2, the *P*-wave velocity in the uppermost layer near Isibuti shot points is 2.51 km/sec, because its intercept time is zero.

(ii) Near Kamaisi shot points.

Travel times near shot points K.1 and K.2 were observed, and they are shown in Fig. 2 and tabulated in Table 2.

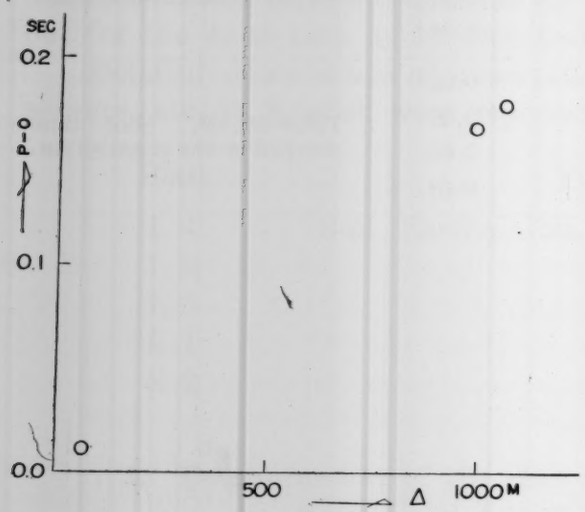

Fig. 2.

Table 2.

Δ in m	6.5	989	1055
$P-O$ in sec	0.011	0.166	0.177

The error of the travel time in the observation is limited within 0.002～0.003 sec.

The accuracy of the epicentral distance Δ did not match to that of the time measurement and was somewhat lower. Blast chambers were complicately located in the mine, however, these were minutely shown in a map of the mine. Positions of the observation points were also determined on a map outside the mine. But a map connecting both maps was found somewhat inaccurate, and errors of a few tens of meters in the epicentral distance are liable to creep in.

From Fig. 2 the velocity of the *P* wave is calculated as 6.0 km/sec with practically zero intercept time, however, owing to the above stated uncertainty in Δ, range of uncertainty about 0.2 km/sec in the velocity must be allowed.

At any rate, it is certain that near Kamaisi shot points a layer with *P*-wave velocity about 6.0 km/sec is exposed practically to the surface.

4. Synthetical travel times and their accuracy

Taking these precautions, synthetical travel times were obtained as tabulated in Table 3 and also given in R.A.R.

Table 3.

Blast	Station	distance km	azimuth from N over E	travel time T in sec	$T-\frac{\Delta}{6}$
		Isibuti South (IS) profile			
I.3		2.70	182°	0.95	0.50
I.2	Hondera	15.3	166	2.96	0.41
I.3	〃	〃	〃	3.02	0.47
I.2	Kurikoma	22.5	175	4.17	0.42
I.3	Hosokura	32.2	180	5.85	0.46
I.1	Hanaizumi	38.5	141	6.83	0.43
I.2	Kawatabi	41.9	196	7.61	0.63
I.3	〃	〃	〃	7.59	0.61
I.1*	Matusima	81.4	169	14.59	1.02
I.2*	〃	〃	〃	14.68	1.08
I.3	Nenosiroisi	87.8	185	15.24	0.61
I.1	Sendai	98.2	102	16.86	0.43
I.1*	Watari	119.4	180	20.03	0.14
I.3	Daiyama	148.8	197	25.07	0.27
I.2	Sinobu	159.9	194	26.75	0.10
I.3	Hatori	216.4	199	34.6	−1.47
I.3*	Motegi	290.7	193	44.50	−3.95
1.3	Tukuba	327.1	192	50.2	−4.32
		Isibuti West (IW) profile			
I.3	Katurazawa	22.20	241	4.41	0.71
I.3	Yuzawa	33.77	280	6.31	0.68
I.3	Innai	45.98	262	8.56	0.90
I.3*	Mamurogawa	58.72	243	10.74	0.95
I.3	Sinasawa	89.99	238	16.04	1.04
		Isibuti East (IE) profile			
I.2	Umadome 1	4.31	69	1.36	0.64
I.2	Umadome 2	4.40	〃	1.39	0.66
I.2	Atago	8.65	78	2.38	0.94
I.2	Dobasi	12.09	83	3.08	1.07
I.2	Wakayanagi	14.62	80	3.21	0.77
I.1	〃	15.06	〃	3.16	0.65
I.2	Mizusawa	21.10	83	4.11	0.59
I.1	Maesawa	21.24	110	4.40	0.87
I.2	Setamai	55.90	86	9.97	0.65
I.2*	Kamaisi	87.54	80	14.84	0.25

(to be continued)

Table 3. (continued)

Blast	Station	distance km	azimuth from N over E	travel time T in sec	$T-\frac{\Delta}{6}$
		Kamaisi South (KS) profile			
K.2	Nakasone	11.1	203	2.03	0.18
K.1	Setamai	20.6	222	3.60	0.17
K.2	Sakari	23.8	182	4.08	0.11
K.1	Kesennuma	45.8	194	7.72	0.09
K.2	〃	45.6	〃	7.58	−0.02
K.2	Sizugawa	72.2	197	11.96	−0.07
K.1*	Onagawa	97.6	193	15.92	−0.25
K.2	〃	97.4	〃	16.03	−0.20
K.2	Mukaiyama	137.3	211	22.93	0.05
K.2	Hunaoka	159.6	209	26.00	−0.60
K.1*	Kaneyama	173.9	207	28.28	−0.70
K.2	〃	173.6	〃	28.13	−0.84
K.1	Kawamata	202.5	209	31.84	−1.94
K.2	〃	202.4	〃	31.82	−1.91
K.1	Siroisi	226.0	208	35.35	−2.32
K.2	〃	225.9	〃	35.31	−2.34
K.1	Nogisawa	261.2	206	39.09	−4.44
K.2	〃	260.9	〃	40.0	−3.48
K.2	Motegi	331.5	201	49.0	−6.25
		Kamaisi West (KW) profile			
K.2	Umanokiuti	4.82	263	0.90	0.10
K.1	Ide	37.1	248	6.39	0.21
K.1	Mizusawa	51.6	250	9.09	0.49
K.1*	Yuzawa	103.5	262	18.13	0.88
K.1	Mamurogawa	130.7	248	22.66	0.88

Data marked with an asterisk * are those, which were corrected in this study and somewhat different from those in other reports.

5. Accuracy of the data

The accuracy of a crustal structure deduced from the observed travel times depends on the accuracy of the data. Therefore, it is important to ensure the accuracy of the latter. Sources of time errors in the travel time are classified as follows:

1. Errors of identification of the commencement of the wave.
2. Errors of time measurements on the record.

3. Irregularities due to the weathered layer.

As to (1), the identification was made by several persons independently, and readings were accepted only when satisfactory agreement was found. Errors of this category are expected to be very small, except for stations at very remote epicentral distances.

As to (2), the maximum error is expected not to exceed 0.1 sec. At most of the observation points, the running speed of the recording paper is 2~3 cm per second or more, and moreover second and minute marks are put directly from the JJY radio time signal. Therefore, the error of time measurement does not exceed 2 or 3 hundredths of a second. At stations very near to the shot point time marks of one hundredth of a second are put, so that accuracy of 2 or 3 thousandths of a second is secured. At some stations, where the JJY reception failed, the time was determined from chronometers, and the error is expected not to exceed 0.1 sec.

As to (3) this is not due to observations, however, it is very local, and in this paper it is treated as a sort of errors. A layer of 2.51 km/sec is accepted as the surface layer, and any local weathered layer other than this one comes under this category. Most observation points were selected in such a way that instruments could be put in caves of the bed rock. From the geological point of view and some trial computations, it was found that the error due to this factor cannot be more than 0.1 sec.

In the next place, the accuracy of the determination of the position of observation and shot points must come under consideration. In the present sets of observations, the positions were identified on the topographical map on a scale of 1/50000 issued by the Geographical Institute, Japan. Hence the error of the relative distance between a shot point and an observation point is expected not to exceed 100 m at most. Therefore, the accuracy of the space determination matches the time accuracy well.

Considering these factors, the total amount of the error is estimated to be less than 0.1 second. In other words, if a fluctuation in travel times exceeds 0.1 sec, the amount must be significant and taken into account in our study.

6. General consideration to the travel time diagram

From the synthetical travel times in Table 3, a travel time diagram as shown in Fig. 3 is obtained.

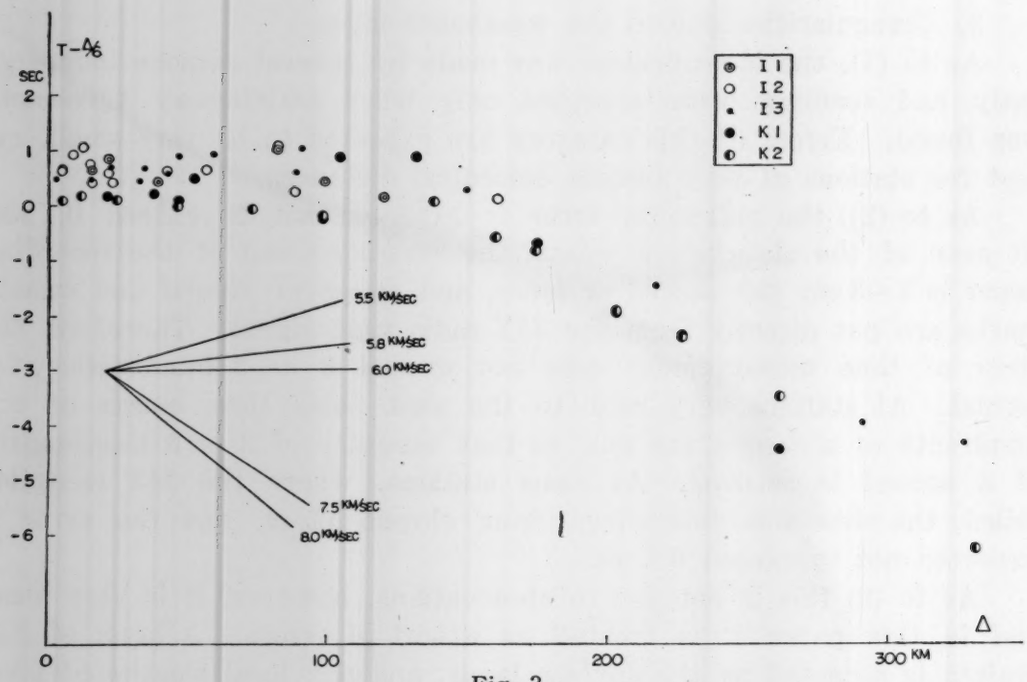

Fig. 3.

Though the plotted points are confined within about 1 sec as far as 150 km, the scatter exceeds far beyond the limit of error already stated, i.e. 0.1 sec. If we classify the points according to the azimuth of the station relative to the shot point, certain systematic deviations are found. This fact suggests that a certain boundary or boundaries of different geological layers are inclined to the horizontal plane with certain dips and strikes.

In deducing the underground structure, we adopt the following guiding principles.

(1) As the first step, seismological data only are used for the interpretation of the crustal structure.

Geological or gravity data are taken into account only to check whether the interpretation is adequate or not.

(2) The proposed model must be as simple a one as possible, that means, a model with the least number of possible assumptions necessary to explain the observed data.

As a natural consequence, a constant velocity of the seismic wave is assumed at least as a first approximation in a certain specified layer.

Under these restrictions a few cases of observed anomalies remain unexplained. These cases are mainly due to the lack of sufficient data in the neighbourhood of the point in question.

7. Discussions on the mode of stratifications of various layers

We can distinguish 4 distinct layers P_1, P_2, P_3 and P_4 specified by velocities of the P waves, i.e. 2.51 km/sec for P_1, 5.75~5.85 km/sec for P_2, 6.1~6.2 km/sec for P_3 and 7.5~8.0 km/sec for P_4.

We will discuss the form of each layer as precisely as possible on the basis of travel time curves which were also given both in tables and figures in R.A.R. Abreviations for profiles here used are the same as those given in that report. For instance, IE stands for the eastern profile of the Isibuti explosion.

8. Remarks on travel times in each profile

(i) *IE profile* (Fig. 4). As stated in section 2, for $\Delta<2$ km travel times are almost exactly on a straight line, giving 2.51 km/sec. In the domain $2.7<\Delta<12$ km they are on a straight line, showing an apparent velocity 4.4 km/sec, and for $\Delta>14$ km they are scattered around a

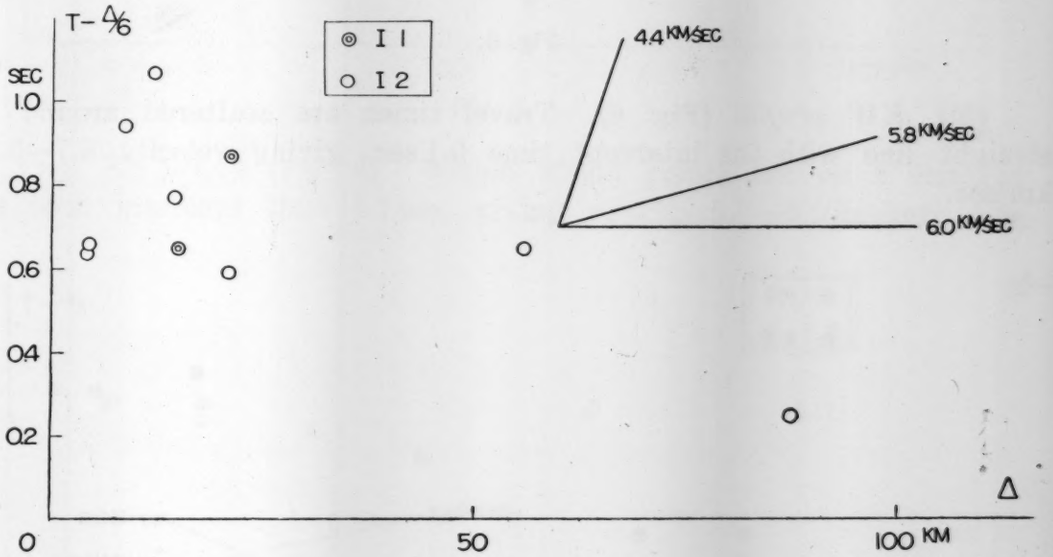

Fig. 4.

straight line, giving approximate velocity 5.8~6.0 km/sec. In the neighbourhood of $\Delta=14$ km, i.e. between Dobasi station and Wakayanagi station, a gap of travel time, amounting to 0.4~0.6 sec, is seen, and the travel time belonging to the remoter branch, i.e. $\Delta>14$ km, appears earlier.

(ii) *IW profile* (Fig. 5). Travel times are scattered around a straight line with the intercept time 0.1 sec, giving velocity 5.5~5.8 km/sec.

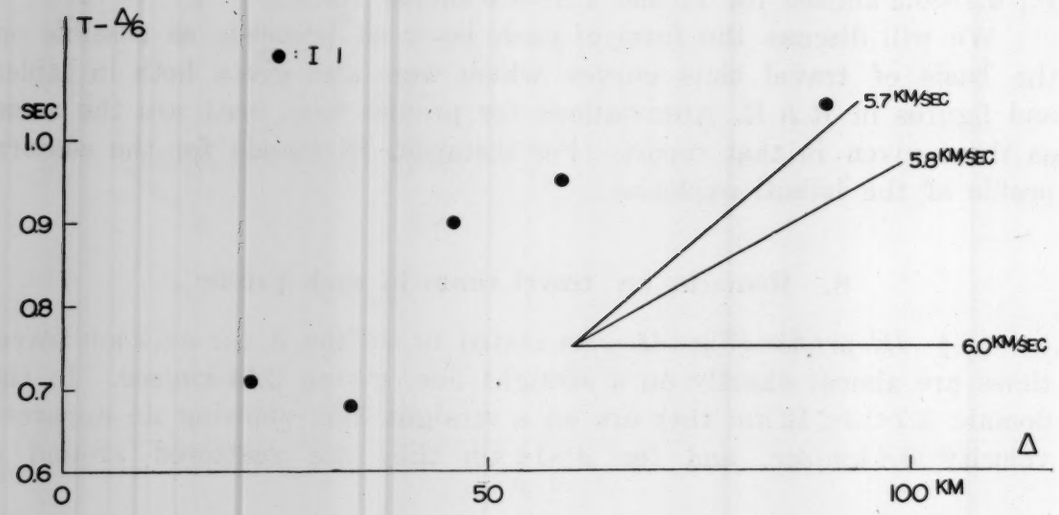

Fig. 5.

(iii) *KW profile* (Fig. 6). Travel times are scattered around a straight line with the intercept time 0.1 sec, giving velocity 5.7~5.8 km/sec.

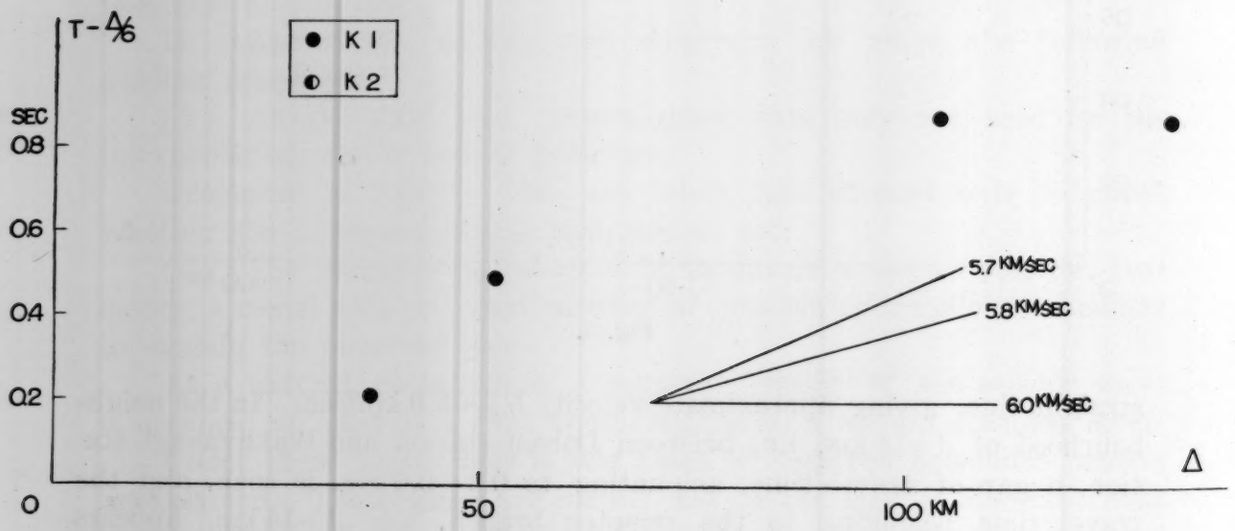

Fig. 6.

(iv) *IS profile* (Fig. 7). For $\Delta < 40$ km travel times are on a straight line with the intercept time 0.2~0.4 sec, giving velocity 5.7~6.0 km/sec. For $40 < \Delta < 150$ km, we can fit a straight line with intercept time 1.0~2.0 sec, giving velocity 6.1~6.3 km/sec. Travel times fluctuate rather remarkably, though the range of fluctuation is confined within 1 sec. It seems probable that crustal domains specified by these 3 velocities would have a stratified structure bounded by discontinuity surfaces.

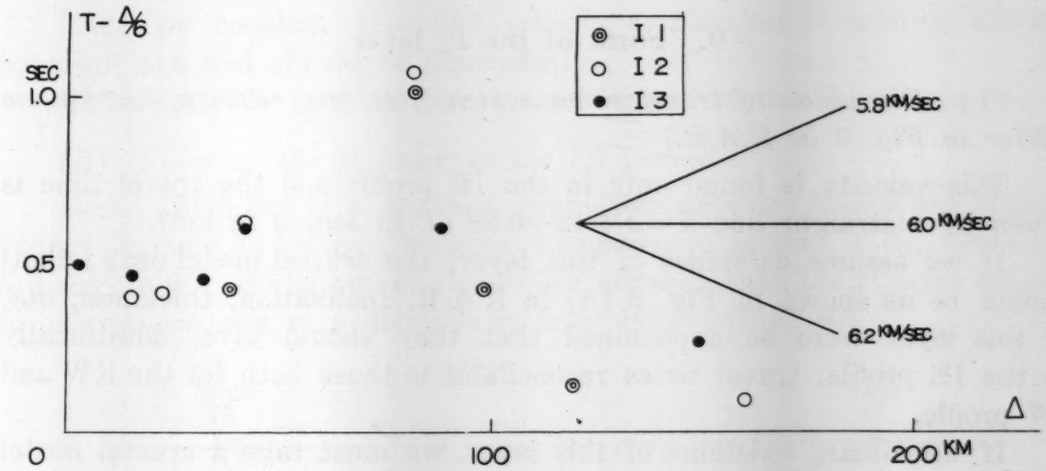

Fig. 7.

(v) *KS profile* (Fig. 8). Within 20 km points are on a straight line with intercept time 0.1 sec, giving velocity 5.7~6.0 km/sec. For

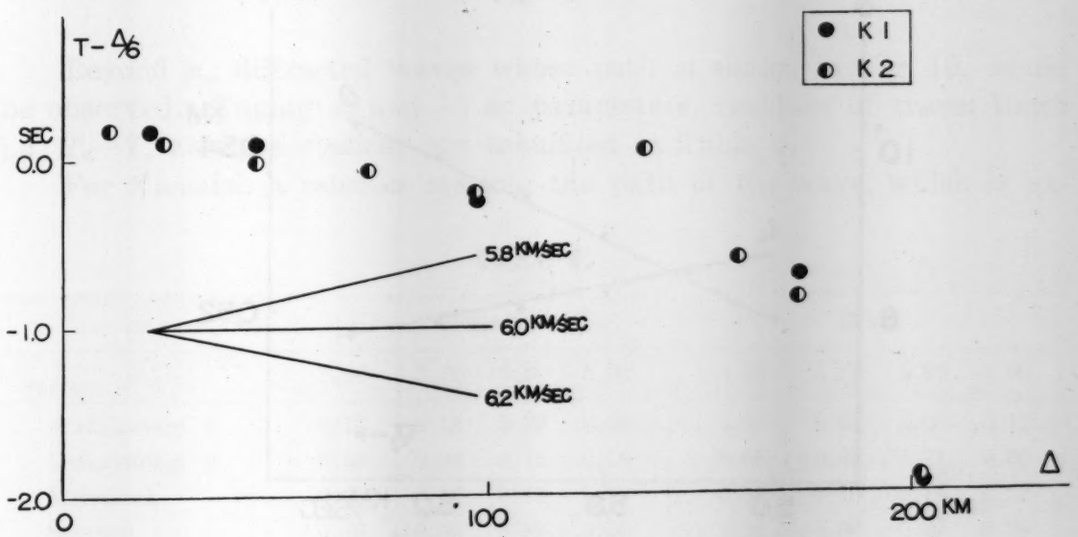

Fig. 8.

$20<\Delta<160$ km, points are scattered around a straight line with intercept time 0.5 sec, giving velocity 6.1～6.3 km/sec. From remoter places the velocity is estimated to 7.5～8.0 km/sec.

In this case also we can infer 3 layers with different velocities. Outlines of the crustal structure deduced from these results are summarized in R.A.R.

Now we proceed to the discussion of the form of each layer.

9. Form of the P_1 layer

(i) *Discussion of travel times which give the velocity 4.42 km/sec (Refer to Fig. 9 in R.A.R.)*

This velocity is found only in the IE profile and the travel time is given by a straight line $T=\Delta/4.42+0.38$ (T in sec, Δ in km).

If we assume existence of this layer, the crustal model near Isibuti should be as shown in Fig. 9 (A) in R.A.R. Inclination, thickness, etc. of this layer were so determined that they should give, additionally to the IE profile, travel times reconcilable to those both for the KW and IW profile.

If we discard existence of this layer, we must take a crustal model as shown in Fig. 9 (B) in R.A.R. Inclination θ and depth under Isibuti are calculated as 8°～10° and 530 m from travel times in the IE profile. In model (B) if we construct a graph for θ and h, taking the velocity in

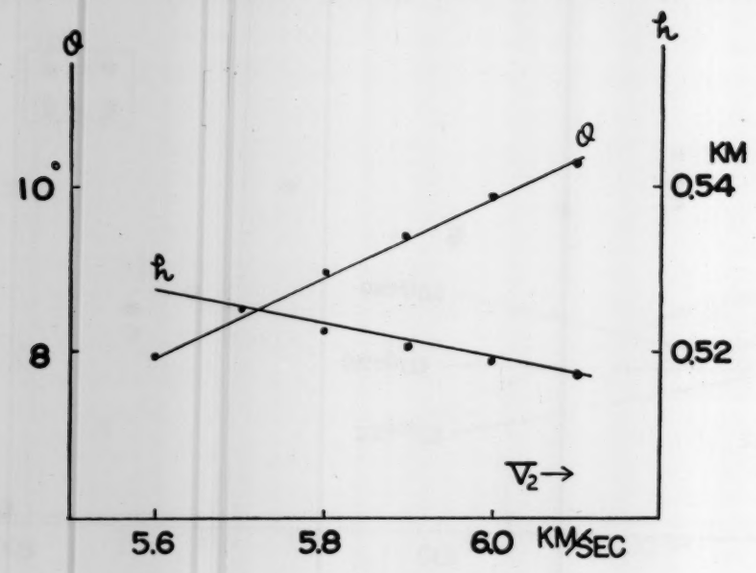

Fig. 9.

the lower layer V_2 as abscissa, we obtain Fig. 9.

It should be remarked that h varies slowly with V_2.

On the other hand, the intercept time of the line giving velocity 5.8 km/sec in the IS profile is 0.3～0.4 sec as shown before.

Assuming that the form of the cross section is invariable in the NS direction both for the (A) and (B) models, we can calculate the intercept times for both models. That for model (A) should be 0.7 sec and 0.36 sec for model (B).

Thus we conclude that the velocity 4.42 km/sec is nothing but an apparent one and should be discarded.

Ultimately, we adopt 4 layers as shown in section 7.

(ii) *Form of the P_1 layer in the IE profile*

Model (B) holds to a distance somewhere between Dobasi and Wakayanagi, namely 14 km ca., because, as shown in section 8 (i), there is a discontinuity of the travel time. We suppose that the P_1 layer ceases to exist there, say at a distance x_0 from Isibuti (Fig. 10).

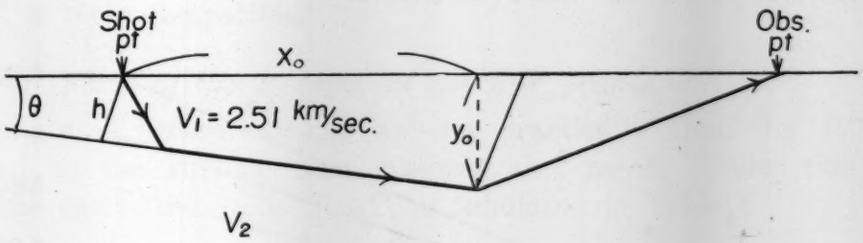

Fig. 10.

Beyond x_0, diffracted waves whose path is shown in Fig. 10, would be observed. Taking x_0 and V_2 as parameters, residues of travel times i.e. $T_0 - T_c$ at some stations are tabulated in Table 4.

For Kamaisi, a remoter station, the path of the wave, which is ex-

Table 4.

x_0	13 km				14 km			
Station \ V_2	5.60	5.70	5.80	5.90	5.60	5.70	5.80	5.90
Wakayanagi I	0.17	0.18	0.22	0.26	0.02	0.05	0.08	0.12
Wakayanagi II	0.04	0.08	0.12	0.16	−0.05	−0.02	0.01	0.05
Mizusawa	0.04	0.12	0.13	0.24	0.03	0.10	0.15	0.22
Setamai	0.26	−0.08	0.09	0.26	−0.28	−0.08	0.09	0.26

pected to arrive there at first, should lie in the P_3 layer. In the above calculation we assume that the P_2 layer is exposed to the surface beyond x_0. The effect of the weathered layer tends to make T_0 late and the judgement of the onset time of the initial motion has also a retarding tendency. Therefore, if the model is a true one and the above mentioned two effects are the only causes of uncertainties, a negative value of T_0-T_c is improbable.

After all, within our criterion of accuracy, x_0 is 14 km with an uncertainty within 1 km and V_2 is 5.75～5.85 km/sec. The residue at Mizusawa is 0.10～0.20 sec and somewhat large compared with other stations. Hence, at Mizusawa the P_2 layer is probably covered by a certain thin surface layer. If it is the P_1 layer, its thickness is estimated to 300～500 m.

(iii) *Form of the P_1 layer in the IW profile*

If the P_2 layer is exposed to the surface in the further west, the expected travel times are shown by full lines in Fig. 11, taking V_2 as the parameter. Dots are observed points.

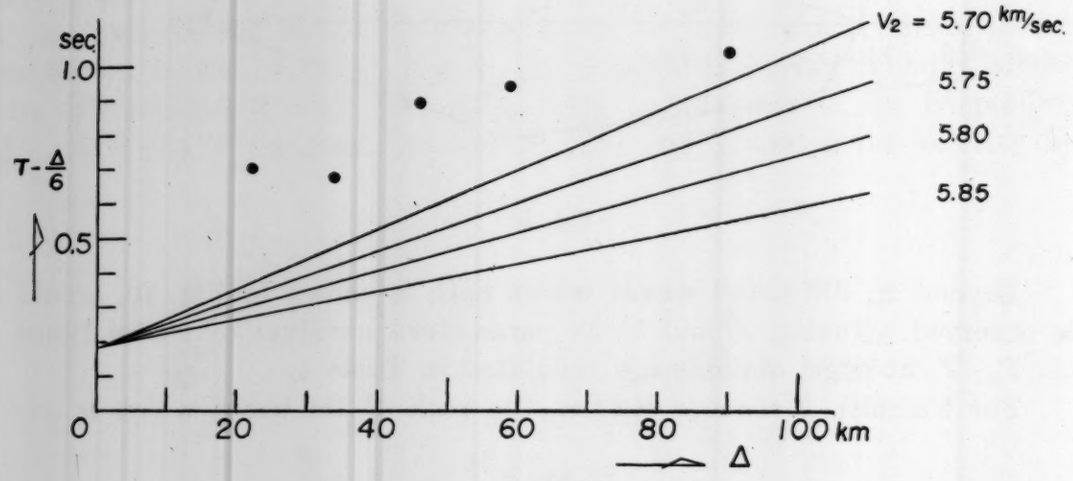

Fig. 11.

As apparent from the figure, observed travel times are systematically much later than the calculated values. Therefore, there should be a certain surface layer on the P_2 layer. As for this surface layer, we have no sufficient data to estimate its velocity. The western extension of the P_1 layer under Isibuti must end at 3 km from Isibuti, if we prolong its lower boundary to the west. Hence, there is no gua-

rantee for taking this layer to be the same one as the P_1 layer.

If we assume the existence of the P_1 layer in the western extension, its thickness can be calculated. Taking V_2 as the parameter, retardation δT of the travel time due to this layer, and the corresponding thicknes of the layer, Z, are tabulated in Table 5.

Table 5.

Station \ V_2	δT				Z			
	5.75	5.80	5.85	5.90	5.75	5.80	5.85	5.90
Katurazawa	0.36	0.40	0.43	0.47	1.0	1.1	1.2	1.3
Yuzawa	0.25	0.31	0.36	0.41	0.70	0.86	1.0	1.1
Innai	0.38	0.46	0.53	0.60	1.1	1.3	1.5	1.7
Mamurogawa	0.34	0.43	0.52	0.61	0.95	1.2	1.4	1.7
Sinasawa	0.20	0.34	0.48	0.62	0.56	0.94	1.3	1.7

Comparing δT with the plot in Fig. 11, we see that 5.80 km/sec for V_2 is most compatible.

(iv) *Form of the P_1 layer in the KW profile*

As stated before, we can assume practically that the P_2 layer is exposed to the surface near Kamaisi shot point. Under this assumption, the calculated value T_0-T_c is tabulated in Table 6.

Table 6.

Station \ V_2	5.75	5.80	5.85	5.90
Umanokiuti	0.06	0.07	0.07	0.08
Ide	−0.6	0.01	0.05	0.11
Mizusawa	0.11	0.19	0.27	0.35

There remains some possibility that the initial pulse observed at Ide or Mizusawa might pass through the P_2 layer. We cannot ascertain this point at present, because the accuracy of determination of the P_3 layer is not sufficient for this purpose.

Here a remark should be added to the travel time at Umanokiuti. At this station we aimed mainly at the observation of reflected waves, and 11 pick-ups were arranged on a nearly straight line. The shot time was marked with the direct connection to the shot point, and the time

mark was put at intervals of 1/100 sec. Travel times at these 11 points are plotted in Fig. 12.

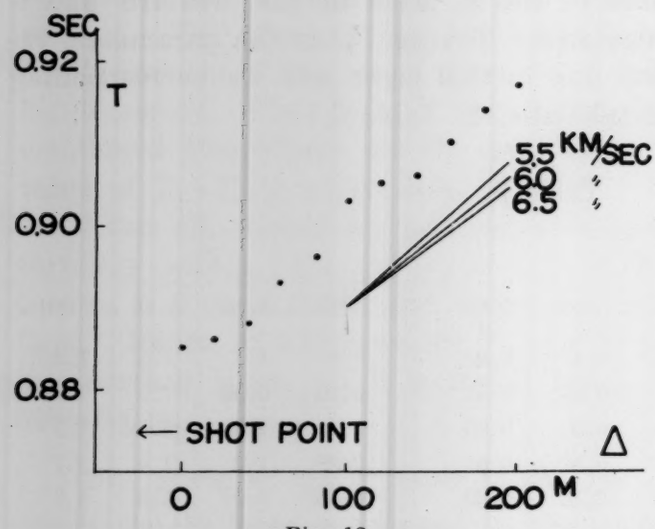

Fig. 12.

The apparent velocity deduced from this travel time curve is nearly the same as V_2. The travel time and epicentral distance adopted for calculating Table 6 are mean values of these 11 points.

The residue, $T_0-T_c=7/100$ sec, reveals the existence of a certain superficial layer, but we have no data for determining its velocity.

(v) *Summary of the study of the form of the P_1 layer in the E–W profile*

Summarizing the results obtained from the IE, IW and KW profiles, we obtain a probable profile of the P_1 layer in the E-W vertical section as shown in Fig. 29.

(vi) *Some considerations on late phases*

At some stations we can distinguish a distinct late phase corresponding to P waves passing exclusively through the P_1 layer. The observed and calculated travel times are shown in Table 7.

Table 7.

Profile	Station	Δ km	T_0 sec	T_c sec
IE	Umadome	4.40	1.74	1.57
〃	Dobasi	12.09	4.70	4.64
IS	Kawatabi	41.9	16.8	16.51

T_0 is always a little larger than T_c. This is probably due to the missing of the very commencement of the said phase in reading the seismogram. In the IE profile we cannot find a corresponding phase at stations beyond Dobasi. In the IW profile we cannot find it anywhere.

These facts are quite compatible with our cross section in the E-W profile. In the IS profile, the corresponding late phase is not distinctly discernible beyond Kawatabi. It may be too hasty, however, to deny the existence of the P_1 layer in the southern extention, because we do not know the exact form of the P_1 layer in the KW profile in the southern part.

10. Form of the lower boundary of the P_2 layer

Our process of analysis was briefly given in R.A.R. We will proceed to detailed discussions.

(i) *Travel time for an inclined layer boundary*

As stated in section 8, as for V_3 (6.1～6.3 km/sec) waves, the intercept time for the Isibuti shots is considerably larger than that for the Kamaisi shots, and the epicentral distance of the intersection with the V_2 curve is also larger for Isibuti shots than for Kamaisi shots. These facts reveal that the depth of the lower boundary of the P_2 layer may be deeper under Isibuti than under Kamaisi, i.e. the boundary is inclined with a certain dip and strike. The relation between shot point O, station P, dip θ, strike Θ_0, azimuth of OP, Θ, etc. is shown in Fig. 10 in R.A.R.[3] Θ_0 and Θ are measured from the north over the east.

The travel time for waves passing through the lower layer is given by

$$T=\frac{2h\cos i}{V_2}+\frac{\Delta\sin(i+\theta')}{V_2}\ ,$$

where

$$\sin i=V_2/V_3 \qquad \text{and} \qquad \sin\theta'=\sin\theta\cdot\sin(\Theta-\Theta_0)\ .$$

θ' is the apparent dip of the boundary in the direction OP, i.e. in the plane including OP and perpendicular to the boundary.

If θ is small and small terms higher than θ^2 are neglected, we obtain

$$T=\frac{2h\cos i}{V_2}+\frac{\Delta}{V_3}+a\Delta\sin(\Theta-\Theta_0)\ ,$$

where

$$a=\theta/V_3\tan i\ .$$

3) In the text of R.A.R., H_0 and H are written for Θ_0 and Θ_1.

The third term on the right hand side represents the effect of the dip of the boundary. When Θ has small fluctuations around Θ_0, corresponding fluctuations appear in the travel time T, or $T-(\Delta/V_3)$.

When the P_2 layer is covered by a thin superficial layer P_1 the following reduction δT for the travel time is necessary in order to apply the above equation directly. Referring to Fig. 13,

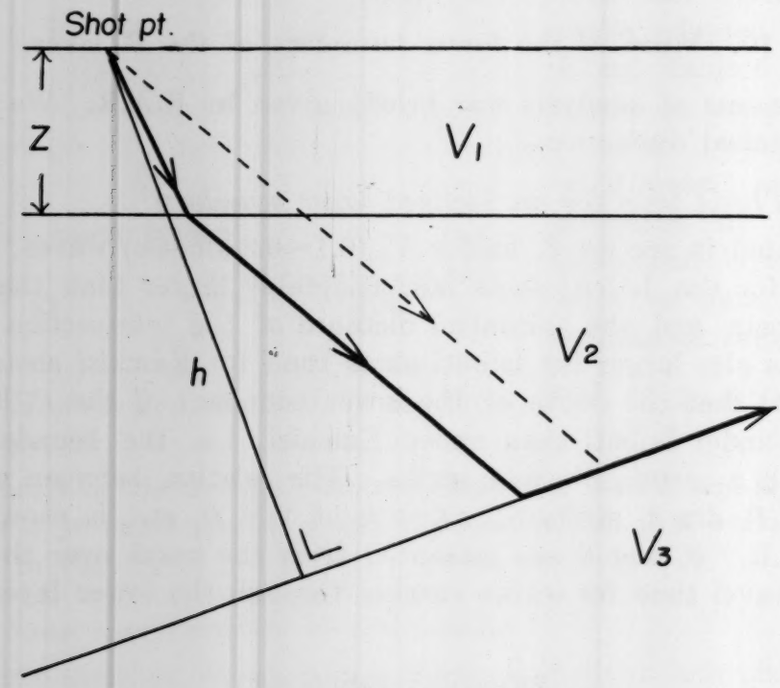

Fig. 13.

$$\frac{\delta T}{Z}=\frac{\tan(i_2+\theta')-\tan i_1}{\cos i_2}\left\{\frac{\cos(i_2+\theta')}{V_3}+\frac{\sin\theta'}{V_2}\right\}+\frac{1}{V_1\cos i_1}-\frac{1}{V_2\cos(i_2+\theta')},$$

where

$$\sin i_1=V_1/V_2\,,\qquad \sin i_2=V_2/V_3\,,\qquad \sin\theta'=\sin\theta\cdot\sin(\Theta-\Theta_0)\,.$$

(ii) *Comparison of the fluctuation of the travel time with* $\Delta\sin(\Theta-\Theta_0)$

Taking V_3 and Θ_0 as parameters, we get graphs for $\Delta\sim T-(\Delta/V_3)$ and $\Delta\sim\Delta\sin(\Theta-\Theta_0)$ in each profile. Figs. 14, 15, and 16.

In these figs, stations, where the first wave does not pass probably through the P_3 layer, are omitted. In the KW profile, the reduction for the superficial layer is applied. In other profiles, it is omitted, as the true superficial layer is not known for certain.

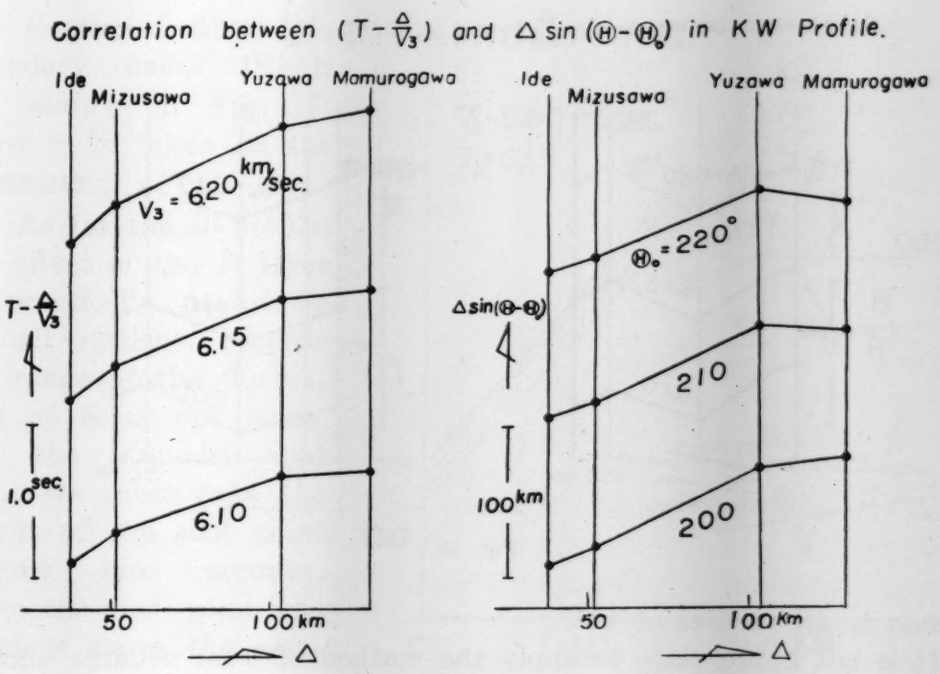

Fig. 14.

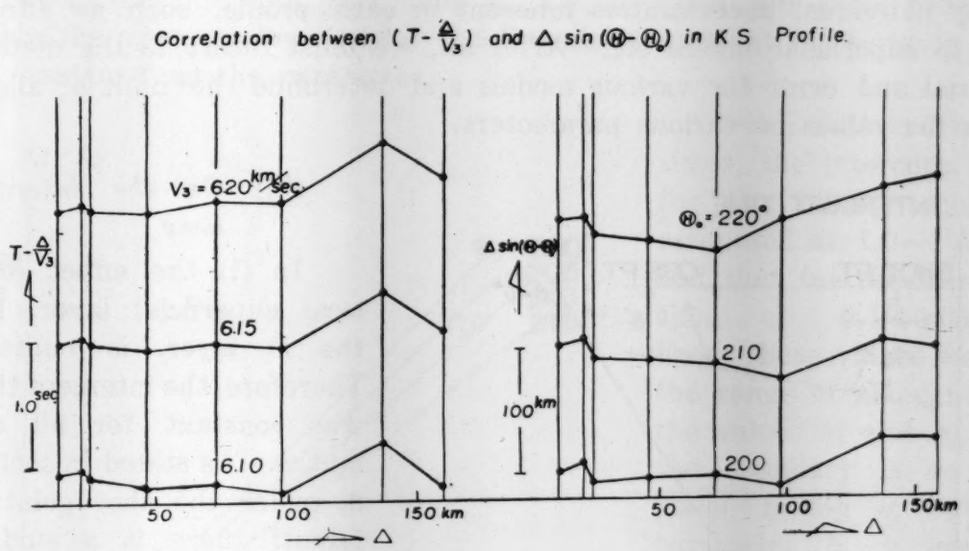

Fig. 15.

In these figs. we can find remarkable correlations between $T-(\Delta/V_3)$ and $\Delta \sin(\Theta-\Theta_0)$. In other words, we can conclude that the boundary between layer P_2 and layer P_3 in each profile is an inclined plane. In the next place, we must discuss, whether the dip, strike, and V_3 are

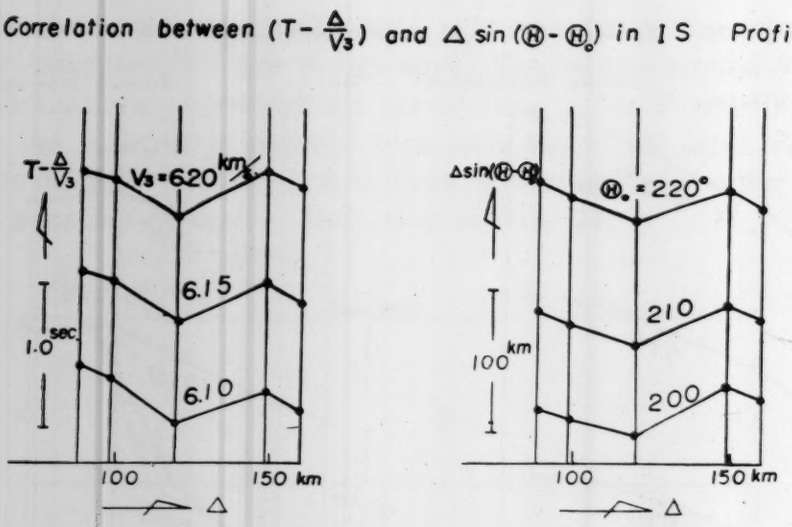

Fig. 16.

common to all profiles or not.

It is not appropriate to apply the method of least squares unconditionally to the result shown in Figs. 14, 15 and 16, because there are many individual uncertainties inherent in each profile, such as effects due to superficial layers etc. After all, we must resort to the method of trial and error for various models and determine the limit of allowance for values of various parameters.

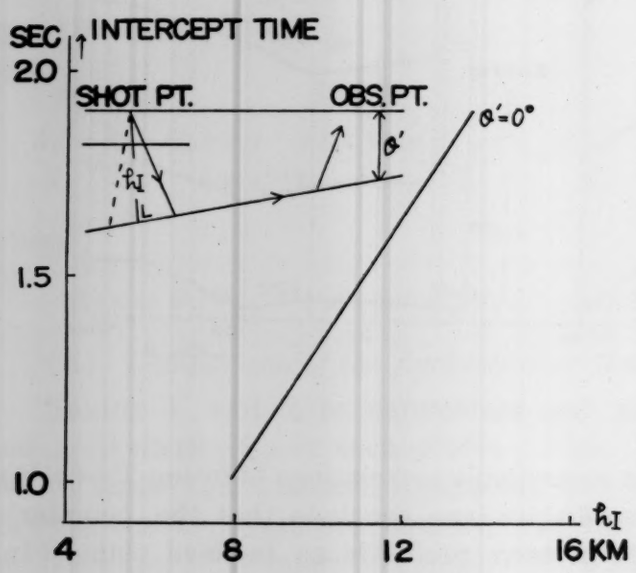

Fig. 17.

(iii) *On the intercept time*

In (i) the effect of a local superficial layer, say the P_1 layer, is omitted. Therefore, the intercept time was constant for all azimuths. As stated in section 9, under the shot point at Isibuti there is a surface layer P_1. This fact must be taken into account. For the IE profile, the path through the P_3 layer and the relation between the intercept time and h_1, i.e.

the depth of the P_2P_3 boundary under Isibuti are shown in Fig. 17. Here θ' is taken as the parameter.

As for the IS profile, the effect of the P_1 layer is practically invariable for all stations, because the range of the fluctuation of Θ is not large. For the Kamaisi shot point we must take the height of the shot point (500 m) into account. When the shot point has a height above the reference surface, the relation between the intercept time and h_k, i.e. depth of the layer boundary below the mean sea level under the Kamaisi shot point is shown in Fig. 18, taking θ' as the parameter.

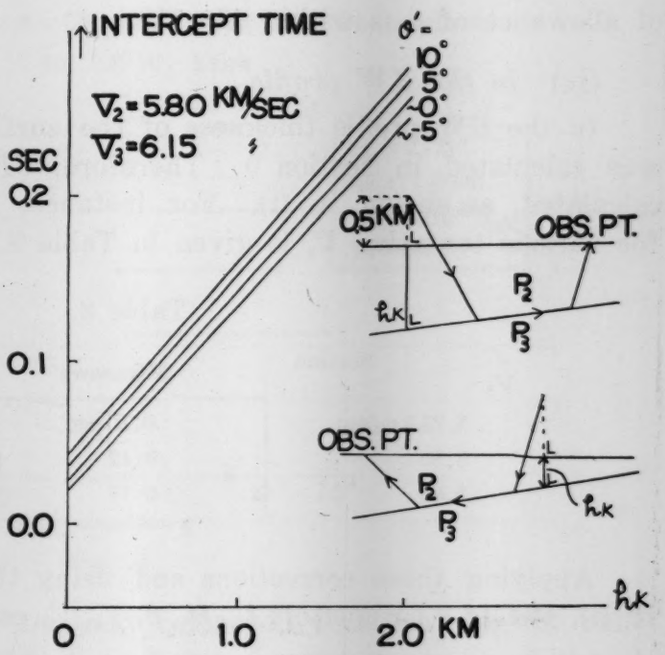

Fig. 18.

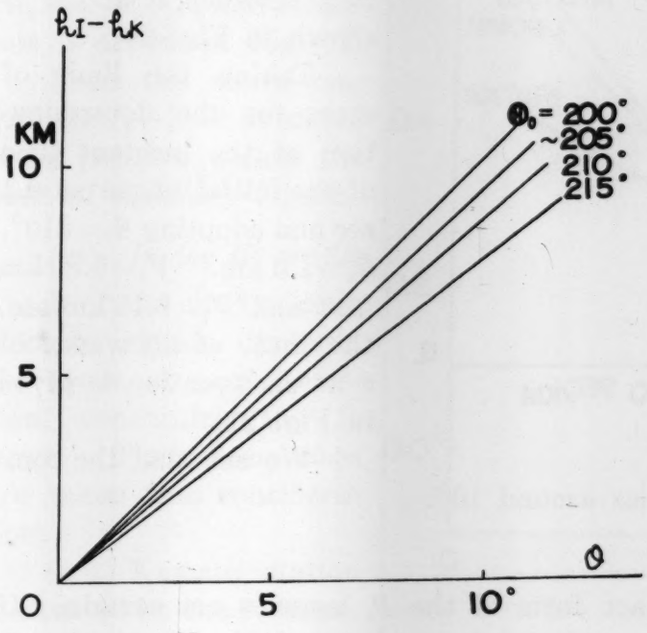

Fig. 19.

From observed travel times, the intercept time for the Isibuti shot is estimated at 1.0～1.6 sec, and that for the Kamaisi shot at 0.1～0.03 sec. From these values we get the range of allowance of the values h_1 and h_k. If the boundary is on one plane, taking Θ_0 as the parameter, h_1-h_k can be calculated geometrically for θ. The result is shown in Fig. 19.

Within the limit of allowance of h_1-h_k and Θ_0, the corresponding limit

of allowance of θ is within 4°~11°.

(iv) *In the KW profile*

In the KW profile thickness of the surface layer at each stations was calculated in section 9. Therefore, δT due to this layer can be calculated, as shown in (i). For instance, taking $V_3=6.20$ km/sec, δT for various tentative V_2 is given in Table 8.

Table 8.

V_2 \ Station	Mizusawa	Yuzawa	Mamurogawa
5.75 km/sec	0.10 sec	0.21 sec	0.28 sec
5.80	0.12	0.26	0.36
5.85	0.17	0.30	0.42

Applying these corrections and using the formula given in section 10 (i), one of 5 parameters h_k, Θ_0, θ, V_3, V_2 can be calculated, if any four of them are given. It is simplest to calculate θ as an unknown. Taking $V_2=5.80$ km/sec and V_3 as the parameter, the relation between θ and a is shown in Fig. 20.

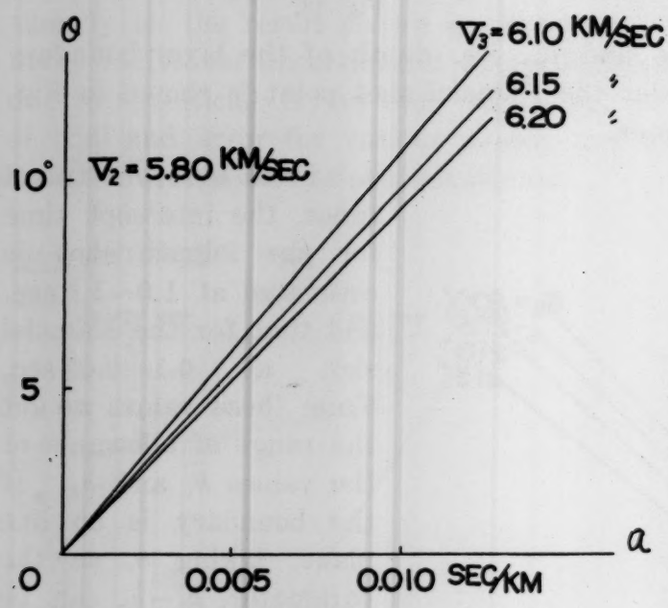

Fig. 20.

Taking the limit of error for the determination of the incident time of the initial phase as 0.1 sec and adopting $\Theta_0=210°$, $h_k=1.0$ km, $V_2=5.80$ km /sec and $V_3=6.15$ km/sec, the limit of allowance of θ at each station is given in Fig. 21.

We see that the common range for all stations lies around 10°.

(v) *In the IS profile*

In the IS profile the exact form of the P_1 layer is not certain. If we calculate the value of θ on the basis of observed T, and if the P_1

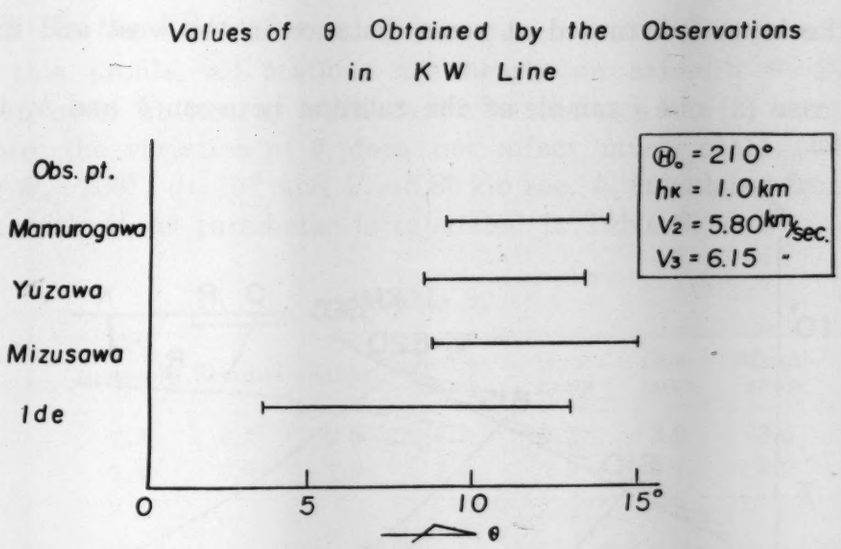

Fig. 21.

layer is absent, it comes out too large compared with that for the existence of the P_1 layer, because T_0 is larger for the existence of the P_1 layer than for its absence.

For instance, taking $\theta_0=215°$, $h_k=1.0$ km, $V_2=5.80$ km/sec and $V_3=6.15$ km/sec, T_0-T_c and θ relation is shown in Fig. 22.

From the above reasoning, T_0-T_c is expected to be positive within the limit of accuracy 0.1 sec.

(vi) *In the IE profile*

In this profile only Kamaisi station comes in the scope of our discussion, concerning the P_3 layer. Then two cases are taken into consideration.

(a) Kamaisi station is situated on the P_2 layer.

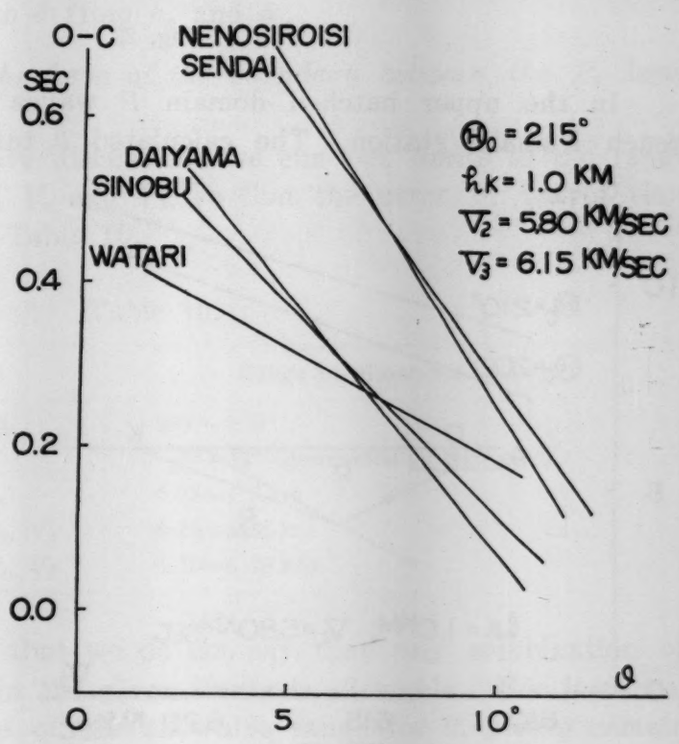

Fig. 22.

(b) It lies directly on the P_3 layer or at least the shallowest posi-

tion of the layer is situated at some distance in the west and its depth is small.

For case (a) one example of the relation between θ and h_k is given in Fig. 23.

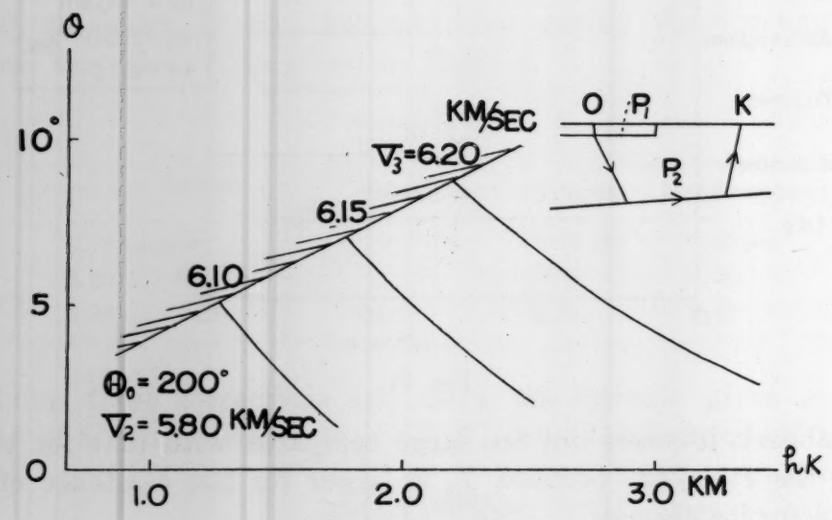

Fig. 23.

In the upper hatched domain P waves through P_3 layer cannot reach Kamaisi station. The calculated θ turns out too small, judging from other data, and untenable.

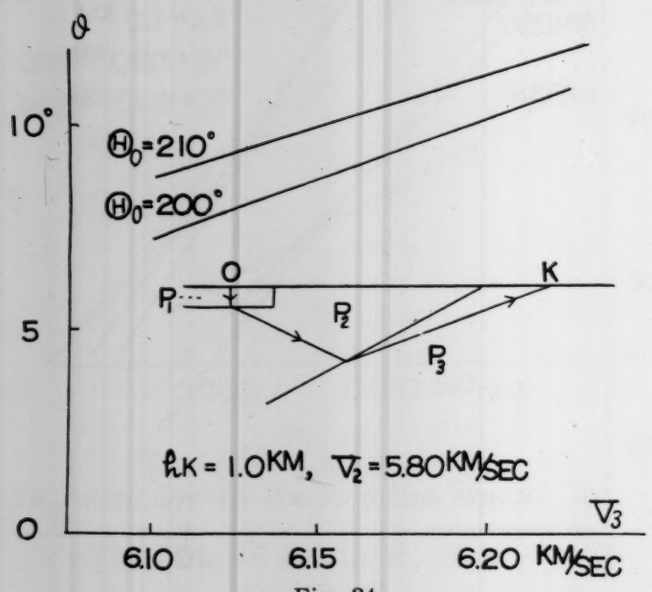

Fig. 24.

For (b) θ and V_3 relation is shown in Fig. 24.

The domain of θ for existence of case (b) is above 3.5°.

It is remarked that the incident time of the first phase at Kamaisi is read 14.84 sec in this investigation instead of 15.33 sec in the 1.2[4] report. The latter value is interpreted as a late phase.

4) Research group for explosion seismology, B.E.R.I., **30** (1953), 279.

(vii) *In the KS profile*

In this profile, all stations are nearly on azimuth $\Theta=200°$, and moreover even at nearby stations waves through the P_3 layer appear. Therefore, the variation of θ does not affect much other parameters. Putting $\Theta_0=200°$, $\theta=10°$ and $V_2=5.80$ km/sec, h_k calculated from various stations with V_3 as parameter is tabulated in Table 9.

Table 9.

V_3 \ Station	Nakasone	Setamai	Sakari	Kesen-numa	Sizu-gawa	Ona-gawa	Mukai-yama	Huna-oka
6.15	2.3	2.1	2.8	2.3	2.7	2.9	3.5	3.5
6.20	2.4	1.9	1.9	2.0	2.9	2.1	4.9	2.7

In this calculation, the effect of a superficial layer on the travel time is not taken into account. Hence, the real h_k cannot be larger than the above shown value, namely it must be smaller than 2.0 km.

In (iii) we put an upper limit to θ from the intercept time. Here we can also put a limit to θ from h_k and h_1.

(viii) *Summary on the form of the boundary between the P_2 layer and P_3 layer.*

Summarizing the above discussions we can put limits to the range of variation for Θ_0, θ, h_k, V_2 and V_3, so that the error of travel time does not exceed 0.1 sec. Table 10.

Table 10.

Parameter		Range of allowance
strike	Θ_0	200°～210°
Dip	θ	6°～11° (downward to the west)
Depth at Kamaisi	h_k	0.75～1.5 km
Velocity in layer	P_2, V_2	5.75～5.85 km
〃	P_3, V_3	6.10～6.20 km

It must be remarked that we do not say that any combination of these five quantities within the given limits is allowable. For instance, we will give an example of the allowable range for θ, giving certain definite values to other parameters (Fig. 25).

In case (a) we can choose a common range of θ, 9°～10°, compatible

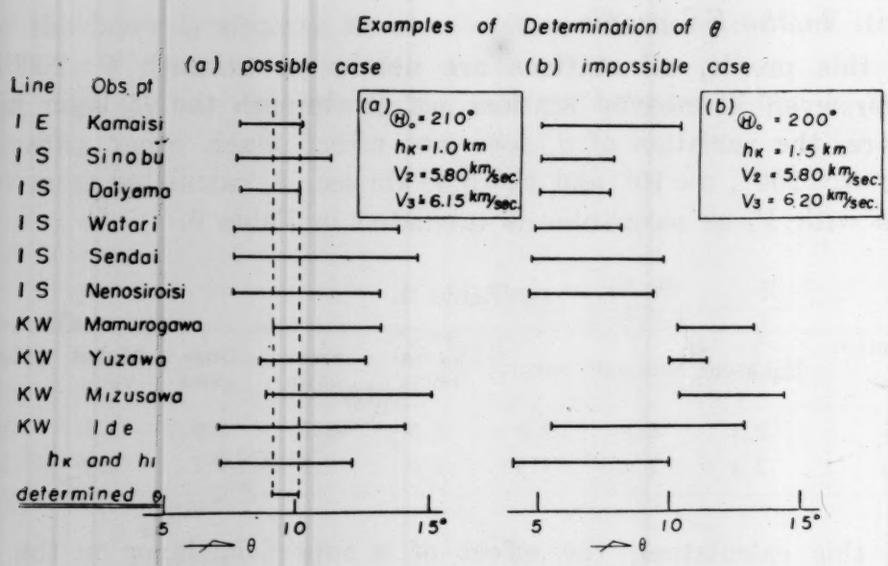

Fig. 25.

for all stations. In case (b) we cannot choose such a common range, and thus such a combination should be rejected.

After all, the range of allowance given in Table 10 is the broadest one within which the compatible range of each parameter falls for some choice of other parameters within their above given range.

(ix) *Consideration from reflected waves*

In profile KW seismograms with 11 elements were obtained at Umanokiuti for the purpose of obtaining reflected waves. On the record very distinct reflected waves can be seen about 0.1 sec after each initial phase. The travel time is given in Fig. 26.

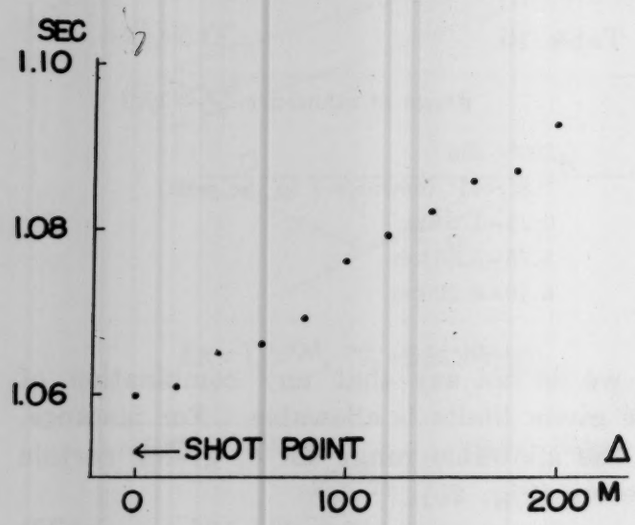

Fig. 26.

If we take these phases for waves reflected at the P_2P_3 boundary, h_k turns out 0.3~0.7 km.

(x) *Consideration from late phases*

The most distinctly ob-

served late phase due to waves through P_2 layer in the IE profile is that at Kamaisi. As stated in (vi) this phase was taken for the initial phase in I.2 report[5]. The path for this phase is expected to be as shown in Fig. 27.

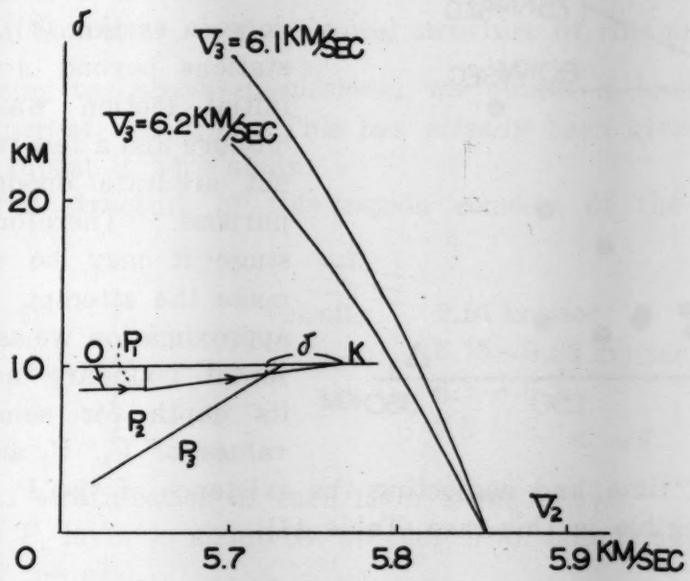

Fig. 27.

Length δ of a part of this path, i.e. the part in P_3 layer, can be calculated from its travel time. Taking V_3 as a parameter, the relation between δ and V_2 is shown in Fig. 27. As apparent from the figure, about 10 km is probable.

In other profiles, late phases expected to be due to waves through P_2 layer are observed at Sendai, Daiyama, and Sinobu for Isibuti explosions and at Sizugawa, Onagawa, Mukaiyama, Hunaoka, Kaneyama, and Kawamata for Kamaisi explosions. These facts will serve as other confirmatory evidences for the existence of the P_2 layer at least under these regions.

(xi) *The* P_4 layer

As stated in section 6, travel times corresponding to velocity 7.5～8.0 km/sec are distinguished at stations beyond 160～170 km on both IS and KS profiles. A graph for $T-(\Delta/8)$ and Δ is shown in Fig. 28.

The intercept time is about 5～6 sec. This fact reveals the existence of a layer, say P_4, under the P_3 layer. This layer may correspond

5) *l. c.* (4)

probably to the so-called P_n layer, because of the velocity.

Travel times are not on a straight line, but fluctuate around it. The exact form of the upper boundary of the P_4 layer cannot be discussed as precisely as was done in section (vi), because at stations beyond $\Delta = 150$ km the initial motion was sometimes obscure and a few readings were not accurate enough for the purpose. Therefore, in this stage it may be wise not to make the attempt. As a rough approximation we assume a horizontal boundary and calculate its depth for some allowable values of V_2, V_3 and V_4, using the intercept time and neglecting the existence of the P_1 layer, as its effect is negligible in this case (Table 11).

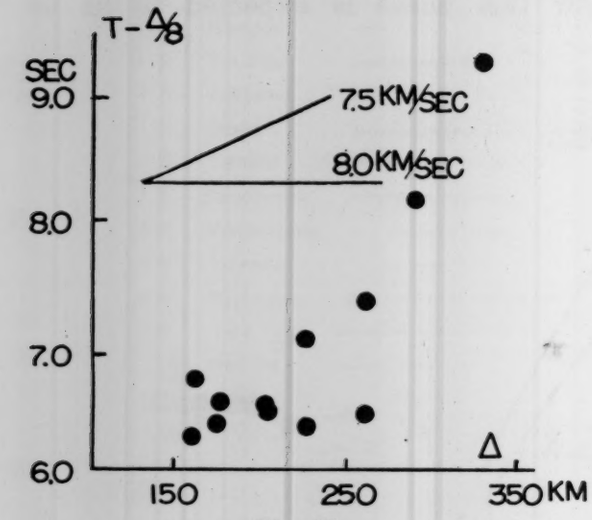

Fig. 28.

Table 11.

Profile	V_3	V_3	V_4	depth of layer P_4
IS	5.8	6.2	8.0	24
KS	5.8	6.2	8.0	24
IS	5.8	6.1	7.5	21
KS	5.8	6.1	7.5	22
IS	5.8	6.1	8.0	20
KS	5.8	6.1	8.0	23

Thus, probable ranges of the apparent depth of the layer and the apparent velocity in it can be taken as 20~25 km and 7.5~8.0 km/sec respectively.

(xii) *Consideration from reflected waves*

In the case of the K.2 explosion a reflected phase with travel time 7.33 sec was observed at Umanokiuti. As stated in 10 (ix), the depth of the P_2P_3 boundary under this station is very small. Thus, it is very probable that these reflected waves are due to the P_3P_4 boundary. Using

the relation $TV_3/2=\sqrt{\Delta^2/4+h^2}$, where T is the travel time, V_3 the velocity in layer P_3, Δ the epicentral distance of Umanokiuti and h the depth of the boundary, we get $h=22\sim23$ km. This value is not affected much by the surface correction, and nearly equal to the value obtain in (xi).

11. Summary on the Crustal structure of this area

Summarizing the above discussions, we obtain a broad aspect of crustal structure of this area. This has already been given in R.A.R., however, we repeat it here again.

The crustal structure of this region consists of the following 4 layers.

Layer		velocity	
	P_1		2.51 km/sec
	P_2		5.75~5.85 km/sec
	P_3		6.1 ~6.2
	P_4		7.5 ~8.0

Pattern of stratification of each layer is as follows.

(1) The P_1 layer is about 530 m deep near Isibuti and inclined at 9° ca. toward the east.

(2) The P_1 layer ends abruptly at a point 14 km east from Isibuti. In the further east near Mizusawa and Umanokiuti a thin surface layer is found.

SCHEMATIC ILLUSTRATION OF CRUSTAL STRUCTURE IN THE AREA

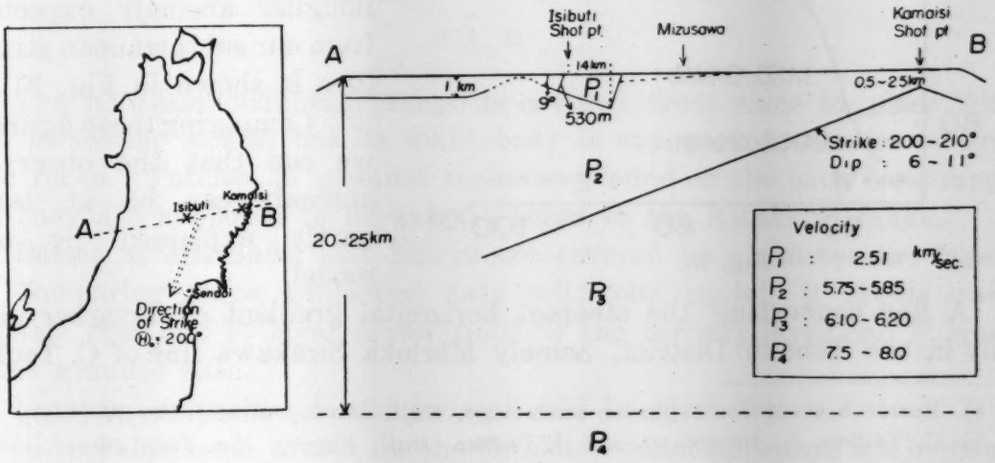

Fig. 29.

(3) In the west near Isibuti the P_1 layer is very thin or lacking. Further west, however, it again takes a depth of about 1 km.

(4) Near the Kamaisi shot point the P_1 layer is not found.

(5) South of the Isibuti shot point the P_1 layer is found, but its exact form is not known.

(6) The boundary between the P_2 and P_3 layers is probably a plane with strike 200°~210°, and dip 6°~11 downward to the west.

(7) The depth of the P_4 layers turns out to be 20~25 km, if it is taken as horizontal.

A general view of the east-west cross section is given in Fig. 29.

Observations of four smaller blasts were made at the east edge of the area studied. A brief sketch of the results was given also in R.A. R., but the details are described in a separate paper[6].

12. Comparison with gravimetry and surface geology

(i) *From gravimetry*

From the Bouguer anomaly of the gravity given by C. Tsuboi[7], A. Jitsukawa, and H. Tajima, Fig. 30, giving those between Isibuti and Kamaisi, is obtained.

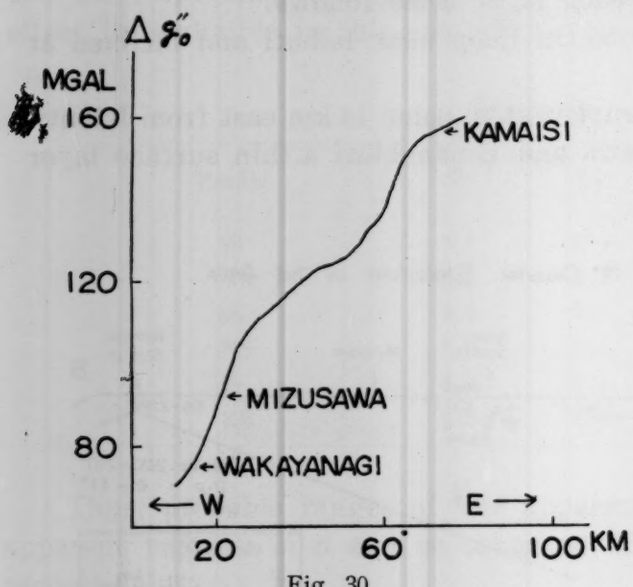

Fig. 30.

On the other hand, assuming the density difference $\Delta\rho$ between P_2 and P_3 layer as 0.05~0.15, the Bouguer anomaly expected from our subterranean structure is shown in Fig. 31.

Comparing these figures, we see that the observed anomaly can be at least partly explained by our model.

A line connecting the steepest horizontal gradient of Bouguer anomaly in the Tôhoku District, namely Morioka–Sirakawa line of C. Tsuboi

6) Research group for explosion seismology, *Bull. Earthq. Res. Inst.*, **37** (1959).

7) C. TSUBOI, A. JITSUKAWA and H. TAJIMA, *Bull. Earthq. Res. Inst., Suppl. Vol.* **4** (1956), 311–406.

et al., has also nearly the same azimuth as the strike of the P_2P_3 boundary as stated in section 11 (6).

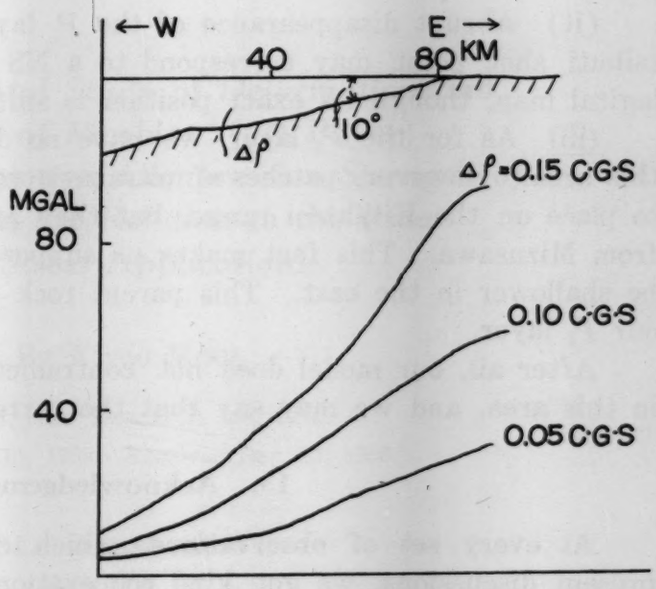

Fig. 31.

(ii) *From surface geology*

Geological structure in the east-west cross section passing Isibuti and Kamaisi inferred from the surface geology is schematically given in Fig. 32.

In the neighbourhood of Isibuti shot point a tertiary layer extends eastward, but it is lacking at Mizusawa. Along the back bone mountain range it is very thin and further west it increases again in depth.

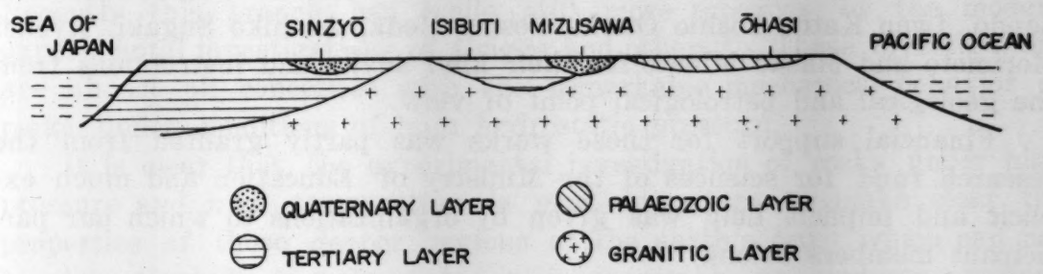

Fig. 32.

The Kitakami mountain range is covered from place to place with thin palaeozoic strata, but its main body is supposed to consist of granitic rocks. Patches of granitic rocks are found on the back bone range and they are supposed to be akin to those in the Kitakami range.

Basins at Mizusawa and Sinzyô are covered by a quarternary layer.

Comparing these geological data with our model, it seems very probable that our P_1 layer corresponds to the tertiary layer and P_2 layer to the granitic base.

Further comparison in some detail will be given below.

(i) Palaeozonic strata on the Kitakami mountain range are omitted in our model. It means their trivial thickness.

(ii) Abrupt disappearance of the P_1 layer at 14 km east from the Isibuti shot point may correspond to a NS fault line shown on a geological map, though its exact position is shifted somewhat eastward.

(iii) As for the P_3 layer, we nave no direct geological evidence in this area. However, patches of ultrabasic rocks are exposed from place to place on the Kitakami range, but they are scarcely found westward from Mizusawa. This fact makes us suppose that their source should be shallower in the east. This parent rock may probably correspond to our P_3 layer.

After all, our model does not contradict the geological knowledge in this area, and we may say that the correspondence is rather good.

13. Acknowledgement

At every set of observations, which constitute the basis of our present discussions, we got kind cooperation of inestimable value from many institutions, organizations, and authorities, for which we are much obliged. They were mentioned in each case in our previous publications, so that we may be allowed not to repeat them here.

Our sincere thanks are due to Professors Kenzo Yagi, Tadamasa Sendo, Iwao Kato, Yoshio Onuki, Yoshio Ueda, Asahiko Sugaki, Ryohei Morimoto and Masao Minato for their kind advice and instructions from the geological and petrological point of view.

Financial support for these works was partly granted from the research fund for sciences of the Ministry of Education and much explicit and implicit help was given by organizations to which our participant members belong.

Last, but not the least the present writer is much obliged to Mr. S. Asano for his devotedly sincere cooperation in preparing this paper and to Miss Yoriko Utida, who prepared many text figures in a short time.

---

7. Bakuha-Zisindô ni yoru Tôhoku-Tihô no Tikaku no Kôzô.

Tôkyô-Daigaku Rigakubu, Tikyû-Buturi-gaku Kyôsitu,

MATUZAWA-Takeo.

Isibuti 3 Kai oyobi Kamaisi 2 Kai no Daibakuha Zisindô no Kansoku wo subete kangaeawasete mitibiki dasita Tikaku no Kôzô ni tuite no Aramasi wa 1954 nen no Roma no I.U.G.G. Kaigi no Hôkoku ni dete iru. Koko dewa sorera wo mitibiki dasu Toki ni okonatta Keisan naisi wa Kenkyû no Tedate ni tuite kuwasiku nobete aru.

BULLETIN OF THE EARTHQUAKE
RESEARCH INSTITUTE
Vol. 37 (1959), pp. 155-170

8. *Experimental Study of Deformation and Fracture of Marble.* (1st Paper) *On the Fluctuation of Compression Strength of Marble and the Relation to the Rate of Stress Application.*

By Kiyoo MOGI,

Earthquake Research Institute.

(Read Sept. 16, 1958.—Received Dec. 25, 1958.)

1. Introduction

Since the experiment of deformation of marble under high pressure by Adams and Nicolson[1], the study of the physical or the mechanical properties of rocks which constitute the earth's crust from the geophysical stand point has been carried out by many investigators. Recently this branch has made still more progress by the modern experimental investigations of Griggs and others[2]. These investigations are almost all concerned with the remarkable mechanical behavior of rocks under conditions of high hydrostatic pressure.

It is clear that the experimental investigation of rocks under high pressure and high temperature is most important to make clear the properties of those deeper regions of the earth's crust which can not be investigated directly. As it is inevitable to undergo various restrictions technically in these experiments of high pressure and high temperature, these experiments have been aimed at some limited subjects, at least, until the present.

On the other hand, the mechanical properties of rocks are very complicated and many fundamental problems under the conditions of

1) F. D. ADAMS and J. T. NICOLSON, *Roy. Soc. London Phil. Trans., Ser. A,* **195** (1901), 363.

2) D. T. GRIGGS and W. B. MILLER, *Bull. Geol. Soc. America,* **62** (1951), 853.
D. T. GRIGGS, F. J. TURNER, I. BORG and J. SOSOKA, *Bull. Geol. Soc. America,* **62** (1951), 1385.
F. J. TURNER, D. T. GRIGGS and H. HEARD, *Bull. Geol. Soc. America,* **65** (1954), 883.
E. C. ROBERTSON, *Bull. Geol. Soc. America,* **66** (1955), 1275.
M. S. PATERSON, *Bull. Geol. Soc. America,* **69** (1958), 465.

atmospheric pressure and room temperature, also should be investigated quantitatively. Particularly about the fracture phenomenon, though the fracture strength of rocks should be necessarily obtained with the statistical consideration, we have scarcely found such quantitative works for geophysical purposes.

In general, the physical properties of rocks which constitute the earth's crust are distributed complexly in space and time. For the purpose of investigating the physical law in these complicated variation in nature, it may be necessary to carry out a large number of experiments and to analysis the results statistically. That is a special character of geophysical experiments, compared with the other branches of applied physics. The writer thinks, the distribution and variation of physical properties of rocks may have a quantitative relation with the statistic law of occurence of earthquakes and the rupture strength of the earth's crust, even if it should be a very difficult problem to find this relation.

From the above mentioned stand point, the writer is planning to investigate the fundamental mechanical properties of rocks; elasticity, fracture strength, viscosity and others, especially in reference to their spatial variations. As the first step, the stress-strain relation and the fracture strength of marble specimen which seems to be macro-scopically uniform were investigated by means of the axial compression in the present paper. Especially the relation between the fracture strength and the rate of stress application and the fluctuation of strength are discussed.

2. Preliminary note on the elasticity and the fracture strength of rocks

In the present experiment, the elasticity and the fracture strength of large number of marble specimens are measured in axial compression. These values scatter considerably. However, physical meanings of scattering are different from one another, in the elasticity and the fracture strength. According to the modern physics of matter[3], elasticity is a structure-insensitive property and fracture is a structure-sensitive phenomenon. Therefore the variation of elasticity depends on the macroscopic factors such as chemical and mineralogical constitution. On the other hand, the fracture strength is also affected strikingly by uncertain factors, such as microcracks, thermal vibration, and micro-unhomo-

3) T. YOKOBORI, *Zairyō-kyōdogaku* (1955), 1 (in Japanese).

geneity of structure, in addition to the above mentioned macroscopic factors. As these uncertain factors are obtained only as statistic values, the fracture strength also should be obtained by the statistical analysis of a large number of the values. For investigation of the elastic deformation and the fracture phenomenon of rocks, the above mentioned physical characters of these phenomena seem to be most worthy. In the present paper this problem (the variations or the distribution of the elasticity and the fracture strength) will be discussed in a later section.

3. Method of experiment

Test specimens of marble. A mass of marble (45 cm × 35 cm × 4 cm) is investigated from various physical points. The sample of marble was obtained from a quarry at Mine city, Yamaguti Pref., Japan. The feature is white and nearly homogeneous with the average grain size 1 mm. But no petrological and chemical observation about the sample have been carried out yet. As a reference, a result of chemical analysis of a white marble in the same district[4] is shown in Table 1.

The specific gravities of all test specimens are measured. The average specific gravity is 2.69 (g/cm^3) and the normal deviation is small (0.005).

192 test specimens are cut off by a diamond cutter from the sample and are given the numbers from 1 to 192, as the indication of the original spatial position (Fig. 1). The dimensions of each specimen are (2.5 × 2.5 × 4.0 cm^3) and their compressed planes (1) and (2) are polished up accurately lest the errors from the complete

Table 1. Chemical Composition of Yamaguti White Marble[4].

SiO_2	0.18%
$Al_2O_3+Fe_2O_3$	0.19
CaO	55.40
MgO	0.54
Na_2O	0.09

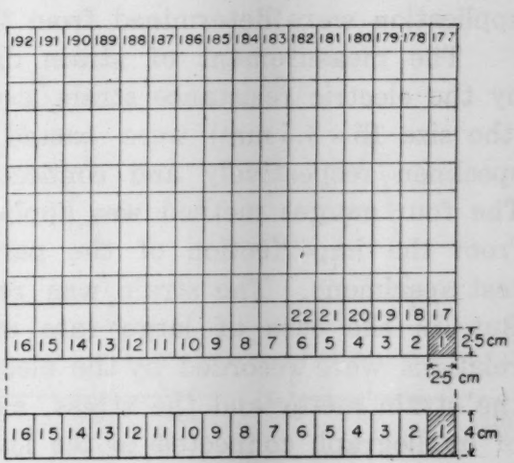

Fig. 1. The sample of marble. The positions of the test specimens from No. 1 to No. 192 are shown.

4) *Honpōsan-kentik u-sekizai* (1921), 259 (in Japanese).

parallel planes should exceed 1/100 mm (Fig. 2).

They were divided to three groups for the following various tests.

(1) About forty specimens were selected to measure the stress-strain curves for various rates of stress application.

(2) About ten, to measure the stress-strain relation for repeated compressional stress.

(3) One hundred and seventeen, to obtain the relation between the fracture strength and the rate of stress application.

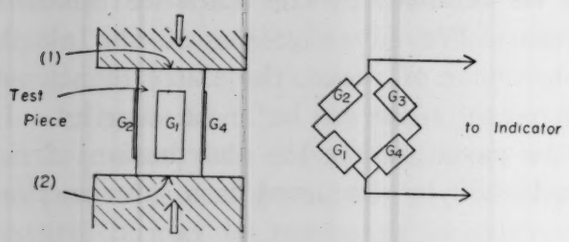

Fig. 2. The strain measurement of axial compression of the test specimen. G_1, G_2, G_3 and G_4 are the paper strain gauges.

Measuring apparatus. The Amsler-type testing machine of 20 tons capacity in the Engineering Research Institute, Faculty of Engineering, University of Tokyo, was used for axial compression of the test specimens of marble. The values of compressional force were read from the load meter of the testing machine and, at the same time, were recorded automatically on the rotating drum with uniform speed. The speed control lever of compression was adjusted by hand-work watching the time-force curves on the drum in order that the compressional force may increase at an approximately constant rate. The rates of stress application were determined from the records of time-force curves.

The measurement of strain of the axial direction was carried out by the electric resistance strain gauge meter. The paper strain gauges (the size 15×3.5 mm) were pasted on the four side planes of the test specimen respectively and connected one another, as shown in Fig. 2. The four gauges method was applied in order to eliminate the errors from the imperfection of the parallelism of compression-planes of the test specimens. The strain was read directly from the strain meter. But, in the case of large rate of stress application, the strain-time relations were recorded by the electromagnetic oscillograph connected to the strain meter and the stress, also, was recorded on the same record of oscillograph connected to the load meter of testing machine by relay system.

The error of the strain measurement is 10^{-6} and of the stress is estimated to be smaller than 5 kg/cm^2 from the many stress-strain curves of elastic deformation of the marble specimens. Thus we can discuss

the fluctuation of fracture strength in the following section.

4. Relation between the compressive fracture strength and the rate of stress application

The mean stress-strain curve for the axial compression tests of several marble specimens under the condition of 1 atmospheric pressure and room temperature is shown in Fig. 9. The curve is linear from zero to about 5×10^{-4} strain and thereafter deviates gradually from the line. And the stress takes an ultimate value and then instantly a brittle fracture occures. But the stress-strain relation in the process of fracture after the stage of ultimate stress value was not acquired in this experiment. The fracture strength in the present experiment is the same as the ultimate stress.

Strictly, the stress distribution in the test specimens in the axial compression is not completely uniform and the concentration of stress takes place at a small degree. However, as the relative values of the elasticity and of the fracture strength are the most important question in the present investigation, the problem of the stress concentration scarcely seems considerable.

A short description of the morphological features of fracture will not be meaningless. The fracture region in the test specimen is shown in Fig. 3. It is interesting that the fluctuation of the angles of

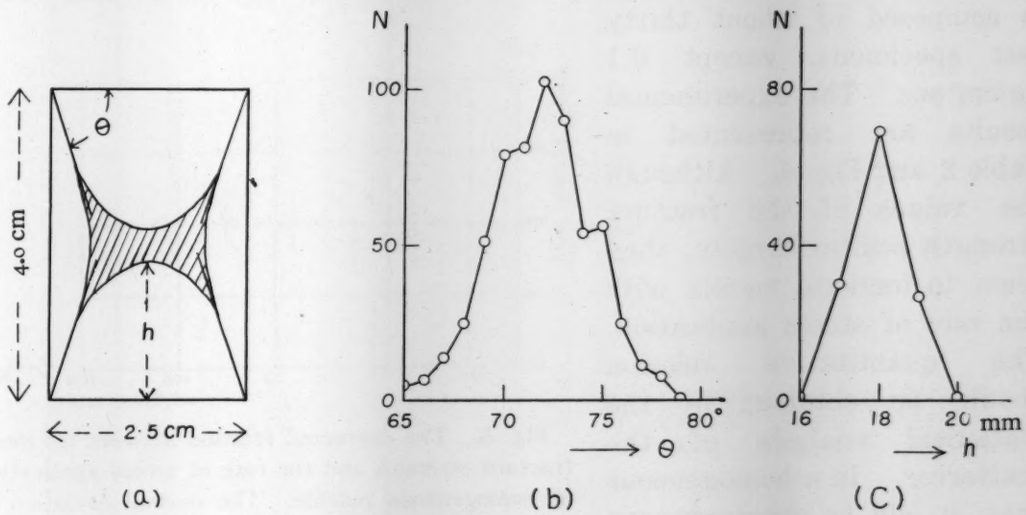

Fig. 3. (a) Fracture region of test specimen. θ: Angle of fracture plane, h: Hight of upper and lower non-fracture parts of pyramid form. (b) Frequency diagram of θ. (c) Frequency diagram of h.

fracture plane is relatively small as illustrated in Fig. 3. The mean values of the angles (θ) and the height of pyramid (h) are as follows.

$$\theta = 71^\circ , \quad h = 18.0 \text{ mm}$$

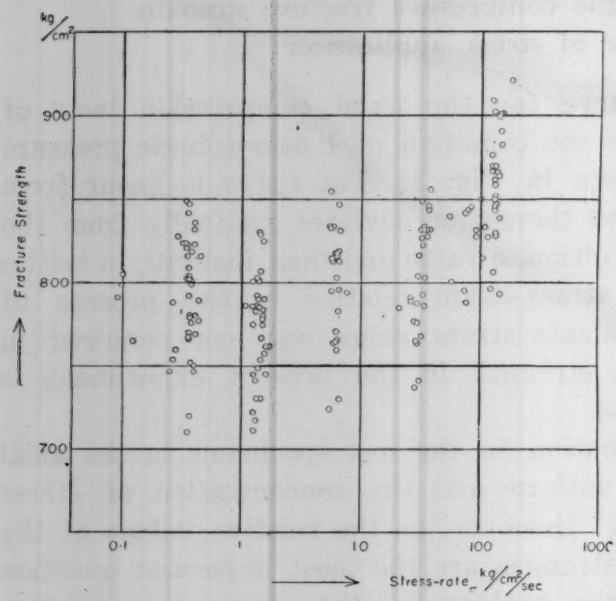

Fig. 4. The measured relation between the fracture strength and the rate of stress application in marble specimens.

The effect of the rate of stress application to the deformation and the fracture strength seems to be an interesting problem from the geophysical stand point.

About concrete, it is known that the fracture strength rises with the increase of the strain rate[5]. However, no systematic investigation on the subject have been carried out about rocks.

To investigate the problem, the fracture strength of marble specimens was measured for the various rates of stress application, that is, about 0.1, 0.36, 1.5, 6.0, 32 and 120 kg/cm² sec. A group tested with similar rates is composed of about thirty test specimens, except 0.1 kg/cm² sec. The experimental results are represented in Table 2 and Fig. 4. Although the values of the fracture strength scatter largely, they seem to increase merely with the rate of stress application. The quantitative relation should be obtained by the statistical analysis of the scattering. In a homogeneous case, it will be obtained very easily by the calculation of

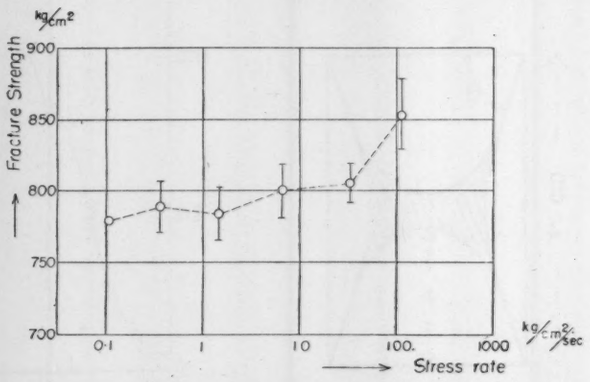

Fig. 5. The corrected relation between the mean fracture strength and the rate of stress application in homogeneous marble. The normal deviation of the fracture strength for each rate of stress application is shown.

5) P. G. JONES and F. E. RICHART, *Amer. Soc. Test. M.*, **36** (1936), 381.

Table 2. The Fracture Strength and Young's Modulus.

No.	Rate of Stress Application	Fracture Strength	Mean Strength	Young's Modulus	No.	Rate of Stress Application	Fracture Strength	Mean Strength	Young's Modulus
	kg/cm² sec	kg/cm²	kg/cm²	× 10⁴ kg/cm²		kg/cm² sec	kg/cm²	kg/cm²	× 10⁴ kg/cm²
1	0.28	760			49	140	792		
2	82	846			50			798	
3	56	840			51	181	921	802	
4	1.07	786			52	0.35	823	792	
5	92	832			53	0.36	770	777	59.6
6	32	827			54	1.28	745	776	61.4
7	1.39	803			55	0.43	789	781	
8	6.2	803			56	73	842	792	
9					57	5.9	764	785	
10					58	0.41	769	783	
11					59	1.34	717	780	58.2
12					60	0.09	791	779	
13					61	103	815	777	
14	1.38	741		59.4	62			748	
15	0.37	710			63	30	741	750	
16	134	852			64	1.52	730		
17	6.4	783			65	6.0	815		
18	0.37	804	801		66	0.27	754	787	
19	57	801	813		67	124	909	793	
20	37	844	809		68	30	817	798	
21	0.28	828	797		69	0.35	766	795	67.2
22	92	828	793		70	128	870	792	
23	26	789	793		71	31	832	799	
24	1.59	790	795		72	1.24	786	805	
25	79	794	789		73	141	866	800	
26	29	766	766		74	33	823	796	
27	1.50	754	759		75	1.37	792	789	
28	5.4	724	758		76	6.7	796	790	
29	32	768	756		77	28	765	759	
30	1.29	711	752		78	1.25	722	757	
31	6.1	771	755		79	6.1	765	748	
32	0.25	747			80	0.40	750		
33	1.57	784			81	1.69	795		
34	6.3	818	801		82	5.6	795	790	
35	0.34	821	815		83	0.43	777	789	
36	1.54	780	805		84	124	877	803	
37	6.2	766	788		85	5.5	834	803	
38	0.40	747	778		86	0.35	809	812	
39	1.42	790	775		87	132	902	815	
40			784		88	34	834	822	
41	75	788	775		89	0.41	823	821	
42	107	834	766		90	134	846	813	
43	28	767	761		91	34	803	794	
44	1.27	775	758		92	1.46	749	776	
45	73	795	759		93	127	796	759	
46	153	793	763		94	29	764	759	
47			759		95	1.36	783	756	
48	0.36	792		61.8	96	6.6	730		

(to be continued)

Table 2. (continued)

No.	Rate of Stress Application	Fracture Strength	Mean Strength	Young's Modulus	No.	Rate of Stress Application	Fracture Strength	Mean Strength	Young's Modulus
	kg/cm² sec	kg/cm²	kg/cm²	× 10⁴ kg/cm²		kg/cm² sec	kg/cm²	kg/cm²	× 10⁴ kg/cm²
97	34	786			145	33	793		
98	1.38	780	793		146	1.46	785	797	
99	6.0	815	796		147	6.2	816	819	
100	0.27	788	810		148			835	
101	1.69	825	818		149	0.36	847	830	65.3
102	6.1	818	815		150	6.7	813	819	
103	0.37	799	824		151	0.35	802	812	66.4
104	0.32	824	828	68.0	152	1.37	786	817	65.8
105	5.5	855	828		153	123	867	826	
106	0.36	802	809		154			826	
107	7.7	794	794	62.8	155	29	804	804	64.2
108	26	791	773	59.8	156			799	
109	0.37	720	762		157	0.096	799	781	
110	1.52	767	766	59.2	158			785	
111	21	785	767		159			804	
112	28	737		58.4	160				
113	1.45	801		60.8	161	0.1	805		61.4
114	150	839	796		162	134	862	813	
115					163			824	
116	0.38	819	817	69.6	164	0.35	842	837	66.8
117	152	891	819		165	0.13	765	835	65.0
118	6.7	831	822	66.6	166			819	
119	1.45	830	822	65.6	167	0.38	801	813	69.0
120	0.33	849	828		168	0.41	836	816	
121	1.24	806	828	65.2	169	6.8	847	815	68.0
122	137	870	814		170	137	859	806	
123	0.41	780	793		171	0.35	816	786	
124	117	828	780		172	136	850	783	
125	139	829	775		173	0.37	779	778	62.0
126	0.37	780	777		174	0.38	752	776	
127	100	850	781		175	148	864	799	
128	29	788			176	37	856		
129	1.62	758			177	0.34	824		
130	5.5	833	798		178	154	901		
131			813		179	32	849		
132	133	844	829		180	1.48	829		
133	5.8	834	827		181	157	901		
134	0.46	816	825		182	37	846		
135	148	900	819		183	1.50	807		
136	36	828	818		184	58	813		
137	0.40	832	820		185	36	832		
138	155	883	811		186	1.54	775		
139	34	832	794		187	6.1	760		
140	1.76	762	794		188	0.38	776		
141	134	806	791		189	1.67	762		
142	38	832	797		190	6.4	819		
143	1.54	778	794		191	0.35	767		66.6
144					192	137	830		

the mean value and the standard deviation. However, for the unhomogeneous case such as the present case, it is necessary to analyse the scattering as statistical distribution after the elimination of the effect of macroscopic-unhomogeneity. As the result of this analysis described in the following section, the relation between the fracture strength and the rate of stress application for marble specimens is obtained as shown in Fig. 5. That is, the compressive fracture strength of marble increases with the rate of stress application, especially remarkable at the large rate, but the effect of stress rate is smaller compared with the case of concrete.

To investigate the relation between the rate of stress application and the deformation, the stress-strain curves were obtained in the cases of various rate of stress application (Fig. 10). According to the result, the effect of rate, also, is not remarkable.

5. The fluctuation and the spatial distribution of fracture strength

The variation of fracture strength seems to depend both on uncertain factors and the macroscopic unhomogeneity. The variation related to the former factors will be in the statistical distribution, "fluctuation" and

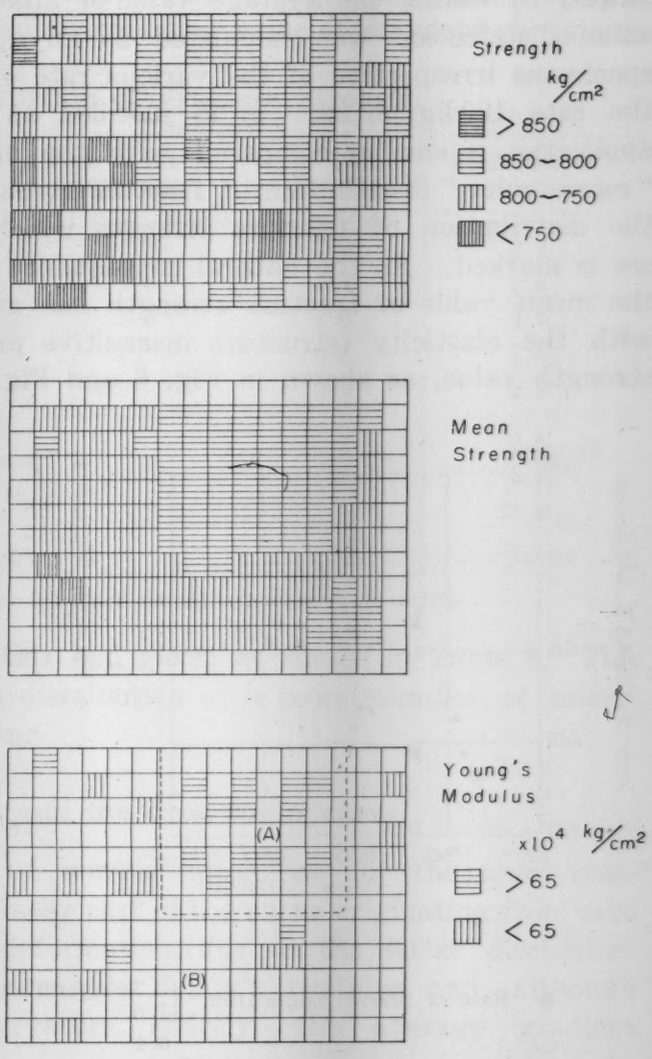

Fig. 6. The distribution of fracture strength and Young's modulus in the sample of marble. "Mean Strength" value of the test specimen is the average value of nine test specimens which consist of the specimens around it and itself.

the one related to the latter has perhaps a tendency of distribution which has a comparatively large dimension in space. These two sorts of variation are discussed in the present section.

The spatial distribution of the fracture strength obtained by compression test is shown in Fig. 6. Although individual values fluctuate, a tendency of distribution is seen. To make clear the spatial distribution related to the macroscopic structure, the fluctuation was eliminated largely by taking the average value of nine test specimens. The mean value distribution was calculated as an approximation of all the test specimens irrespective of the various rate of stress application, except the rate 120 kg/cm² sec. It is justified as the effect of rate of stress application is smaller compared with the spatial variation. Thus, the "mean value" distribution of fracture strength is shown in Fig. 6, and the distribution of fracture strength which has a dimension of 15~20 cm is marked. As the natural consequence of the preceding discussion, the mean value of fracture strength has sufficiently higher correlation with the elasticity (structure insensitive property) than the individual strength value, as shown in Fig. 6 and Fig. 7.

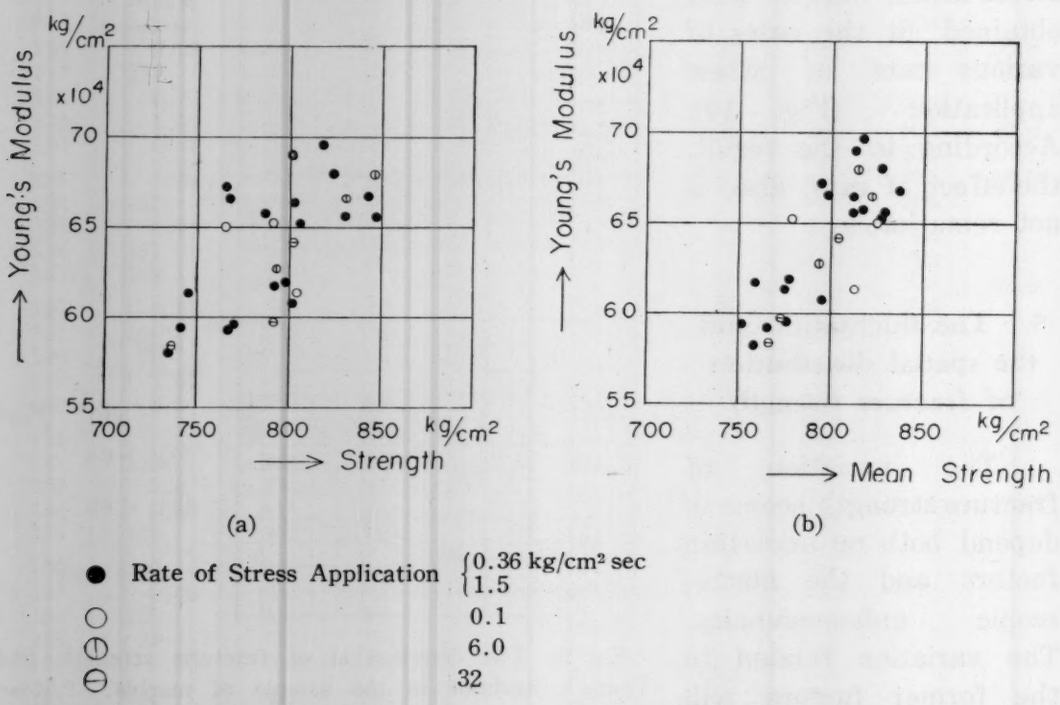

Fig. 7. (a) Relation between the fracture strength and Young's modulus, in the various rate of stress application. (b) Relation between the mean fracture strength and Young's modulus.

The fluctuation of individual strength is obtained as the difference from each mean value. About the group of the various rates of stress application, the total mean value and the standard deviation of the fluctuation of strength were calculated. These relative values of total mean strength for the various rates of stress application are to represent the relative strength of homogeneous marble for the respective rate of stress application. Thus the above obtained relation is shown in Fig. 5, as mentioned in the preceding section. It is interesting that the fluctuation of fracture strength of marble (the value of standard deviation)

Table 3. Fluctuation of Fracture Strength.

Test Specimen	Rate of Stress Application	Mean Value of Strength	Coefficient of Variation
	(kg/cm^2 sec)	(kg/cm^2)	(%)
Marble (homogeneous)	0.36	789	2.2
	1.5	784	2.4
	6.0	799	2.4
	32	805	1.6
	120	853	2.9
Steel (Davidencov et al)[6]			7.6
Cast Iron (Yokobori)[7]			8.8
Glass (Hirata, Terao)[8]			24.0
Glass Filament (Joffe)[9]			23.4

Coefficient of variation=Standard deviation/mean vaule $\times 100$.

is smaller than that of metals and glass, as shown in Table 3. This seems to signify the uniform distribution of a large number of microcracks in the marble specimen.

6. Elasticity and the stress-strain curve

The stress-strain curves of marble specimens for the axial compression are measured. The linear part of the curve originating from zero strain represents the elastic deformation, due to the latter discussion. The gradient of the linear curve is Young's modulus and, although the curve has a small curvature strictly, the average gradient

6) N. DAVIDENCOV, E. SHEVANDIN and F. WITTMAN, *J. Appl. Mech.*, **14** (1947), A63.
7) T. YOKOBORI, *loc. cit.*, (3), 4.
8) M. HIRATA and N. TERAO, *J. Appl. Phys., Japan*, **20** (1952), 234 (in Japanese).
9) A. JOFFE, *Int. Conf. Phys. II.* "The Solid State of Matter," *Phys. Soc. London* (1934), 72.

between zero and 5×10^{-4} strain is obtained as Young's modulus at present. As mentioned above, Young's modulus seems to be independent of the rate of stress application (Fig. 7 and 10).

The spatial distribution of Young's modulus is shown in Fig. 6. As pointed out in the preceding section, it is remarkable that the elasticity has the sufficiently clear relation with the mean values of fracture strength than the original strength values (Fig. 7).

Considering the distribution of the elasticity and the mean fracture

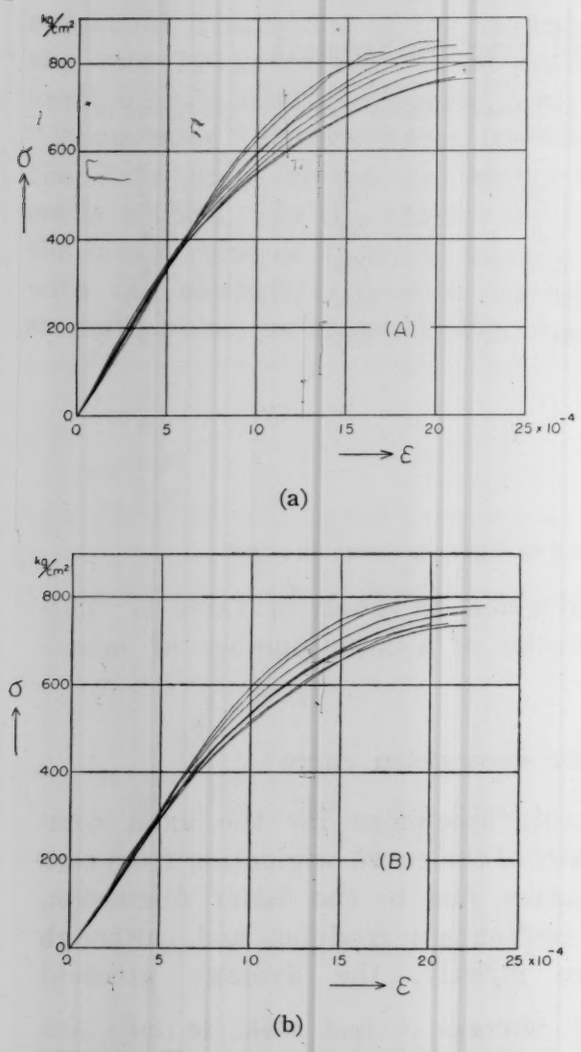

Fig. 8. The two groups of stress-strain curves of the test specimens in the parts (A) and (B) which seem to be homogeneous in the respective parts.

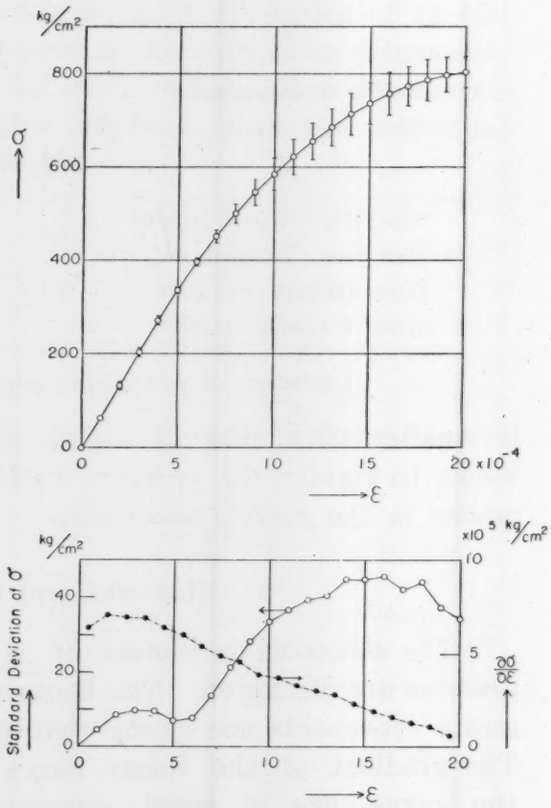

Fig. 9. (above) The mean value and standard deviation of stress in the various stages of deformatiom in the test specimens of (A) group. (below) Open circle: standard deviation of stress value. Closed circle: gradient of ε–σ curve.

strength, the marble sample was divided into the two parts (A) and (B) (Fig. 6), for convenience in later discussion. The parts (A) and (B) are regarded as nearly homogeneous, in their respective parts.

The groups of the stress-strain curves of each homogeneous part are shown in Fig. 8 (a) and (b), respectively. It is a interesting fact that the linear parts of all curves are similar and the nonlinear parts fluctuate remarkably, like the fracture strength. Expressed quantitatively the fluctuation, the mean curve of stress-strain relation and the standard deviation of the fluctuation in the various stages of deformation for the part (A) are shown in Fig. 9. That is, the standard deviation of stress values at various strain begins to increase suddenly in the earlier stage of nonlinear deformation.

From the result, it is presumed that the linear part of the curve

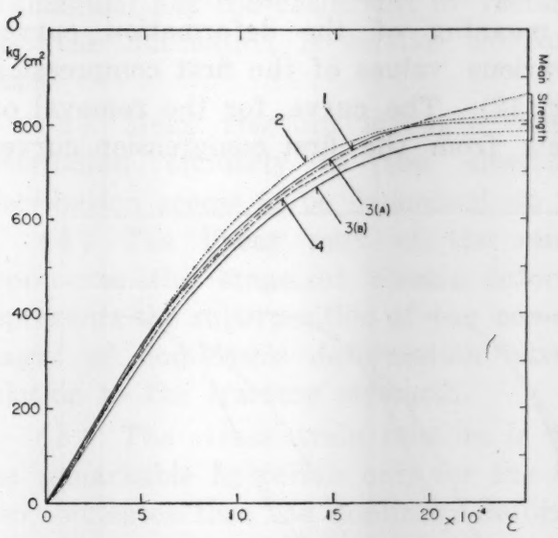

Fig. 10. Mean stress-strain curves for various rate of stress application.

curve 1: Mean stress-strain curve of 6 specimens of rate 120 kg/cm² sec.

2: Mean stress-strain curve of 6 specimens of rate 6 kg/cm² sec.

3: Mean stress-strain curve of 8 specimens of rate 1.5–0.3 kg/cm² sec.

3(A): specimens of A-part,

3(B): specimens of B-part.

4: Mean stress-strain curve of 3 specimens of rate 0.1 kg/cm² sec.

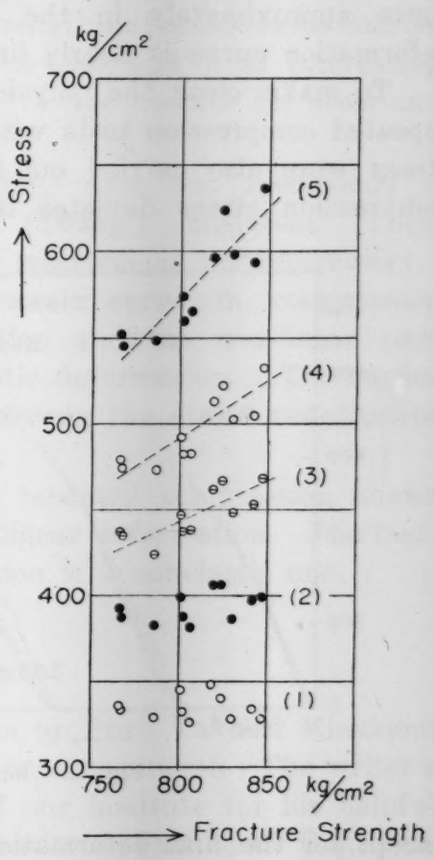

Fig. 11. The relation between the fracture strength and the stress values at the various strain.

(1): Strain 5×10^{-4}, (2): 6×10^{-4}, (3): 7×10^{-4}, (4): 8×10^{-4}, (5): 10^{-3}.

represents the elastic deformation, and in the nonlinear part the nonelastic deformation takes place. Then the relation between the fracture strength and the stress in the various stages of deformation is shown in Fig. 11. The correlation between them has a high value instantly exceeding the elastic limit. It has important meanings that the nonlinear part of the deformation curve, already at the earlier stage, has a direct quantitative connection with the fracture strength. Thus, it is reasonably concluded that the fracture strength of marble is decided already in the earlier stage of nonlinear deformation, and therefore the stage should be a phenomenon similar to the fracture, and although the elastic deformation is structure-insensitive, the deformation of nonlinear stage is structure-sensitive as the fracture.

As the last problem, about the shape of the curve, it is a quadric curve approximately in the latter part, as the gradient of mean deformation curve is nearly linear for the strain (Fig. 9).

To make clear the physical meaning of the deformation curve, repeated compression tests with various values of the first compression stress were also carried out (Fig. 12). The curve for the removal of compression stress deviates largely from the first compression curve,

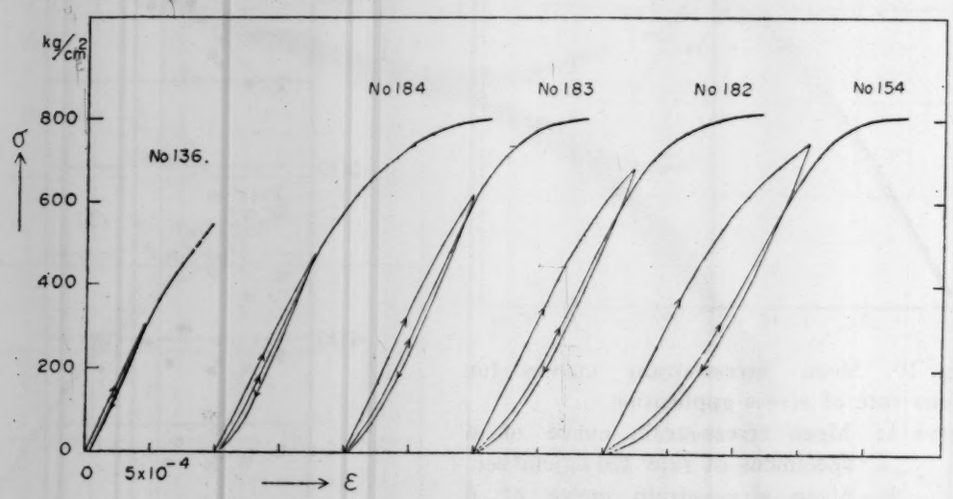

Fig. 12. Repeated stress-strain curve.

except for the first deformation in elastic stage. The larger the first deformation is, the more remarkable the hysterisis is. The hysterisis curve of the stress-strain relation also proves that the nonlinear deformation is nonelastic.

7. Conclusion

As the first step to investigate the deformation and the fracture of rocks, the writer studied experimentally the mechanical properties of a marble sample which has a simple chemical composition and nearly uniform structure.

For 192 specimens of marble test specimens cut off from a mass sample, the fracture strength and the elasticity in compression are measured. The main points of the results are as follows.

(1) The compressive fracture strength rises merely with the increase of rate of stress application. But the effect of rate of stress application in the marble is not remarkable as compared with the case of concrete.

(2) The fluctuation of the fracture strength in homogeneous marble (Yamaguti) has the coefficient of variation 2～3% and it is interesting that the fluctuation is smaller compared to the results for steel and glass.

(3) Mean fracture strength (averaging nine test specimens) is distributed similarly as the elasticity (Young's modulus). Their distribution seems to be dependent on the macroscopic unhomogeneity.

(4) The linear part of the stress-strain curve in compression represents the stage of elastic deformation and the non-linear part represents the superposition of the non-elastic deformation. The earlier stages of non-elastic deformation have already the direct quantitative relation to the fracture strength.

(5) The stress-strain relation in the repeated compression shows the remarkable hysterisis only for the nonlinear deformation. The fact, also, indicates that the nonlinear deformation is a nonelastic one.

8. Acknowledgement

The writer expresses his hearty thanks to Prof. Takeshi Minakami of our institute for his valuable advice and encouragement. The writer's thanks are also due to Mr. Jōyo Ossaka of our institute for his helpful discussion and the Engineering Research Institute, Faculty of Engineering, University of Tokyo which kindly allowed me to use the testing machine, especially to Mr. Nakamura of the institute.

A part of the expenses for this experiment was granted by the Ministry of Education.

8. 大理石の変形及び破壊についての実験的研究 (第1報) 特に圧縮強度のバラツキ及び強度と荷重速度との関係について

地震研究所 茂木清夫

地殻に発生する力学的諸現象は極めて複雑且つ大規模なものではあるが，結局は構成要素たる岩石の物理的性質に起因するものであるから，岩石の物性を明かにすることは地球物理学的に重要な意義をもちうるものである．岩石の物性を研究するに当つて，これが天然の産物である為にその諸性質が著しくバラツキを示すことを考慮することなしで定量的な論議をなすことはゆるされない．破壊現象の様に組織敏感な現象の場合は更に統計的取扱いを必要とする．この様な考慮のもとに研究する為には多数回且多種類の実験を必要としよう．

今回はその第一歩として比較的均質且構造簡単な大理石について，常温常圧のもとで実験を行つた．試料は 40 cm×40 cm×4 cm の大理石の塊から約 200 個の角柱試料を切りとつて，それらについて比重，圧縮強度及び応力-歪曲線を求めてその空間的バラツキを調べた．圧縮試験にはアムスラー型の油圧式万能試験機を，歪測定には電気抵抗線式歪計を用いた．その結果によれば，個々の強度は著しいバラツキを示すけれども，同時に或る傾向をもつた巨視的な分布を示している．9個の移動平均をとるとその傾向が一層明瞭に認められる．一方弾性係数の分布はこの分布とほとんど同一で，これらは構造の状態を示すものと考えられる．尚強度のバラツキは硝子や金属に比較して予想外に小さいことが明らかになつた．またほぼ完全に均質と考えられる部分から切りとられた多数の試料について応力-歪曲線を求めると，これらの曲線は直線部分（弾性変形）に於いてはよく一致するが，非直線部分（非弾性変形を伴う段階）に於いてバラツキが起る．このことは繰返し荷重の結果と共に変形から破壊に至る過程の機構を暗示するものである．

また荷重速度と強度との関係をこの様な強度のバラツキを考慮して求めると，圧縮強度は荷重速度の増加とともにわづかに増大するが，コンクリートの場合に比して著しくない．

BULLETIN OF THE EARTHQUAKE
RESEARCH INSTITUTE
Vol. 37 (1959), pp. 171-176

9. *Microseisms and Typhoons.*

By Fuyuhiko KISHINOUYE and Mieko KOTAKA,

Earthquake Research Institute.

(Read Jan. 28, 1958.—Received Dec. 28, 1958.)

In Japan relation between microseisms and typhoons had been investigated and published in many papers. But most studies were made with observed data obtained at one or a few stations. Recently "Report of Microseisms Observation 1956"[1] was published by the Japan Meteorological Agency. In this report data of microseisms at several places in Japan are printed. The authors began to study the relation between microseisms and typhoons widely in Japan. The variation of microseisms in two dimensions and that in time could be discussed.

Tracks of typhoons adopted in this study are shown in Fig. 1. Relations between microseisms and central pressure of typhoon, travelling velocity of typhoon, wind velocity at the stations were studied and some parts are shown in Figs. 2 and 3. From these we attained following results.

Travelling velocity was considered to be re-

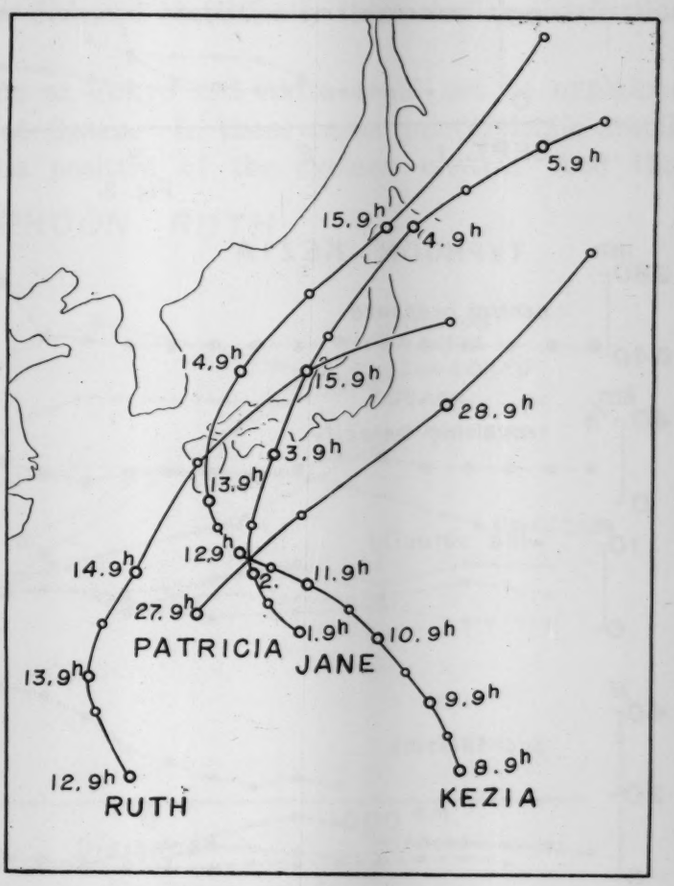

Fig. 1. Track of cyclones.

1) *Quaterly Journ. Seismology, Supplementary Volume* **21** (1956).

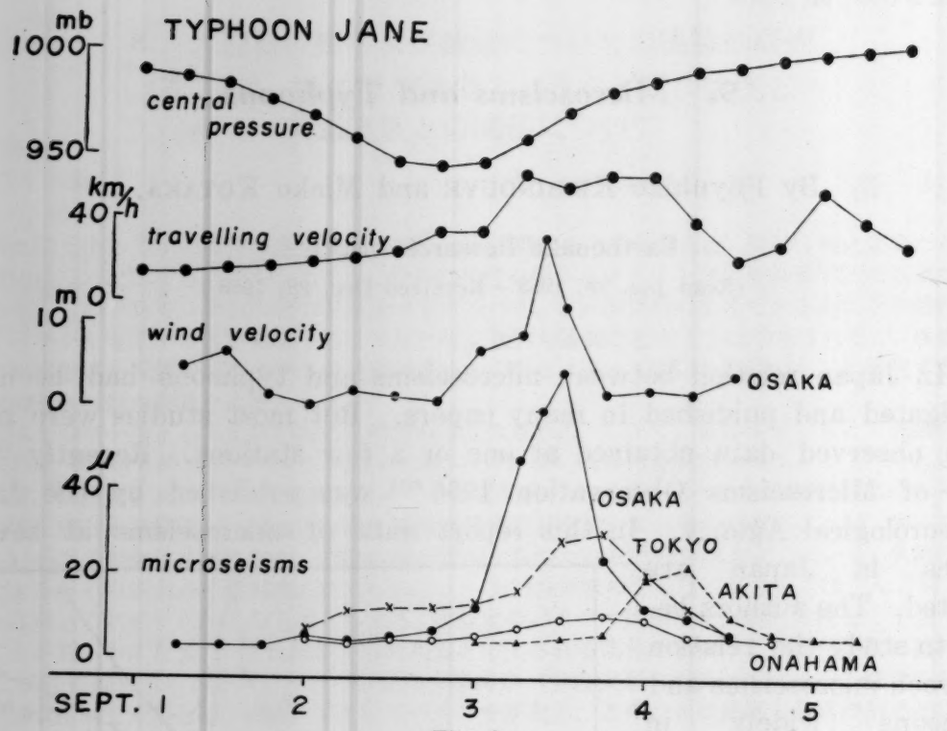
TYPHOON JANE
mb
1000
950
central pressure
km/h
40
travelling velocity
m
10
0
wind velocity
OSAKA
μ
40
20
0
microseisms
OSAKA
TOKYO
AKITA
ONAHAMA
SEPT. 1
2
3
4
5

Fig. 2.

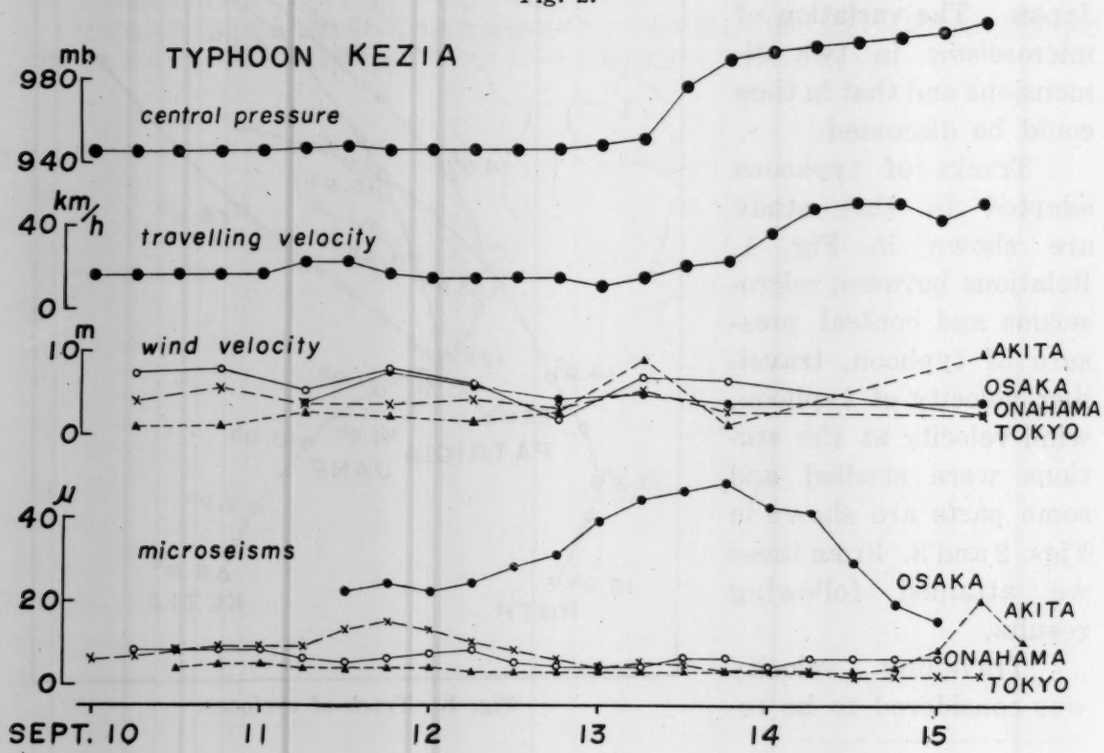
TYPHOON KEZIA
mb
980
940
central pressure
km/h
40
0
travelling velocity
m
10
0
wind velocity
AKITA
OSAKA
ONAHAMA
TOKYO
μ
40
20
0
microseisms
OSAKA
AKITA
ONAHAMA
TOKYO
SEPT. 10
11
12
13
14
15

Fig. 3.

lated to growth of swells of the sea and to be parallel to amplitude of microseisms. Microseisms at Osaka seem to vary with the travelling velocity, but others do not.

Data at Osaka also presents some relation to wind velocity. But at other stations amplitude of microseisms might depend upon distance of the centre of cyclone from there.

In general energy of propagated waves is inversely proportional to distance from the origin of waves for surface waves, and to square of distance for bodily waves or spherical waves. To examine whether microseismic waves are surface waves or bodily waves, diagrams in Figs. 4 and 5 were drawn which show relation between amplitude and distance from the typhoon centre. From these diagrams, the writers deduced amplitude at Osaka was inversely proportional to distance from the data. One of the writers considers that "micro-ratio chart" studied by M. H. Gilmore[2] may be deduced statistically from similar distribution of amplitude.

Results of observations at Tokyo and Akita could not be explained by the above hypothesis at Osaka. In these cases microseismic amplitude might depend on the position of the cyclone centre. And this

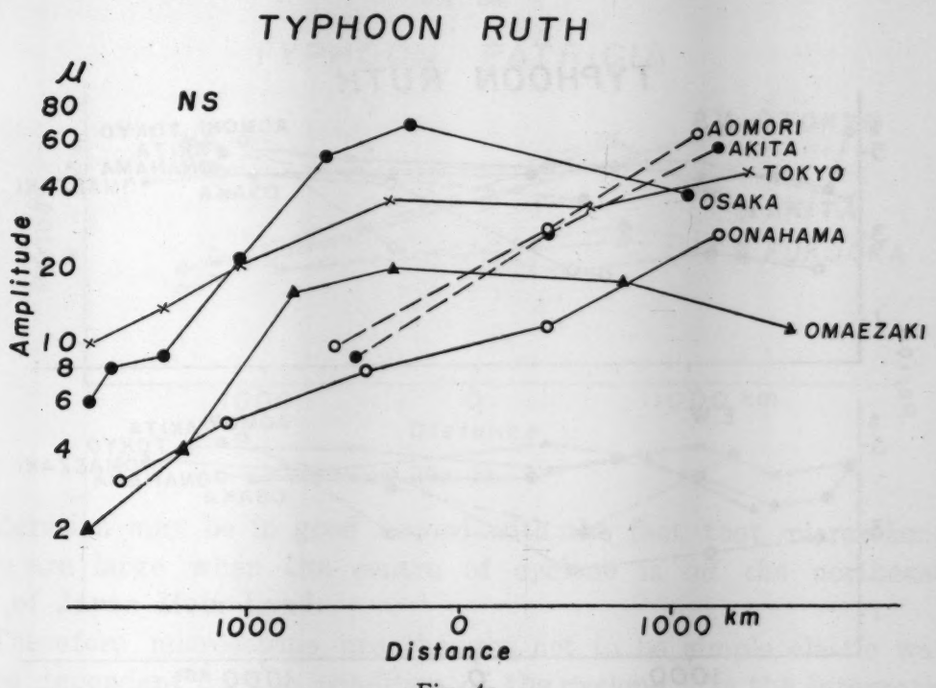

Fig. 4a.

2) M. H. GILMORE, "Amplitude Distribution of Storm Microseisms," *Symposium on Microseisms (1952)*, 20–55, Washington D.C. 1953.

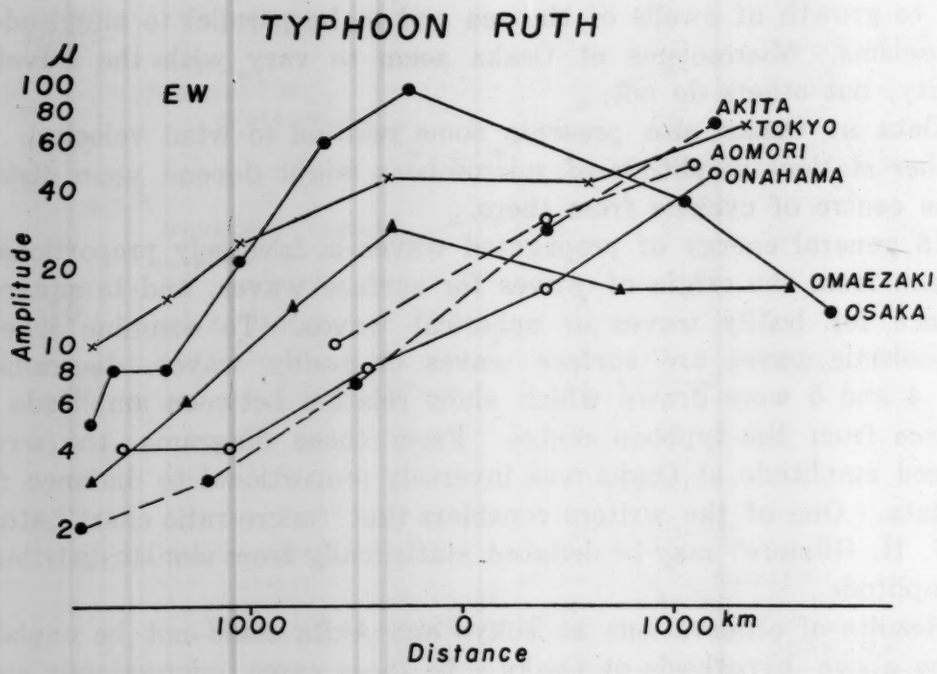
TYPHOON RUTH
μ
100
80
60
40
20
10
8
6
4
2
EW
Amplitude
AKITA
TOKYO
AOMORI
ONAHAMA
OMAEZAKI
OSAKA
1000
0
1000 km
Distance

Fig. 4b.

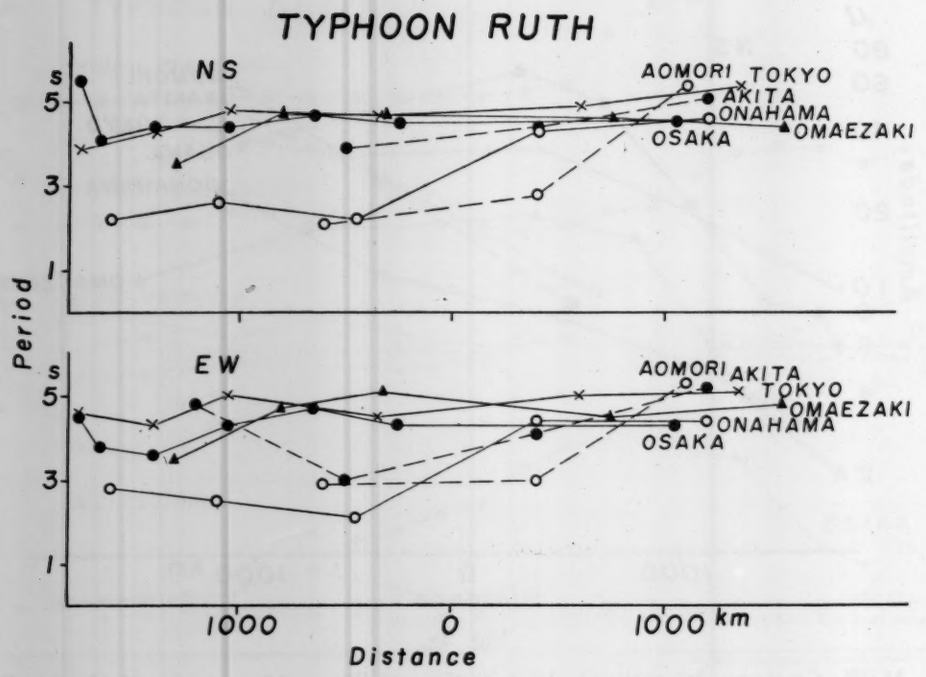
TYPHOON RUTH
NS
s
5
3
1
AOMORI
TOKYO
AKITA
ONAHAMA
OSAKA
OMAEZAKI
Period
EW
s
5
3
1
AOMORI
AKITA
TOKYO
OMAEZAKI
ONAHAMA
OSAKA
1000
0
1000 km
Distance

Fig. 4c.

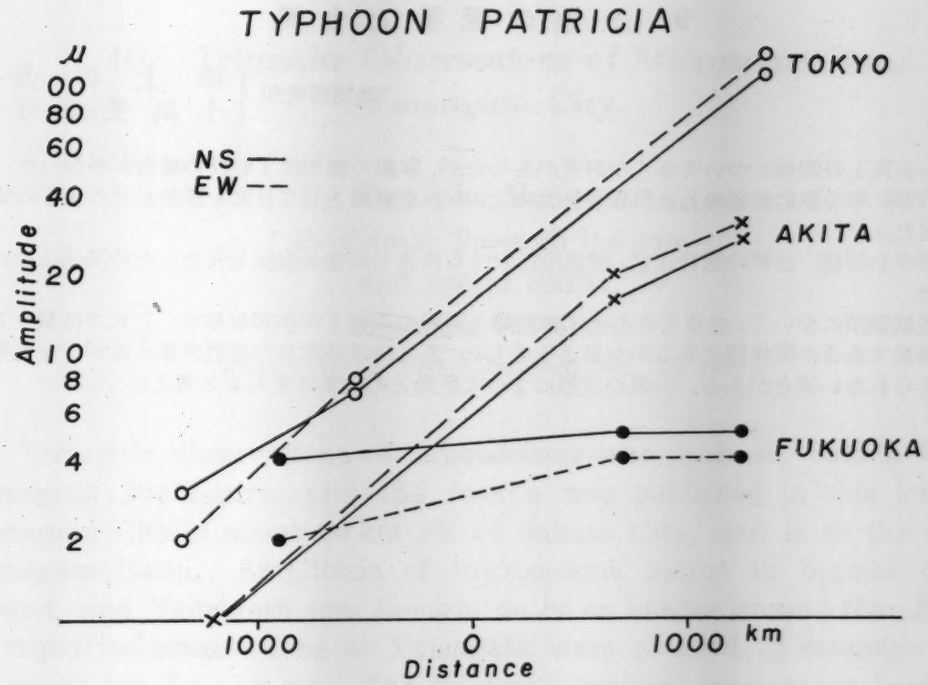

Fig. 5a.

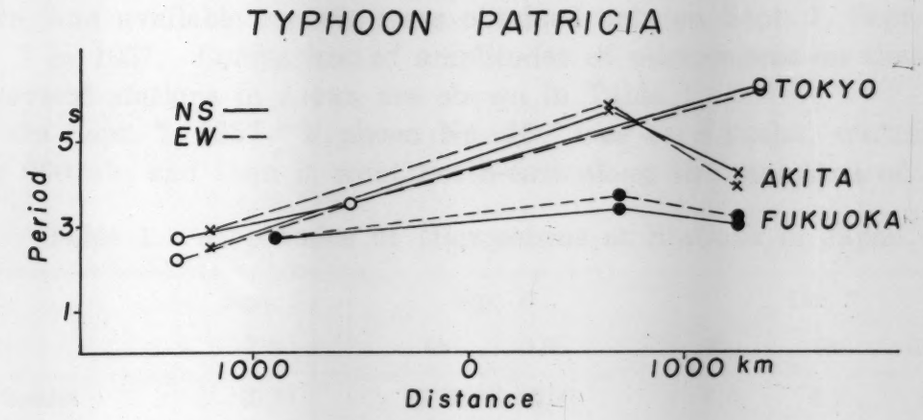

Fig. 5b.

consideration may be in good accord with the fact that microseisms at Tokyo are large when the centre of cyclone is off the northeastern coast of Japan Main Land.

Therefore microseisms are thought not to be simple elastic waves, but be dependent on the condition of the cyclone. In the International Geophysical Year of 1958, many detailed data may be obtained, so the nature of microseisms will be studied in progress.

9. 土地の脈動と台風

地震研究所 { 岸上冬彦 / 小高美江子 }

脈動と台風との関係について多くの研究があつたが，脈動の観測は1個所の場合が多かつた．気象庁から1956年の脈動観測報告が出版されたので，それを材料として日本を脈動がどのように伝わるかを調べた．

台風の中心示度，台風の進行速度，観測所における風速と脈動の関係を見た．その関係はないようであつた．

次に各観測所において，台風の中心までの距離と脈動の振幅との関係を見た．これでは減り方によつて表面波であるか実体波であるかを見ようとした，ある時は表面波の性質が見えるが，全くそのように考えられない場合がある．台風の状態によつて脈動との関係は変わると考えた．

BULLETIN OF THE EARTHQUAKE
RESEARCH INSTITUTE
Vol. 37 (1959), pp. 177-181

10. *Tripartite Observations of Microseisms in Yamagata City.*

By Fuyuhiko KISHINOUYE,
Earthquake Research Institute
and Isamu SHIDA,
Yamagata University.

(Read Feb. 25, 1958.—Received Dec. 28, 1958.)

Tripartite observations of microseisms was made at Sakata City in Yamagata Prefecture, and the results was published in this journal[1]. Yamagata City is about 90 km SE of Sakata City, and is at the end of Yamagata Basin. Amplitude of microseisms seems to depend on the ground, and Yamagata was thought to be on harder ground than Sakata. So tripartite observations at Yamagata were planned to compare microseisms at the two places. The tripartite stations were set in September and October of 1957, but amplitudes at Yamagata were too small to observe, and available records were obtained only on Sept. 7, Sept. 8 and Oct. 7 in 1957. Comparison of amplitudes of microseisms on these days at several stations in Japan are shown in Table 1.

On Sept. 7, 1957 "Typhoon No. 10" was at Kyushu, central pressure 960 mb, and then it went north-east along the mainland of Japan.

Table 1. Amplitudes of Microseisms at Stations in Japan.

	Sept. 7	Sept. 8		Oct. 7		
	21h	8h	11h	3h	5h	16h
Sendai	(0.5)	(2.2)	(3.3)	6.0	8.7	6.6
Tukuba	0.1	0.4	0.4	0.8	0.8	0.5
Mitaka	8.0	12.0	14.1	20.1	22.2	14.7
Nagoya	20.5	18.7	8.1	12.6	12.6	10.5
Abuyama	1.6	1.0	0.6	1.1	0.6	0.7
Matsushiro	1.0	1.2	1.1	0.3	0.3	0.5
Nagasaki	0.6	1.3	—	—	—	0.6
Yamagata	0.7	1.1	1.3	1.9	1.8	1.6

(NS component in micron, except in ( ) EW component).

1) F. KISHINOUYE and I. SHIDA, *Bull. Earthq. Res. Inst.* **34** (1956), 301-306.

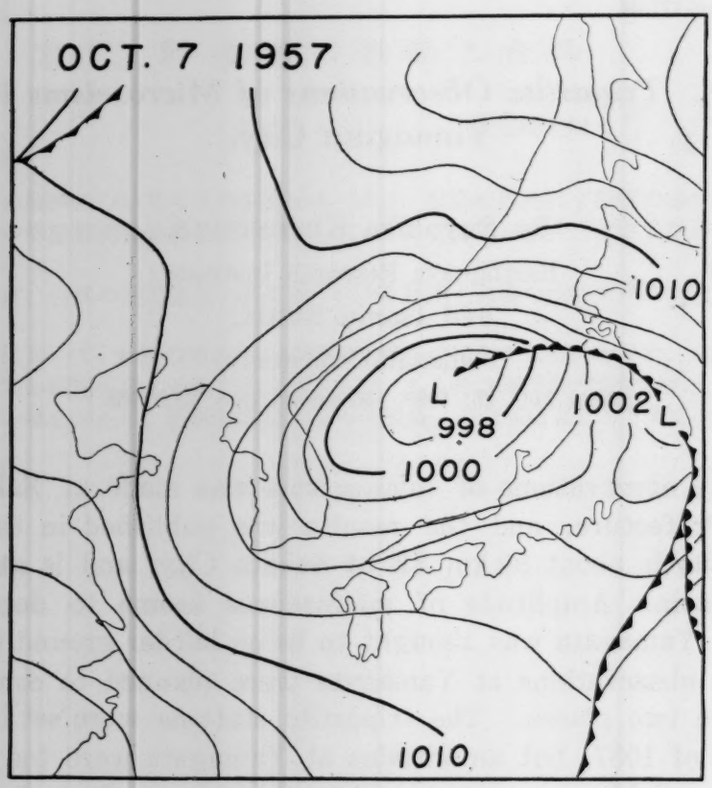

Fig. 1. Weather Map.

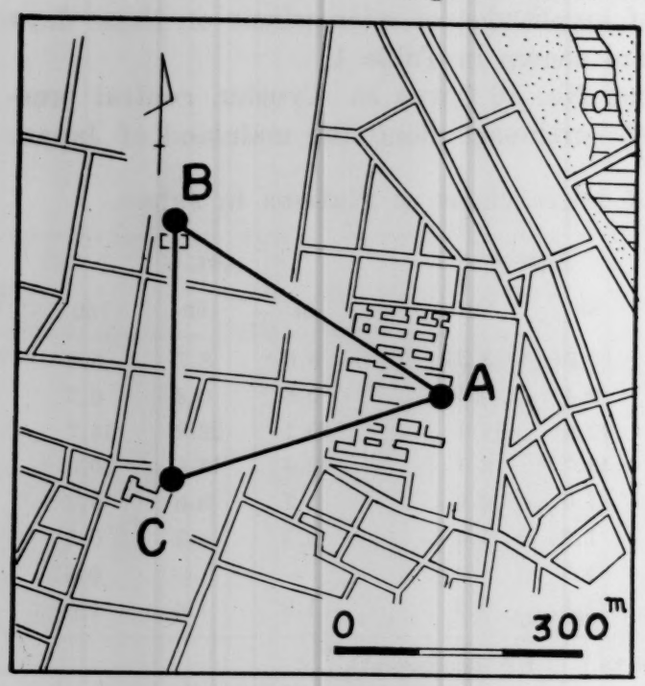

Fig. 2. Observation net.

On the next day, it rained heavily in Kyushu and Shikoku and passed off the eastern coast of Hokkaido.

On Oct. 7, a cyclone about 996 mb was near at the centre of Japan Sea, and Tokyo and its neighbourhood suffered from heavy rains and flood. (Fig. 1).

In the above-mentioned meteorological conditions microseisms at Yamagata became large, and tripartite observations could be made. Three temporary stations were set up at the labora-

tory of physics in the Faculty of Education of the Yamagata University (A), the Yamagata Meteorological Station (B) and Shinoda Hospital (C). The positions are shown in Fig. 2, and distances between these stations AB 353 m, BC 310 m and CA 339 m. Seismographs were mechano-optical ones frequently employed by the writers for study of microseisms[2].

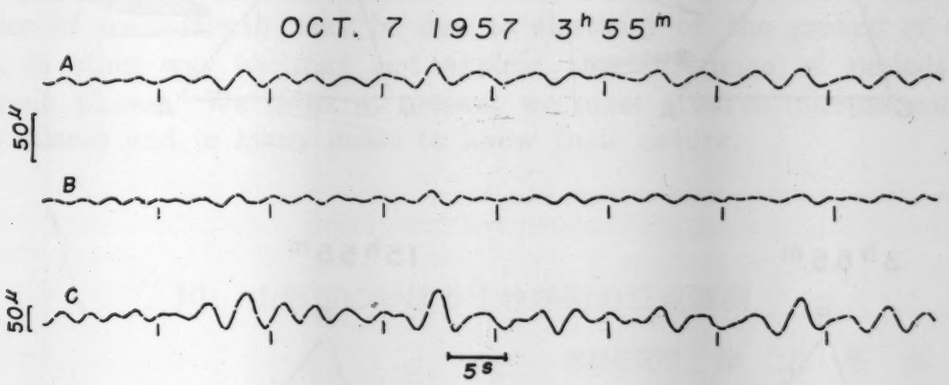

Fig. 3. Records of microseisms.

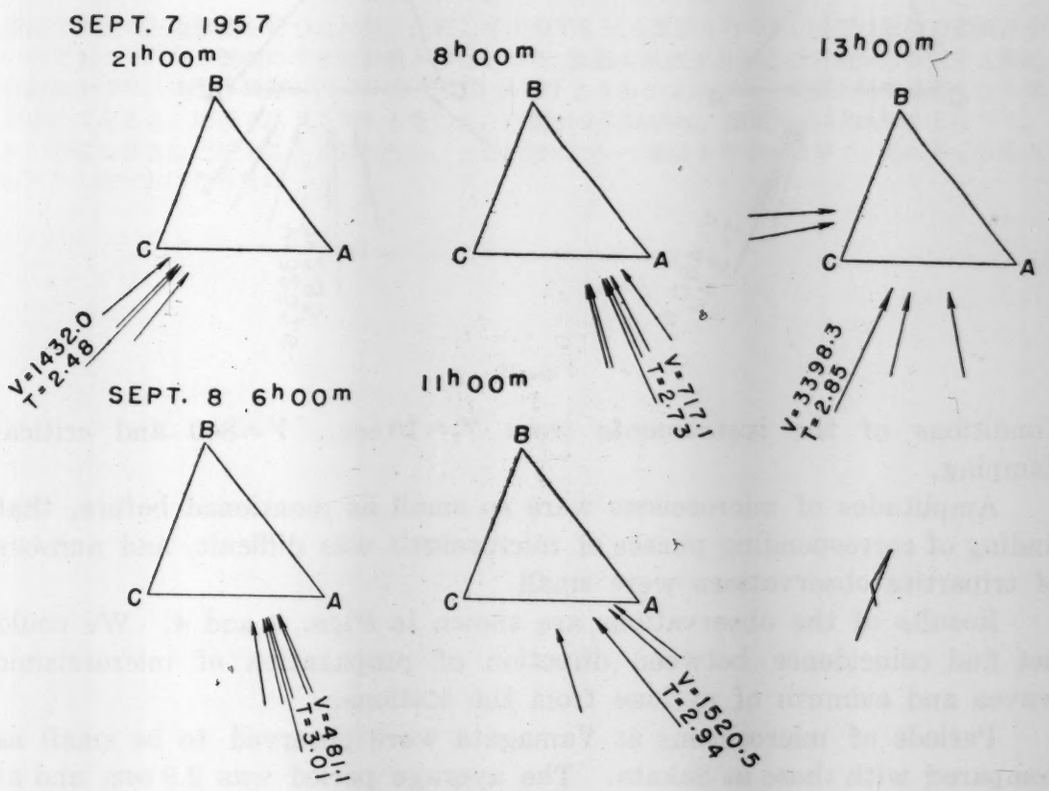

Fig. 4a.

2) F. KISHINOUYE, *Bull. Earthq. Res. Inst.* **20** (1942), 215–219.

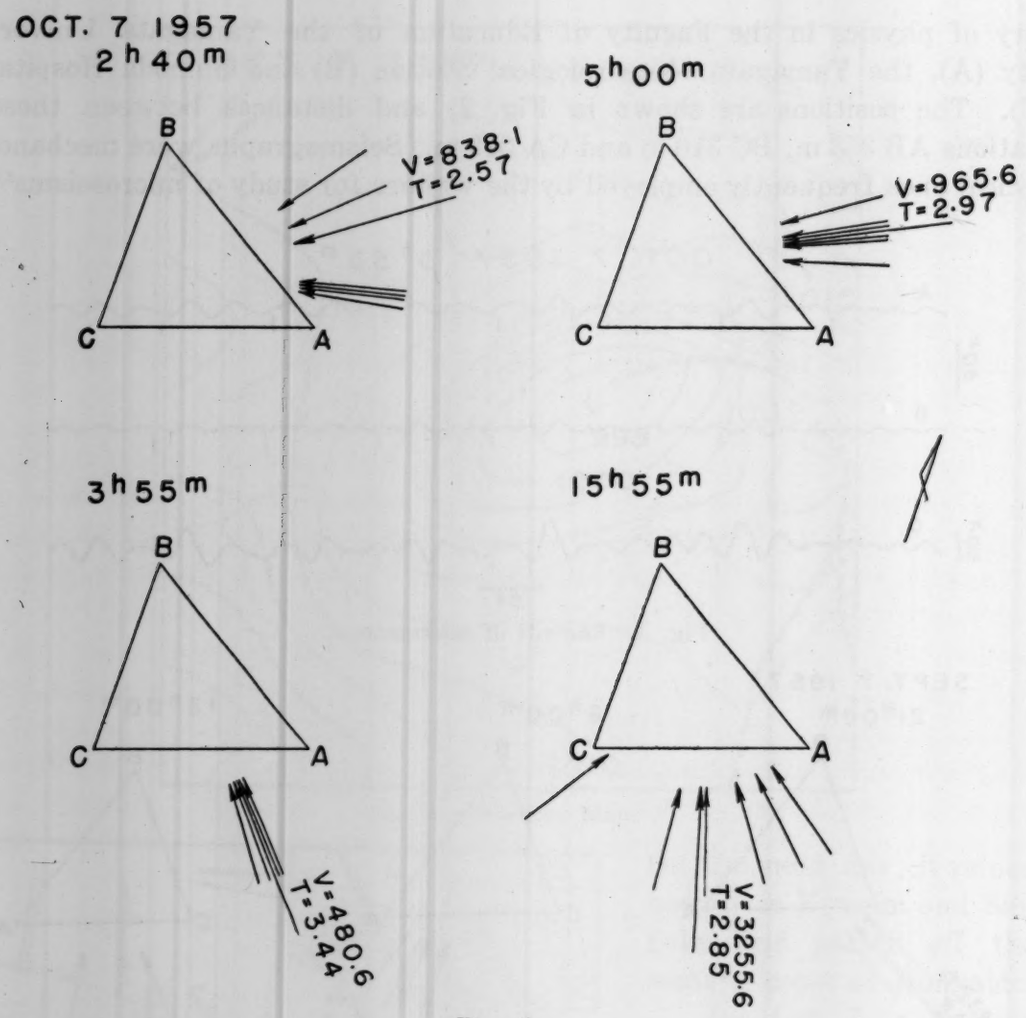

Fig. 4b.

Conditions of the instruments were $T_0=10$ sec., $V=800$ and critical damping.

Amplitudes of microseisms were so small as mentioned before, that finding of corresponding phases of microseisms was difficult, and number of tripartite observations were small.

Results of the observations are shown in Figs. 3 and 4. We could not find coincidence between direction of propagation of microseismic waves and azimuth of cyclone from the stations.

Periods of microseisms at Yamagata were observed to be small as compared with those at Sakata. The average period was 2.9 sec, and at Sakata 4.0 sec. The velocity of propagation was obtained here as a mean

3) R. IKEGAMI, *Bull. Earthq. Res. Inst.*, **29** (1941), 313–325.

1450 m/sec. In the investigation at Mitaka[3], dispersion of microseismic waves was discussed, but here we could not tell about dispersion for variation of periods was small in this case.

Wave-length was calculated by multiplying wave velocity by vibration period. The wave-length was obtained as 4.5 km. The value is larger than those at other places; Mitaka 2.2 km, and Sakata 2.0 km. The difference of wave-length may be due to elasticity of the ground of stations, in other way we may not explain the difference of periods of different places. We think at present we must observe microseisms at many places and in many cases to know their nature.

---

10. 山形市における土地脈動の三点観測

地震研究所 岸 上 冬 彦
山形大学 志 田 勇

酒田で脈動の三点観測を行つた結果と比較して山形でも三点観測を行つた．山形は脈動の振幅が小さい所であつて，三点観測のできた回数が少なかつた．脈動が低気圧の中心の方向から伝播する説には合わなかつた．山形は周期が約 2.9 秒で酒田 (4 秒) よりも小さかつた．周期と伝播速度とから波長を求めてみると，山形では 4.5 km となつた，三鷹が 2.2 km/sec，酒田が 2.0 km/sec となつて，波長が地盤の強さに比例するかも知れない．まだ脈動について結論を出すには早く，更に多くの地点で測定をしなければならない．

BULLETIN OF THE EARTHQUAKE
RESEARCH INSTITUTE
Vol. 37 (1959), pp. 183-188

11. *Tripartite Observations of Microseisms at Sakata (Second Paper).*

By Fuyuhiko KISHINOUYE,
Earthquake Research Institute
and Isamu SHIDA,
Yamagata University.

(Read March 25, 1958.—Received Dec. 25, 1958.)

The first tripartite observations has been made at the northern part of the city of Sakata in February 1956, and the results was reported in this journal[1]. In December of the same year the second observations were carried out about 2 km SE from the first ones, or at the south-eastern end of the city, on alluvial plain. The first ones were on a sand dune, so the authors aimed to find the effect of geology of station on microseisms. Seismographs used were equal in both cases, but in the former case the length of sides of the triangle net of observation were about 380 m. This time, sides were elongated to about 600 m, and moreover, the number of stations was increased to four to study the accuracy of the tripartite observatins. Namely, in a few cases, observations were made at four stations simultaneously, and direction of propagation and velocity of microseisms were calculated for two tripartite observations.

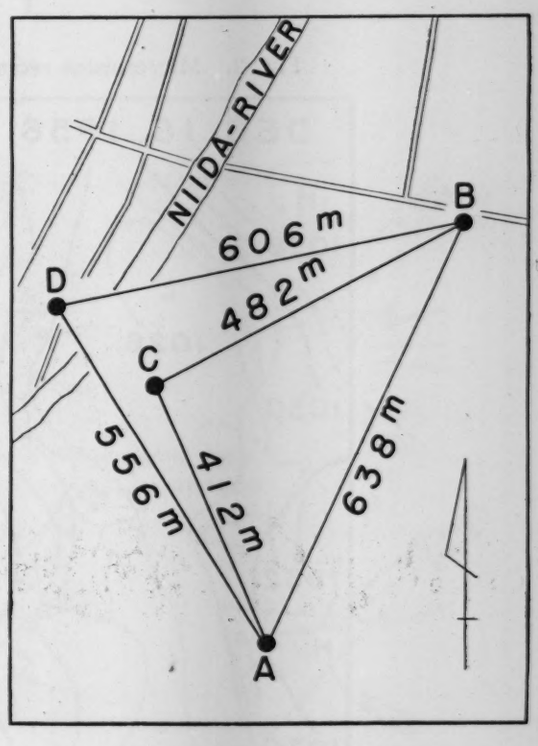

Fig. 1. Observation net.

The positions of the stations are shown in Fig. 1; station A was set up in the Kamegasaki Primary School, station B in the Pump Station of the Sakata Water

1) F. KISHINOUYE and I. SHIDA, *Bull. Earthq. Res. Inst.*, **34** (1956), 301–306.

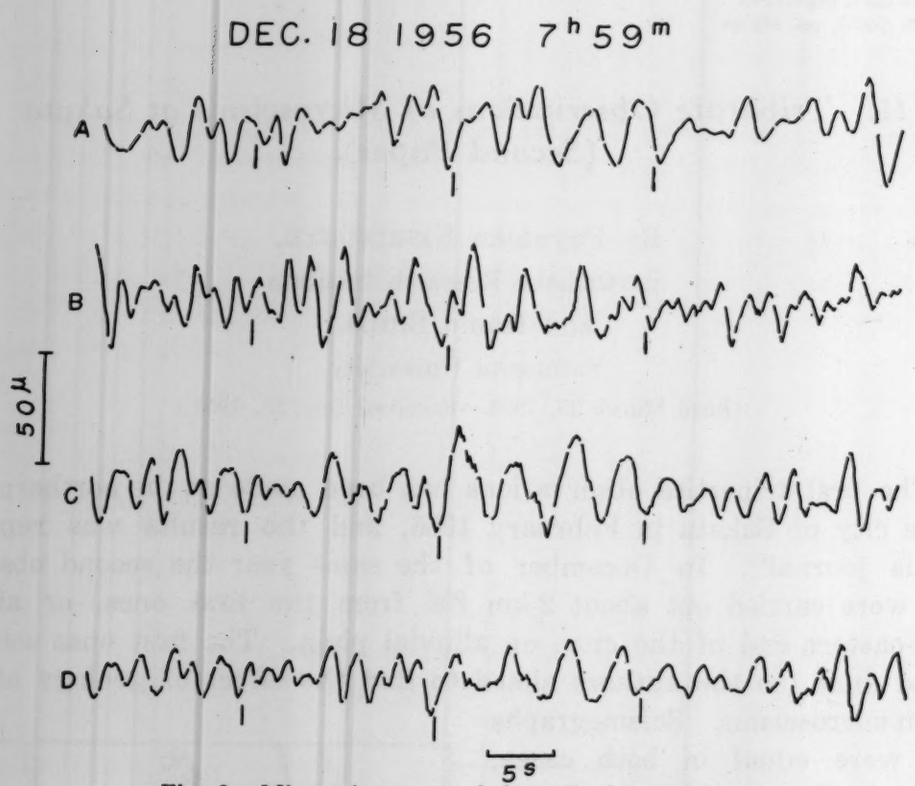

Fig. 2. Microseisms recorded at the four stations.

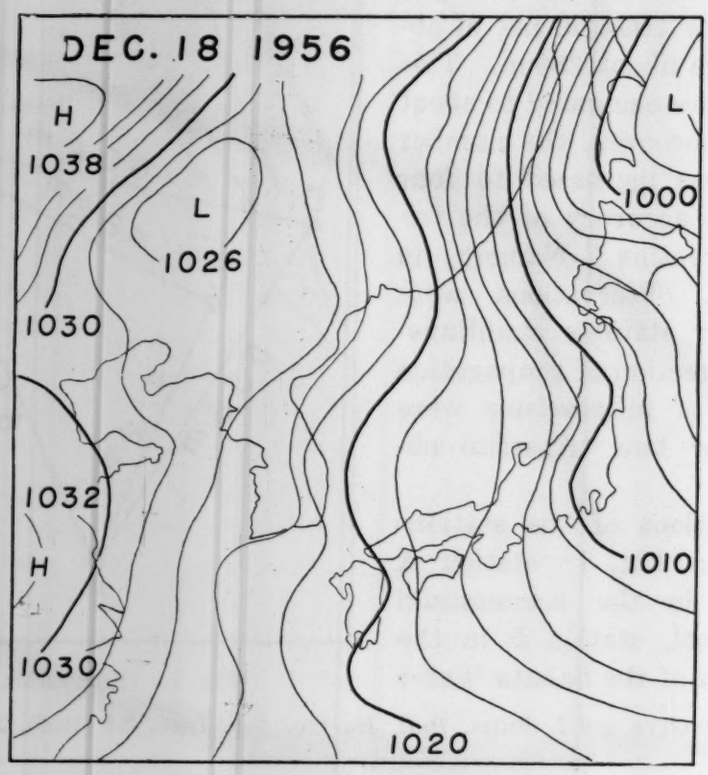

Fig. 3. Weather map.

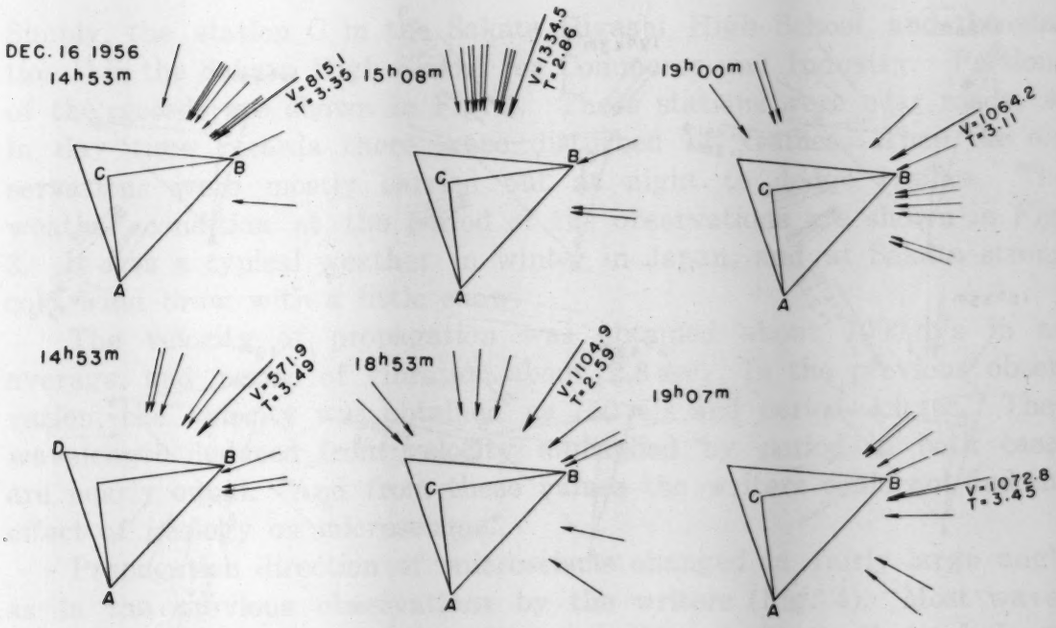
DEC. 16 1956
14h53m
V=815.1
T=3.35
15h08m
V=1334.5
T=2.86
19h00m
V=1064.2
T=3.11
14h53m
V=571.9
T=3.49
18h53m
V=1104.9
T=2.59
19h07m
V=1072.8
T=3.45
A
B
C
D

Fig. 4a.

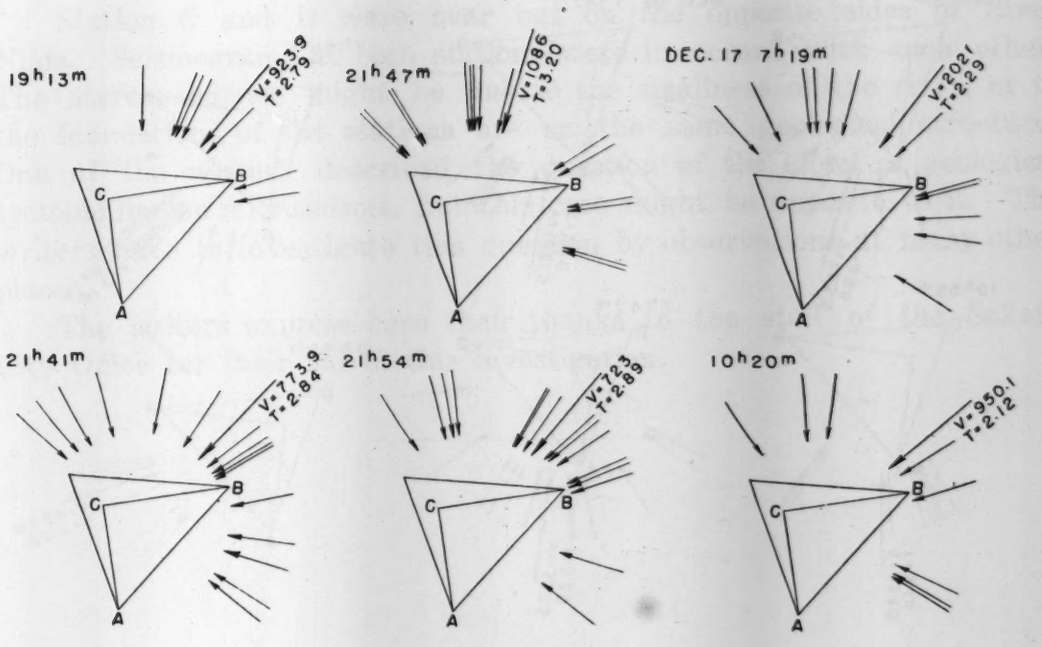
19h13m
V=923.9
T=2.79
21h47m
V=1086
T=3.20
DEC. 17 7h19m
V=2021
T=2.29
21h41m
V=773.9
T=2.84
21h54m
V=723
T=2.89
10h20m
V=950.1
T=2.12
A
B
C

Fig. 4b.

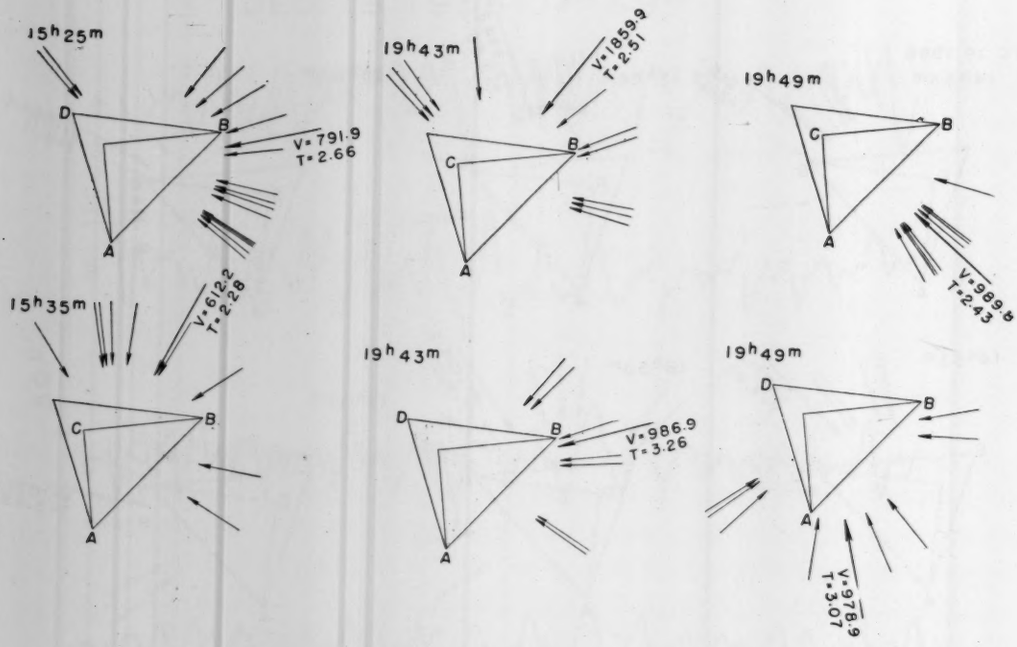
15h25m
V=791.9
T=2.66
19h43m
V=1859.9
T=2.51
19h49m
V=989.6
T=2.43
15h35m
V=612.2
T=2.28
19h43m
V=986.9
T=3.26
19h49m
V=978.9
T=3.07

Fig. 4c.

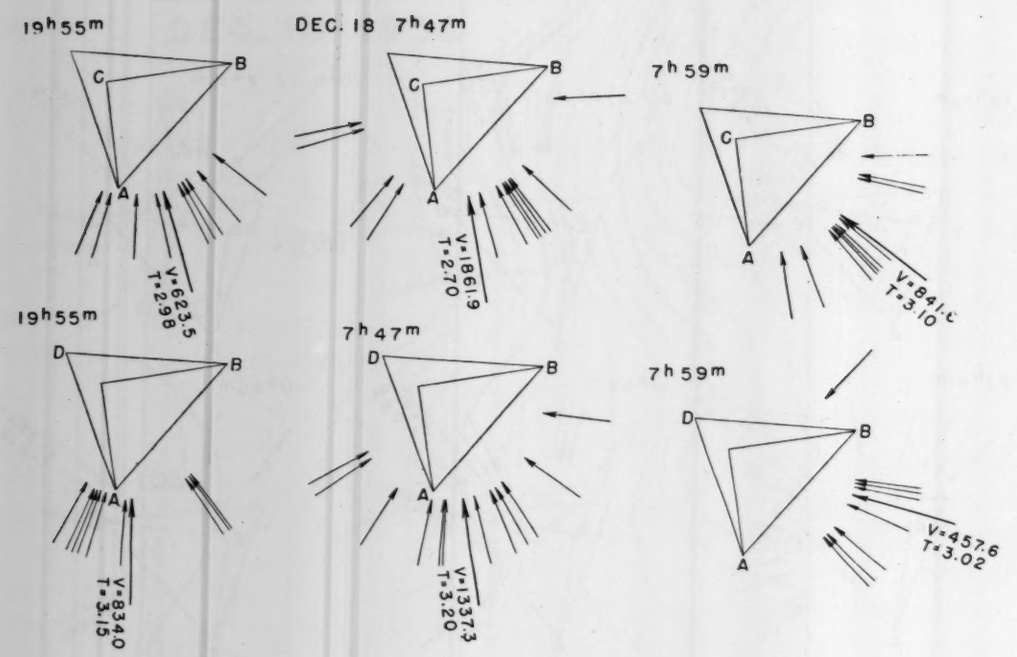
19h55m
V=623.5
T=2.98
DEC. 18 7h47m
V=1861.9
T=2.70
7h59m
V=841.0
T=3.10
19h55m
V=834.0
T=3.15
7h47m
V=1337.3
T=3.20
7h59m
V=457.6
T=3.02

Fig. 4d.

Supply, the station C in the Sakata Higashi High School, and the station D in the Sakata High School for Commerce and Industry. Portions of the records are shown in Fig. 2. These stations were near roads, so in day time records there were disturbed by traffics. Then the observations were mostly carried out at night to dodge traffics. The weather condition at the period of the observations are shown in Fig. 3. It was a typical weather in winter in Japan, and at Sakata strong cold wind brew with a little snow.

The velocity of propagation was obtained about 1000 m/s in an average, and period of vibration about 2.8 sec. In the previous observation, the velocity was obtained as 750 m/s and period 4.0 sec. Then wavelength deduced from velocity multiplied by period in both cases are nearly equal. And from these values the writers could not find the effect of geology on microseisms.

Propagation direction of microseisms changed in fairly large angle as in the previous observations by the writers (Fig. 4). Most waves come from N or NE, and this direction did not fit to that of Japan Sea which was very rough at that time. The direction of microseisms pointed to Northeastern Sea off the Japan Main Land which was also very rough. This result might agree with that in the writers' first paper.

Station C and D were near but on the opposite sides of River Niida. Seismograms at both stations were in accord with each other. The correspondence might be due to the smallness of the river, or to the foundations of the stations are on the same geological structure. One of the writer[2] described the question of the effect of geological tectonic line on microseisms, but this case might be opposite to it. The writers have to investigate this question by observations at many other places.

The writers express here their thanks to the staff of the Sakata City Office for their aid in this investigation.

---

2) F. KISHINOUYE, *Bull. Earthq. Res. Inst.*, **35** (1957), 541.

11. 酒田における土地の脈動の三点観測 (第2報)

地震研究所 岸上冬彦
山形大学 志田勇

脈動が地盤によつてどのように違うかを見るために，前回は砂丘の上で測定したが今回は沖積地である酒田市街の南東端において同様の観測を行つた．気圧配置は「西高東低」で酒田においては少し雪を伴つた強風が吹いていた．観測結果は図に示した通りである．伝播速度は 1000 m/s で周期 2.8 秒で．前回は 750 m/s で 4 秒であつたので，これ等の値から波長を求めると殆ど等しい．このような結果から地盤の影響について結論を出すにはまだ早いと思う．伝播方向は．日本海が荒れていたにも拘らずその方をむかず，前回と同様脈動は北太平洋の波によつて起されるように見える．観測点 C と D とは新井田川の両岸にあつた．以前に東京附近で多摩川の両岸で脈動の差異を認めたのでその点を調べたが，その差は認められなかつた，ここは地質の差がはつきりした所でないので脈動に差が表われなかつたのかも知れないが，この問題は更に他の場所で調べて見たい．

BULLETIN OF THE EARTHQUAKE
RESEARCH INSTITUTE
Vol. 37 (1959), pp. 189-192

12. *Tripartite Observations of Microseisms in Shōnai Plain, Yamagata Prefecture.*

By Fuyuhiko KISHINOUYE,
Earthquake Research Institute
and Isamu SHIDA,
Yamagata University.

(Read April 22, 1958.—Received Dec. 28, 1958)

Amplitude of microseisms is generally considered to be larger on alluvial plain than on hard rocks. Shōnai plain is thickly covered with alluvial soils. This observation was made to find the relation between microseisms and subsoil condition, and between microseisms and damage of Shōnai earthquake of 1897. The method and instruments used were the same described in the former papers about microseisms in Yama-

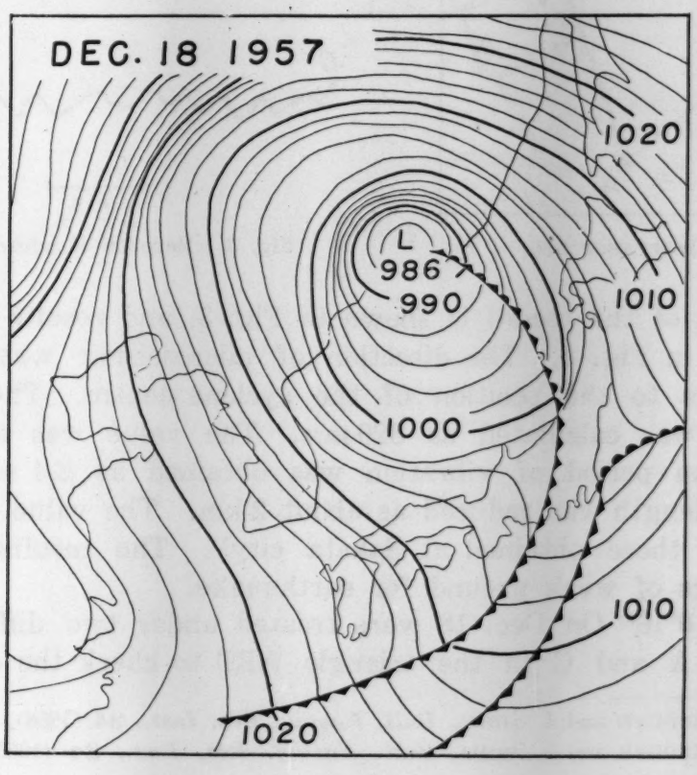

Fig. 1. Weather map.

gata Prefecture[1].

On Dec. 12, 1957, a cyclone appeared on the northern part of Eastern China Sea, and on 13 it passed Japan Sea becoming violent (986 mb at the centre). After then it went north east in direction to the Kuriles (Fig. 1). Microseisms grew large on 13, but unfortunately observations could not be made for the electric supply was disrupted by the storm.

The stations were set at the Nakasone public hall A, the North-Hirata branch office of the Sakata city office B, and a farmer's warehouse C (Fig. 2).

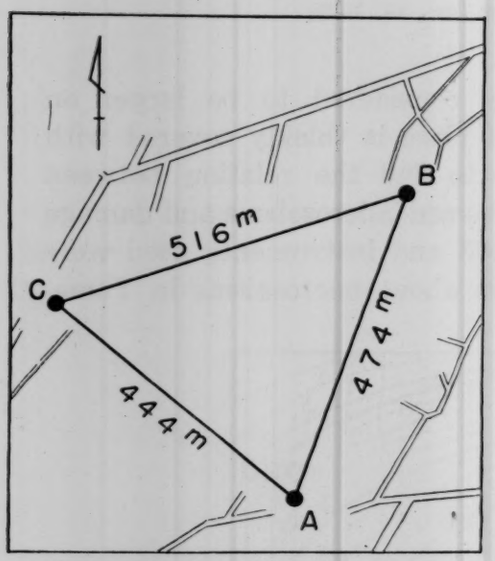

Fig. 2. Observation net.

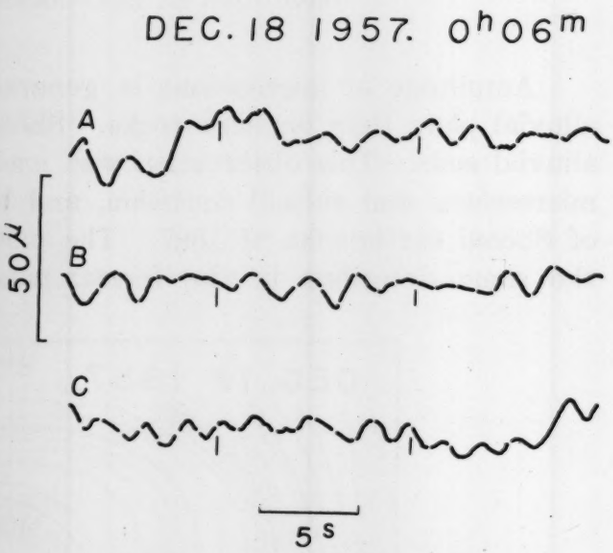

Fig. 3. Records of microseisms.

A potion of the record is shown in Fig. 3, and results of tripartite observations in Fig. 4. The direction of microseismic waves were almost opposite to the position of the cyclone centre. The velocity of propagation was calculated as 820 m/s. The value was small as expected. Mean period of vibration was obtained as 2.4 seconds, then mean wave length was reduced as about 2 km. The value was not different from those obtained at Sakata city[2]. The results may show characteristics of weak ground for earthquake.

Data at 0^h16^m On Dec. 18 were treated under two different reference points A and C in the triangle ABC to check the difference of

1) F. KISHINOUYE and I. SHIDA, *Bull. Earthq. Res. Inst.*, **34** (1956), 301–306.

2) F. KISHINOUYE and I. SHIDA, *Bull. Earthq. Res. Inst.*, **24** (1956), 301–306; **37** (1959).

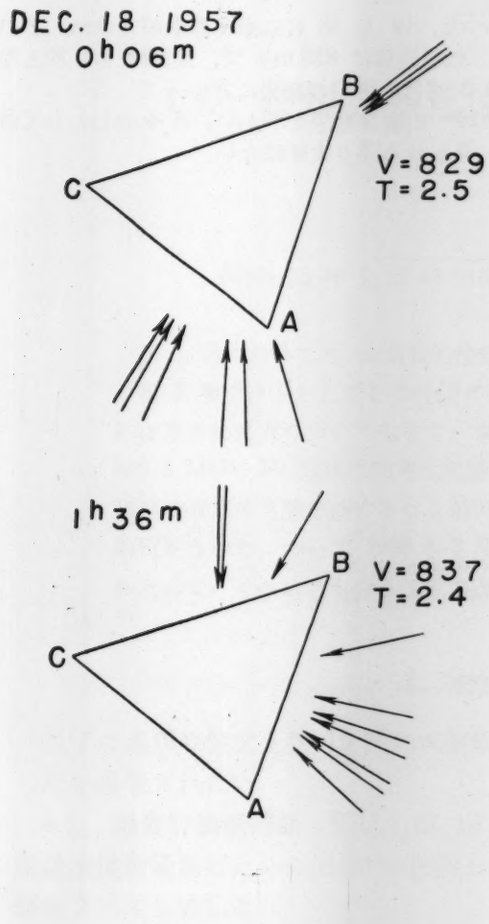

Fig. 4.

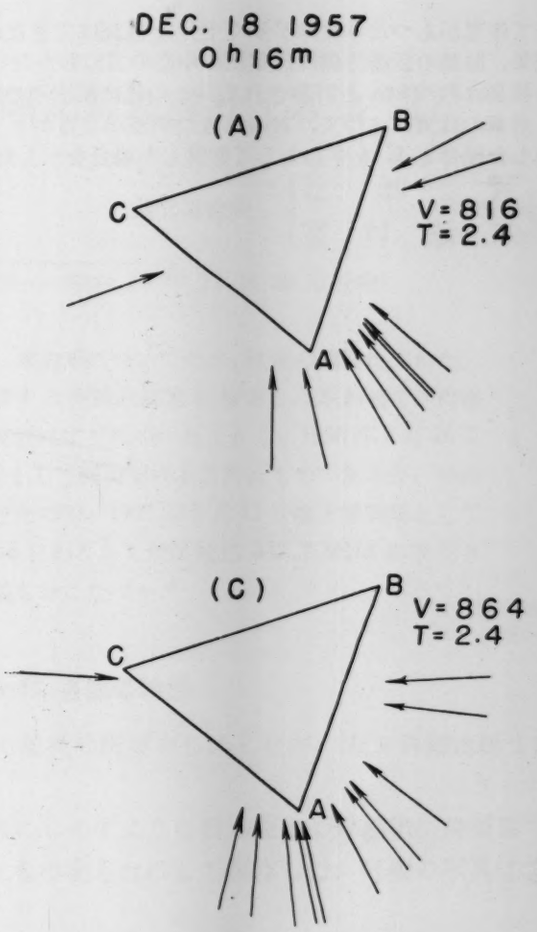

Fig. 5. Check of calcutation.

calculation process. The results are shown in Fig. 5, and the difference may be small.

Lastly the authors express their thanks to the staff of the Office of Sakata City for their aid in the study.

---

12. 庄内平野における土地脈動三点観測

地震研究所　岸　上　冬　彦
山形大学　志　田　　勇

厚い沖積層の上にあると考えられる庄内平野の平田において脈動の測定をした．ここは 1897 年の地震の時に被害の大きかつた所である．1957 年 12 月で著しい大風が吹いたが，その時は電線が切

れて停電があつたり故障が多く十分な観測はできなかつた．12 月 18 日に漸く測定ができた．その結果，脈動の伝播方向は低気圧の中心の方にむかない．伝播速度は 820 m/s で，周期は 2.4 秒となり波長は約 2 km と計算される．この値は酒田市の第 2 回目の測定の結果に近い．

計算の仕方によつて，どの程度の誤差がでるかと 0^h16^m の観測結果をつかい，A を中心として計算した場合と C を中心として計算した場合を示した，見られる通り大差はない．

地震研究所彙報
第37号(1959)193-206頁

13. 超短波多重遠隔記録地震計（第 2 報）

地震研究所 辻浦賢
宮村攝三

（昭和 33 年 7 月 15 日発表——昭和 33 年 12 月 28 日受理）

第 1 報においては，本装置の設計，構造等についてのべ，性能の概要にふれた．

第 2 報では主としてその性能に関する実験的結果を報告し，あわせてその後に改造された点についてしるす．本装置はすでにのべたごとく，1956 年 3 月 26 日 419.8 MHz, F9 電波の実用化試験局として開局をゆるされたものであるが，ほぼ所期の実用化目的を達することができたので，1957 年 5 月 17 日陸上移動局として許可をうけた．ついで 1958 年 3 月 18 日わりあて周波数が 417.7 MHz に変更されたので，それにともなう所要の改装もおこなつた.*

6. RTS–II 各部の特性

以下の説明の便宜上第 15 図に本装置の構成の概要をしめしたが，なお詳細は第 1 報[1]の図を参照されたい．

6.1. 地震計換振器部 P.U. 第 16 図にしめすような構造をもつ動線輪型換振器で，爆破地震動観測のために田望[2]の設計したものをもとにして製作した．外観の写真は第 1 報第 2 図にしめした．

本所技術部において，振動台**をもちいて測定した感度特性の試験結果は第 17 図にしめすとおりである．速度感度 V は 4～40 Hz にて 3 volts/kine 一定，変位感度 D は 4 Hz で 5 mV/μ, 40 Hz にて 70 mV/μ 程度になつている．

---

1) S. MIYAMURA and M. TSUJIURA, "UHF Multi-channel Radio Tele-recording Seismograph. Part I." *Bull. Earthq. Res. Inst.*, **35** (1957), 381–394.

2) N. DEN, *Seism. Soc. Japan, Autumn Meeting* (1954), Kyoto.

* わりあて周波数の変更にともない第 1 報第 3 節以下において 419.8 MHz としてあつた箇所はすべて 417.7 MHz となる．そのための訂正をふくめて，なお第 1 報につぎの訂正をくわえたい．

p. 385 10 行 15 m →15 mm
p. 387 Fig. 5 説明 "(for 1st channel) To be....respectively.", "(第 1 回線に....同様である.)" 削除
p. 388 3～5 行 "沪波器は....に設計した." 削除 14 行 2.915 MHz→2.901 MHz
p. 391 Fig. 12 説明 7.31 MHz→ 7.27 MHz
p. 392 1～ 2 行 "するという....を採用" 削除 17～18 行 "沪波器の....である." 削除
p. 394 5 行 1 mm/mA→2 mm/mA

** 明石製作所製振動台の基準超低周波を東亜電波工業製超低周波発振器 (CR–1型) にかえてもちいた．検定にあたつた技術部後藤健一技官に感謝する．

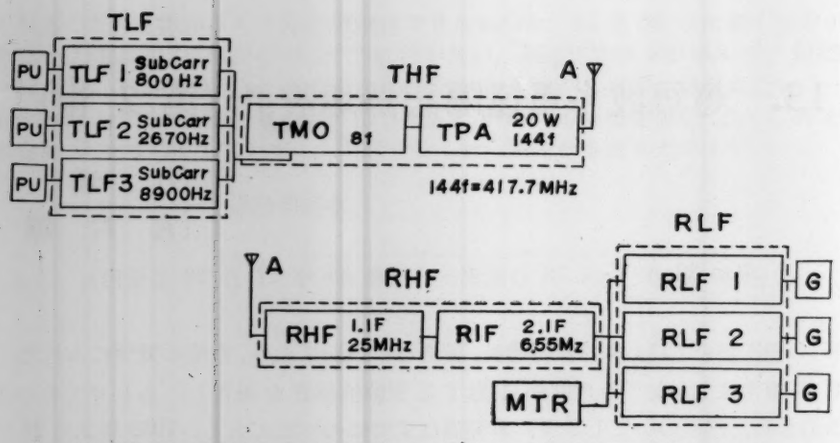

第 15 図 RTS-II の構成概要図. General scheme of RTS-II.

PU, Pick up or transducer. TLF, Transmitter low frequency part. THF, Transmitter high frequency part. TMO, Transmitter master oscillator. TPA, Transmitter power amplifier. A, Aerial. RHF, Receiver high frequency part. RLF, Receiver low frequency part. RIF, Receiver intermediate frequency part. G, Recording galvanometer. MTR, Magnetic tape recorder (Single track commercial set with endless reel. To be stopped by seismic signals and newly set manually.)

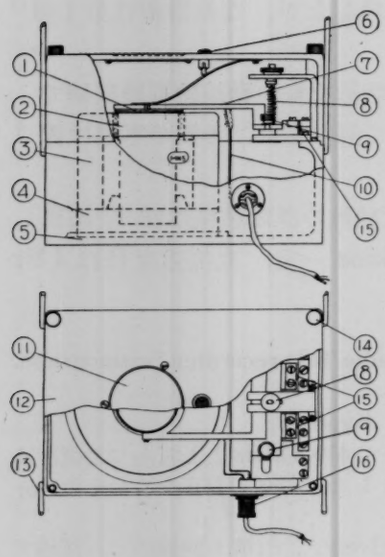

第 16 図 RTS-II に使用した動電型換振器，立面および平面略図.

Elevation and plan of the moving coil type electrodynamic transducer.

1, Moving coil on cylinder tube of plastics. 2, Soft iron pole piece. 3, Permanent magnet, MK-5. 4, Soft iron magnetic circuit. 5, Cast metal case. 6, Temporary cramp of pendulum. 7, Pendulum metal frame. 8, Spiral steel spring. 9, Cramp for transportation. 10, Lead wire from the coil. 11, Peep window of plastics. 12, Cast metal cover. 13, Handle. 14, Fix screw of the cover. 15, Plate steel spring. 16, Socket.

6.2. 送信装置部

6.2.1 送信低周波部 TLF

ELF 段 (第 1 報第 5 図にて 6AU6–6AU6–6AU6–6C4–12AU7–) の最大利得は 10 Hz にて 70 db, 周波数特性は 1～50 Hz にて偏差 ±10 db である. レベル特性は直線部約

40 db，それ以上では飽和特性をしめす．ここは各回線まつたく同様である．

副搬送波変調部における変調特性は，各回線とも，入力信号零のときの周波数（中心周波数）からの周波数偏移 ±20 % をうるための入力電圧がそれぞれ ±20 volts であり，それ以上の入力に対しては上述の飽和特性によつて，過変調をきたすことを防止している．

各回線副搬送波部に挿入された低域濾波器の cut off frequency は第 1 回線 1,000 Hz, 第 2 回線 3,333 Hz 第 3 回線 11,100 Hz である．これは矩形波を正弦波になおすためのものであつて，特にのべるべきことはない．

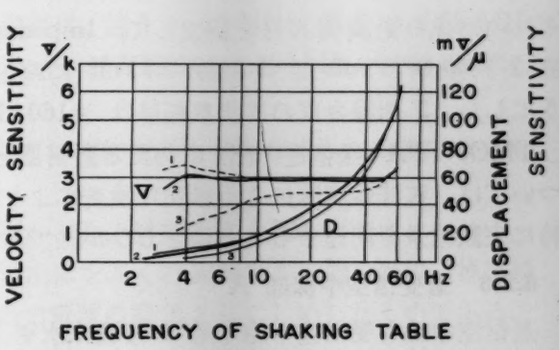

第 17 図　RTS-II に使用した換振器の振動台による特性試験（技術部後藤健一技官による）．
Shaking table test of frequency characteristics of the transducer. (By K. Gotô, Techn. Div., E.R.I.)
Curve V, Velocity sensitivity. (Volt per kine) Curve D, Displacement sensitivity. (Milivolt per micron) 1, Shunt resistance, 80 kilo-ohms. 2, Shunt resistance, 60 kilo-ohms (practically adopted value). 3, Shunt resistance, 30 kilo-ohms.

6.2.2　送信高周波部 THF

送信主発振部 TMO における変調特性は副搬送波周波数の全域（0.4～12 kHz）にわたつて平坦であることが当然のぞましい．しかしながら，変調器の入力回路には蓄電器および変成器がもちいられているため，実際には変調器の入力レベルに対する高周波の周波数偏移は副搬送波の周波数によつてことなつてくる．第 18 図には，この変調特性をしめすために，TMO 変調器の混合器（第 6 図 MIX 段）の入力として，一定電圧を周波数をかえてあたえて変調し，受信機の検波出力（第 12 図 DISCR 段の出力）電圧を測定した結果を図示した．受信高周波部 RHF の特性は後述のごとくほぼ ±150 kHz にわたり直線性をもつているので，変調周波数のひくい部分（0.4～2 kHz）における出力の低下は主として送信の変調特性によるものであるといえる．

このような変調特性を考慮した結果，各回数に規定の周波数偏移をあたえるため，それ

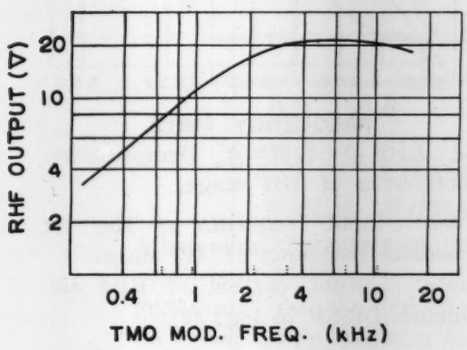

第 18 図　RTS-II 送受信変調復調特性（第 20 図にしめす受信機復調特性を考慮すると，これは送信変調特性をしめすものであるともいえる）．
Modulation and demodulation characteristics of UHF stage.
Abscissa: Frequency of the constant input voltage supplied to the mixer of TMO (MIX in Fig. 6)
Ordinate: Output voltage of the discriminator of RIF (DISCR in Fig. 12).

それの回線の変調器入力を調整して，Impedance 600 ohms として第 1 回線 1.6 volts，第 2 回線 0.75 volt 第 3 回線 0.4 volt におさえ，各回線の周波数偏移を均一にするようにした．3 回線合成の周波数偏移は ±160 kHz にとつた．

TMO, TPA (送信電力部) にわたる逓倍部と 2B94 による送信電力部の電気的性能については，電波監理法による厳密な検査により第1表記載の特性が保証されているので，特に実験結果を記述することはさしひかえておく．

6.2.3 送受信空中線部 A

送信空中線も受信空中線も第 1 号機は水平 8 素子，第 2 号機は垂直複合 5 素子の八木空中線をもちいており，それぞれの特性は八木アンテナ株式会社にて発表されている．実際にもちいられた場所での測定結果は周囲の建物の影響等により，設計とはかなりずれている．第 29 a, b 図にそれぞれの理論値と，受信空中線を送信点の方向に対し 360° 廻転してえられた実験値の一例をしめした．

6.3 受信装置部

6.3.1 受信高周波部 RHF

第 15 図でしめしたように受信高周波部はさらに狭義の高周波部 RHF と中間周波部 RIF とにわかれるが (第 12 図をも参照)，これらをあわせた RHF 全体の特性をしめしたものが第 19 図である．これは RHF 入力つまり受信アンテナからの電圧として信号発生器 SG の出力をいれ，RIF の出力の信号対雑音比 S/N レベルを測定した結果であり，UHF 搬送波の入力レベルが 27 db (1 μV＝0 db とす) 以上あれば，副搬送波増巾段 (SC) の抑圧効果のために，最終段の記録部に充分な S/N をあたえうることをしめしている．

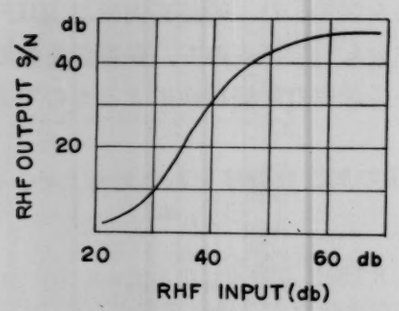

第 19 図 RHF 段のレベル特性．
Level character of RHF stage.
Abscissa: Input voltage of RHF supplied by standard signal generator.
Ordinate: Output voltage of RHF.

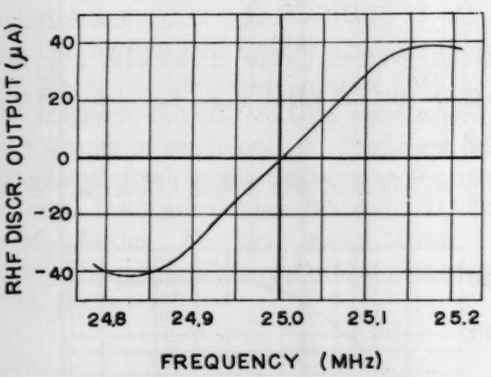

第 20 図 RHF 段の復調特性．Demodulation characteristics of RHF stage.
Abscissa: Input frequency of the 1st intermediate frequency (1. IF) stage.
Ordinate: Output current of RHF discriminator (DISCR in Fig. 12).

RHF, RIF にまたがる第 1，第 2 中間周波部は，第 1 が 25 MHz，第 2 が 6.55 MHz で，この部分の利得として70 db がえられており，減衰特性は ±500 kHz で 40 db になつている．

周波数弁別回路（第 12 図の DISCR）としては対称型のものを採用したので，ひろい周波数範囲にわたり直線性がたもたれている．

2 同調回路の共振周波数は 6 MHz, 7.1 MHz とし，減衰抵抗 3 kΩ とした．

第 20 図はこれらの第 1，第 2 中間周波増巾器をふくむ周波数弁別器の特性（検波特性）を，第 1 中間周波の周波数偏移と検波出力電流の関係としてしめしたものである．

6.3.2　受信低周波部 RLF

前段における第 1 検波の出力は前置増巾器（第 12 図 SC 段 6CB6，第 13 図 SC 段 6BD6）により約 20 db の補償増巾をうけ，各回線別の濾波器をへて分離，増巾され，制限器をへて第 2 検波（副搬送波 FM 検波）にはいり復調され，それぞれ各回線別の地震周波電圧をあたえる．

第 21 図に各回線の濾波器の減衰特性をしめす．記録振巾（ペンがきオツシロ電流計による）において，各回線間相互の漏話を 40 db 以下におさえるには，他回線にあたえる減衰量が 40 db よりおおきいことが必要であり，それ以下のばあいは記録の混入が生ずる．

本装置製作の初期には濾波器に使用した変成器の鉄心の損失とくみたて板の鉄板による漏洩により，最大変調波においては 3 回線を通じ 20 db/octave 程度の減衰しかえられなかつた．（第21図実線）したがつて ELF の最大変調においては第 22 図 b にしめすよう

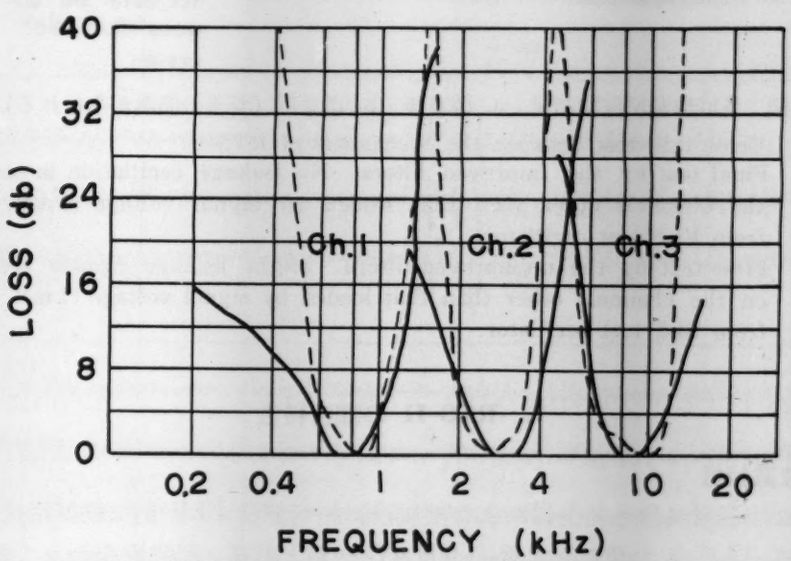

第 21 図　受信副搬送波濾波器の減衰特性．

Attenuation characters of the filters for the 1st, 2nd, and 3rd channels of RLF.
Full lines: for the unimproved design. Broken lines: for the improved design, showing better band pass nature.

に若干の漏話がみられた．その後濾波器の改良をこころみ，定K型の2個を対称T型として接続した設計に変更，これを2段縦続接続したものを計算し，くみたてにおいては補助シャーシを使用し，各部を遮蔽し，さらに全体の遮蔽もおこない，第21図破線のごとき，所要の帯域はばの選択度をうることができた．この改良をおこなつたのちの，各回線の ELF 最大変調の状況は第 22 図 a のごとくであり，40 db 以上の D/U (所要信号対不要信号比) がとれている．

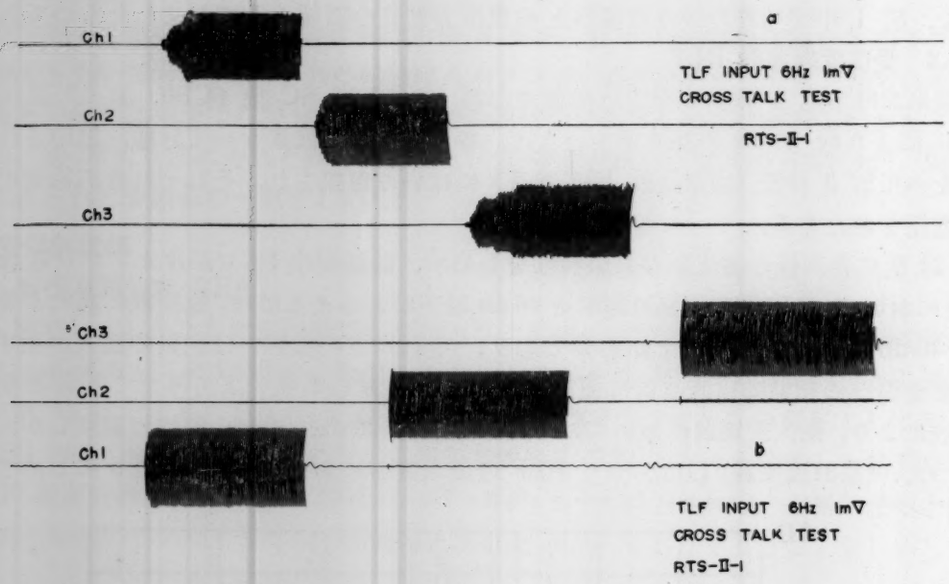

第 22 図　各回線漏話試験結果．a, 改良後　b, 改良前 (若干の漏話がみられる)．
Cross talk test between the 3 channels of RTS-II.

a. Final test by the improved filters. No leakage oscillation is seen on the channels other than that loaded by signal voltage (1 mV, 6 Hz) from ELF test oscillator.

b. First test by the unimproved filters. Slight leakage ripples are seen on the channels other than that loaded by signal voltage (1 mV, 6 Hz) from ELF test oscillator.

7. RTS-II の綜合特性

7.1. 周波数特性

第 23 図は超低周波信号発生器により地震波に相当する ELF 正弦振動電圧を本装置の送信低周波部 TLF 入力端に入力電圧 500 μV 一定として，周波数をかえておくりこみ，受信低周波部 RLF 出力の Pen writer oscillograph による記録振巾をよみとつた結果である．これによつてみるに本装置の綜合周波数特性は ELF 帯 (3～30 Hz) において，ほぼ 10 db 以下の偏差におさまつているといえる．

換振器をふくめた綜合周波数特性としては，第 24 図に，振動台を振巾 0.025 μ 一定

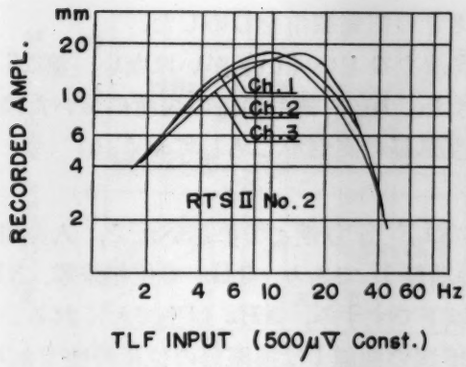

Fig. 23.

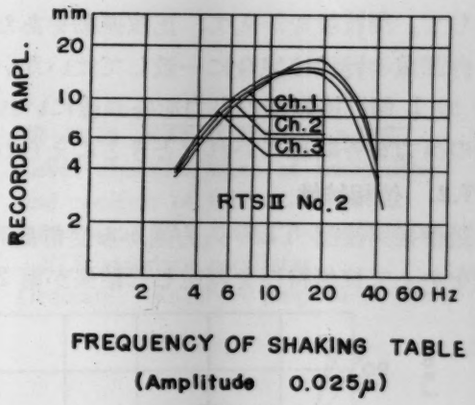

Fig. 24.

第 23 図 RTS-II 送受信部綜合振巾周波数特性.
Amplitude-frequency characteristics of the transmitter and receiver of RTS-II.
Abscissa: Frequency of TLF input (500 micro-volts constant) from standard ELF oscillator.
Ordinate: Recorded amplitude by ink writing oscillograph used. With arbitrary volume set.

第 24 図 RTS-II 綜合振巾周波数特性 (PU をふくむ).
Over all amplitude-frequency characteristics of RTS-II. (Including PU).
Abscissa: Frequency of the shaking table with constant displacement of 0.025 micron.
Ordinate: Recorded amplitude by ink writing oscillograph used. With arbitrary volume set.

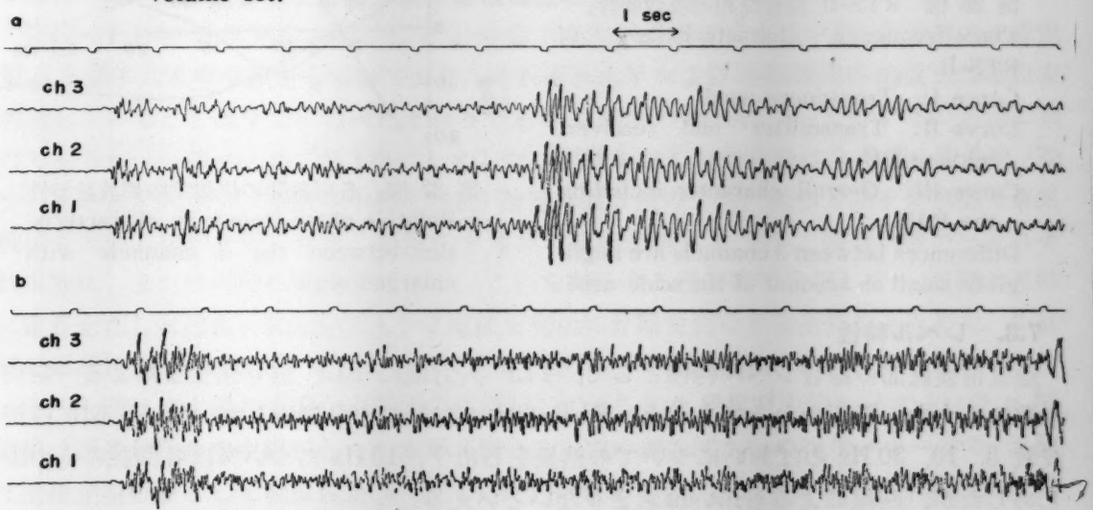

第 25 図 各回線の記録の比較 a, 同一の PU 出力を各回線に, b, 同一場所に並置した 3 台の PU の出力を各回線に, (磁気テープを通じ再生, 記録紙速度 3 cm/sec).
Comparison of overall characters of the 3 channels of RTS-II.
a. An example of seismograms of the 3 channels from one transducer.
b. An example of seismograms of the 3 channels from 3 transducers set on the same place. (Reproduced through the magnetic tape recorder by ink writing oscillograph with paper speed of 3 cm/sec.)

として，周波数をかえて，正弦振動をあたえたときの記録振巾をしめした．

各回線の特性は完全に一致してはいないが，あまりひどいくいちがいはない．第 25 図に a) 1 個の換振器の出力を各回線にいれたときと，b) 3 個の同一の場所においた換振器の出力を各回線にいれたときとにえられた地震記録の実例をしめしておく．

7.2. 位相特性

送信低周波部 TLF 入力端から受信低周波部 RLF 出力端までのあいだで，入力周波数をかえて位相特性を測定した結果が第 26 図の曲線 II であり，3 Hz で位相差零，3 Hz 以下ですすみ，3 Hz 以上でおくれる．第 26 図の曲線 I は換振器の位相特性であり，曲線 III は換振器をふくめた RTS–II 全体の位相特性である．

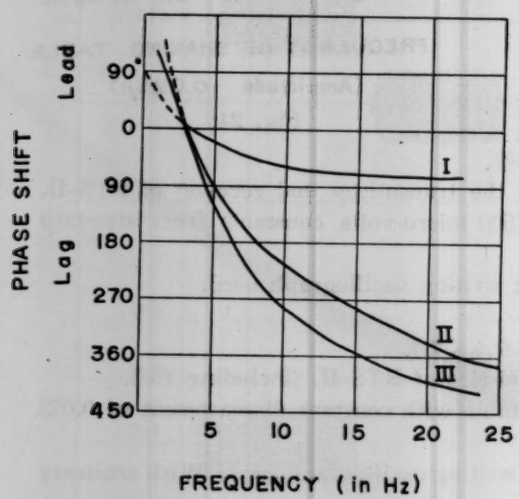

第 26 図 RTS–II 綜合位相周波数特性.
Phase-frequency characteristics of RTS–II.
Curve I: Transducer used.
Curve II: Transmitter and receiver, without PU.
Curve III: Overall character including the P.U.
Differences between 3 channels are negligibly small on account of the scale used.

第 27 図は各回線相互間の位相差を拡大してしめしたもので，3～25 Hz において，第 1，第 3 回線間で 1 号機 (No. 1) では最大 20°，2 号機 (No. 2) で最大 12° である．

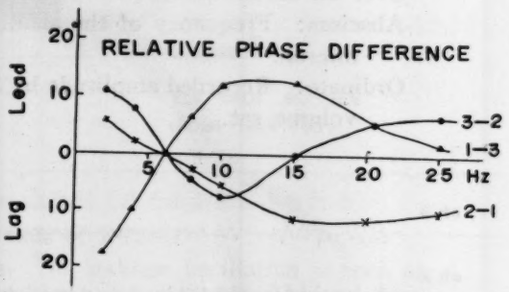

第 27 図 各回線間の位相差の周波数特性.
Relative phase-frequency characteristics between the 3 channels with enlarged scale.

7.3. レベル特性

送受信装置部の綜合レベル特性として，TLF 入力端に ELF 信号発生器による一定周波数の入力を，電圧をかえてあたえ，RLF 出力の記録振巾を測定した．第 28 図には周波数 3, 10, 30 Hz のばあいについての結果をしめす．10 Hz については各回線のものをしめしたが，回線によるちがいはあまりないといえる．

レベル特性は直線性 (対数グラフにて 45° の直線でしめされる) においては RTS–I[3] にくらべおとるが，それだけ記録振巾範囲は拡大されている．波動解析を厳密におこなうには，レベル特性としての直線性が必要であるが，位相的験測に主眼をおけば，多少のひず

3) S. MIYAMURA and M. TSUJIURA, "A VHF Radio Telerecording Seismograph," *Bull. Earthq. Res. Inst.*, **33** (1955), 725–731.

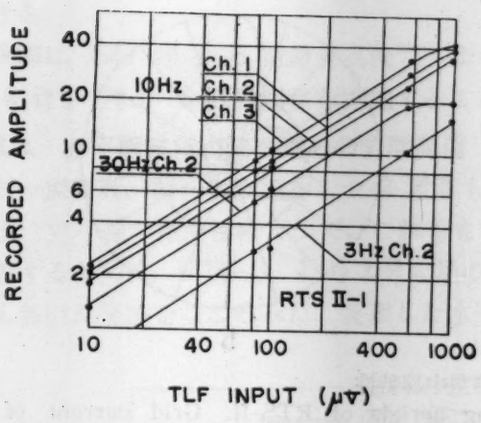

第 28 図 RTS–II 綜合レベル特性.
Level characteristics of transmitter and receiver of RTS–II.
Abscissa: TLF input voltage from ELF standard oscillator.
Ordinate: Recorded amplitude. (mm)

みはあつても，記録範囲のひろいことがのぞまれる．しかし，本装置程度のひずみをもつていても，おおづかみの波動解析には支障がないようである[4].

8. 同一周波電波の空中線による分離

第1報においてのべたように，ひとつのわりあて周波数だけをもちいて，多数の RTS による無人観測点をもうけるための基礎として，空中線の形式によりえられる電波の偏波面の相違と空中線の指向性とを利用して同一周波数の 2 電波を同一地点において分離受信することをこころみた．つぎにその実験結果についてのべる．

8.1. 同一周波数をもつ垂直・水平偏波電波の分離受信

RTS–II の送受信用空中線として 1 号機では水平 8 素子八木空中線，2 号機では垂直複合 5 素子八木空中線をもちいており，それぞれ水平および垂直面内に偏波した電波を利用していることはすでにのべたとおりである．装置の特性についてもすでに記述したのであるが，一応まとめて第1表にしめした．実験をおこなつたのは 1 号機，2 号機（送受ともそれぞれ水平，垂直空中線を接続）送受信機 2 組のうち，送信 2 局を東京都目黒区駒場東大理工学研究所におき，受信点を本郷地震研究所にもうけ，両送信機からそれぞれ単独に，または同時に電波をだして，これを対応する受信機で受信して，両局が同時に電波をだしたばあいにおいても，2 電波を完全に分離受信できる条件をもとめた．2 点間の距離は約 10 km で，みとおしは受信点附近で若干建物にかかる程度である．

第 29 図は空中線の方向を水平面内に廻転してえられた受信空中線のパターンで a 図実線は送受信局の空中線がともに水平 8 素子八木空中線のばあいの受信パターンで，点線は送信用空中線として垂直複合 5 素子八木空中線をもちいたときの水平空中線による受信パターンである．また b 図実線は送受信とも垂直複合 5 素子八木空中線をもちいたときの受信パターンで点線は送信用空中線として水平 8 素子八木空中をもちいたときの垂直空中線の受信パターンである．a, b ともに実線と点線との差は，各受信局において，い

4) K. Aki, M. Tsujiura, M. Hori and K. Gotô, "A Spectral Study of Near Earthquake Waves," *Bull. Earthq. Res. Inst.*, **36** (1958), 71–98.

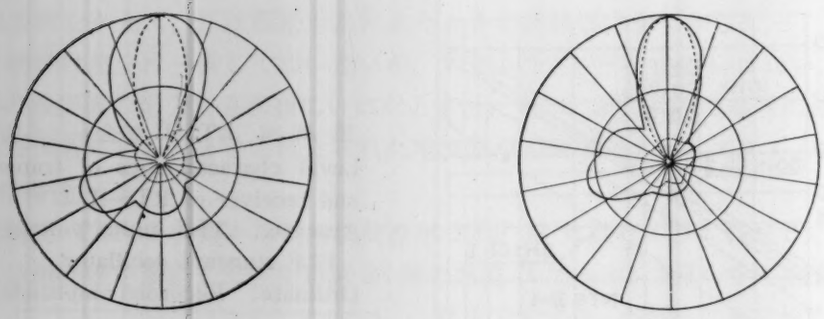

a b

第 29 図 受信空中線特性.

Directional character of the receiving aerials of RTS–II. Grid current of the 2nd limitter of RHF is measured, rotating the receiving aerial. Transmitters of RTS–II, No. 1 (horizontal) and No. 2 (vertical) are set at Komaba, ca. 10 km from Hongo, and the receivers are in E.R.I., Hongo.

a. No. 1. horizontal antenna. Full line, from No. 1 transmitter with horizontal antenna. Dotted line, from No. 2 transmitter with vertical antenna. Broken line, Calculated value from horizontal to horizontal case.

b. No. 2 vertical antenna. Full line, from No. 2 transmitter with vertical antenna. Dotted line, from No. 1 with horizontal antenna. Broken line, Calculated value of from vertical to vertical case.

Small bulge to the left is due to the effect of tall building near E.R.I.

づれもその相手局および非相手局がおのおの単独に電波をだし，これを受信したばあいのレベル差をしめすもので，受信機の第 2 振巾制限器段 (Lim2G) で測定した結果としてしめしてある．これを db に換算すると最大値すなわち，送信点の方向に受信空中線が一致したばあい約 15 db である．したがつて，今回の実験では，同一地点から同一電力で送信した 2 局のそれぞれの受信電界はほぼひとしく，相手局と非相手局の受信電界のレベル差 (D/U) 約 15 db において完全に分離受信が可能である．両送信局からのそれぞれの受信電界がことなるばあい，すなわち送信局 2 局のうちいずれか 1 局の送信電力が強力か，あるいは 1 局が他局にくらべて受信点にちかづいて設置されたばあいは，当然受信電界がことなるわけで，このようなばあいの実験として 1 局を送受信点をむすぶ線上の地点に移動して同様な実験をおこない，実用しうる条件をもとめた．それによると両送信局からの受信電界のレベル差を最高 9 db 以内にすれば完全に分離受信が可能となることもわかつた．もし，いずれか一方の電界がこれ以上に強力であるばあいは，送信電力を低下して送信するか，または送信空中線の方向をずらすか，空中線の高度を調節することなどによつて，受信電界の差を 9 db 以内にすれば 2 電波の分離受信が可能となる．

また両局間の beat は両局の sub-carrier をきつたとき，すなわち無変調の状態では感じられたが，実際には RTS–II ではつねに sub-carrier による変調がおこなわれているのでその影響はない．したがつて同一周波数の RTS 送信局が同一場所乃至同一直線上にあつても，以上の条件のもとでは同一受信基地で完全に分離して受信記録することが

できる．

実際に 1957 年 7～8 月鎌倉高校*** より送信，油壷にて受信して RTS–II, 1 号，2 号 2 台をもちい 6 成分観測を実施することができた.[5]

8.2. 水平偏波指向性 2 電波の分離受信

同一周波数，同一偏波面をもつ 2 電波も受信基地からみてある程度の方位角の差があれば，空中線の指向性によつて，これもまた分離受信が可能とかんがえられる．これを実証するために，RTS–II, 1 号 2 号両局の空中線として，ともに水平 8 素子八木空中線をもちいた実験をこころみた．使用した水平 8 素子八木空中線のパターンは第 29 図 a の

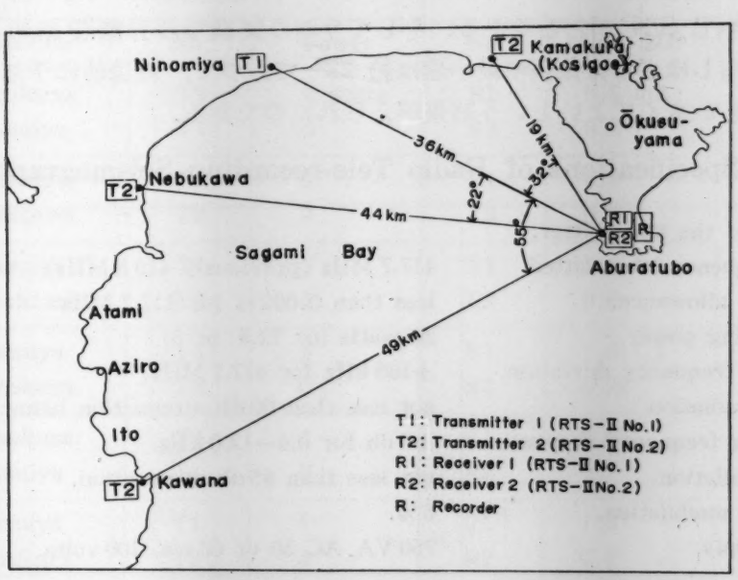

第 30 図　同一周波数，同一偏波電波同時分離受信野外実験要図.
Stations occupied for the experiment of simultaneous separate receiving of radio waves from the transmitters with exactly same frequency and same polarization.

破線にしめすように，電圧半値はば ±20° であつて，受信空中線が充分にたかく，周囲からの反射がなければ，40° 以上の方位角差において，われわれの 2 局は完全に分離受信が可能であるとかんがえられる．実際には装置の抑圧効果のためにこの角度よりさらにちいさくとも良好な結果がえられるものとおもわれる．第 30 図にしめすように，同一周波数の，ともに水平偏波面をもつ送信 2 局のうち 1局 [T1] を二宮に固定し，他局 [T2] を川奈を起点として，受信点油壷にむかいあう相模湾岸を伊東，熱海をへて小田原方面に移動し，ところどころで送信して実験をこころみた．川奈，熱海では充分 2 局の分離

*** 神奈川県立鎌倉高校（神奈川県鎌倉市腰越）の御厚意により，これらの有意義な実験をおこなうことができたことを，特にこの場所をかりてあつく感謝したい．

5) K. Aki, M. Tsujiura, M. Hori, and K. Gotô, *loc. cit.*, 4).

受信ができた．2局がもつとも近接して分離受信が可能であつた根府川と，二宮をすぎて逆にはじめて分離受信が可能となつた，鎌倉における実験の結果を第2表にしめす．入力電界強度は各点とも大体 45 db であつた．これも **8.1** と同様に，2送信局それぞれ単独に，または同時に電波をだし，これを対応する両受信機で受信し，受信機第2振巾制限器段 Lim2G の電流を測定し，充分実用しうる条件をもとめた．これによると自号の受信機 R1 で非相手局 T2 のみの電波を受信したとき（相手局 T1 は送信してないとき）の Lim2G のよみと，相手局 [T1] と非相手局 [T2] の電波を同時に受信したときの Lim2G のよみの差が倍 (6db) 以上あれば分離受信が可能である．しかし，このときおのおの単独の入力電界強度は，ひとしいことが必要であつて，1局がつよいときは第2表 3, 4, のように漏話が生じ S/N がわるくなる．そして今回の実験での分離受信可能なる両送信点の受信点に対しはさむ方位角の最小値は約 22° であつて，理論的に予想された角度よりもはるかにちいさくてよいという結果がえられたのである．

Table 1. Specifications of Radio Tele-recording Seismograph, RTS-II.

Characters of the transmitter.	
Radio frequency transmitted.	417.7 MHz (previously 419.8 MHz)
Frequency allowance.	less than 0.005 % for 417.7 MHz
Transmitting power.	20 watts (or 12.5, or 5)
Maximum frequency deviation.	±160 kHz for 417.7 MHz.
Spurious radiation.	not less than 60 db attenuation below 417.7 MHz.
Modulating frequency response.	±6 db for 0.4 – 12.0 kHz.
Noise modulation.	not less than 45 db attenuation.
Amplitude modulation.	5 %.
Power supply.	750 VA, AC 50 or 60 c/s, 100 volts.
Characters of the receiver.	
Radio frequency received.	417.7 MHz.
Frequency allowance.	less than 0.005 % for 417.7 MHz.
Band width (pass band).	not less than 5 db attenuation at 200 kHz off tune.
Selectivity.	not less than 40 db attenuation at 500 kHz off tune.
Image frequency selectivity.	not less than 60 db attenuation below 417.7 MHz.
Signal to noise ratio.	not lesst han 42 db for input signal 50 db (1μV=0 db) three radian modulation signal.
Power supply.	500 VA, AC 50 or 60 c/s, 100 volts.
Over-all characteristics.	
Number of channels.	3.
Maximum sensitivity.	1 mm/2.5 μV for 10 Hz.
Signal to noise ratio.	40 db. (input signal, 500 μV, 10 Hz)
Cross talk between the channels.	40 db.
Frequency characteristics.	±6 db in 4–40 Hz.
Sensitivity of P.U. used.	20 mV/μ in 10 Hz.

Table 2. Results of the experiments on simultaneous separate receiving of two radio waves with exactly same frequency and same polarization from two transmitters of different azimuths by way of directional character of aerials.

f=417.7 MHz, Aerials: 8 elements horizontal Yagi.
Transmitter No. 1····Ninomiya. Transmitter No. 2····From Kawana, via Ito, Atami, Nebukawa through Ninomiya to Kamakura. Receivers No. 1 & 2····Aburatubo.

No.	Transmitter			Receiver		
	Station	No.	Power	No.	Lim. 2G*	S/N
1	Nebukawa	T2	4 watts	R1	0.5 mA	
	Ninomiya	T1	0	R2	0.6	
	Ninomiya	T1	5	R1	0.9	
	Nebukawa	T2	0	R2	0.2	
	Ninomiya	T1	5	R1	1.0–1.1	
	Nebukawa	T2	4	R2	0.6	> 40 db
2	Ninomiya	T1	5	R1	1.0–1.1	
	Kamakura	T2	0	R2	0.22	
	Kamakura	T2	4	R1	0.62	
	Ninomiya	T1	0	R2	0.7	
	Ninomiya	T1	5	R1	1.3	
	Kamakura	T2	4	R2	0.7	> 40 db
3	Ninomiya	T1	5	R1	1.1	
	Kamakura	T2	0	R2	0.22	
	Kamakura	T2	14	R1	1.0	
	Ninomiya	T1	0	R2	1.0	
	Ninomiya	T1	5	R1	1.4	
	Kamakura	T2	14	R2	1.0	< 6 db
4	Ninomiya	T1	5	R1	1.1	
	Kamakura	T2	0	R2	0.22	
	Kamakura	T2	9	R1	0.7	
	Ninomiya	T1	0	R2	0.75–0.8	
	Ninomiya	T1	5	R1	1.2–1.25	
	Kamakura	T2	9	R2	0.8	=30 db

* Lim 2G means grid current of 2nd limitter of the receiver.

13. *UHF Multi-channel Radio Tele-recording Seismograph. Part II.*

By Masaru TSUJIURA and Setumi MIYAMURA,
Earthquake Research Institute.

In Part I a general description of construction and performance of the apparatus, RTS-II was given. Here in Part II data of experiments obtained for the test of RTS-II are described in some detail.

Section 6 gives characteristics of the constituent parts of the apparatus. Section 7 shows over-all characters of RTS-II. In Section 8 experimental results of simultaneous separate receiving of two radio waves with exactly same frequency and with perpendicular or parallel polarization, are given.

昭和34年5月10日印刷
昭和34年5月15日発行

東京都文京区本富士町一番地
東京大学構内
編纂兼
発行者　東京大学地震研究所

東京都新宿区山吹町一八四番地
印刷者　笠井康頼

東京都新宿区山吹町一八四番地
印刷所　株式会社国際文献印刷社

売捌所
東京都中央区日本橋通二丁目六番地
丸善株式会社

Sold by Maruzen Co., Ltd., Nihonbashi-dôri, Chûô-ku, Tôkyô.
Price of this copy: 640 Yen. (Postage exclusive.)